UNIVERSIDAD DE VALENCIA

DEPARTAMENTO DE FÍSICA ATÓMICA, MOLECULAR Y NUCLEAR

INSTITUTO DE FÍSICA CORPUSCULAR

UNIVERSITAT DE VALÈNCIA

High spin studies
in Bromine nuclei with $N\simeq Z$

TRINITARIO MARTÍNEZ PÉREZ

TESIS DOCTORAL

JUNIO 2003

UNIVERSITAT DE VALÈNCIA

INSTITUT DE FÍSICA CORPUSCULAR

DEPARTAMENT DE FÍSICA ATÒMICA,
MOLECULAR I NUCLEAR

High spin studies

in Bromine nuclei with N$\simeq$Z

TRINITARIO MARTÍNEZ PÉREZ
TESIS DOCTORAL
JUNIO 2003

Berta Rubio Barroso, Científico Titular del Consejo Superior de Investigaciones Científicas (CSIC)

CERTIFICA: Que la presente memoria **"High spin studies in Bromine nuclei with N$\simeq$Z"** ha sido realizada bajo su dirección en el Instituto de Física Corpuscular (Centro Mixto Universidad de Valencia - CSIC) por **Trinitario Martínez Pérez** y constituye su Tesis para optar al grado de Doctor en Ciencias Físicas.

Y para que así conste, en cumplimiento con la legislación vigente, presenta ante la Facultad de Físicas de la Universidad de Valencia la referida Tesis, firmando el presente certificado en Burjassot (Valencia) a 25 de Junio de 2003.

Fdo. Berta Rubio Barroso

"Esiste nella nostra mente una sorta di
confine che nella vita di tutti i giorni
ci manca lo stimolo necesario a raggiungere,
ma superato il quale tutto si fa possibile"

P.Maurensig. "La variante Lüneburg"

A mis padres y a mi familia

Agradecimientos

Esta tesis se ha podido llevar a cabo gracias a la financiación económica por parte de las siguientes instituciones:

-la Comunidad Europea, dentro del programa de formación y movilidad de investigadores TMR, contrato n. HPRI-1999-CT-00083,

-el INFN, mediante un contrato de trabajo de Tecnólogo nivel III, una beca Post-Doctoral, y varios Fondos FAI,

-el CSIC, a través de los proyectos de investigación otorgados al grupo de Espectroscopía Gamma del IFIC.

En primer lugar, quiero agradecer a Berta Rubio por haber dirigido este trabajo de tesis, por todo lo que he aprendido de la física nuclear trabajando juntos y por haberme ofrecido, junto a Jose Luis Tain, la oportunidad de formar parte del grupo de Espectroscopía Gamma del IFIC que ambos coordinan. Les agradezco toda la dedicación y experiencia que han compartido conmigo.

Secondly, I am also very grateful to W. Gelletly for the scientific advices, lesons and support during all the thesis period. Vorrei anche ringraziare Giacomo de Angelis e Andres Gadea che hanno partecipato in questa ricerca aportando le sue conoscenze e i suoi commenti ed aiuti. Grazie a loro due sono riuscito a rimanere in questo laboratorio per tutti questi anni.

In seguito, vorrei ringraziare tutto il gruppo di spettroscopia gamma dei Laboratori Nazionali di Legnaro e della sezione dell'INFN a Padova così come al personale tecnico che hanno fatto possibile e piacevole tanti anni di ricerca scientifica con GASP ed EUROBALL: M. Axiotis, D. Bazzacco, F. Brandolini, M. De Poli, E. Farnea, R. Isocrate, S.M. Lenzi, S. Lunardi, N. Marginean, R. Menegazzo, D.R. Napoli, P. Pavan, C. Rossi-Alvarez, D. Rosso, P. Spolaore, C. Ur e R. Venturelli. E come no a tutti i ricercatori che hanno passato parte della loro formazione in queste sede: N. Belcari, Th. Kröll, N.H. Medina e specialmente Zsolt Podolyák. Ringrazio in modo particolare all'INFN e alla direzione dei Laboratori Nazionali di Legnaro per il supporto economico e scientifico ricevuto durante questi anni. Al personale tecnico ed amministrativo per la disponibilità e la cordialità di tanti giorni.

I am also very grateful to the Research Staff of the HIRBF Facility at the Oak Ridge National Laboratory for the help during the perfomance of the ^{71}Kr experiment, in particular to C.J. Gross, D.C. Radford, A. Galindo-Uribarri and C-H. Yu. In this sense the help of the staff of the Vivitron facility at the IReS

(Strasbourg) is also grateful, in particular many thanks to D. Curien, P. Bednarczyk and J. Devin. I would also thank all the participants in the experiments and the technical staff of both laboratories.

Quiero tambien recordar y agradecer a los miembros y amigos del grupo Gamma del IFIC: Pepe Bea y Luis M. Garcia-Raffi, quienes me ayudaron a iniciar esta aventura y a quienes tanto debo (especialmente a Pepe y sus lecciones en La Fe), Daniel Cano y su amistad durante “aquellos maravillosos años en la casa de Godella”, Alejandro Algora (y por supuesto su familia) con quien nos une una buena amistad ademas de muchos buenos momentos en Valencia, en Italia y adonde nos lleve este mundillo. Luis Caballero y Kike Nacher (the one) (futuros controladores aereos de categoria espacial), sin olvidarme de Jorge Agramunt, Cesar Domingo y M. Kaci.

Vorrei anche ringraziare tutti i miei amici di Padova: Mixalis e Carla, Moreno, Francesca, Luisa e specialmente Patrizia che tanto mi hanno aiutato con la loro amicizia e il loro sostegno. Grazie anche a Roberta, Federica, Alessandro, Gloria, Sofia, Davide, Marco, Matteo, Simonetta, i vicini (e Mosè), Alda e il suo appartamento e tanti altri, perchè hanno fatto che questi anni siano stati felici e indimenticabili.

Agradezco muchisimo a Inma todo su esfuerzo y amistad para animarme a seguir escribiendo y no abandonar en esta empresa. También quiero recordar y agradecer a todos mis amigos de Valencia: Carmen, Verdú, Jesús, Josefer, Maria, Yolanda, Javi, y tanto otros, porque también ellos pusieron su granito de arena en este curro.

Por último y no por eso menos, agradezco de todo corazón a mis padres y hermanos todo el apoyo y el cariño que me han dedicado durante todo este tiempo fuera de casa. Esta tesis esta dedicada a ellos.

Resumen del trabajo

1. Introducción

La motivación del trabajo expuesto en la presente tesis doctoral se basa fundamentalmente en el interés que desde hace años han despertado los núcleos de la región de masa A$\sim$60-80 (con N$\simeq$Z). En dicha región, debido a la baja densidad de niveles de partícula independiente, la forma de los núcleos depende fuertemente de la configuración de los nucleones de valencia. Dichas formas varian no solo con el número de partículas sino además con la energía de excitación y el momento angular (espín).

El espaciado en energía de los niveles de partícula independiente en función de la deformación dado por los modelos de campo medio presenta una serie de "gaps" similares (aunque más pequeños) a los gaps que caracterizan los núcleos mágicos en el modelo de capas esférico. Estos gaps gobiernan la estructura de los núcleos en esta región. Dichos gaps se observan para valores de N,Z=34,36,38,40 y para diferentes valores de β, dando lugar a deformaciones estables en el estado fundamental para ciertos núcleos. Por ejemplo, se ha predicho que el estado fundamental de algunos isótopos de Kr, Rb y Sr sea muy deformado. Para otros núcleos la teoría predice coexistencia de forma oblada-prolada, así como fenómenos de "shape-mixing". Muchas de las predicciones teóricas han sido confirmadas experimentalmente, por ejemplo una banda con deformación oblada ha sido documentada en el ^{72}Kr (N=Z=36) y en los isótopos más ligeros de Se (Z=34). Deformación prolada ha sido en cambio observada en los isótopos ligeros de Sr (Z=38) y Rb (Z=37). Fenómenos de "shape-coexistence": estructuras proladas y obladas se han visto en el mismo núcleo en el caso del ^{82}Sr, o mezcladas con la banda del estado fundamental en el caso del ^{74}Kr.

Esta región de núcleos ricos en protones, presentan además un gran interés desde el punto de vista astrofísico. En concreto, estos núcleos intervienen en el proceso de nucleosíntesis que permiten explicar las abundancias anómalas de algunos isótopos ricos en protones con masa A$\sim$100, el llamado proceso de captura rápida de protones (proceso rp). Este tipo de reacciones tiene lugar en condiciones de alta densidad y alta temperatura de la materia estelar, como por ejemplo en las llamadas *novas* o en la zona de acreción que se produce en sistemas binarios con un componente masivo (estrella de neutrones o enana blanca).

Este tipo de procesos y reacciones son evaluados mediante cálculos llamados "network reaction rate" y para obtener buenos resultados es importante que las condiciones iniciales sean lo más precisas posible. Por este motivo el conocimiento de las propiedades estáticas y dinámicas de los núcleos implicados es de fundamental importancia.

En nuestro trabajo nos hemos centrado en el estudio de los dos isótopos ligados más ligeros del Bromo, el ^{71}Br y ^{70}Br. Estos núcleos son interesantes desde el punto de vista experimental así como desde el punto de vista teórico. Al ser núcleos lejanos al valle de la estabilidad y por tanto dificiles de poblar, la puesta a punto de las técnicas de detección y de análisis de datos suponen un reto para los actuales sistemas de detección. Así el uso de grandes "arrays" de detectores gamma acoplados a eficientes sistemas de detección de las partículas evaporadas en la reacción permite acceder de modo unívoco a estos núcleos poblados con secciones eficaces muy bajas. Desde el punto de vista teórico, los cálculos realizados hasta la fecha presentan divergencias respecto a asignar una deformación de un tipo u otro al estado fundamental de los núcleos ligeros en los que se predice una transición de la forma prolada a la forma oblada al disminuir del número de neutrones. Así algunos autores [Ben84] preveían una deformación oblada para el estado fundamental del ^{71}Br. Por otro lado, un primer estudio experimental [Arr90] parecía indicar deformación prolada deducida por la presencia de una banda yrast con rasgos de deformación prolada similar a isótopos más pesados $^{73-77}$Br. Un estudio más detallado de los estados de bajo espín del núcleo se hace necesario para testear y mejorar los modelos utilizados.

El estudio del núcleo impar-impar ^{70}Br, supone un gran aliciente en espectroscopía gamma por dos razones principales: por una parte siendo un núcleo autoconjugado (N=Z), impar-impar se caracteriza por la competición a baja energía de excitación de estados con isospín T=1 y estados con T=0. El estudio de estos estados y de las posibles transiciones entre ellos es uno de los aspectos que más interés despierta en la física nuclear hoy en día por cuanto puede dar una indicación de las posibles características de la interacción residual protón-neutrón con T=0. Por otro lado, el núcleo ^{70}Br se encuentra cercano a la llamada "proton drip-line", por donde circula el proceso rp, en este sentido el conocimiento detallado de los estados de bajo espín así como la ubicación de posibles estados isoméricos, junto al estudio de propiedades estáticas (masa, vida media, etc), es de una especial relevancia para la mejora de los modelos de cálculo de la tasa de reacción ("network reaction rates calculation").

2. Antecedentes

Anteriormente a nuestro trabajo había varios estudios relacionados con el núcleo ^{71}Br. En un trabajo similar al nuestro [Arr90] pero con un nivel de sensibilidad menor, los estados de alto espín fueron poblados mediante varias reacciones,$^{40}Ca+^{34}S$, $^{58}Ni+^{16}O$ and $^{40}Ca+^{35}Cl$. Usando técnicas de espectroscopía gamma, Arrison *et al.* identificaron las principales transiciones que desexcitan los estados yrast del núcleo ^{71}Br. Basandose en las coincidencias γ-γ y la coincidencia con partículas evaporadas establecieron un primer esquema de niveles así como las intensidades de dichas transiciones. El espín y paridad de los diferentes estados fueron deducidos asumiendo el valor de espín y paridad de $9/2^+$ para el estado isomérico a 759 keV de energía de excitación por una parte y a través de las distribuciones y correlaciones angulares (DCO) de las diferentes transiciones por otra.

Los resultados más significativos obtenidos por Arrison *et al.* son: el espín del estado fundamental asignado como $5/2^-$ a diferencia de los otros isótopos ligeros de Bromo de masa impar, cuyos valores son $3/2^-$ en el ^{75}Br y $1/2^-$ en el ^{73}Br. La banda yrast observada correspondiente a una banda rotacional basada en el orbital $g_{9/2}$ (paridad positiva) similar a las bandas observadas en los otros núcleos de masa impar en esta región. La vida media del estado $9/2^+$ deducida a partir de las coincidencias estimada en $T_{1/2}$=32.5 (25) ns

Por lo que respecta al núcleo ^{70}Br, nuestro estudio constituye la primera identificación de los estados excitados [Dea01], ya que un trabajo anterior [Bor99] fue retirado por identificación errónea. Estudios sobre la desintegración β han sido publicados anteriormente [Vos81, Bur88, Pie00] y sus resultados muestran la existencia no sólo de la desintegración superpermitida ($0^+ \rightarrow 0^+$) del estado fundamental del ^{70}Br al estado fundamental del ^{70}Se, sino que también la desintegración beta de un estado isomérico con vida media $T_{1/2}$=2.2 (2) s. Dicho estado ha sido interpretado a través de la sistemática de los núcleos N=Z impar-impar, como el estado más bajo en energía de excitación con isospín T=0. De entre los posibles estados generados al acoplar un protón y un neutrón en los orbitales por encima del nivel de Fermi,$f_{5/2}p_{1/2}g_{9/2}$, las reglas de selección Gamow-Teller de la desintegración al estado 4604.1 keV del ^{70}Se con espín I^π=(8,9^+) respalda la asignación del estado isomérico como I^π=9^+.

Otro trabajo sobre los estados excitados del ^{70}Br, [Jen02], realizado contemporáneamente al nuestro ha sido publicado durante la redacción de esta tesis. En él se obtienen prácticamente los mismos resultados a baja energía de excitación excepto para los estados con isospín T=1 y aporta nuevos resultados en la parte de alto espín, donde gracias a una reacción llevada a cabo a mayor energía y mayor momento angular, consiguen poblar la banda rotacional construida sobre el estado isomérico I^π=9^+.

3. Técnicas experimentales

El mejor modo de acceder a estos núcleos alejados del valle de la estabilidad y poblar estados de alto espín es mediante reacciones de fusión-evaporación de iones pesados que permiten formar el núcleo compuesto con alta enegia de excitación y alto momento angular. Este sistema compuesto, una vez formado se desexcita mediante la evaporación de partículas ligeras, en un proceso estadístico: el tipo de partículas evaporadas (cargadas y/o neutras) depende de la energía disponible, de la densidad de estados así como de la energía de ligadura de dichas partículas. Una vez llegados al umbral de emisión de partículas el sistema ha alcanzado uno de los posibles núcleos residuos y se encuentra en un estado a alta energía del que se desexcita a través de la emisión de radiación gamma estadística, de alta energía y de radiación gamma no estadística en la zona yrast hasta alcanzar el estado fundamental del núcleo residuo.

Mediante la detección y posterior identificación de las características de la radiación gamma es posible construir el esquema de niveles del núcleo objeto del estudio y así poder determinar sus propiedades estructurales que serán objeto de posterior comparación con los modelos teóricos.

En este tipo de reacciones de núcleo compuesto, el proceso de evaporación de partículas es un proceso estadístico lo cual da lugar a que en la misma reacción se pueblen diferentes canales según el número y el tipo de partículas evaporadas. De este modo se obtienen transiciones gamma pertenecientes a diferentes núcleos y que a menudo son muy próximas en energía. Para resolver o minimizar el problema de la “contaminación” se recurre a diferentes métodos. Por un lado se evalúa la energía y la combinación de haz-blanco de modo que la sección eficaz de producción del núcleo de interés sea optimizada, esto se consigue mediante el uso de códigos estadísticos ampliamente contrastados (Hivap, Cascade, etc). Por otro lado el empleo de la llamada “Técnica de coincidencias” mediante el uso conjunto de multidetectores o “arrays” de gammas y de partículas ligeras, cargadas y neutras, permite seleccionar el canal de producción del núcleo de interés y reducir de este modo la contaminación.

Otro tipo de consideraciones, como son la pureza del blanco, el correcto funcionamiento de los detectores y el correcto alineamiento temporal entre ellos es de vital importancia a la hora de analizar los resultados obtenidos. La cadena electrónica asociada a los detectores y el sistema de adquisición de datos, constituyen otra de las piezas fundamentales del exito de un experimento.

3.1 Detectores

Como hemos comentado, el objetivo de este trabajo de tesis es identificar la radiación gamma emitida en la desexcitación del núcleo en estudio utilizando para ello un detector que nos de la mayor información posible y más fiable. Para tal fin se han empleado algunos de los más eficientes espectrómetros de radiación gamma. Las principales características que hacen a estos detectores especiales son: la eficiencia, la buena resolución energética, la buena resolución temporal, la alta granularidad y la simetría. Estas características permiten a su vez, obtener información de la radiación emitida como son la energía y la intensidad, el carácter y la multipolaridad, etc.

En concreto, en los experimentos que componen este trabajo de tesis, los espectrómetros utilizados han sido el ”array” GASP, que cuenta con una eficiencia absoluta del 3% para una energía de 1.33 MeV en su configuración estándar, el ”array” EUROBALL en sus fases III (Legnaro) y IV (Strasbourg), con una eficiencia del 9% y el ”array” CLARION que cuenta con una eficiencia de casi el 2.5 % para dicha energía.

Es de especial importancia a la hora de identificar el núcleo de interés de entre todos los producidos en la reacción los detectores auxiliares (ancillary detectors). Éstos permiten seleccionar el canal y así limpiar en gran medida las matrices gamma-gamma. Los detectores auxiliares usados han sido de varios tipos: detectores de partículas cargadas ligeras, como ISIS, EUCLIDES y HyBALL; detectores de neutrones como N-Ring y Neutron-WALL y el separador de masa, RMS, al que se acoplan un detector PSAC y una cámara de ionización (IC). Una amplia descripción de estos sistemas se puede encontrar en el capítulo 3 de esta tesis.

3.2 Experimentos Los resultados obtenidos en esta tesis han sido fruto de varios experimentos llevados a cabo en algunos de los laboratorios dedicados a la investigación en física nuclear en Europa y en los EEUU. Así hemos realizado tres experimentos en el Laboratorio Nacional de Legnaro (LNL, Italia), uno en el Instituto de Investigaciones Subatómicas de Estrasburgo (IReS, Francia) y otro en el Laboratorio Nacional de Oak Ridge (EEUU).

En la siguiente tabla resumimos los experimentos realizados así como las principales características de cada uno de ellos.

reacción	^{40}Ca(^{40}Ca,2α1p)^{71}Br			^{40}Ca(^{32}S,2p1n)^{70}Br	
Energía:	160 MeV	180 MeV	156 MeV	95 MeV	95 MeV
Target:	1mg/cm^2	1mg/cm^2	0.5mg/cm^2	1mg/cm^2	1mg/cm^2
Backing:	12mg/cm^2	16mg/cm^2	-	14mg/cm^2	13mg/cm^2
Set-up	GASP	EUROBALL	CLARION	GASP	EUROBALL
	ISIS	ISIS	HYBALL	ISIS	EUCLIDE
			PSAC IC	N-Ring	N-WALL
eficiencia:	ϵ_γ=0.03	ϵ_γ=0.09	ϵ_γ=0.026	ϵ_γ=0.03	ϵ_γ=0.09
	ϵ_p=0.40	ϵ_p=0.45	ϵ_p=0.68	ϵ_p=0.53	ϵ_p=0.60
	ϵ_α=0.20	ϵ_α=0.22	ϵ_α=0.43	ϵ_α=0.29	ϵ_α=0.32
				ϵ_n=0.03	ϵ_n=0.30

Table 1: *Resumen de los experimentos realizados durante el trabajo de tesis.*

4. Análisis de datos

Las señales de los diferentes detectores son convertidas y registradas por el sistema de adquisición de datos cada vez que se cumplen las condiciones impuestas al sistema, es decir cada vez que se verifica la condición de “trigger”. Los datos son además almacenados suceso a suceso en cintas para su posterior análisis. El proceso de análisis “off-line” comprende diversas fases: a) preparación, donde los datos son sometidos a un proceso de verificación, b) creación de matrices, donde los datos de los diferentes detectores son seleccionados en función de unos criterios establecidos por el usuario, c) análisis de las matrices propiamente dicho que proporcionará los resultados.

En la fase de preparación hemos realizado el alineamiento o “gain matching” de los detectores y la calibración de algunos de los parámetros como la energía y el tiempo de los detectores gamma y la corrección Doppler en el caso del experimento en Oak Ridge donde el target utilizado no tenía backing. Posteriormente hemos determinado el tipo de partículas evaporadas estableciendo “gates” bidimensionales en combinaciones adecuadas de los parámetros de los detectores de partículas.

Con estas condiciones, en la siguiente fase se preparan los diferentes tipos de matrices que proporcionarán la información necesaria. Así para identificar las transiciones gamma pertenecientes al núcleo en estudio hemos creado matrices γ-γ con diferentes condiciones en las partículas evaporadas, con estas matrices y con el posterior estudio de las coincidencias en el cubo γ-γ-γ hemos establecido el esquema de niveles de los núcleos en estudio. La intensidad de las transiciones ha sido determinadas con la ayuda de la calibración en eficiencia.

Para la determinación del carácter y multipolaridad de las transiciones hemos creado matrices de distribución angular y de correlaciones angulares (DCO y PDCO) donde en un eje se representa los gammas coincidentes detectados en los detectores situados a un ángulo polar determinado y en el otro eje los gammas detectados bajo otro ángulo, básicamente $E_\gamma(\theta_1)$ vs $E_\gamma(\theta_2)$.

5. Resultados

Del análisis de las matrices γ-γ con condiciones en las partículas y del cubo γ-γ-γ, así como de las distribuciones y correlaciones angulares hemos obtenido una serie de resultados para los núcleos objeto de estudio en este trabajo de tesis, que resumimos a continuación.

5.1 Resultados del ^{71}Br. El ^{71}Br ha sido estudiado principalmente en dos reacciones ^{40}Ca+^{40}Ca llevadas a cabo en el tandem XTU del Laboratorio Nacional de Legnaro (Italia), a energías de laboratorio de 160 y 180 MeV respectivamente. La radiación gamma emitida ha sido detectada haciendo uso de dos de los espectrómetros gamma más completos que existen en la actualidad: GASP y EUROBALL.

Del análisis de los datos experimentales registrados en ambos experimentos hemos obtenido una serie de resultados que por un lado modifican en parte anteriores resultados sobre la estructura del ^{71}Br deducidos por otros investigadores [Arr90] y por otro lado amplian nuestro conocimiento sobre dicha estructura al obtener un mayor número de resultados. Estos resultados han sido deducidos mediante el análisis de matrices γ-γ en coincidencia con partículas cargadas y de cubos γ-γ-γ con y sin coincidencia de partículas. Así hemos construido el esquema de niveles basándonos en “gates” sobre transiciones conocidas y comparando las nuevas en diferentes matrices, con diferentes condiciones de partículas con el fin de evitar posibles contaminaciones con otros núcleos. Las intensidades de las transiciones han sido establecidas a través de la proyección cuando ha sido posible y a través de “gates” en aquellos casos en los que la proyección no era suficientemente limpia.

La información sobre la multipolaridad de las transiciones ha sido obtenida mediante el análisis de las matrices creadas para el estudio de las distribuciones angulares. Esto ha sido posible para las transiciones más intensas. Para las transiciones menos intensas ha sido muy útil el análisis de las matrices de DCO, creadas a partir de los Clover y los Clusters, a 90 y 153 grados respectivamente, permitiendo así obtener el cociente DCO. La polarización se ha obtenido a partir de la medida de la asimetría deducida para las transiciones más intensas gracias a la sensibilidad a la polarización de los detectores Clover.

Con estos resultados ha sido posible establecer el espín y paridad de los estados deducidos en el esquema de niveles del ^{71}Br. En la siguiente tabla 2 se resumen los resultados obtenidos, y en la figura 1 se muestra el esquema de niveles.

Table 2: Resumen de los principales resultados de las transiciones γ pertenecientes al núcleo ^{71}Br.

E_x (keV)	E_γ	Intensidad	R_{DCO}	A_2	A_4	Asimetría	$I_i^\pi \rightarrow I_f^\pi$
9.7 (2)	not obs.						$1/2^- \rightarrow 5/2^-$
208.2 (2)	198.4	854 (30)	0.35 (3)			-0.17 (4)	$3/2^- \rightarrow 1/2^-$
	208.1	239 (15)	0.70 (10)			-0.04 (8)	$3/2^- \rightarrow 5/2^-$
407.3 (2)	199.5	42 (30)					$3/2^- \rightarrow 3/2^-$
	397.7	103 (20)	1.5 (2)[d]			<0	$3/2^- \rightarrow 1/2^-$
	407.3	203 (20)	1.1 (2)[d]			<0	$3/2^- \rightarrow 5/2^-$
615.9 (3)	208.9	30 (10)					$3/2^+ \rightarrow 3/2^-$
	408.1	145 (20)	1.4 (1)[d]			0.01 (4)	$3/2^+ \rightarrow 3/2^-$
670.2 (2)	54.3	107 (32)[a]					$5/2^+ \rightarrow 3/2^+$
	263.1	122 (24)	0.31 (11)			0.10 (5)	$5/2^+ \rightarrow 3/2^-$
	462.2	359 (24)	0.65 (6)			0.002 (30)	$5/2^+ \rightarrow 3/2^-$
	669.8	261 (7)	0.98 (11)			-0.11 (4)	$5/2^+ \rightarrow 5/2^-$
759.6 (2)	89.8	456 (91)[b]					$9/2^+ \rightarrow 5/2^+$
	759.2	279 (3)	0.85 (8)			-0.12 (5)	$9/2^+ \rightarrow 5/2^-$
892.5 (2)	133.6	89 (4)[c]					$7/2^+ \rightarrow 9/2^+$
	223.1	135 (12)	0.87 (9)			-0.08 (12)	$7/2^+ \rightarrow 5/2^+$
	276.7	17 (10)					$7/2^+ \rightarrow 3/2^+$
929.4 (3)	522.4	47 (10)	1.0 (7)			>0	$5/2^- \rightarrow 3/2^-$
	721.5	40 (10)	0.8 (3)				$5/2^- \rightarrow 3/2^-$
	929.3	103 (10)	1.2 (4)			<0	$5/2^- \rightarrow 5/2^-$
952.0 (3)	952.2	127 (16)	0.6 (2)				$(7/2^-) \rightarrow 5/2^-$
1020.7 (5)	613.3	24 (4)					$(7/2^-) \rightarrow 3/2^-$
1115.3 (3)	907.2	407 (30)	1.09 (7)	0.334 (61)	-0.036 (82)	0.06 (4)	$7/2^- \rightarrow 3/2^-$
	1114.7	66 (10)					$7/2^- \rightarrow 5/2^-$
1175.3 (3)	282.1	45 (12)	0.6 (3)[d]				$9/2^+ \rightarrow 7/2^+$
	415.3	83 (3)					$9/2^+ \rightarrow 9/2^+$
	504.7	69 (12)					$9/2^+ \rightarrow 5/2^+$
1199.3 (7)	991.7	126 (18)	0.8 (3)				$(7/2^-) \rightarrow 3/2^-$
1492.1 (3)	316.4	38 (3)					$11/2^+ \rightarrow 9/2^+$
	598.3	168 (25)	2.5 (9)[d]				$11/2^+ \rightarrow 7/2^+$
1492.7 (4)	562.7	169 (4)	1.0 (6)			>0	$9/2^- \rightarrow 5/2^-$
1497.3 (3)	737.7	1000 (47)	1.19 (5)	0.255 (35)	-0.052 (46)	0.05 (2)	$13/2^+ \rightarrow 9/2^+$
1682.3 (6)	662.8	21 (4)					$(11/2^-) \rightarrow (7/2^-)$
1714.2 (3)	222.1	12 (5)					$11/2^- \rightarrow 9/2^-$
	514.5	105 (9)	0.6 (3)				$11/2^- \rightarrow (7/2^-)$
	598.9	389 (33)	1.16 (7)	0.402 (47)	-0.019 (64)	0.08 (3)	$11/2^- \rightarrow 7/2^-$
	762.0	113 (8)	0.89 (20)				$11/2^- \rightarrow (7/2^-)$
	955.0	113 (16)	0.4 (3)				$11/2^- \rightarrow 9/2^+$

Table 2: (continuación)

E_x (keV)	E_γ	Intensidad	R_{DCO}	A_2	A_4	Asimetría	$I_i^\pi \rightarrow I_f^\pi$
1831.1 (5)	655.9	61 (6)					$(13/2^+)\rightarrow 9/2^+$
2217.7 (5)	724.5	146 (14)	1.3 (3)				$(13/2^-)\rightarrow 9/2^-$
2353.3 (6)	862.0	98 (11)	1.6 (14)^d				$(15/2^+)\rightarrow 11/2^+$
2393.4 (4)	896.1	680 (30)	1.15 (5)	0.260 (34)	-0.067 (46)	0.06 (2)	$17/2^+\rightarrow 13/2^+$
2478.6 (6)	764.2	52 (8)					$(15/2^-)\rightarrow 11/2^-$
	794.5	18 (3)					$(15/2^-)\rightarrow (11/2^-)$
2520.2 (3)	805.8	598 (46)	0.95 (6)	0.309 (52)	-0.120 (70)	0.04 (3)	$15/2^-\rightarrow 11/2^-$
2777.8 (7)	947.6	94 (20)					$(17/2^+)\rightarrow (13/2^+)$
3189.4 (5)	971.4	81 (9)	0.9 (3)				$(17/2^-)\rightarrow (13/2^-)$
3377.9 (4)	857.1	134 (20)	0.35 (14)	-0.716 (91)	$<<0$	0.01 (8)	$17/2^-\rightarrow 15/2^-$
	899.3	140 (30)					$17/2^-\rightarrow (15/2^-)$
3475.7 (5)	1082.2	470 (32)	0.95 (6)	0.158 (35)	-0.094 (49)	0.12 (3)	$21/2^+\rightarrow 17/2^+$
3529.8 (4)	1009.0	323 (30)	0.68 (15)	0.142 (56)	-0.167 (76)	0.05 (4)	$19/2^-\rightarrow 17/2^-$
3829.3 (5)	1051.5	56 (18)					$(21/2^+)\rightarrow (17/2^+)$
4017.1 (4)	487.2	114 (7)	0.38 (12)	-0.437 (56)	0.005 (84)	-0.04 (5)	$21/2^-\rightarrow 19/2^-$
	638.8	96 (15)	0.5 (4)				$21/2^-\rightarrow 17/2^-$
4311.8 (4)	781.9	81 (8)	0.7 (3)				$(21/2^-)\rightarrow 19/2^-$
	933.7	81 (11)					$(21/2^-)\rightarrow 17/2^-$
	1123.1	59 (6)					$(21/2^-)\rightarrow (17/2^-)$
4503.4 (5)	1027.7	304 (22)	1.01 (10)	0.274 (39)	-0.173 (53)	0.06 (3)	$25/2^+\rightarrow 21/2^+$
4742.1 (6)	1212.5	75 (10)					$(23/2^-)\rightarrow 19/2^-$
4968.9 (7)	1493.5	102 (24)	0.9 (3)			0.08 (18)	$25/2^+\rightarrow 21/2^+$
5375.7 (5)	633	43 (4)					$(25/2^-)\rightarrow (23/2^-)$
	1063.8	111 (10)					$(25/2^-)\rightarrow (21/2^-)$
	1358.4	67 (10)					$(25/2^-)\rightarrow 21/2^-$
5811.6 (7)	842.6	46 (10)					$(29/2^+)\rightarrow 25/2^+$
	1308.2	97 (8)	0.6 (5)			0.03 (10)	$(29/2^+)\rightarrow 25/2^+$
6612.8 (6)	1237.7	152 (15)					$(29/2^-)\rightarrow (25/2^-)$
7714.9 (7)	1101.9	114 (15)		0.35 (5)	-0.10 (8)		$(33/2^-)\rightarrow (29/2^-)$

[a] $I_{tot}=I_\gamma(1+\alpha_t)$=177 (26) (supuesta M1)

[b] I_{tot}= 1067 (212) (supuesta E2)

[c] I_{tot}= 94 (5) (supuesta M1)

[d] R_{DCO} gate en transición dipolar.

De una primera inspección de estos resultados podemos destacar la existencia de dos bandas yrast rotacionales fuertemente pobladas, y otras cuatro menos intensas, pero que parecen seguir un patrón de banda rotacional.

5.2 Resultados del ^{71}Kr. El núcleo espejo ^{71}Kr con T_z=1/2 ha sido objeto de un experimento realizado en el Laboratorio Nacional de Oak Ridge, en Tennessee (EE.UU.). La reacción ^{40}Ca+^{40}Ca ha sido de nuevo utilizada a una energía de 156 MeV de modo que los datos fueran comparables a los obtenidos en el anterior experimento a 180 MeV y que el separador de masa tuviera las condiciones de funcionamiento más favorables posibles.

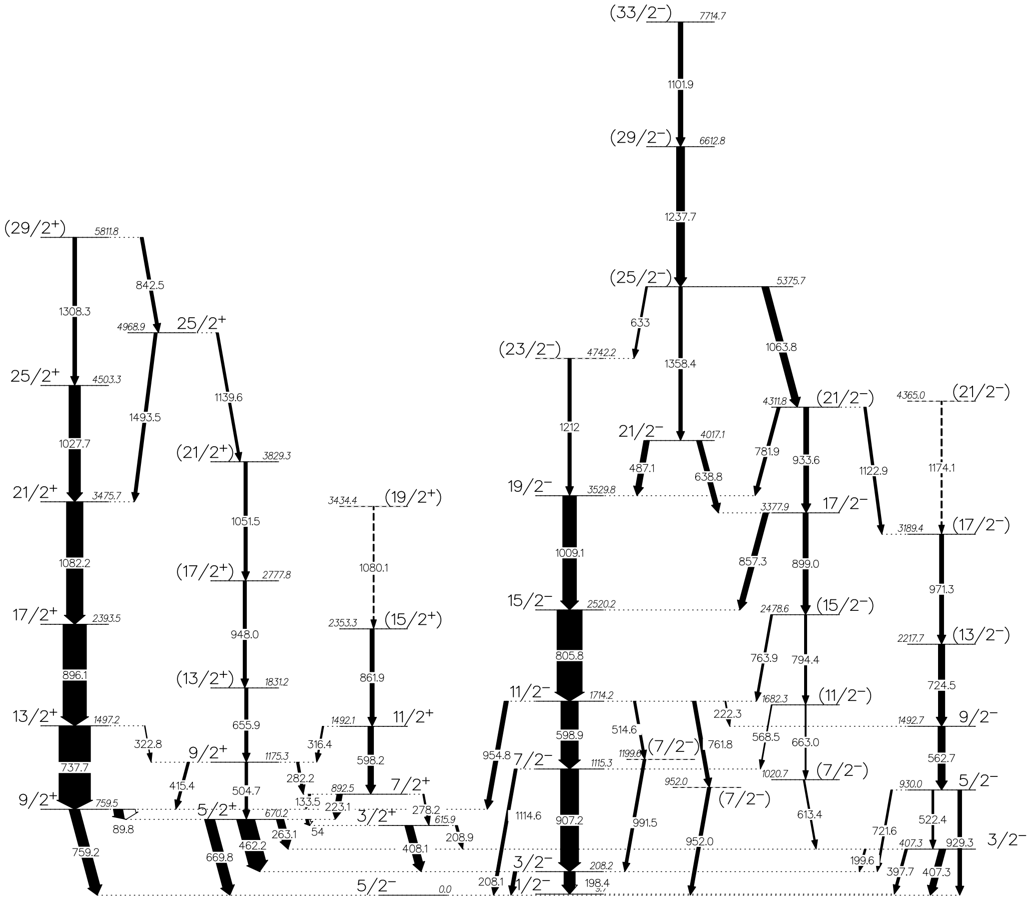

Figure 1: *Esquema de niveles del núcleo ^{71}Br obtenido en este trabajo de tesis.*

El dispositivo experimental utilizado se basa en la técnica de identificación de núcleos en retroceso producidos en reacción de fusión-evaporación mediante el uso de un separador de masa que, con el uso conjunto de un espectrómetro gamma en la posición del blanco y un detector en el plano focal del separador para la determinación de la masa y del número atómico de los productos de la reacción, permite identificar núcleos poblados con una sección eficaz del orden de 1-10 μb

Tras un análisis exhaustivo de los datos obtenidos con los detectores utilizados, ningún resultado positivo ha sido obtenido, las posibles transiciones observadas como picos en los espectros candidatas a pertenecer al ^{71}Kr no han sido confirmados en un posterior análisis de coincidencias. Hemos creado espectros gamma con condiciones en la masa y en el Z de los residuos, en las partículas evaporadas, combinaciones de ellos, etc. Con estos espectros hemos realizado las sustracciones pertinentes para poder obtener un espectro de ^{71}Kr puro. Este se muestra en la parte inferior de la figura 2.

Dada la dificultad para observar el núcleo ^{71}Kr, hemos realizado una estimación de la sensibilidad del sistema de medida usado, a través de la medida de la sección

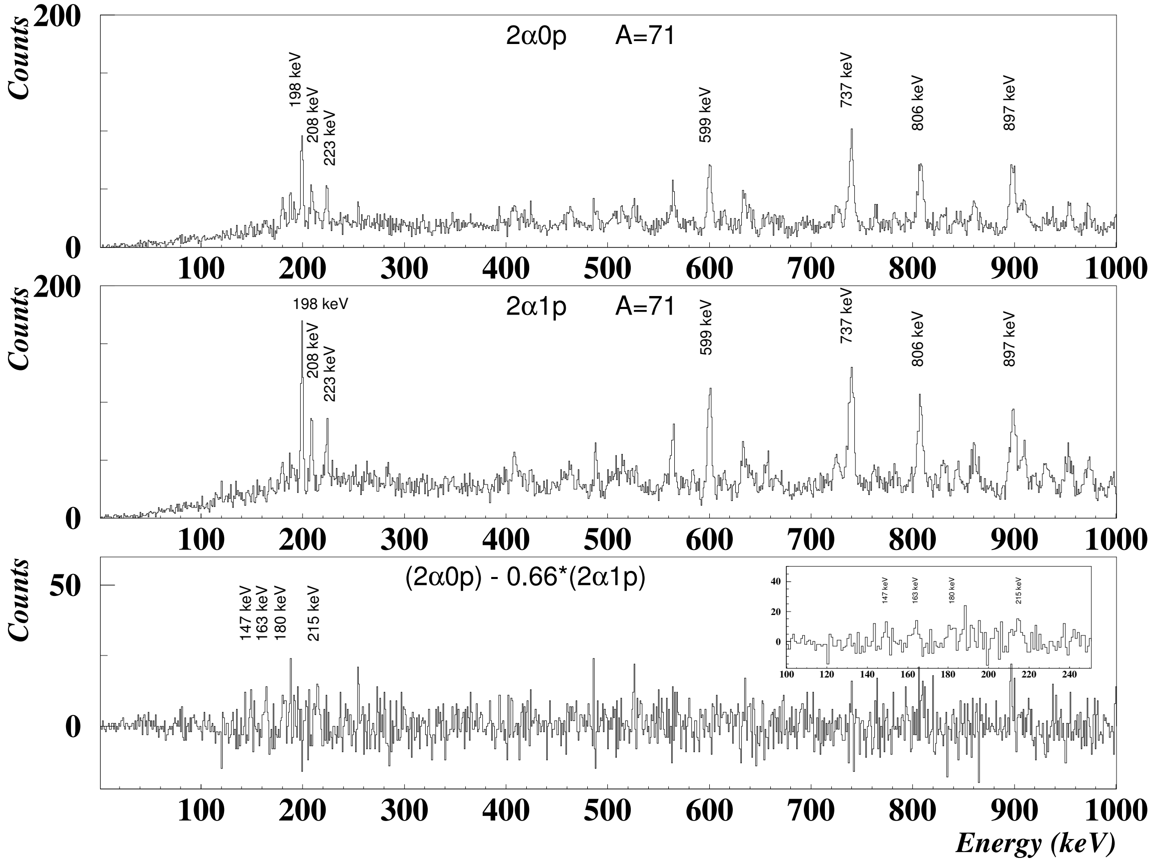

Figure 2: *Espectros gamma obtenidos con condición en masa 71 y en partículas evaporadas, $2\alpha 0p$ (arriba) y $2\alpha 1p$ (centro) respectivamente. En la parte inferior se muestra el espectro resultante de la substracción, donde se observa algunos posible picos, candidatos a pertenecer al ^{71}Kr, a bajas energías.*

eficaz de producción del ^{71}Kr. Para ello, hemos realizado una medida de "singles" en condiciones controladas de modo que, conocidas las características del blanco, del haz y del número de reacciones producidas por unidad de superficie, la sección eficaz se puede obtener a través de la fórmula:

$$\sigma = \frac{N_{cr}}{F_b \cdot N_{at}} \tag{1}$$

Así el "counting rate", N$_{cr}$, lo determinamos mediante la intensidad total de las transiciones que desexcitan al estado fundamental, I$_\gamma(2^+ \rightarrow 0^+)$ en el caso de un núcleo par-par y $\sum$ I$_\gamma$(i→gs) en el resto de núcleos. El flujo de los iones del haz, F$_b$, por unidad de tiempo lo determinamos a través de la intensidad de corriente del haz y el numero de atomos, N$_{atom}$, se obtiene a través del espesor del blanco. De este modo hemos obtenido los siguientes valores de sección eficaz para los núcleos conocidos comparado con el valor previsto por el codigo HIVAP:

A	Canal	E_γ	σ_{exp} (mb)	σ_{calc} (mb)
^{72}Se	$1\alpha4$p	862.0	19 (4)	50
^{70}Se	$2\alpha2$p	944.6	15 (5)	40
^{73}Br	$1\alpha3$p	$\sum$	62 (9)	75
^{71}Br	$2\alpha1$p	$\sum$	19 (3)	0.8
^{76}Kr	4p	424.0	224 (10)	280
^{74}Kr	$1\alpha2$p	455.8	89 (10)	48

Suponiendo que el ^{71}Kr debería ser menor que la transición más débil de ^{71}Br que somos capaces de observar nos permite establecer un límite a nuestra sensibilidad y por tanto a la sección eficaz de producción del ^{71}Kr que es del orden de 100 μb, muy por encima de la sección eficaz estimada que es $\leq$10 μb.

5.3 Resultados del ^{70}Br. Hemos identificado los estados excitados del núcleo N=Z ^{70}Br por primera vez en la reacción ^{32}S+^{40}Ca a 95 MeV de energía. Dicha reacción ha sido estudiada primero en el tandem XTU de LNL con GASP y posteriormente con EUROBALL en el tandem VIVITRON del Instituto de Investigaciones Subatómicas de Extrasburgo, IReS, (Francia).

El resultado más importante ha sido su identificación, lograda mediante la selección del canal gracias al detector de neutrones utilizado. En la reacción mencionada el núcleo ^{70}Br se produce como resultado de la evaporación de 1p1n del núcleo compuesto. Así la utilización conjunta de un detector de partículas cargadas ligeras (ISIS o EUCLIDES) con el detector de neutrones (N-ring o Neutron WALL) permite establecer una condición sobre las partículas evaporadas con la consiguiente selección del canal. De este modo comparando las proyecciones de las matrices γ-γ para diferentes condiciones de partículas y observando las diferencias en los espectros hemos podido determinar ciertas transiciones como posibles candidatos que se han comprobado posteriormente mediante “gates” en las diferentes matrices.

Basandonos en la sistemática y por similitud con la transición análoga de 944 keV en el ^{70}Se, se esperaba una transición de entre 900 y 1000 keV para la desexcitación de $2^+ \rightarrow 0^+$ en el ^{70}Br. Una transición ha sido observada a 933 keV y mediante el analisis de las coincidencias hemos observado otras transiciones cuyos cocientes de intensidades $\frac{I_\gamma(1p1n)}{I_\gamma(0p1n)}$ y $\frac{I_\gamma(1p1n)}{I_\gamma(1p0n)}$ nos ha permitido asociarlas al canal 1p1n. De la ausencia de tales transiciones en los posibles contaminantes hemos deducido su pertenencia al núcleo ^{70}Br.

El análisis de las matrices γ-γ y de las matrices de correlaciones angulares nos ha permitido deducir la intensidad y el carácter y multipolaridad de las transiciones más intensas cuyos resultados se muestran en la tabla 3.

6. Interpretación

Table 3: Energías, intensidades relativas y correlaciones angulares (DCO) o cociente de distribución angular (en el caso de la transición de 933.4 keV) y asimetrías de las transiciones γ correspondientes a ^{70}Br. Las intensidades están normalizadas al valor de la transición de 933.4 keV (tomada como 100). Los cocientes de DCO han sido obtenidos mediante un gate en la transición cuadrupolar, ΔI=2, 933.4 keV.

E_γ (keV)	Intensidad	DCO	Asimetría	E_x (keV)	$I^i \rightarrow I^f$
274 (1)	2 (1)			1931	$\rightarrow(5^+)$
320.9 (4)	35 (4)	1.1 (3)	0.27 (17)	1657	$(5^+) \rightarrow(3^+)$
326.2 (5)	13 (2)	0.31 (14)	0.29 (17)	2678	
343.1 (5)	9 (2)	0.9 (2)	-0.09 (8)	3025	$\rightarrow(7^+)$
349.6 (5)	16 (2)	0.83 (15)	0.3 (4)	2352	$(5^+) \rightarrow(4^+)$
402.7 (4)	59 (6)	0.77 (11)	-0.06 (8)	1336	$(3^+) \rightarrow(2^+)$
421.0 (6)	4 (2)			2352	
470.4 (6)	11 (2)			3148	
595 (1)	3 (1)			1931	$\rightarrow(3^+)$
654 (1)	2 (1)			3679	
665.6 (6)	8 (2)			2002	$(4^+)\rightarrow(3^+)$
694.7 (5)	4 (1)			2352	$\rightarrow(5^+)$
933.4 (4)	100 (8)	1.1 (3)^a	0.11 (10)	933	$(2^+)\rightarrow(0^+)$
963.4 (6)	5 (2)			2965	
997.0 (5)	6 (2)			3679	$\rightarrow(7^+)$
1024.8 (5)	20 (2)	1.2 (3)	0.05 (27)	2682	$(7^+) \rightarrow(5^+)$
1025 (1)	3 (2)			3990	
1069.0 (5)	41 (5)	1.1 (3)	0.04 (8)	2002	$(4^+)\rightarrow(2^+)$
1104 (1)	3 (1)			2761	$\rightarrow(5^+)$
1468 (1)	3 (1)			2682	

[a] Cociente de distribución angular.

Los resultados obtenidos nos han permitido sugerir una interpretación de las estructuras observadas en los núcleos en estudio a través de una comparación con los núcleos conocidos de la región, que por características similares presentan fenómenos análogos. Así, en el caso del ^{71}Br damos una comparación cualitativa con los fenomenos observados en los isótopos de masa impar más pesados. En el caso del ^{70}Br se compara con otros núcleos auto-conjugados N=Z impar-impar y con el núcleo isóbaro ^{70}Se.

En el caso del ^{71}Br una comparación con el modelo de partícula acoplado a un rotor puede ofrecer una visión más completa de las características observadas y está previsto que se lleve a cabo en un futuro inmediato.

6.1 Estructura del ^{71}Br. En el núcleo Z-impar N-par, ^{71}Br, la estructura está gobernada por el protón impar como en el caso de los isótopos de masa impar ^{73,75}Br. La asignación de espín y paridad a los niveles observados y el esquema de niveles obtenidos del estudio de las coincidencias, permite distinguir entre estados intrínsecos de bajo espín y estados colectivos agrupados en bandas rotacionales que se extienden hasta valores de alto espín, típicos de núcleos deformados.

Como en el caso del núcleo ^{73}Br, los estados que aparecen a bajo espín encierran una dificultad a la hora de entender el orden y el espín de dichos estados. En el trabajo de Hesse *et al.* [Hee90] se sugiere el recurso a la triaxialidad para explicar dichos estados. Sin embargo en un trabajo posterior, Griffiths *et al.* [Gri92] reproducen el orden de dichos estados si la deformación es oblada. Esto es válido también en el caso del ^{71}Br, donde el estado fundamental y el primer estado excitado están intercambiados respecto al ^{73}Br. Dos estados excitados con espín $I^{\pi}=3/2^{-}$ aparecen a diferentes energías de excitación. Uno de ellos a 208 keV que se corresponde con el estado oblado reproducido por Griffiths *et al.*, y otro a 407 keV que correspondería con el estado prolado observado en los isótopos $^{73-77}$Br.

El estado isomérico a 759 keV de energía de excitación ha sido interpretado como $9/2^{+}$ correspondiente a un protón ocupando el orbital $g_{9/2}$ por analogía con la sistemática de estados isoméricos presentes en los núcleos de la región.

Los estados a alta energía de excitación y alto espín han sido asociados a bandas rotacionales en función de las coincidencias y de la asignación de espín y paridad. En primer lugar se observa la banda yrast, de paridad positiva, que se extiende hasta espín $29/2^{+}$. En términos del modelo de acoplamiento rotor-partícula, este tipo de banda se verifica en el llamado límite de alineamiento al eje de rotación por parte de la partícula impar. Este límite se produce cuando la partícula impar "ocupa" un orbital de Nilsson caracterizado por un valor alto de j y un valor pequeño de Ω. En nuestro caso $j = 9/2$ y $\Omega = 1/2$ o $3/2$.

Otras dos bandas de paridad positiva han sido observadas a pesar de la poca estadística con que se pueblan. Una de ellas se piensa que puede estar asociada al "unfavoured signature partner" de la banda $g_{9/2}$.

La banda con paridad negativa yrast, presenta un comportamiento "anómalo" ya que sus características no se corresponden con la banda de paridad negativa

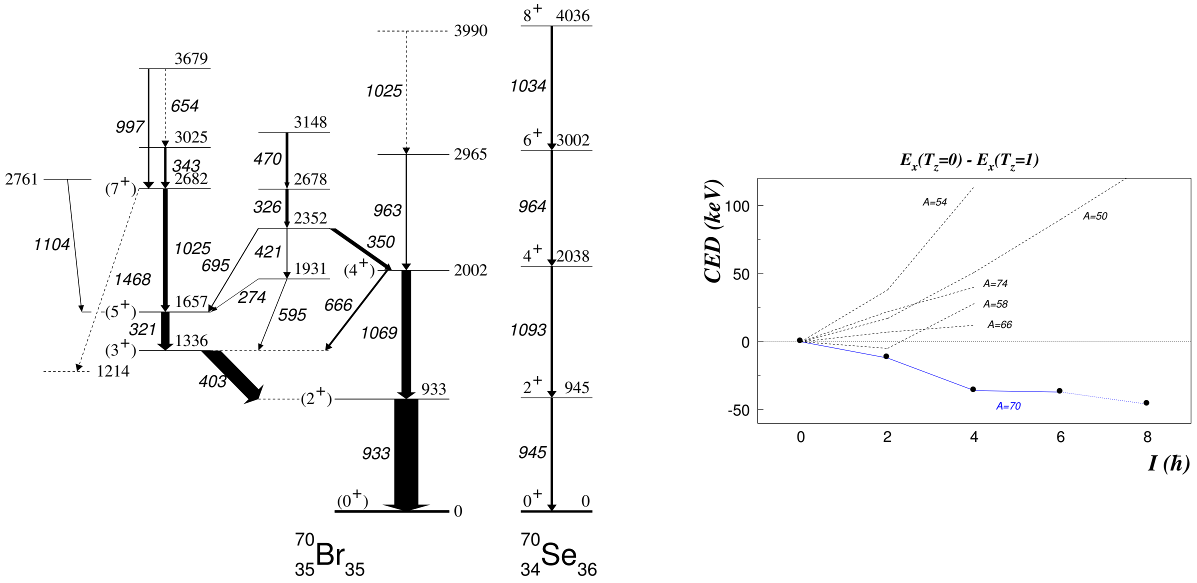

Figure 3: *Esquema de niveles del ^{70}Br deducido del presente trabajo (izquierda) En el centro se muestran los estados del ^{70}Se con isospín T=1. A la derecha de la figura, hemos representado el CED (Coulomb Energy Difference) entre estados isobáricos análogos en ambos núcleos ^{70}Br (T_z=0) y ^{70}Se (T_z=1) en función del momento angular total.*

observada en los otro isótopos de Br. Las otras dos bandas de paridad negativa podrian corresponder a las bandas proladas de paridad negativa observadas en el ^{75}Br.

6.2 Estructura del ^{70}Br El caso del núcleo N=Z impar-impar, ^{70}Br, resulta más complicado de interpretar por la limitación en el cálculo de los modelos de las interacciones residuales que en gran medida van a condicionar la estructura nuclear. De todas formas, la estructura va a estar gobernada fundamentalmente por los orbitales vecinos a la superfice de Fermi, que en la parte prolada son los orbitales de Nilsson [301]1/2$^-$, [301]3/2$^-$, [303]5/2$^-$ y el orbital "intruder" $g_{9/2}$ y en la parte oblada los orbitales [310]1/2$^-$, [301]3/2$^-$ y el orbital "intruder" $g_{9/2}$, y por las interacción residual entre el protón y el neutrón impares.

Los estados observados han sido clasificados en función del isospín como estados con T=0 y estados con T=1. El estado fundamental, $J = 0^+$, $T = 1$ así como el resto de estados con $T = 1$ presentan un comportamiento que en cierto modo constituye una anomalía respecto a otros núcleos impar-impar de la zona. Las diferencia de energía de excitación entre estados isobáricos análogos, cuya causa se atribuye a la interacción culombiana, presenta valores negativos para el caso del ^{70}Br-^{70}Se, a diferencia de lo que ocurre en otros núcleos impar-impar con N=Z, de la zona como ^{66}As-^{66}Ge, ^{58}Cu-^{58}Ni, etc.

7. Conclusiones

Este trabajo de tesis, basado en el estudio mediante técnicas de espectroscopía gamma de la estructura nuclear de los isótopos más ligeros del bromo, supone un gran paso en el estudio de núcleos alejados del valle de la estabilidad ya que nos permite conocer con un poco más de detalle las particularidades de los efectos de la interacción nuclear en sistemas bajo condiciones extremas de energía de excitación, momento angular e isospín.

Las conclusiones que podemos extraer de dicho estudio, nos llevan a profundizar en la estructura y a suministrar datos experimentales de especial interés en el desarrollo y mejora de los modelos teóricos necesarios para la interpretación de la estructura nuclear.

Como resultados importantes a destacar en este estudio podemos enumerar los siguientes:

1. El esquema de niveles del núcleo ^{71}Br ha sido notoriamente ampliado: las dos bandas rotacionales conocidas han sido aumentadas en espín y se ha determinado la secuencia de las transiciones. Cuatro nuevas bandas han sido identificadas y estudiadas.

2. El análisis de las distribuciones angulares, DCO y asimetría de las transiciones más intensas ha permitido la determinación del espín y paridad, I^{π}, de los estados excitados. El uso de EUROBALL como espectrómetro gamma ha sido por tanto de fundamental importancia.

3. Una mejor determinación de los estados de bajo espín, permite una interpretación de la estructura del estado fundamental como un estado con deformación oblata, como había sido sugerida en cálculos realizados por Griffiths *et al.*

4. La banda yrast de paridad positiva nos ha permitido establecer una valor para la deformación del núcleo en dichas condiciones de excitación, la deformación prolada con un valor de β_2=0.35 ha sido obtenido a partir de la vida media del estado isomérico $9/2^+$ y de la intensidad de la transición de 89.9 keV

5. Los estados excitados del núcleo N=Z ^{70}Br, han sido identificados por primera vez a través de una reacción de fusión-evaporación. El uso de los detectores de neutrones (N-Ring y Neutron Wall) ha sido fundamental para poder separar los eventos pertenecientes al canal pn.

6. La asignación de espín y paridad basada en la sistemática y en los resultados de las correlaciones angulares nos ha permitido distinguir entre estados de isospín T=0 y estados con T=1. Estos estados obtenidos experimentalmente muestran un buen acuerdo con los cálculos teóricos (IBM-4) disponibles hasta la fecha.

7. Los estados de isospín T=1 del ^{70}Br junto con los estados isobáricos análogos en el ^{70}Se, muestran un CED cuyo comportamiento con el momento angular

difiere del observado en la sistemática. Efectos relacionados con la proximidad a la “proton drip-line” y con el desplazamiento Thomas-Ehrman has sido sugeridos como posibles causas.

8. No ha sido posible establecer sin ambigüedad el estado isomérico $I^{\pi}=9^{+}$, el cual ha sido sugerido a través de la transición 1468 keV estar situado a una energía de excitación de 1214 keV.

Contents

List of Figures

List of Tables

Chapter 1

Physics of N$\sim$Z nuclei around A$\simeq$70

1.1 Introduction

The medium mass nuclei around the A$\simeq$70 mass region display a remarkable diversity of shapes and rapid changes in structure with particle number, angular momentum and excitation energy. Qualitatively, this can be understood in terms of the deformed independent particle shell model, which predicts the occurrence of large gaps at different deformations in the single particle spectra of many nuclei in this mass region [Naz85, Abe90].

Proton-rich nuclei also display many interesting properties which are important both for nuclear physics and astrophysics. These nuclei are characterized by special ground-state decay properties such as direct emission of charged particles and beta-decays with large Q-values. The properties of most proton-rich nuclei with N$\simeq$Z close to the drip-line also play an important role in the process of nucleosynthesis by rapid-proton capture. In addition to decay properties (particle emission, beta-decay), of fundamental importance are studies of atomic masses and separation energies, and especially the precise location of the proton drip-line. Also very important are the dynamic properties of these nuclei: excitation energies, spin-parity of excited levels, transition probabilities between the states, ... This properties allows us to extract information on the structure of the nuclei of interest. The major part of this work is dedicated to this kind of studies.

Particularly interesting are nuclear systems with an equal number of protons and neutrons. The high degree of symmetry between the proton and neutron degrees of freedom provides an excellent opportunity to study the effective n-p interaction. Protons and neutrons occupy the same shell-model orbitals and therefore these nuclei present unique systems in which (S=0, T=1) and (S=1, T=0) pairing can be studied. While for A$\leq$40 the N=Z nuclei are beta-stable, in heavier systems the Coulomb interaction drives the beta-stability line towards neutron-rich isotopes and heavier N=Z nuclei approach the proton drip-line becoming unstable. They also display a variety of structure phenomena: shape coexistence, superdeformation, alignment of proton-neutron pairs.

This thesis work focus on the study of two proton rich nuclei: ^{70}Br and ^{71}Br. In the following chapters we will present an overview of the different theoretical models developped in the last decades (chap. 1), we will introduce the problematic of the region and the previous knowledge on the nuclei of interest (chap. 2). Then, we will describe the experimental tools used to populate this kind of nuclei and the experiments carried out (chap.3). We will comment the techniques used in the analysis of the data (chap. 4) and we will present the results and the interpretation of those data for the ^{71}Br nucleus (chap. 5 and 6), the ^{71}Kr nucleus (chap. 7) and finally for the ^{70}Br nucleus (chap. 8).

1.2 Approaching the drip line. Models.

Several models were developed during the second half of the last century. Among them the Nuclear Shell Model was in a sense the most successful and gave a good interpretation of the gaps observed in the nucleon separation energies, the level sequences for nuclei near the closed shells, the values of the magnetic moments for odd-A nuclei, etc.

Although we believe that the Shell Model gives a good description of nuclear properties the model space for A$\simeq$70 nuclei is too large for us to be able to use it. In the Shell Model, the nucleus is described in terms of a core, the nucleons occupying the closed shells, plus the valence nucleons outside these closed shells. Good descriptions have been obtained for nuclei with few particles (holes) outside the core. When more particles fill the shells outside the inert core, for example in the case of ^{71}Br up to 15 particles, larger is the basis space of single particle states and it becomes an unafordable problem in terms of computing capabilities.

Accordingly we must have recourse to simplified models to describe their observed properties. Thus, the level schemes we have found for the A$\simeq$70 nuclei are characterized by the interplay of single particle states and collective states. We can observe rotational bands related to stable nuclear deformations, that in some of the nuclei of the region ranges up to values of β_2~0.3-0.4. Hence, models that combine a microscopic approach with macroscopic features have been the most successful in terms of explaining and predicting the behaviour of many deformed nuclei.

The main characteristics of some of the models used are described briefly below.

1.2.1 Deformed Shell model

The shell model describes the nucleus in terms of interacting nucleons moving in an average potential produced by the rest of nucleons. In this way the nuclear

Hamiltonian described by:

$$H = -\frac{\hbar^2}{2m}\sum_{i=1}^{A}\nabla_i^2 + \sum_{i<j} V_{ij}, \tag{1.1}$$

can be decomposed into two terms: a mean field Hamiltonian and a residual interaction

$$H = H_0 + V_{res} \tag{1.2}$$

where

$$H_0 = \sum_{i=1}^{A}\nabla_i^2 + \sum_{i=1}^{A} V(i), \tag{1.3}$$

with $\sum_{i=1}^{A} V(i)$ being the mean field created by the rest of nucleons, and

$$V_{res} = \sum V(ij) - \sum_{i=1}^{A} V(i). \tag{1.4}$$

being the residual interaction.

At this point a mean field potential has to be chosen which satisfies certain constraints and minimizes the residual interactions. An additional term that depends on the spin-orbit interaction between nucleon spin and orbital angular momentum is added and the observed experimental magic numbers are reproduced. Phenomenological potentials such as the harmonic oscillator (HO) or Woods-Saxon (WS) potential are normally used to reproduce the nuclear features. However, this model assumes spherical shapes, which is true for nuclei with closed or nearly closed shells, but it should be noted that some nuclei can be deformed, namely the nuclei far from closed shells. Moreover this model is limited to light nuclei, due to the large basis needed to account for medium and heavy nuclei, as noted earlier.

Nilsson [Nil55] introduced the deformation into the mean field potential $V(i)$, via a parametrization of the oscillator frequencies as a function of quadrupole deformation (for the case of axially-symmetric deformations) (ε) and the modified oscillator potential (V_{MO}), can then be described by:

$$V_{MO} = \frac{1}{2}m\omega_0^2(\varepsilon)\left[\left(x_1^2 + x_2^2\right)\left(1+\frac{1}{3}\varepsilon\right)^2 + x_3^2\left(1-\frac{2}{3}\varepsilon\right)^2\right] + C\vec{l}\cdot\vec{s} + D(\vec{l}^2 - \langle\vec{l}^2\rangle_N). \tag{1.5}$$

where $\vec{l}\cdot\vec{s}$ is the spin-orbit interaction that reproduces the magic numbers for spherical nuclei, $\vec{l}^2 - \langle\vec{l}^2\rangle_N$ has the effect of flattening the oscillator potential to give a radial dependence in the interior of the nucleus, $\omega_0(\varepsilon)$is the deformed frequency related to the spherical frequency by

$$\omega_0(\varepsilon) = \omega_0(0)\left(1 - \frac{1}{3}\varepsilon^2 - \frac{2}{27}\varepsilon^3\right)^{-1/3} \tag{1.6}$$

where $\hbar\omega_0(0) = 41A^{-1/3}(1 \pm \frac{N-Z}{3A})$ MeV and C and D are constants related to two adjustable parameters κ and μ:

$$C = -2\hbar\omega_0\kappa, \qquad D = -\hbar\omega_0\kappa\mu. \tag{1.7}$$

The values of C and D are determined from global fits to experimental data and are usually adjusted independently for protons and neutrons and typically range from 0.05 to 0.12 for κ and from 0.00 to 0.07 for μ.

The Nilsson single-particle energy levels of the deformed Hamiltonian are referred to as “Nilsson diagrams”. These one particle orbits are often labelled by the asymptotic quantum numbers $[\mathrm{N}\mathrm{n}_z\Lambda]\Omega^\pi$, where N is the principal quantum number, n_z is its component on the symmetry axis and Λ and Ω are the projections of the orbital and total angular momentum along the symmetry axis, and $\pi = (-1)^N$ is the parity. For axially symmetric nuclei π and Ω are the only good quantum numbers, at large deformations all the quantum numbers are conserved and the configuration is specified by all the “asymptotic quantum numbers”. At small deformations the spherical shell model quantum numbers l and j are the most appropriate.

The Nilsson model, describes the spectrum of orbits for deformed nuclei reasonably well, but some particular details disagree with experimental results. Thus, the phenomenological term in l^2 in the Nilsson potential introduces some systematic effects, especially on the high-j orbitals, of importance for high-spin calculations. In addition the harmonic oscillator potential deviates from the shape of the nuclear charge distribution expected from measurements, for which, the radial dependence of the charge density ρ, can be approximated by a Fermi distribution:

$$\rho(r) = \frac{\rho_0}{1 + exp(\frac{r-R_0}{a})} \tag{1.8}$$

where R_0 is the mean-radius and a is the surface diffuseness parameter.

A more realistic potential, the Woods-Saxon potential, reproduces the shape of the nuclear charge distribution and can be expressed in the form [Naz85, Voi83]:

$$\begin{aligned} V_{WS} =& \frac{V_0}{1 + exp[dist_\Sigma(r;\beta;R_0)/a]} - \\ & - \lambda_{so}\left(\frac{\hbar}{2mc}\right)^2 \nabla\left(\frac{V_0}{1 + exp[dist_{\Sigma_{so}}(r;\beta;R_{so})/a_{so}]}\right) \cdot (\vec{\sigma} \times \vec{p}) + \\ & + \frac{1}{2}(1+\tau_3)V_{Coul}(r;\beta) \end{aligned} \tag{1.9}$$

where the three terms represent, respectively, the central part of the potential, the spin-orbit term, and the Coulomb term for protons. The nuclear surface, Σ, for the central potential, is defined in terms of an expansion into spherical harmonics with the deformation parameters $\beta = \beta(\beta_2, \beta_4, ...)$ as the coefficients in the expansion. Thus, for axially symmetric deformations with respect to the z-axis, the distance

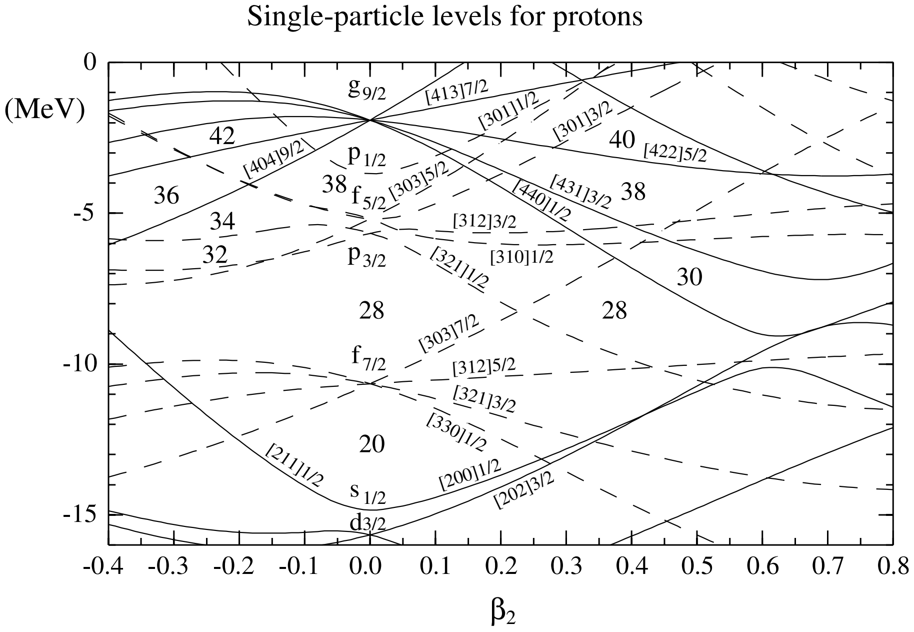

Figure 1.1: *Single-particle energy levels for protons as a function of deformation for A=80 calculated with a Woods-Saxon potential [Wys99] (private comm). Positive values of* β_2 *correspond to prolate shapes and negative values to oblate shapes.*

from the origin of the coordinates to any point on the surface is given by:

$$R(\theta) = c(\beta_2, \beta_4, ...)R_0[1 + \beta_2 Y_{20}(cos\theta) + \beta_4 Y_{40}(cos\theta) + ...] \tag{1.10}$$

The function $dist_\Sigma(r; \beta; R_0)$ is the distance of a point r to the surface Σ. The spin-orbit term is defined in the usual way, with an equivalent definition of the surface Σ_{so} because of a large fluctuation of the effective spin-orbit potential with the shell filling, whereas the central potential fluctuates in a smooth way. The Coulomb potential for protons is generated by the charge $(Z - 1)e$ uniformly distributed inside the surface Σ.

The Woods-Saxon potential gives a good description of the nuclear single-particle states, at least in nuclei with $A \geq 40$, using a set of parameters referred to as the universal Woods-Saxon parameters [Naz85]. The great disadvantage of this potential is the amount of computer time consumed in the numerical solutions of the matrix element diagonalization. An example of the single-particle orbitals as a function of deformation obtained with this kind of potential is shown in fig 1.1. In this figure we can see how the single-particle orbits are disposed and how the gaps or magic numbers change with deformation and give rise to stable deformations.

In addition to the average nuclear potential determining the properties of the nucleonic single-particle orbitals, a residual two-body interaction V$_{res}$ (1.4) must be added in order to account for many specific properties of nuclei. Among the residual interactions to be taken into account the Pairing interaction is the dominant contribution and is the responsible for the coupling of pairs of like-nucleons with total spin I=0, giving rise to the superconducting or superfluid phase in nuclei. In a first order approximation the pairing interaction can be included in the Hamiltonian through the operator in the second quantization picture:

$$H_{pair} = -G \sum_{\nu_1,\nu_2} a^{+}_{\nu_1} a^{+}_{\bar{\nu_1}} a_{\bar{\nu_2}} a_{\nu_2} \tag{1.11}$$

where a^{+}_{ν}, a_{ν} are the particle creation and annhilation operators, respectively, and G is the strength of the interaction. The pairing force annhilates a pair of particles in the time-reversed states $|\nu_2\rangle$ and $|\bar{\nu_2}\rangle$ and creates a pair of particles in the time reversed states $|\nu_1\rangle$ and $|\bar{\nu_1}\rangle$. A complete description of the problem can be found in many textbooks [Rin80] and reviews.

The Shell correction method

Although the Deformed Shell Model is able to reproduce the correct deformed magic numbers and is very successful in describing nuclear properties in which only the nucleons in the vicinity of the Fermi surface are involved, its main deficiency is the inability to describe bulk nuclear properties such as the total nuclear energy or the binding energies. Some authors, Strutinsky, Swiatecki, etc., have solved this problem by combining the liquid drop model qualities with the microscopic approach. Thus in the so-called "Nilsson-Strutinsky Shell Correction Method"[Str67, Str68], the total energy of an n-particle configuration is approximated by the sum of a macroscopic part, E_{macr}, which varies smoothly with particle number and represents the bulk properties of the nucleus, and a microscopic part, E_{micr}, describing the properties of the nuclear energy which depend on the shell effects.

$$E_{tot} = E_{macr} + E_{micr} = E_{LDM} + \delta E_{shell} \tag{1.12}$$

The macroscopic part of the energy is usually replaced by the classical liquid drop model value, E_{LDM}, which is known to give a good average approximation to the binding energies. E_{micr} is the shell correction term derived from the shell model δE_{shell}. This shell correction is obtained as the difference between the actual shell model energy E_{shell} and its smooth average value $\tilde{E}_{shell}$, where

$$\delta E_{shell} = E_{shell} - \tilde{E}_{shell} \tag{1.13}$$

This shell correction term already gives a reasonable contribution when only the single particle energies and level density values in the neighborhood of the Fermi surface are used.

This kind of calculation has been applied to estimate nuclear masses and to calculate the energy as a function of the deformation, which is important if we are to estimate ground-state (equilibrium) shapes.

1.2.2 Rotational Energy. The Particle plus Rotor model.

Collective features in nuclei were observed almost from the very beginning and were explained first in terms of the liquid drop model (LDM) as vibrations and rotations of the nucleus as a whole. In the case of the collective rotations of an axially symmetric deformed rotor, the nucleus is supposed to rotate around an axis perpendicular to the symmetry axis[1]. Thus, the collective Hamiltonian can be expressed as a function of the rotational angular momentum of the nucleus as a whole, R, by:

$$H_{rot} = \frac{\hbar^2}{2\Im}\vec{R}^2, \tag{1.14}$$

This collective Hamiltonian gives rise to the observed rotational bands of levels with spacing given by:

$$E(I) = \frac{\hbar^2}{2\Im}I(I+1) \tag{1.15}$$

where $\Im$ is the moment of inertia. However, this formula corresponds to pure rotation, with the lowest rotational state (bandhead) having zero-values for energy and spin, as in the case of the ground state rotational band in even-even nuclei. Real nuclei, have bandheads with values that depend on the intrinsic nuclear state upon which the band is built.

Thus there is an interplay between collective excitations and the single particle degree of freedom and this should be reflected in the models. One of the first models that combined both interpretations is the Particle plus Rotor model, proposed by Bohr and Mottelson [Boh98]. In this model, the nucleus is considered as a core that undergoes collective rotation plus a few valence particles that are treated separately. The total angular momentum, I, formed by the vector sum of the collective rotational angular momentum, R, of the core and the single-particle angular momentum J, of the valence particles is given by:

$$\vec{I} = \vec{R} + \vec{J} \tag{1.16}$$

Let us consider the simple case of an odd-A nucleus. Here, the Hamiltonian can be decomposed into two terms: an intrinsic motion term that depends on the odd particle and a collective rotation component:

$$\begin{aligned} H =& H_{intr} + H_{coll} = H_{intr} + \frac{\hbar^2}{2\Im}R^2 \\ =& H_{intr} + \frac{\hbar^2}{2\Im}(I-J)^2 \end{aligned} \tag{1.17}$$

The wave functions of the nuclear states are then written as a product of an intrinsic wavefunction, χ_K, which describes the motion of the nucleons in the body-fixed reference system and a rotational wave function, $\phi_{IKM}(\omega)$, which describes the

---

[1] A rotation around one of the symmetry axis does not change the wave function.

rotation of the nucleus in the laboratory frame. ω denotes the Euler angles which define the orientation of the nucleus.

$$\Phi_{IMK}(\omega) = \chi_K \cdot \phi_{IKM}(\omega) \tag{1.18}$$

Using the invariance of the system under rotations around the symmetry axis, the projection of the total angular momentum on it, K, is a constant of the motion as is its projection on the z-axis, M. The rotational states can then be specified by the I^2, M, K quantum numbers

$$\phi_{IMK}(\omega) = \left(\frac{2I+1}{8\pi^2}\right)^{1/2} D^I_{MK}(\omega) \tag{1.19}$$

where $D^I_{MK}(\omega)$ are the rotational matrices. In addition, for axially symmetric nuclei, the reflection symmetry or a rotation of 180^o about the perperdicular axis requires the wave function to be symmetrized with respect to ±K. Then, the total wave function can be expressed as:

$$\Phi_{IMK}(\omega) = \left(\frac{2I+1}{16\pi^2}\right)^{1/2} [\chi_K D^I_{MK}(\omega) + (-1)^{I+K} \chi_{-K} D^I_{M-K}(\omega)] \tag{1.20}$$

For the special case of $K = 0$ which occurs in even-even nuclei where the ground state has $I = 0^+$, only even values of I are allowed and the states form a band with values I=0,2,4,... for positive parities and I=1,3,5,.. for negative parities. The sequence of energies is given by:

$$E(I) = \frac{\hbar^2}{2\Im} I(I+1) \tag{1.21}$$

as mentioned before. The moment-of-inertia, which is assumed to be constant, is not an observable and can be derived from a measurement of the energy sequence. Thus,

$$\Im = \frac{3\hbar^2}{E(2^+) - E(0^+)} \tag{1.22}$$

For $K \neq 0$, as happens when the rotational motion is superimposed on an intrinsic excitation, the total angular momentum, I, can take all values I=K, K+1, K+2, K+3,... forming a sequence of states that can be considered as two separate ΔI=2 bands:

$$\begin{aligned} I &= K, K+2, K+4, ... \\ I &= K+1, K+3, K+5, ... \end{aligned} \tag{1.23}$$

Using the ladder operators $I_\pm$ and that K=Ω, we can describe the collective

Hamiltonian in the form:

$$\begin{aligned} H_{coll} =& \frac{\hbar^2}{2\Im}(I^2 - I_3) + \\ &+ \frac{\hbar^2}{2\Im}(J_1^2 + J_2^2) - \\ &- \frac{\hbar^2}{2\Im}(I_+ J_- + I_- J_+) \end{aligned} \tag{1.24}$$

The first term is the rotational term. The second term depends only on the intrinsic degree of freedom and can be absorbed in the intrinsic component of the Hamiltonian. The final term is the Coriolis term and represents the coupling of the single-particle and rotational motion. The $I_\pm$ and $J_\pm$operators change K by one unit ($\Delta K = \pm 1$) leading to an admixture of states with different K values.

Two important cases emerge depending on the relative weights of these terms: **Deformation alignment limit (DAL) or strong coupling.** This limit is recognised when the level splitting of the deformed shell model single-particle energies for different Ω values is large compared with the Coriolis perturbation. This occurs at large deformation or small Coriolis matrix elements (low-J or high-Ω when J is large). In this limit, the single particle motion is assumed to be independent of the collective rotation.

The angular momentum vector J is coupled to the deformation and K is approximately a good quantum number. For $K \neq \frac{1}{2}$ bands, there is little signature splitting and the rotational band is given by a ΔI=1 sequence with: I = K, K+1, K+2,... The energies of the levels are given by:

$$E_K(I) = E_0 + \frac{\hbar^2}{2\Im}\left[I(I+1) - K^2\right] \tag{1.25}$$

For $K = \frac{1}{2}$ bands, a perturbative calculation of the Coriolis interaction gives us the energies of the levels as:

$$E_{K=\frac{1}{2}}(I) = E_0 + \frac{\hbar^2}{2\Im}[I(I+1) - \frac{1}{4} + a^{(-1)}(I+1/2)(I+1/2)] \tag{1.26}$$

where the decoupling parameter, a, for a $K = \frac{1}{2}$ band is given by the expectation value of the J_+ operator:

$$a = i\langle\chi_{1/2}|J_+|\chi_{1/2}\rangle \tag{1.27}$$

Rotational alignment limit (RAL). For moderately deformed nuclei, or fast enough rotation, the Coriolis force may be so strong that the coupling of the nucleon to the deformed core is negligible. The Coriolis interaction aligns the intrinsic angular momentum J of the particle with the rotational angular momentum of the core, R. In this limit, the projection of the intrinsic angular momentum on the rotation axis, J_x, becomes a good quantum number. The band properties are then

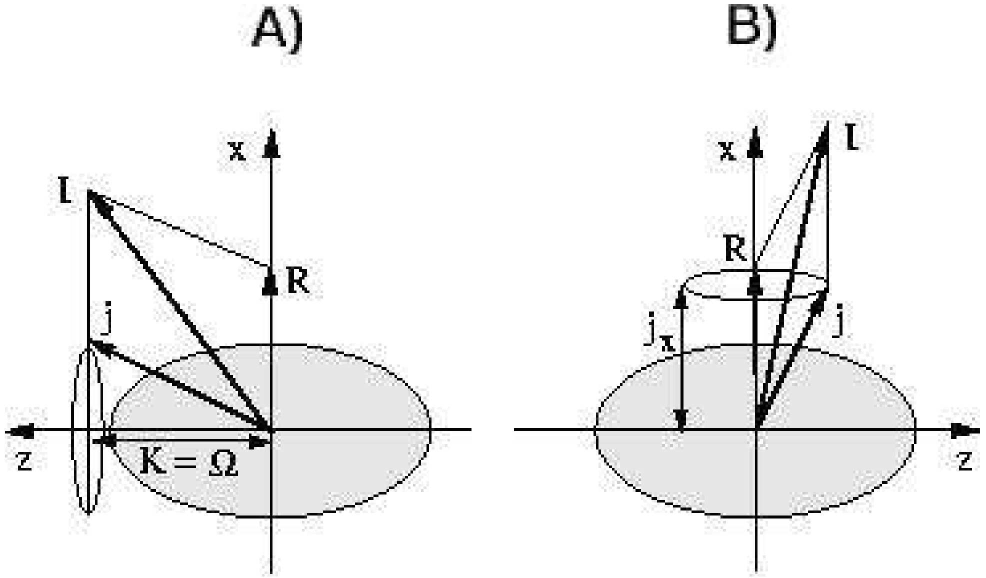

Figure 1.2: *Schematic view of coupling scheme limits.A) Deformed alignment scheme, B) Rotational alignment scheme.*

determined by the wave function of the odd-particle and the spin members of the band are given by:

$$I = J_x, J_x + 2, J_x + 4, ... \tag{1.28}$$

The lowest lying states are therefore the ones which are maximally aligned, $J_x = J$ (*favoured* states). The energies of the band levels are given by:

$$E_K(I) = E_0 + \frac{\hbar^2}{2\Im} R(R+1) \tag{1.29}$$

where $R = I - J_x$

Lesser aligned states, *unfavoured* states, have $J_x = J - 1$ and the spin sequence for the unfavoured band is:

$$I = J_x - 1, J_x + 1, J_x + 3, ... \tag{1.30}$$

These unfavoured states often lie at higher energies and are populated with less intensity than the favoured ones in heavy ion reactions.

1.2.3 Rotational Energy. The Cranking Shell model.

The collective features have been described so far in terms of a macroscopic approach. A successful interpretation should include a treatment of the collective rotation motion in term of the microscopic shell approach. This method was proposed by Inglis [Ing54].

From a semi-classical point of view, the basic idea suggested by Inglis is the introduction of a coordinate system which rotates with constant angular velocity, ω, around a fixed axis in space, in this way the motion of the nucleons in the rotating frame is rather simple if the angular frequency is properly chosen. In particular, the nucleons can be described as independent particles moving in an average potential (mean field) which is rotating with the coordinate frame. Thus, without taking into account any residual interaction, the rotating mean field potential will introduce an explicit time dependence to the Schrödinger equation.

$$i\hbar\frac{\partial\psi_l(t)}{\partial t} = H_l\psi_l(t) \tag{1.31}$$

where H_l and ψ_l are the Hamiltonian and the wave function in the laboratory coordinate system. Assuming a collective rotation around an axis perpendicular to the symmetry axis we find that the rotation axis coincides with the x-axis. We can eliminate the time dependence, transforming H_l and ψ_l into the rotating frame, using the rotation operator $\Re(\alpha)$, which corresponds to a rotation by an angle $\alpha = \omega \cdot t$, defined by:

$$\Re(\alpha) = exp(-iI_x\omega t) \tag{1.32}$$

where I_x denotes the x component of the total angular momentum on the rotational axis. Thus, we obtain:

$$\begin{aligned} \psi_l &= \Re(\alpha)\psi_{intr} \\ H_l &= \Re(\alpha)H_{intr}\Re^{-1}(\alpha). \end{aligned} \tag{1.33}$$

Thus, substituing eq 1.33 in the equation 1.31 and multiplying by $\Re^{-1}$, the Schödinger equation can be written in the intrinsic rotating system as

$$i\hbar\frac{\partial\psi_{intr}}{\partial t} = (H_{intr} - \hbar\omega I_x)\psi_{intr} = H^\omega\psi_{intr} \tag{1.34}$$

This equation is now stationary and the H^ω is called the cranking Hamiltonian or Routhian, H_{intr} is the intrinsic single-particle Hamiltonian and $\hbar\omega I_x$ corresponds to the classical Coriolis force. The Cranking Hamiltonian can be expressed in term of single particle states as:

$$H^\omega = \sum_{i=1}^{A} h^\omega(i) = \sum_{i=1}^{A}[h_{intr}(i) - \hbar\omega j_x(i)] \tag{1.35}$$

Since H^ω, and therefore h^ω does not depend on time, the solution of eq. 1.34 is then reduced to the solution of the eigenvalue problem.

$$h^\omega|\chi_\nu^\omega\rangle = \varepsilon_\nu^\omega|\chi_\nu^\omega\rangle, \tag{1.36}$$

where, each solution ε^ω denotes the corresponding single-particle Routhian. However these energies are expressed in the rotating frame and therefore can not be compared to the measured energy values in the laboratory frame. Thus, the true energies are defined as the expectation values of the intrinsic Hamiltonian $h_{intr}(i)$ with the eigenfunction χ_ν^ω

$$\begin{aligned} e_\nu = e_\nu(\omega) &= \langle \chi_\nu^\omega | h_{intr} | \chi_\nu^\omega \rangle \\ &= \varepsilon_\nu^\omega + \hbar\omega \langle \chi_\nu^\omega | j_x | \chi_\nu^\omega \rangle . \end{aligned} \tag{1.37}$$

The total energies are then expressed as sums:

$$\mathcal{E} = \sum_\nu \varepsilon_\nu^\omega + \hbar\omega \sum_\nu \langle \chi_\nu^\omega | j_x | \chi_\nu^\omega \rangle \tag{1.38}$$

In the ground state the summation over ν is understood to include the states with the lowest single-particle Routhians, ε_ν^ω.

Rotational spectra: symmetries.

In the case of axially symmetric deformed nuclei (with even multipolarity components only), the intrinsic Hamiltonian is invariant with respect to the rotation of π angle about the three principal axes, called reflection symmetry. However, the cranking Hamiltonian H^ω, is only symmetric for rotation around the x'-axis, represented by:

$$\Re_{x'} = e^{-i\pi I_{x'}} \tag{1.39}$$

Under a rotation of 2π, given by $\Re^2$, there is no influence on the wave function of an even-A nucleus, but for a odd-A nucleus the wave function will change sign under such a transformation. Hence, we can write:

$$(\Re_{x'})^2 = (-1)^A \tag{1.40}$$

If we define the eigenvalues of $\Re_{x'}$ as $r = e^{-i\pi\alpha}$, then it will take values of $r = \pm 1$ for even-A nuclei and $r = \pm i$ for odd-A nuclei. The spin sequences compatible with these values are:

$$\begin{aligned} &r = +1 \quad \alpha = 0 \quad I = 0, 2, 4, ... \\ &r = -1 \quad \alpha = 1 \quad I = 1, 3, 5, ... \\ &r = -i \quad \alpha = +1/2 \quad I = 1/2, 5/2, 9/2, ... \\ &r = +i \quad \alpha = -1/2 \quad I = 3/2, 7/2, 11/2, ... \end{aligned} \tag{1.41}$$

The eigenvalue r of the $\Re_{x'}$ operator is called the signature, but often the α number is used because of its additive nature.

Parity, π is the remaining symmetry and the cranking routhians are often labelled by parity and signature (π, α). The total parity and signature of a multi(quasi)particle configuration are given by:

$$\pi_{tot} = \prod_i \pi_i \qquad \alpha_{tot} = \sum_i \alpha_i \tag{1.42}$$

These are some of the theoretical models that achieve a good description of the rotational behaviour of the deformed nuclei as the ones we are interested in. In addition, the nuclei in the mass region we are centred display other phenomena related with the fact that they have N$\simeq$Z and they are near the proton drip line. Let us give an overview of some of these phenomena.

1.3 Approaching the drip line. Phenomena

In this section I will mention briefly some of the interesting phenomena that characterise the nuclei in the region we are interested in, where a better understanding and a deeper knowledge can serve to test the existing models. Thus, near the proton drip-line the following phenomena have been identified.

1.3.1 Shape coexistence

At the beginning of the 1980s calculations were done in order to explain the new region of large prolate deformation associated with shell gaps at N,Z=38. From these calculations two important facts became crucial to our understanding of the data obtained in previous experiments on light Kr and Sr nuclei: the proton and neutron gaps at large deformation and the reinforcing of proton and neutron driving forces when both N and Z are at or near shell gaps with the same deformation. Moreover, shell gaps appear also at oblate deformation for N=Z=34 and N=Z=36, as it has been confirmed from the experiments on Se isotopes [Ham74, Wio88] as we can observe in single particle spectrum as the one showed in fig. 1.1.

Potential energy surface (PES) calculations which are minimization of the total energy as a function of the deformation parameters, have shown the existence of competing minima on the prolate and oblate sides which lie within a few hundred keV of each other. Experimental results, first in Se isotopes and then in Kr nuclei have confirmed the presence of both spherical, prolate and oblate shapes in the yrast band. In fig 1.3 the moment of inertia show how the low levels in the yrast band that belongs to near spherical an even oblate shapes compete with prolate band that dominate the yrast band at higher spin. In ^{68}Se the oblate band develops even up to high spin competing with a prolate band.

1.3.2 Pairing correlations. T=0 vs T=1 competition.

The residual interactions that have not been included in the mean field interaction can contribute significantly to the nuclear structure of the nucleus. Particularly evident is the fact that the ground states of all even-even nuclei have $I^{\pi} = 0^{+}$. In principle, a pair of like nucleons occupying a single j-shell could couple their angular momenta to the values I=0,2,4,...,(2j-1). In the independent-particle shell model these states are degenerate and the inclusion of a short range attractive interaction acting on two identical particles in spatially symmetric (time-reversed)

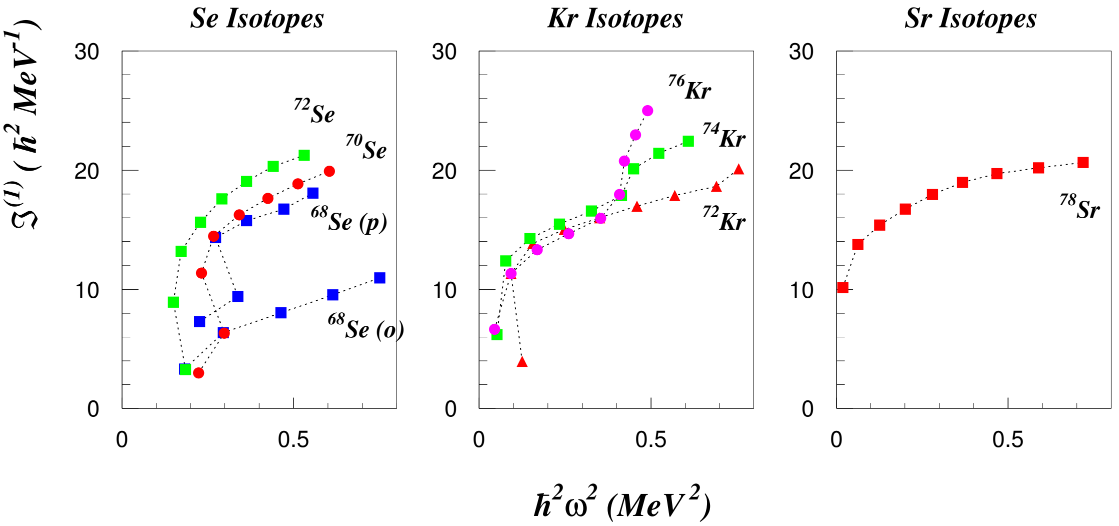

Figure 1.3: *Kinematical moment of inertia* $\Im^{(1)}$*, as a function of the frequency squared for light Se, Kr and Sr isotopes. The first two species show the competion between shapes at low spin, the Sr panel correspond to a good rotor.*

orbits, lowers the state with I= 0^+. Another effect that reveals the need to include an interaction that correlates like nucleons is the difference in binding energy. For a fixed A number the behaviour of B(N,Z) follows a parabola as a function of Z for odd A but for even A it seems to follow 2 different parabolae depending on whether it is odd-odd or even-even. This means that a term, the pairing term Δ_{pair} has to be introduced in the semiempirical mass formula to account for the increased stability of the even-even nuclei. Empirically it is observed to depend on A and from fits to nuclear masses it is given by:

$$\Delta_{pair} = \frac{12}{\sqrt{A}} MeV \tag{1.43}$$

Even more, the N=Z nuclei seem to be more stable (more bound) than their neighbours, and this empirical fact, known as the Wigner term in the mass formula, is not easy to explain. Assuming the charge independence of the strong nuclear force, the pairing correlations between unlike nucleons in time reversed orbits becomes important in light nuclei where the Fermi energies of the proton and neutron distribution lie close together and the neutrons and protons fill the same spatial orbits. Moreover, in these nuclei, particularly in N=Z nuclei the correlations between p-n coupled to isospin T=0 become important, even stronger than the T=1 pairing. This gives rise to a competition between both pairing modes.

In this context it is known that odd-odd, N=Z nuclei with A≤40 have ground states with T=0 while in odd-odd, N=Z nuclei with A>40 the ground state should prefer the T=1 pairing mode. Thus, the region with N,Z≈28-50, where the proton and neutron fill the pfg shell is particularly interesting in terms of testing models.

1.3.3 Coulomb energy differences (CED)

The charge independence of the nuclear force (or isospin symmetry) and charge symmetry mean that self-conjugate nuclei (i.e. mirror nuclei) present the same level scheme energies except for the Coulomb interaction effects. The absolute difference between the binding energies of the ground states (called Coulomb displacement energies) should be due only to Coulomb effects.

The total Coulomb energy of a nucleus is the sum of the Coulomb interactions between all the protons in the nucleus. Thus in a isobaric multiplet [2]we can define the Coulomb Energy Difference (CED) as the difference in energy between the excited states of two of the members of the multiplet normalised to the ground state.

$$CED = E_x^{(T,T_z<)} - E_x^{(T,T_z>)} = CDE - (E_{g.s.}^{(T,T_z<)} - E_{g.s.}^{(T,T_z>)}) \tag{1.44}$$

where CDE is the Coulomb Displacement Energy or difference between the energies of the members of a isospin multiplet.

The study of the CDE over a wide range of isobaric nuclei has shown some discrepancies between experimental values and theoretical expectations. This anomaly (Nolen-Schiffer anomaly) amounts to 6-8% and even assuming some other corrections is not completely understood. Various effects have been suggested to explain this including a charge-asymmetry component of the nuclear potential, the effect of differences of isospin impurities in the g.s., the Coulomb distortion of the wave function of the orbit occupied by the excess nucleon (Thomas-Ehrman Shift), etc.

1.3.4 Astrophysics interest

Two of the major aims of nuclear astrophysics are: a) the understanding of energy generation in stars at all stages of stellar evolution and, closely related b) the understanding of the nuclear processes, in the astrophysical context, which produce the observed relative abundances of the elements and their isotopes in nature: the nucleosynthesis processes. Both are closely related and their understanding and how the nuclear physics can help are the key to improve our knowledge of the connection between what we measure in the laboratory and our observations of the Cosmos.

The way a star generates its energy is principally through nuclear fusion processes. Depending on the initial composition and mass, the star evolves through several stages, burning the "fuel" and generating heat and pressure to counterbalance the gravitational force. Thus, the stars begin with the Hydrogen burning stage, mainly through $^1H +^1 H$ and $^2H +^1 H$ fusion reactions creating ^4He and energy in

---

[2] The isobaric multiplet is defined as states which have all quantum numbers equal, icluding the Isospin T, except the third isospin component T_z.

the so-called pp-chains that are briefly summarized through the net reaction:

$$4^1H \rightarrow ^4He + 2e^+ + 2\nu + 24.7MeV \tag{1.45}$$

If heavier elements, such as ^{12}C and ^{16}O, are present in the initial composition and the stellar temperature is high enough, proton reactions can ignite other Hydrogen burning processes: the CNO cycles. In these processes, C, N and O isotopes act simply as catalysts for the reactions. The CNO cycles dominate over the pp-chains in the energy production in massive stars where the temperatures are higher and the proton can overcome the higher Coulomb barrier of the C, N and O isotopes.

$$\begin{aligned} &^{12}C(p,\gamma)^{13}N[e^+\nu]^{13}C(p,\gamma)^{14}N(p,\gamma)^{15}O[e^+\nu]^{15}N(p,\alpha)^{12}C, \\ &^{16}O(p,\gamma)^{17}F[e^+\nu]^{17}O(p,\alpha)^{14}N(p,\gamma)^{15}O[e^+\nu]^{15}N(p,\gamma)^{16}O. \end{aligned} \tag{1.46}$$

Once the hydrogen fuel has been exhausted the centre of the star collapses under gravity producing an increase in the temperature that overcomes the $^4He +^4 He$ Coulomb barrier. Thus, the Helium burning phase sets in combining three ^4He nuclei together to form ^{12}C and later combining ^4He with ^{12}C to form ^{16}O. This stage could be the last for stars like our Sun. If the stellar temperature is high enough, this process can continue and more alphas fuse together creating heavier elements ^{20}Ne, ^{24}Mg, ^{28}Si,... etc. Also the products from the CNO cycles from the previous hydrogen burning could capture α nuclei and contribute to the process. When the helium fuel begins to be exhausted, gravitational collapse sets in again increasing the temperature and beginning the subsequent fusion stage, but only if the star is very massive. The new energetic phase implies ^{12}C- and ^{16}O burning that leads to the production of ^{20}Ne and ^{28}Si. Finally, the star contracts its core again and the temperature rises but the Coulomb barrier is too high for nuclei such as ^{20}Ne or ^{28}Si to fuse. Instead, the high temperatures reached make possible the photodesintegration reaction of these nuclei, followed by fusion of the dissociated products creating heavier elements. The end products of this complex process, called "photonuclear rearrangement", are nuclei of mass A=56, the most tightly bound nuclei. Afterwards no further nuclear fusion reactions can occur and the core begins a gravitational collapse. A massive explosion is then produced, a supernova, that eject the outer envelope of the star leaving a neutron star or a black hole depending on the mass.

During the processes that generate the energy in the stars, the different nuclei of the nuclide chart can be produced according to the time-scale of the nuclear process involved. Thus, in main sequence stars, the nuclear burning processes, such as the pp-chains, CNO-cycles, He-burning, etc. occur with time scales much longer than a typical nuclear β-decay lifetime. Nuclei with mass $A \leq 56$ are created in this kind of quiescent environment, as a result of the fusion reactions. Heavier elements are created through slow neutron capture reactions that take place with the neutrons produced during the helium burning stage. This is the so-called *s-process*, in which a stable nucleus captures a neutron at a reaction rate around $10^{-9}/s$ forming another stable isotope and the process will continue until a radiactive isotope is formed. It will then β-decay to other stable elements which will subsequently capture a neutron and so on.

These processes cannot account for all the observed isotopes abundances in the universe. In fact, the s-process path proceeds near the stability line up to the last stable nucleus, ^{209}Bi. Thus, further research has propose other processes that can explain the abundances of nuclei originated further away from the valley of stability. In particular, neutron rich nuclei can be formed if a higher flux of neutrons was available, in this situation the interval between neutron captures is much shorter than the lifetime for beta decay. A rapid succesion of neutron captures would produce nuclei beyond the valley of stability, up to nuclei in which the rate of photodesintegration induced by energetic photons is of the order of the neutron capture reaction, the so-called "waiting points". After some time at this waiting point, a beta-decay occurs and the capture process can begin again. This rapid process is named the *r-process* and it is suggested to be very important in supernova scenarios.

Other nuclei, such as the proton rich nuclei between the valley of stability and the proton drip line depend for their formation on the rate of the proton and alpha capture reactions. Thus, if the rates are greater or comparable to the beta-decay, the CNO cycles can be bypassed and the Hot CNO (HCNO) cycles will come into operation, creating higher mass elements through (p,γ) reactions. The products of these HCNO cycles will act as seeds of the *rp-processes* and even higher mass isotopes will be produced depending on the temperature and density conditions. These particular conditions are only found in astrophysical scenarios like novae, X-ray burst and supernovae, in which the burning of the hydrogen occurs in an explosive way.

In order to confirm the existence of these suggested processes, we need a considerable knowledge of the nuclear properties. In particular, the proton rich nuclei around A$\simeq$80, near the proton drip line, are important for the process of nucleosynthesis during explosive hydrogen burning. In a recent extensive analysis [Sch98] the influence of nuclear structure on the rp-process has been studied with a number of theoretical models for nuclear masses, deformations, reaction rates and β-decay rates. In connection with the present work, it is very important to determine the properties of these nuclei such as the deformation, the lifetime of ground states and low-lying isomer states, to model all these nucleosynthesis processes.

1.4 Modern experimental Tools

Access to the nuclei in the region near the drip lines has been and is being made possible due to improvements in several aspects of the scientific research. Among these aspects we can mention the development of new accelerators, improvements in the detection systems and electronics, refinements in the experimental techniques, etc.

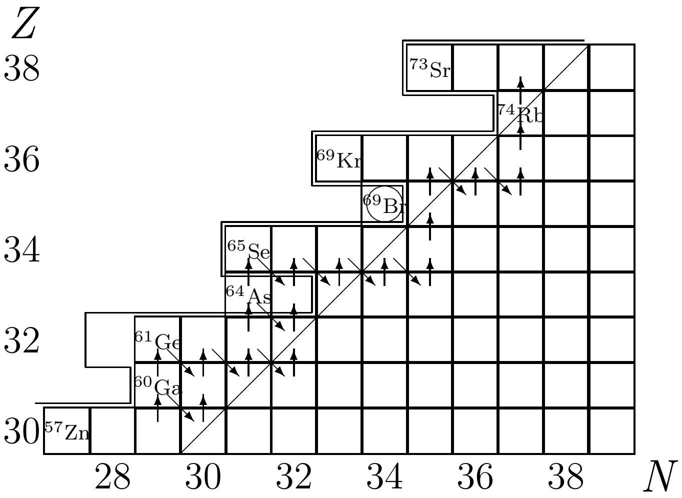

Figure 1.4: *Possible path for the rp-process along the proton drip-line as deduced from calculations.*

From the beginning of the 1960s Tandem Van de Graaff accelerators able to deliver from light to heavy ions with currents of considerable intensity (of the order of 10pnA) were coming into widespread use. These machines supplied ion beams up to energies of the order of tens of MeV per nucleon allowing us to populate high spin states of neutron deficient nuclei in a wide range of the nuclear chart. Different kinds of reactions have been used to study the nuclear structures features. Thus Coulomb excitation has provided the most solid information about the collective behaviour exhibited by nuclei. This technique allows us to measure absolute γ-ray transition probabilities, especially B(E2), and nuclear quadrupole moments for stable or nowadays for nuclei produced in the new radioactive beam facilities. Other techniques such as transfer reactions and α- and neutron-induced reactions have been used extensively to explore the nature of low-lying nuclear states in nuclei near the line of β-stability.

In recent decades the reactions induced by heavy ions have been of particular relevance due to the ability to populate high spin states. This has led to the discovery of superdeformation, the backbending and other exciting phenomena related to high spin. Moreover, with heavy ions it is possible to reach nuclei far from the stability, although with low cross sections in general. The residual nuclei populated in this way decay to their ground state by the emission of cascades of gamma rays. By measuring the properties of these gamma transitions (γ-ray energies, angular distributions, polarization, etc.) it is possible to build the level scheme and comparing with the models to obtain information on the nuclear structure.

The study of the properties of the atomic nucleus through γ-ray spectroscopy has evolved through the development of the γ-ray detector arrays. Relatively recently, with the advent of large gamma-ray detector arrays, coupled to highly efficient ancillary detectors and/or recoil mass spectrometers, it has been possible to extend the study of the nuclear structure of nuclei close to the drip lines, particularly on the proton-rich side.

1.4.1 Detection systems

Many of the major discoveries in nuclear structure studies over the last 30 years there is strongly associated to the developments in detection technology and in the area of particular with the improvement of arrays of γ-ray detectors [Nol94].

The first multi-detector arrays were based on the use of scintillators such as NaI(Tl) and BaF_2, with a large number of detectors covering a solid angle as close to 4π as possible. These arrays were mainly devoted to measurements of the multiplicities and total energies of the γ-ray cascades emitted in the de-excitation of the compound nucleus in fusion -evaporation reactions, quantities that allowed a better knowledge of the reaction mechanism. The sensitivity of theses arrays and their application to high spin studies were limited by the poor energy resolution of the scintillation detectors. Examples of such arrays were the 72-element Spin Spectrometer [Jaa83] at ORNL and the 162-element Crystal Ball [Sim80] at MPI-Heidelberg and at GSI-Darmstadt.

The development of Ge detectors, first Ge(Li) and later Hyperpure Ge detectors, offered an increase in the energy resolution and provided suitable detectors for high resolution γ-ray studies. The efficiencies reached by these Ge detectors were ≈25% (compared with a 76x76 mm NaI at 25 cm for 1.3MeV γ rays) giving rise to Ge arrays with absolute photopeak efficiencies around 0.5-1.0%. The Ge detectors were sometimes used with an active shield of NaI or BGO to create a Compton Suppression Spectrometer (CSS) thus reducing the background due to the Compton scattering process in the Ge crystal and increasing the peak-to-total ratio. This is crucial in $\gamma\gamma$ coincidence spectroscopy. In order to improve the low sensitivity caused by the low efficiency of the Ge detectors, multiplicity filters based on scintillation detectors were used. Examples of these first compact arrays included up to 30 Compton suppressed Ge detectors as in the case of TESSA III [Nol85] 32 Compton suppressed Ge detectors as in the case of NORDBALL [Her85], etc. The total efficiencies were optimal for two-fold γ-ray coincidences.

A new step followed the development of large volume HpGe detectors (70-80% relative efficiency of the 3"x3" NaI detector efficiency), that allowed an increase in the absolute photopeak efficiency of the arrays up to ∼5%, whilst keeping the good energy resolution despite the size. Arrays based on these large volume detectors, such as GASP [Baz92] and EUROGAM I [Bea92, Bec92], have good P/T response, high granularity that minimizes pile-up and Doppler broadening, etc. This improvement has allowed us to study excited states in nuclei populated with a cross section of the order of 10^{-6} b (Typical total cross sections are of the order of 1b).

Finally, the last innovation was the use of newly developed segmented or composite HpGe detectors in order to increase the granularity and the total photopeak efficiency of the arrays. Examples of the use of these kinds of detectors are EUROGAM II, GAMMASPHERE [Lee90] and EUROBALL [Ger92]. The later of

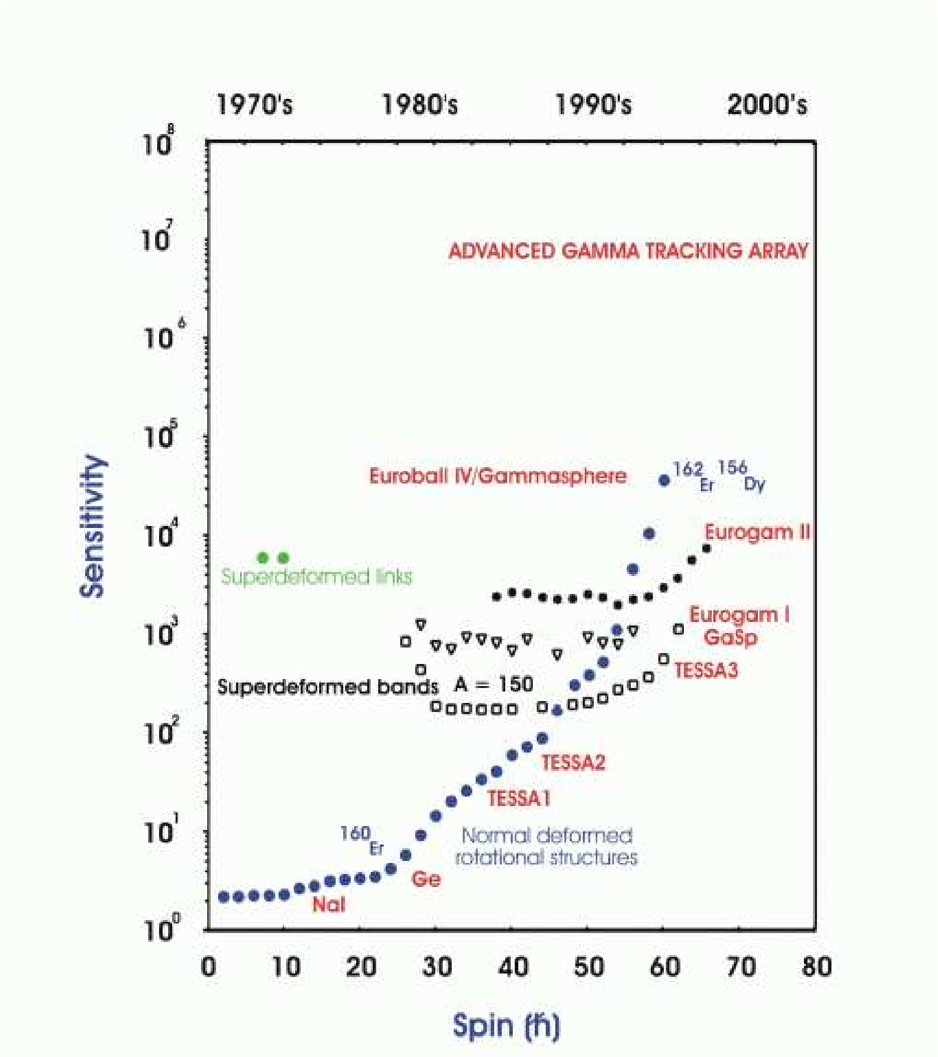

Figure 1.5: *The relative spectroscopic sensitivity of various gamma-arrays as a function of spin. In essence the improvement follows the development of improved detectors as a function of time. The figure is taken from the AGATA proposal document [Ger01].*

these uses two types of composite detector namely CLOVERs and CLUSTERs. A description of these detectors can be found in chapter three below.

Figure 1.5 demonstrates the improvement in sensitivity with time. For instance, if we compare TESSA (early 1980s) with EUROBALL IV and GAMMASPHERE spectrometers (in operation today).

1.4.2 Future prospects

The limits to the study of nuclear properties have partly been imposed by the production cross sections and partly by the detector efficiencies. For these reasons two major efforts are occupying the attention of the nuclear physics research community.

On the one hand, the development of radioactive ion beams will make it possible to produce nuclei far from the valley of stability with higher cross sections. In broad terms there are two principal methods to produce and accelerate radioactive beams: the projectile fragmentation (In-flight) and the ISOL methods.

In the in-flight technique, using the projectile fragmentation reactions in peripheral collisions, the different fragments produced are refocused and passed through a spectrometer to identify and select the ions that will be used as secondary beams. This method is easy to apply at the facilities with intense beams of high energy stable ions.

The ISOL method is a two step process. First the radioactive species of interest are produced in reactions induced by a charged particle beam or by neutron reactions in a target and diffuse out into an ion source. Following ionisation the ion is extracted and selected in a mass separator. The species of interest can then be injected into a post-accelerator. Acceleration to the energy required in the experiments then follows.

Over the last few years these methods have been used in a number of laboratories around the world to produced accelerated radioactive beams e.g. GANIL, RIKEN, MSU, GSI, NotreDame, REX-ISOLDE, etc. New projects for more intense beams are under development in two large programmes: RIA in USA and EURISOL in Europe.

On the other hand, further improvements in the efficiency of γ detector arrays can be achieved if the detectors are designed to allow the recovery of the events that have been lost by interacting in the Compton suppression shield. To achieve this only Ge detectors, without anticompton shields, highly segmented and new algorithms are being studied in detail. The idea is to locate the precise point of the gamma interaction inside the detector material. This can be done by segmenting the Ge detectors, and then subdividing the physical segmentation by means of the pulse-shape analysis and advanced digital signal processing techniques. We extract information about the energy, timing and position of the interaction. The gamma rays follow certain well known rules which relate scattering angle with energy: the Compton scattering formula and the Klein-Nishina formula. In this way, evaluating the position of the interaction and the energy deposited, we can reconstruct the gamma ray paths by looking for groups of interaction points which fulfill the formulae.

Two main gamma ray tracking projects are under study: GRETA in the USA and AGATA in Europe. Currently they have reached the stage of creating and testing prototype detectors, performing simulations for the pulseshape analysis and designing new electronics.

Chapter 2

The Problem (Our Physics case)

2.1 Introduction

The present work deals with the in-beam study of A=70 and A=71 bromine isotopes. Why should we study these neutron-deficient bromine isotopes?. In very general terms they share the general interest in the N$\sim$Z, A$\sim$70 nuclei, where we observe shape co-existence, n-p pairing effects and rapid changes in structure with Z, A, ω, etc. In terms of our macroscopic-microscopic models our aim in describing the properties of the Br isotopes is to understand how they change with the number of neutrons. In the case of ^{71}Br there is conflicting information from experiment on the properties of the lowest-lying levels as we will see below. The principal aim of the present work was to remove the discrepancies and provide a reliable basis for comparison with our theoretical calculations.

2.2 Previous knowledge of ^{71}Br

As we move from ^{64}Ge to ^{100}Sn along the N=Z line we find experimentally that we move from a spherical shape through the highly deformed, prolate ^{76}Sr and ^{80}Zr ground states back towards sphericity. On the way it is predicted by various authors [Ben84, Naz85] that we will pass through a region of oblate deformation centred on ^{70}Br. This alone would make the Br nuclei an interesting case.

Why are oblate shapes interesting?. Experimentally prolate shapes for the ground state are found to dominate throughout the nuclide chart when, in principle, energy-favoured or down-sloping orbits and large shell gaps can be found on both sides of sphericity. This fact can be understood from a simple point of view as being due to the combination of two factors [Cas90]. On the one hand, the shell model potential, with the l^2 term in the harmonic oscillator potential or the Woods-Saxon central potential term, favour lower energy for higher j orbitals after a shell closure, because of a stronger atractive interaction. And, on the other hand, one finds for a high j orbital, a higher density of energy-favoured low-K orbits on the prolate side than the energy-favoured high-K orbits on the oblate side of the single particle Nilsson diagram. This clearly will lead to the observed prolate shapes. Further, the liquid drop energy, when expanded to higher order, has terms in odd powers of beta, making prolates shapes more bound and with larger deformation.

We will find that Mean Field calculations suggest that the lowest energy prolate and oblate states lie close together for the odd Br-isotopes. This adds to the complexity of the level schemes and the resulting spectra observed in their study. Below I shall summarize our knowledge of ^{71}Br prior to the present work.

2.2.1 From In-Beam study or Arrison's work

High spin states in ^{71}Br were populated and their decay observed for the first time in fusion-evaporation reactions carried out at the Tandem Van de Graaff accelerator of the University of Pennsylvania by Arrison and co-workers [Arr90]. The γ-ray transitions belonging to ^{71}Br were identified in coincidence with evaporated particles, protons and neutrons, in the reactions: $^{40}Ca(^{32}S, p2n)^{71}Br$, $^{58}Ni(^{16}O, p2n)^{71}Br$ and $^{40}Ca(^{35}Cl, 2p2n)^{71}Br$. The set-up consisted of seven neutron detectors, four Ge detectors and a particle array. Thus, events in coincidence with exactly one proton and one or more neutrons were recorded. The events related to ^{71}Br (p2n channel) were separated from those related to ^{72}Br (pn channel) using both the neutron multiplicity and the measured excitation energy. From n-γ-γ coincidences the level scheme shown in fig. 2.1 was deduced. The four Ge detectors, were placed at 90 and 135 degrees to the beam direction allowing the measurement of partial angular distributions and angular correlations (DCO ratios). Hence values of I^π for the levels were deduced.

The isomeric level observed at 759 keV was asociated with the $g_{9/2}$ orbital as suggested by the level systematics in the region and it was assigned $I^\pi = 9/2^+$. The ground state of ^{71}Br was known to be $(3/2,5/2,7/2)^-$ from its β-decay to ^{71}Se. From the observed quadrupole distribution of the 759 keV transition and the value of the half-life, a B(M2)=0.068(10) was deduced which agrees with data in neighbouring nuclei and allowed them to assign $I^\pi = 5/2^-$ to the ground state. The level at 670 keV was assigned as $I^\pi = 5/2^+$ based on the quadrupole nature of the 89 keV transition, which is required by intensity arguments and the B(E2) according to measurements in neighbouring nuclei.

The ordering of the low-lying levels at 0, 9 and 207 keV levels is based on similarities with the ^{73}Br level scheme, but a 0, 198 and 207 keV level ordering could not be ruled out. From the angular distribution of the 198 keV transition they assigned spins 1/2 and 3/2 to the first two excited states.

The sequence of transitions above the $9/2^+$ state with ΔI=2 was assigned on the basis of the angular distributions of the 737 and 896 keV transitions and from the DCO ratio of the 737 keV transition gated on the 198 keV transition.

From this work one can conclude that the ΔI=2 rotational yrast band and the

Table 2.1: *Summary of the results obtained in the work of Arrison et al.*

E_{level} (keV)	E_γ (keV)	A. D.	I^π	E_{level} (keV)	E_γ (keV)	A. D.	DCO	I^π
0			$5/2^-$	759	89			$9/2^+$
9			$(1/2^-)$		759	Q		
207	198	D	$(3/2^-)$	806	599		0.49±0.20 [a]	$(7/2^-)$
	207			1496	737	Q	0.43±0.29 [a]	$13/2^+$
262	54		$(3/2^-)$	1611	805			$(11/2^-)$
	262			2392	896	Q		$(17/2^+)$
670	408		$5/2^+$	2518	907			$(15/2^-)$
	462			3473	1081			$(21/2^+)$
	670							

[a] DCO ratio obtained when gating on 198 keV transition.

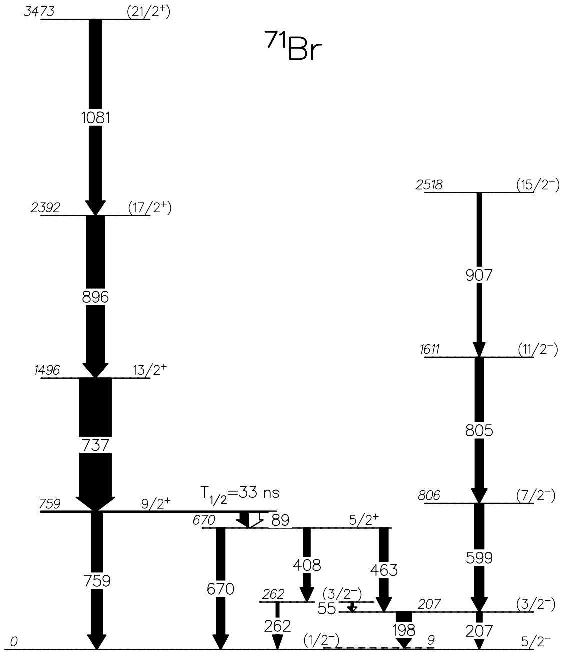

Figure 2.1: *Level scheme of ^{71}Br from the work of Arrison et al. [Arr90]. The transition intensities are proportional to the width of the arrows.*

lack of evidence for an yrast cascade of low energy, ΔI=1 transitions, as suggested by other authors, imply that there is no clear evidence of oblate deformation in^{71}Br. Moreover, the ΔI=2 band is typical for neighbourg nuclei with prolate deformations, see fig 6.5.

2.2.2 β-decay studies.

Beta decay transitions between mirror nuclei with T=1/2 are interesting because the B(GT) strength depends on the wave function of the states involved. Due to the selection rules in β^+-EC decay, low spin states that cannot be reached via fusion-evaporation reactions are populated here, thus allowing us to investigate the wave functions of these states. The measurement of the half-life and the partial branching ratios to these states are essential to understand their structure.

Oinonen *et al.* [Oin97] have studied the decay of ^{71}Kr to levels in ^{71}Br. The ^{71}Kr activity was produced in the spallation of a Nb target using 1 GeV protons from the PS Booster at CERN-ISOLDE facility [Klu92]. The nuclei produced were separated in mass with the ISOLDE on-line mass separator. Typically an activity of 1 atom per second of ^{71}Kr arrived at the measuring station. These nuclei were implanted on to a moving tape system with the deposition part viewed by a gas-Si detector telescope, a 20 mm thick Ge detector, a 70% HpGe detector and a β-telescope.

They observed the population of the low-lying states by detecting the gamma transitions resulting from the de-excitation of these levels and the population of states at higher excitation energy, ~4 MeV, through the β^- delayed proton emission. Their results can be summarized in the following table:

Table 2.2: *Summary of the results obtained in the work of Oinonen et al.*

E_x (keV)	I^π	I_β (%)	log *ft*	$\lvert < \sigma\tau > \rvert$
0 + 9	$(5/2)^-$	82.1±1.6	3.71±0.07	0.33±0.19
207	$(3/2)^-$	15.8±1.4	4.38±0.08	0.40±0.04
262	$(3/2^-)$	<1	>5.6	
806	$(7/2^-)$	<1.1	>5.4	
p unbound		<2.1		

Only direct β-feeding to the 0 and/or 9 keV states and 207 keV state have been observed and no other low-lying states appear to be fed. Due to the low excitation energy of the first excited states (9 keV) the contribution to the g.s. and first excited states could not be separated. They assign to the ^{71}Kr ground state $I^\pi = (5/2)^-$ based on the $5/2^-$ g.s. of the^{71}Br mirror nuclus, but due to the above mentioned limitations on the g.s. and the 9 keV state population, the I^π assignment remains still uncertain. Anyway, the absence in the gamma spectra of transitions dexciting the E_x=262 and 806 keV levels could contradict the assignments made by Arrison in favour of the new assignation of Urkedal and Hamamoto [Urk98].

2.3 The odd-odd nucleus ^{70}Br

Prior to the present work little was known about the odd-odd, N=Z nucleus ^{70}Br. In fact, only the lifetimes of the ground state and an isomeric state have been measured previouly. A first reported identification of the excited states [Bor99] was later revised [Bor99a] due to misidentification of the reaction product.

As mentioned before, the energy levels in the N=Z, odd-odd nuclei are of particular interest because of the competition between T=0 and T=1 n-p pairing modes. Although T=1 and T=0 states are expected in N=Z nuclei, both even-even as well as in odd-odd nuclei, only in the latter are both sequences almost degenerate. In the even-even N=Z nuclei, the $I^{\pi}=0^{+}$ T=0 ground state is separated from excited T=1 states by a reasonably large energy gap[1]. The occurrence of strong magnetic dipole, M1, transitions between the lowest T=0 and T=1 states in odd-odd nuclei along the N=Z line is another interesting phenomenon that can be tested [Bre02].

Other structural effects related to the Coulomb interaction of the protons can be studied through the Coulomb energy displacement (CED) between isobaric analog states. Thus, in the $f_{7/2}$ region the CEDs in T=1/2, T=1 nuclei has been found to be very useful, allowing to study the spatial behaviour of the active valence nucleons [Ben98, Ole99]. The dependence of the excitation energy differences of T=1 states as a function of T_z can be investigated in isobaric triplets, which is of particular interest in nuclei close to the dripline where differences in proton radii should manifest themselves through differences in the behaviour of CEDs. In addition, it may be possible to deduce new information on np pairing effects from the CED in these nuclei.

2.3.1 Beta-decay studies

Both the ground state and an excited, isomeric state in ^{70}Br are known to beta decay. The β-decay of the ground state of this self-conjugate, odd-odd nucleus was measured by Burch *et al.* [Bur88] to have a half-life of 78.54(59) ms, which is consistent with the superallowed Fermi-decay of a T=1, $J^{\pi} = 0^{+}$ state to the g.s. of the daughter nucleus ^{70}Se.

Vosicki *et al.* were the first to report on the decay of an isomeric level in ^{70}Br. The activity was produced in spallation and mass-separated. A beta spectrum with $T_{1/2}$=2.2 (2) s was observed and attributed to ^{70m}Br. More recently Piechaczek *et al.* [Pie00] have observed β-delayed gamma rays in ^{70}Se from the decay of ^{70}Br and ^{70m}Br produced in the $^{40}Ca(^{32}S, pn)^{70}Br$ reaction at 110 MeV bombarding energy. The Oak Ridge Recoil Mass Separator (RMS) was used to separate the A=70 nuclei and transport them to be implanted into the transport tape of a moving tape collector [Zga99]. The ground state activity decayed away during transport of the activity to a detection station. This allowed a study of the γ-rays from ^{70m}Br. The

---

[1] This energy gap will depend on various aspects as the pairing gap, the deformation of the nucleus, etc.

authors concluded that ^{70m}Br has T=0, $J^{\pi} = 9^{+}$ and a $\{\pi[404]9/2^{+} \otimes \nu[404]9/2^{+}\}_{9^{+}}$ configuration. They were unable to determine the excitation energy of the isomer in ^{70}Br from their experiment.

2.3.2 The present work.

In the present work the principal aim was to realize the complete spectroscopy of the low-lying states, in order to identify the different isospin structures that characterise the N=Z nuclei in the A=60-80 region. By establishing the I^{π} of the low levels one can deduce the energy differences of the T=0 and T=1 states and to shed some light on the role of the isovector and isoscalar pairing correlations.

In this sense the reaction ^{40}Ca on ^{40}Ca at a bombarding energy of 95 MeV have been proposed first at GASP γ-array facility and later at the EUROBALL γ-array facility, in order to improve the experimental sensitivity and get a confirmation of the results. The positive results on the identification of the ^{70}Br from these experiments are reported in the next chapters.

Chapter 3

Experimental Techniques

One of the main vehicles for the study of proton rich nuclei is the fusion-evaporation reaction. Fig 3.1 shows schematically how such a reaction proceeds. Initially, if fast fission does not occur, a compound nucleus is formed. It has high angular momentum, high linear momentum and high excitation energy. In other words it is a charged, rapidly rotating and hot object, which behaves like a liquid drop because of the short-range nature of nuclear forces. Like any hot, liquid drop it acts to reduce its temperature by evaporating particles: protons, neutrons and alpha particles in this case. These particles carry away a lot of energy (heat) but very little angular momentum because of the centrifugal barrier that they face. After particle evaporation the nucleus has cooled down but is still rotating rapidly. It loses now its energy and angular momentum by long series of electromagnetic transitions, mostly in the form of gamma rays. In this work we will study the emitted gamma rays and then deduce the properties of the associated levels.

Near stability most of the evaporated particles are neutrons because they don't feel the Coulomb barrier. As we move away from stability the relative binding energies of the various types of particle change and the emission of charged particles becomes favoured. Since neutron emission leads furthest from stability and the nuclei produced are very neutron-deficient, at some point it becomes very difficult to evaporate more neutrons and the cross section drops rapidly. Along the $N = Z$ line it also drops as Z increases because the stable nuclei are progressively more neutron rich. Thus the heaviest $N = Z$ nuclei studied so far, ^{84}Mo [Gel91, Buc97] and ^{88}Ru [Mar01], have cross-sections of only a few μb out of a total reaction cross-section of ∼1 b.

All of this makes the study of nuclei with A∼70, $N \sim Z$ very difficult. Several major steps have been taken over the last two decades to allow the study of γ-rays from such reaction channels. They include a) an increase in the absolute efficiency of γ-ray detection by building large arrays of Compton-suppressed Ge detectors and b) the development of ancillary detectors and recoil separators to allow sensitive channel selection. Under a) it has also been essential to build γ-ray arrays of high

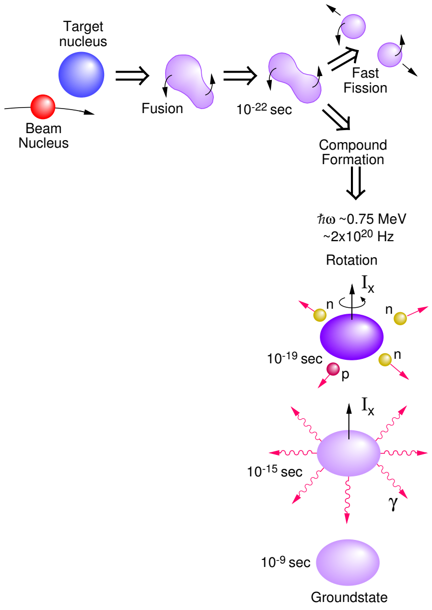

Figure 3.1: *Schematic of the fusion-evaporation process. Taken from [Ril98]*

granularity in order to avoid i) summing effects, ii) Doppler broadening and iii) to allow the use of high-fold coincidences to clean the spectra.

In this chapter I will describe further details of the fusion-evaporation reaction, the detection of gamma rays and the use of ancillary detectors and recoil separators.

3.1 Fusion-evaporation reactions

In the study of high spin states, one tries, in general, to populate the nucleus at the highest possible angular momentum (L) with the largest cross section (σ). As mentioned earlier the most commonly used method to achieve this is through heavy-ion fusion-evaporation reactions where a compound nucleus is produced at high excitation energy and high angular momentum.

When a beam of particles is accelerated against a fixed target various types of reactions can occur depending on the mass and energy of the projectile and on the impact parameter (fig 3.1) Thus, for heavy ions at energies above the Coulomb barrier, fusion reaction will be the dominant process for values of the impact parameter smaller than the distance of “closest approach”. In these conditions, due to the strong nuclear interaction, the nuclei fuse together in a compound nucleus (CN) and reach the thermal equilibrium status after $\sim 10^{-20}$ s in which the kinematic energy in the centre of mass is transformed into excitation energy, and the relative angular momentum between target and projectile is transferred to the compound system. The CN loses all memory of the entrance channel except for the conservation of mass, charge, energy and angular momentum.

The excitation energy at which the compound nucleus is formed is fixed by the reaction and can be expressed by:

$$E_{exc} = E_{cm} + Q_{fus} = \left(\frac{M_T}{M_p + M_T}\right) E_{lab} + Q_{fus}(MeV) \tag{3.1}$$

where M_p and M_T are the masses of projectile and target nuclei, in a.m.u., E_{lab} is the energy of the projectile and Q_{fus} is the Q-value for the fusion reaction in MeV.

The semi-classical angular momentum imparted to the compound nucleus by the projectile with a linear momentum, mv, depends on the impact parameter, b, as $l = mvb$ and so, the maximum angular momentum will correspond to a peripheral collision. Using the "sharp cut-off" approximation in which nuclei are considered hard spheres without a diffuse surface, and remembering the conservation law of energy and angular momentum we can estimate l_{max} as:

$$l^2_{max} = \left(\frac{2\mu R^2}{\hbar^2}\right)(E_{cm} - V_{cb}) \tag{3.2}$$

where μ is the reduced mass of the system, $R = R_p + R_T$ is the distance of closest approximation (or grazing distance) and is given empirically by [Wil73]

$$R = 1.36(A_p^{1/3} + A_T^{1/3}) + 0.5(fm) \tag{3.3}$$

E_{cm} is the beam energy in the centre of mass and V_{cb} is the Coulomb barrier in MeV.

The population probability for states of different angular momenta follows a distribution given by the partial cross section:

$$\sigma(l) = \pi \lambda\!\!\!^{-2}(2l+1)T_l \tag{3.4}$$

where T_l is the transmission coefficient for the nuclear reaction. This gives the familiar "triangular" distribution of cross section with l, where the larger angular momenta have the greater cross sections (fig 3.2). Hence, the total fusion cross section will be the sum over all possible l values. In the "sharp cut-off" approximation, it is assumed that the transmission coefficient T_l is zero for $l > l_{max}$ and has a value of 1 for $l \leq l_{max}$ leading to:

$$\sigma_R = \pi \lambda\!\!\!^{-2} \sum_{l=0}^{l_{max}} (2l+1)T_l \approx \pi \lambda\!\!\!^{-2}(l_{max}+1)^2 \tag{3.5}$$

From experiment it has been found that at increasing bombarding energy, and hence increasing E_{exc}, complete fusion is not the dominant process in peripheral collisions; instead deep inelastic or fragmentation reactions take over because of the large, repulsive centrifugal force. Therefore it is necessary to define in another way the maximum angular momentum transferred to the compound nucleus. *Wilczyński et al.* [Wil82] define the critical angular momentum l_{cr} as the upper limit at which

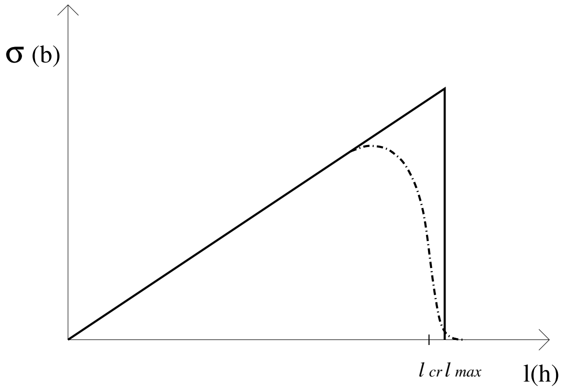

Figure 3.2: *Cross section as a function of angular momentum for a given reaction and projectile energy. The solid line shows the sharp cut-off interpretation, in dashed line a more empirical picture.*

complete fusion takes place. Thus, at low energies l_{cr} may be calculated from eqn.3.2 replacing l_{max} by l_{cr} and R by R_{cr}, where the latter is the distance up to which the target and projectile can be considered as separate ions. At high energies *Wilczyński et al.* find :

$$\left(l_{cr}+\frac{1}{2}\right)= \frac{\mu(R_p+R_T)^3}{\hbar^2}\left(4\pi\gamma\frac{R_pR_T}{R_p+R_T}-\frac{Z_pZ_Te^2}{(R_p+R_T)^2}\right) \tag{3.6}$$

where γ is the surface tension of the compound nucleus.

Another limit to the maximum angular momentum reached by the compound nucleus is imposed by fast fission. For a mass system around A=130 the maximum angular momentum at which the compound can be formed is, for a non-vanishing fission barrier (B$_f$ ∼8 MeV) around 70$\hbar$ and around 100$\hbar$ for a vanishing barrier, B$_f$=0 MeV, as shown by Cohen *et al.* [Coh74] in fig 3.3. In our case, with a compound nucleus in the mass region of A=80, the maximum angular momentum that can survive fission is around 50-60$\hbar$.

As an example to illustrate these concepts let us consider the ^{40}Ca+^{40}Ca reaction at a beam energy of 160 MeV, one of the reactions we have used. The centre of mass bombarding energy for a symmetric system is 80 MeV, well above the 41.1 MeV Coulomb barrier at the closest distance of R=9.8 fm. The Q-value of the reaction is -14.3 MeV, so that the compound nucleus, ^{80}Zr is formed at an excitation energy of 65.7 MeV. The expected value of the maximum angular momentum is 59.9 units for a total cross section of 1.3 barn.

3.1.1 Compound-nucleus decay

The compound nucleus is formed in a state at very high excitation energy ($\sim$ 50-80 MeV) and large angular momentum within time intervals of $10^{-22}-10^{-21}s$. The

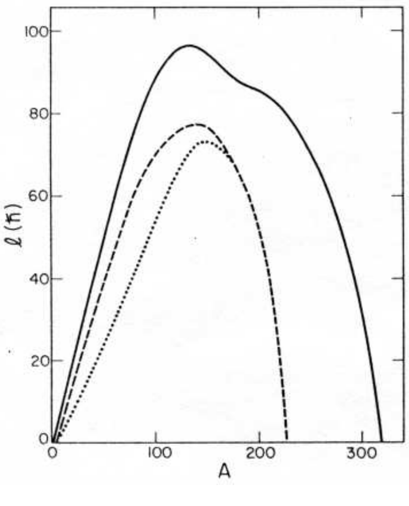

Figure 3.3: *The maximum angular momentum that a β-stable nuclei can support. The solid line correspond to the angular momentum reached when the fission barrier vanishes according to the liquid drop model. The dashed line correspond to the angular momentum that can survive to fission if the fission barrier is around 8 MeV (at that barrier height particle emission begins to be possible)*

most likely decay process if the compound nucleus survives fission is particle evaporation which take place with lifetimes of $\sim 10^{-19}s$. The evaporation of particles (neutrons, protons and alpha particles) from the compound system is a complex process that depends on binding energies, Coulomb and centrifugal barriers, level densities, etc., and it requires a statistical treatment. Each evaporated particle removes both kinetic and binding energy from the compound nucleus leading to a large decrease of the excitation energy. At the same time, the particle removes only a small amount of the angular momentum, usually 1-2$\hbar$ for protons and neutrons and 5-10$\hbar$ for alpha particles. Depending on the number and type of evaporated particles a large number of different final nuclei (or channels) may be produced at a given bombarding energy.

The decay process is schematically represented in fig 3.4 in a plot of excitation energy versus angular momentum (yrast diagram). The type of evaporated particle depends on the binding energy (or separation energy) and Coulomb barrier, thus for example in heavy compound systems near the stability line, where the separation energies are similar ($\sim 8-9MeV$), neutron is favoured over proton evaporation, because the proton has to overcome the high Coulomb barrier. However for medium mass compound systems far from stability, with a relative excess of protons, the separation energies for protons ($\sim 4MeV$) are much smaller than for neutrons ($\sim 15MeV$) and the Coulomb barriers are relatively low giving rise to a higher charged particle evaporation probability. The competition between proton, alpha

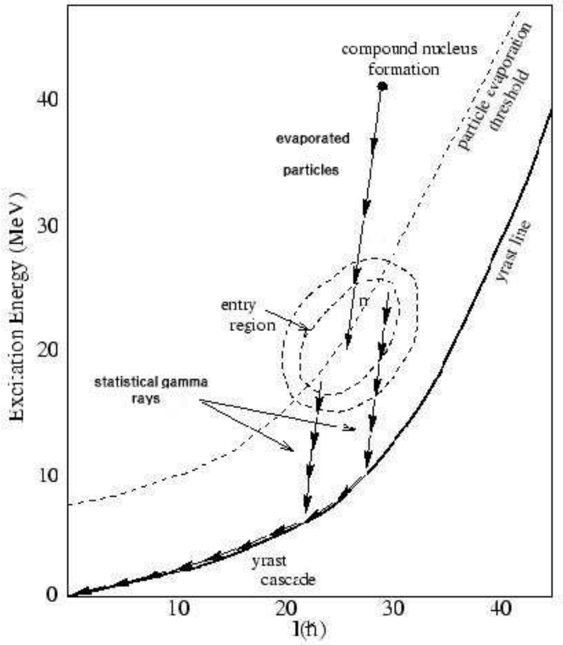

Figure 3.4: *The decay of the compound nucleus. Charged particles and neutrons are emitted first carrying away large amounts of excitation energy, but little angular momentum. Then, below the threshold, the de-excitation continues through γ-rays to the ground state.*

and neutron particle evaporation leads to a fragmentation of the total fusion cross section into a large number of exit channels.

When the excitation energy is below the particle evaporation threshold (approximately ∼8 MeV above the yrast line) the residual nucleus (produced in the entry region) continues to de-excite through γ-ray emission. These can be high energy dipole transitions (statistical transitions), carrying away large amounts of excitation energy, but again very little angular momentum. And then, as the nucleus approaches the yrast region, γ-ray emission proceeds through transitions of lower energy, carrying more angular momentum, until the ground state is reached. It is the analysis of these yrast and near-yrast transitions that reveals the properties of the low-lying states in the nucleus being studied.

3.2 Cross Sections and Channel selection

Ideally to determine the best possible experimental conditions to study a fusion-evaporation reaction one should measure excitation functions carefully. However, this is very time-consuming. Accordingly one often has recourse to codes which simulate the reaction process and predict the best combinations of target, projectile and energy to study a particular nucleus. Several such codes are available, amongst the most popular being HIVAP [Rei81], CASCADE [Puh77] and PACE (or EVAPOR) [Gav80].

Figures 3.5 and 3.6 show examples of the output of the HIVAP code for the $^{40}Ca +^{40} Ca$ and $^{32}S +^{40} Ca$ reactions, used in the present study, as a function of bombarding energy.

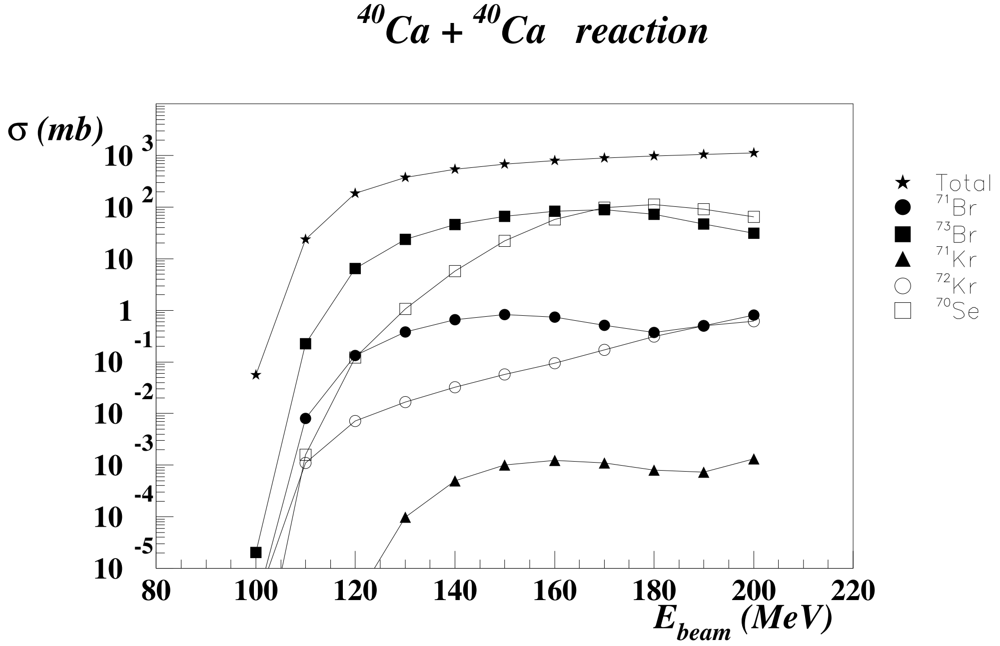

Figure 3.5: *Plot of the reaction cross sections for the production of various nuclei as a function of the beam energy for the reaction* $^{40}Ca +^{40} Ca$.

As we can see from figures 3.5 and 3.6 many reaction channels are open and they have a significant cross-section at any given bombarding energy. This emphasizes the point that when we are trying to detect radiation from a channel produced with a small cross-section the signals will be masked by the much more intense radiation from many other reaction channels. It is for this reason that it becomes vital to have clean selection of the channels of interest. This can be done by detecting the γ-rays in coincidence with: a) the identified, evaporated particles, b) the recoilling nuclei identified by A and Z, or c) by a combination of a) and b). To this end various methods of channel selection have been developed. To understand them requires some understanding of the detection systems used. Those of importance in the present work are described in the sections which follow.

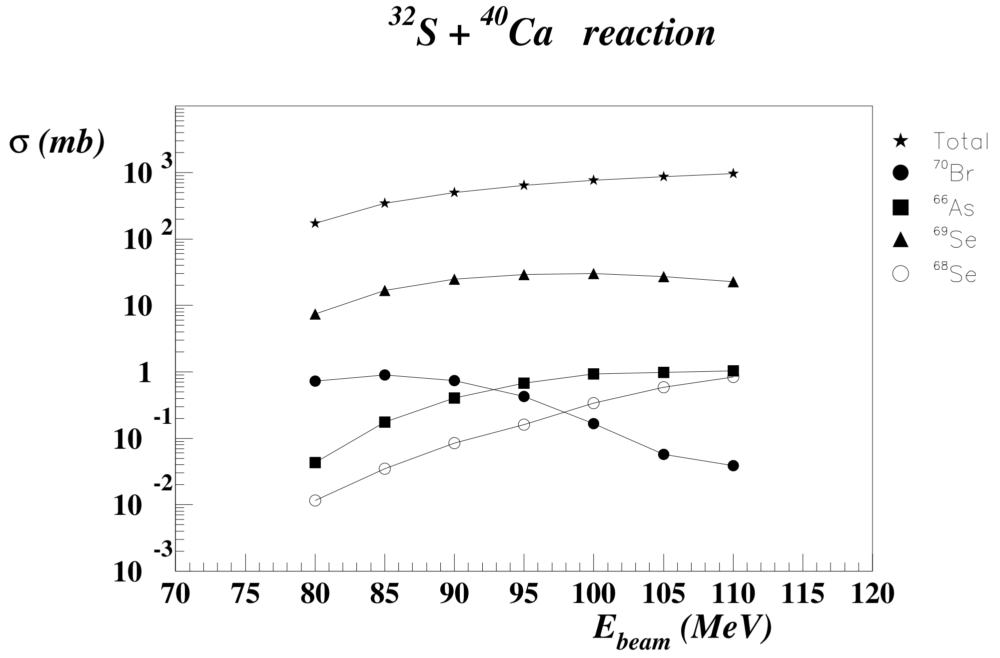

Figure 3.6: *Cross section as a function of energy of the beam for the reaction* $^{32}S+^{40}Ca$.

3.3 Detection Systems

As stated above a range of particles and γ-rays are emitted in the decay of the compound nucleus in a fusion-evaporation reaction. All of them carry information about the properties of the compound and the residual nucleus. They carry information which allows us both to identify the nuclear residues and determine their structural features.

In this section I will describe briefly how the various type of radiation interact with matter and the salient features of the various radiation detectors used in the present work.

3.3.1 Interaction of γ-rays with matter. Detectors.

Gamma rays are detected through their electromagnetic interaction within the detector material. This interaction occurs mainly through the photoelectric effect, Compton scattering and pair production. The relative importance of each of the mechanisms depends on the gamma-ray photon energy and the atomic number of the detector material. Thus for low photon energy and for high Z materials the dominant process is the photoelectric effect. At intermediate energies the Compton effect becomes more important than the photoelectric effect and for high energy photons ($E_\gamma > 1.022$ MeV) pair production becomes possible and eventually dominates at high energy.

In all of these processes the photon transfers its energy, totally or partially, to atomic electrons, creating pairs of electrons and ions that are subsequently collected to give an electrical pulse. Commonly we can obtain the response function of the detector using the differential pulse height distribution. By analysing the response function we can determine how the deposition of the energy in the material took place.

In gamma spectroscopy the main requirement in the operational characteristics of a good detector are: good resolution, good photopeak efficiency and good timing.

- The energy resolution is defined for a single energy source as the FWHM of the full-energy peak in the response function of the detector divided by the position of the peak (or energy).

  $$R = FWHM/E_0 \quad (\%) \tag{3.7}$$

  The width of the distribution is due to the fluctuations in the recorded pulse signal. The main source of fluctuations is the statistical nature of the number of pairs produced by the radiation. This gives us a limit to the resolution of

  $$R = 2.35\sqrt{\frac{F}{N}} \tag{3.8}$$

  where N is the number of charge carriers and F is the Fano factor [Fan47] which takes into account deviations from the Poisson statistical distribution.

- The efficiency measures the sensitivity of the detector to recording the interaction of the radiation. Thus, we can define the photopeak efficiency, ε_{ph}, as the fraction of recorded events in which the interactions have deposited the full energy, and the total efficiency, ε_{tot}, as all the events recorded. The ratio between the photopeak and the total efficiency is defined as peak-to-total ratio, P/T.

  The photopeak efficiency, that is usually tabulated for gamma-ray detectors, depends on the energy of the radiation and on the solid angle subtended by the detector.

- The time response of the detectors is fundamental to how well we can perform timing measurements related with the nuclear processess. The accuracy with which timing can be performed depends both on the properties of the specific detector and the type of electronics used to process the signal. The best timing performance is obtained for the fastest detectors, that is, those in which the signal charge is collected most rapidly.

Germanium detectors.

For many applications including the experiments described here, semiconductor crystals of hyper-pure germanium (HPGe) provide the best means of γ-ray detection for spectroscopy studies due to their excellent energy resolution. These HPGe detectors can be operated as a fully depleted diode by the application of a large reversed bias voltage [Kno89].

In the interaction of the radiation with the material of a Ge crystal, many electron-hole pairs (charge carriers) are created in the depleted region, exciting electrons across the band gap to the conduction band and leaving a hole in the valence band. Then, the electrons and holes move under the influence of the electrical field created by the reversed voltage forming the output signal, in the charge collection process. The number of electron-hole pairs created, and hence the output pulse, is proportional to the energy of the incident γ-ray. In fact, the average energy per electron-hole pair produced is very small, ~3 eV which leads to a very good energy resolution becuase many e-h pairs can be produced for typical gamma energies. Typically values of ~2.0 keV at 1.3 MeV are obtained in practice.

One disadvantage of the Ge detectors is the relatively small band gap, about 0.7 eV at room temperature, that make possible the thermal generation of electron-hole pairs giving rise to leakage current and therefore to unwanted noise. To reduce this effect Ge crystals are operated at the temperature of liquid nitrogen (77 K).

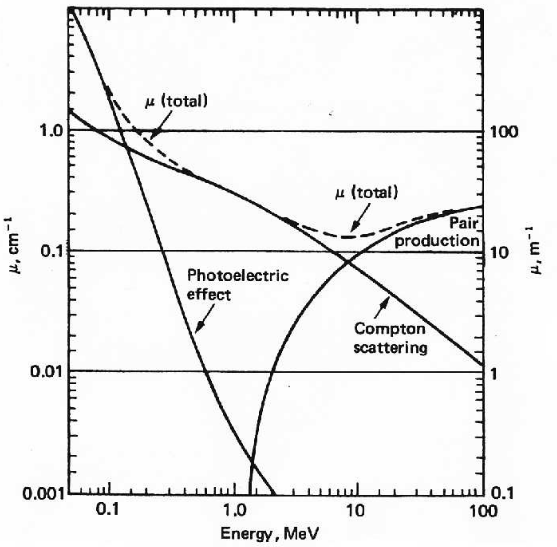

Figure 3.7: *Attenuation coefficient for the different radiation interaction processes in germanium.The Compton process dominates over photoelectric process since 200 keV*

Crystals of Hyper-pure Ge (HPGe) can be grown up to 70 mm in diameter and they are used in modern detector arrays, with each detector having a photo-peak efficiency, ε_{ph}, of $\sim$ 80% of that of a 3 in×3 in NaI(Tl) scintillation detector for 1.33 MeV γ-ray at a distance of 25 cm. . As we can see in fig. 3.7 there is a large probability that photons interact with Ge via Compton scattering over the energy range 200 keV-2 MeV. Most of the time the scattered photon will escape from the detector with the result that only part of the photon energy is detected. This will contribute to the general continuous background in the spectrum and hence to a decrease in the ratio peak-to total, P/T. Typical values of P/T are $\sim$ 20%.

To counteract this effect Ge detectors are often surrounded with an active shield consisting of BGO scintillator. The purpose is to detect the photons scattered out of the Ge crystal. The Ge detector and the BGO shield are operated in anticoincidence and the pulse from the BGO can then be used as a veto signal for the Ge events. With this procedure a substantial improvement in the photopeak-to-total ratio is obtained allowing values of 55-60% to be reached. The P/T ratio is very important in coincidence measurements as we will see in the following.

Arrays of Ge detectors

Individual Ge detectors are limited in size and hence detection efficiency. In addition, in the high spin studies, coincidences between more than two detectors are needed in order to increase statistics and therefore correlate the gamma-rays emitted in the de-excitation of the residual nuclei produced in fusion-evaporation reactions.

One of the major developments in γ-ray spectroscopy has been the building of arrays of such detectors just to overcome these constraints. Amongst the most important properties which characterize good performance in such an array are the *total photo-peak efficiency*, ε_{ph}, which defines the probability to fully collect the energy of the γ-rays and the *resolving power*, R, which provides a measure of the spectrum quality obtainable with a particular array.

In an array that consists of N single detectors, the total photo-peak efficiency is defined as:

$$\varepsilon_{ph} = N \epsilon_{ph} \Omega P_i P_n \tag{3.9}$$

where ϵ_{ph} is the intrinsic photo-peak efficiency of each single detector, Ω is the total solid angle covered by the detectors, P_i is the single hit probability and P_n is a factor that account for losses due to neutron induced events.

The resolving power, R, has been defined [Twi86, Nol94] for rotational bands with high γ-multiplicity as:

$$R = \left(\frac{S_{E_\gamma}}{\Delta E_\gamma} \right) P/T \tag{3.10}$$

where S_{E_γ} is the average energy separation between consecutive γ rays in a typical cascade, ΔE_γ is the FWHM or energy resolution of the measured γ rays and P/T is the peak-to-total ratio.

To improve the performance of an array we have to act on these variables, increasing the total photopeak efficiency and/or by improving the resolving power.

For the later case we must increase the P/T ratio or increase the energy resolution. The total energy resolution ΔE_γ, is determined by:

$$\Delta E_\gamma = \left(\Delta E_{int}^2 + \Delta E_{open}^2 + \Delta E_{ang}^2 + \Delta E_{vel}^2\right)^{1/2} \tag{3.11}$$

where the various terms are as follows:

- The intrinsic resolution of the detector, ΔE_{int}^2 (including the contribution of electronic components used to process the signal).
- The Doppler broadening due to the the opening angle of the detector ΔE_{open}^2. If the nucleus recoils out of the target with a velocity, v, its energy is Doppler shifted to a value E_s when measured in a detector at angle θ to the recoil direction

  $$E_s = E_0\left(1 + \frac{v}{c}cos\theta\right) \tag{3.12}$$

  Since the Ge detector has a finite opening angle, there will be a spread in the Doppler shifted energies:

  $$\Delta E_s = E_0\frac{v}{c}sin\theta\Delta\theta \tag{3.13}$$

- The Doppler broadening arising from the angular spread of recoils in the target, ΔE_{ang}^2.
- The Doppler broadening caused by the variation in velocity of the recoils across the target, ΔE_{vel}^2.

Therefore a high granularity of the array is needed in order to keep the good energy resolution of the a single Ge detector. One way to increase the energy resolution is to divide a single detector in two halves (Gammasphere) or to segment the contacts (next generation).

To improve the total photopeak efficiency, we can pack together several Ge detectors in a close-packed arrangement with a common escape suppression shield. This allows one to increase the total photopeak efficiency without loosing granularity (EUROBALL project).

When comparing the performance of such detector arrays, it is usual to introduce as a figure of merit the so-called observational limit (or sensitivity) which gives the minimum channel intensity α that can be detected in the presence of both correlated and uncorrelated background, usually quasi-continuum gamma transitions or random coincidences. In other words, the significant smallest intensity peak that we can be detected with our γ detector array. The observational limit is reached as a balance of two aspects in every measurement: the request that a multi-dimensional peak should have a minimum number of counts N_F to be considered as a peak, defines the statistical limit α_{stat}, whereas the request that the peak-to-background ratio $(N_p/N_b)_F$ should be larger than a minimum value defines the α_{back} limit.

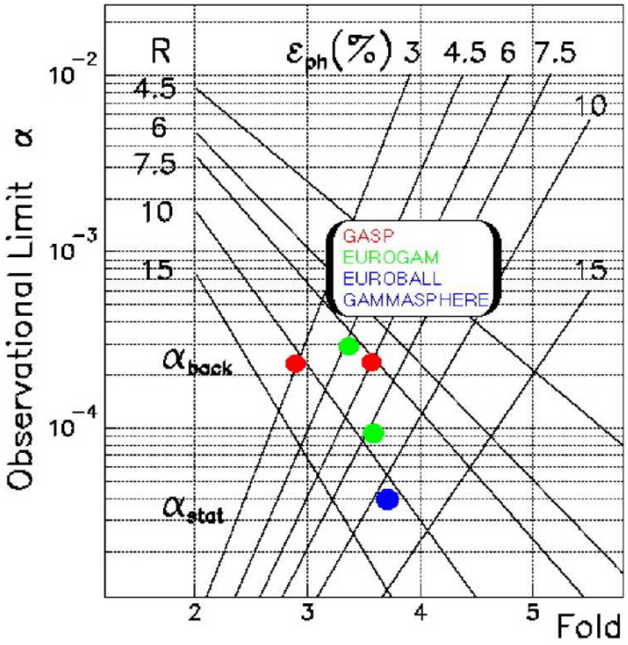

Figure 3.8: *Observational limit for different Ge arrays. Lines labelled with ε_{ph} correspond to the α_{stat} for different fold values. Lines labelled with R values correspond to the α_{back} for different fold values. The observational limit reached for each array is the point at which the pair of lines crosses.*

With crude assumptions these quantities can be defined as follows. The statistical limit can be expressed by:

$$\alpha_{stat} = \frac{N_F}{N\epsilon_0(k\varepsilon_{ph})^F} \tag{3.14}$$

where N_F is the area of the multi-dimensional gamma peak under investigation, N is the total number of events produced in the reaction, F is the coincidence fold used in the analysis (assuming the unfolding of higher order events), k is the fraction of the peak area between the gate limits, ϵ_0 is the efficiency of any ancillary detectors used and ε_{ph} is the total photo-peak efficiency of the array.

The sensitivity to detect a peak above the background can be determined by:

$$\alpha_{back} = \frac{\left(\frac{N_p}{N_b}\right)_F}{R_0(kR)^F} \tag{3.15}$$

where $(N_p/N_b)^F$ is the peak-to-background ratio of the line in the F-dimensional space, R_0 is the resolving power of the ancillary detector, R is the resolving power of the array and expresses the reduction of background under a gamma peak which is obtained by increasing by one unit the fold of the analysis.

In fig 3.8 we have plotted the values of the two quantities, α_{stat} and α_{back} for different gamma arrays, and different values of R and ε_{ph} as a function of the number of coincident detectors, the fold. These curves have been calculated assuming a peak intensity of 100 counts from a total number of 10^{10} events and a peak to background ratio, N_p/N_b of 0.2. The optimun point for each array is the one at which the pair of lines crosses.

Arrays of Composite Ge detectors

The current generation of high efficiency Ge detector arrays makes use of composite Ge detectors of various types. The two main types of composite detectors are called clovers and clusters [Duc99, Ebe96].

The Clover detector consists of four 20% efficient HPGe crystals encapsulated in a single aluminium housing. The Cluster consists of seven 60% efficient Ge crystals in a single housing. Amongst the advantages of the composite detectors are that a lower volume is occupied by lead collimators and BGO shielding, so the detectors can be packed close together to cover a large percentage of the full 4π sphere around the target. In addition γ-rays which Compton scatter from one crystal to another, can have the associated individual signals summed to reproduce the full energy (add-back mode). As mentioned before, this increases the overall efficiency of the detector whilst maintaining its granularity. Overall high granularity comes from having more small crystals rather then large crystals. This also means better charge collection, timing properties and smaller solid angle. The later is important for the reduction of the Doppler broadening. This composite detectors have also a high sensitivity to the linear polarization, as we will see in chapter 4.

Current Large Arrays

During the work described in this thesis three separate gamma-ray arrays were used. The main characteristics of these arrays are described briefly below.

The GASP array, figure 3.12, is installed at the Tandem XTU facility of the Legnaro National Laboratories (LNL) in Italy. It consists of 40 Compton suppressed, single HpGe detectors placed at 27 cm from the target position (configuration I) covering a total solid angle of 10% of 4π, corresponding to a total absolute photo-peak efficiency of about 3% at a gamma-ray energy of 1.33 MeV. For the same energy the Compton suppressed spectra have an average peak-to-total ratio (P/T) of about 60-65%. The average energy resolution of the germanium detectors at 1333 keV is better than 2.3 keV and their average relative efficiency is about 82%.

The array can be used in two main configurations (called I and II respectively) depending on whether the inner ball BGO is mounted or not. When the inner ball BGO multiplicity filter is removed (Conf. II) the detectors are placed at $\sim$22 cm from the target giving a total photo-peak efficiency of 5.8% at 1.3 MeV.

The array has a 4π Inner Ball composed of 80 BGO scintillation crystals which cover 80% of the solid angle. (The geometry of GASP is based on a polyhedron with

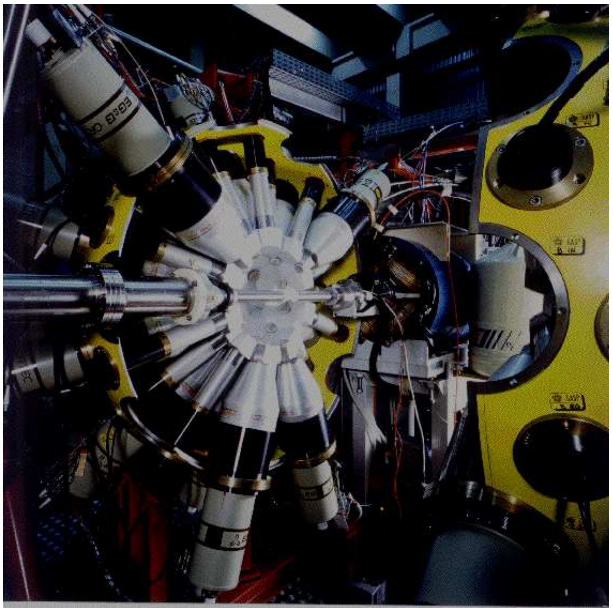

Figure 3.9: *Picture of Gasp array with the BGO inner ball mounted.*

122 faces, of which 40 are used for the Germanium detectors, 2 are devoted to the beam pipe, and the remaining 80 are used for the BGO ball detectors). The BGO crystals are 65 mm thick: and this gives 95% absorption for a 1 MeV gamma-ray, resulting in a total efficiency of 70%. The BGO ball is normally used for the trigger signal. For high gamma-multiplicity events, the trigger efficiency of the BGO ball is essentially $\varepsilon_0 = 1$.

The BGO ball is also used to determine, event by event, the gamma-ray multiplicity and total energy of the gamma cascade. By gating on these quantities one can enhance the reaction channels of interest obtaining a background reduction factor that is reaction dependent although it can be conservatively estimated as $R_0 = 2 - 4$.

The EUROBALL array, figure 3.10, was installed initially at the tandem XTU facility and later at the tandem Vivitron facility of IRES (France). This array is the final result of a European collaboration to construct a powerful instrument, able to improve by an order-of-magnitude the observational limit of the previous generation of arrays. The spectrometer combines the large volume HpGe detectors with the composite detector generation: clovers and clusters. It consists of 239 detectors mounted in three independent structures as follows:

a) 30 Single HpGe with dimensions 72mm length and 82 mm diameter and hence a relative intrinsic efficiency of ~80%. Each detector has its own Compton Suppression Shield made of BGO. The average energy resolution is ~2.4 keV for 1.33 MeV. These detectors cover the 1π solid angle in the forward direction where the damage due to neutrons is highest.

b) 26 Clover detectors, each consisting of four individual crystals with dimensions 70 mm length and 50 mm diameter and cut longitudinally to create a close-packed structure in a "four-leaf clover shape". The four detectors are cooled in the same cryostat and have a common BGO shield. The clover detectors are placed in two rings around $\theta = 90^o$ and cover a solid angle of 2π.

c) 15 Cluster detectors, each composed of seven sealed capsules of dimensions 78 mm length and 70 mm diameter mounted in a common cryostat, with individual bias supplies.

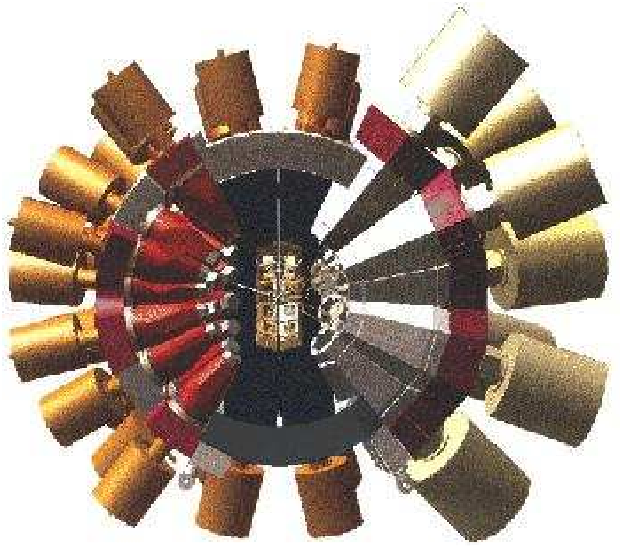

Figure 3.10: *Picture of Euroball array.*

The CLARION array is installed at the HRIBF facility of the Oak Ridge National Laboratory (ORNL) in the Tennesse, USA. The ORNL Ge array consists of eleven segmented Clover detectors and ten single Compton Suppressed Ge detectors. The array is coupled to the RMS [Gro00] beam line. Most of the detectors are placed in the backward hemisphere, approximately 22 cm from the target. This large distance reduces Doppler broadening and allows the use of ancillary detectors such as the HyBall charged particle array.

The Clover detectors are slightly modified versions of those used in EUROGAM II and EUROBALL. Each crystal is electronically segmented into two halves, and has an individual efficiency of 25%. By minimizing the dead layer between the adjacent crystals, the signals from all four crystals may be added together (add-back mode) to obtain the total pulse height for an incident gamma ray that scatters from one crystal to one or more of the other three crystals. At the distance of 22 cm, when operated in the add-back mode, a single Clover detector has a photo-peak efficiency of 0.2% for the detection of 1.33 MeV gamma rays. Furthermore, since the segmented Ge crystals have an effective width of 2 cm, the resulting Doppler broadening is minimized. The peak-to-total ratio of the Compton-suppressed clover detectors, when operated in add-back mode, is approx. 0.55 for ^{60}Co lines. The Clover detector may also be used as a polarimeter.

The CSS elements consist of 25% Ge detectors equipped with BGO Compton Suppression Shields. The Ge crystals have a length of approximately 7 cm, a diameter of 5 cm and provide a peak-to-total of nearly 0.5 for ^{60}Co lines when operated in the Compton-suppressed mode. At a distance of 22 cm, the 10 detectors provide a total photo-peak efficiency of 0.3% for a 1.33 MeV gamma-ray.

The combination of 10 CSS elements and 11 Clover detectors always placed at 22 cm from the target will have a total photo-peak efficiency of about 2.6% for a 1.33 MeV gamma ray. The Clovers may be placed at three target-to-Ge distances of 20, 21.7, and 23.5 cm. Five of the Clover detectors are placed at 90 deg. with respect to the beam axis; these detectors can provide linear polarization information. The angles of the remaining Ge detectors are: 5 CSS at 57 deg., 1 CSS at 90 deg., 4 CSS at 120 deg., 4 Clovers at 132 deg. and 2 Clovers at 155 deg. No Ge detector is placed at very forward angles, where Rutherford scattering of the radioactive ion beams used at ORNL would cause an excessive background of positrons and 511 keV annihilation radiation. The design of the array shell is such that the positions of the detectors are interchangeable. However, due to the large faces of the Clovers, some crystals may lie face-to-face resulting in the enhanced detection of annihilation radiation.

The Electronics and Data Acquisition system

When working with multidetector arrays, most of the electronics has to be designed to meet the main requirements of high resolution and be a compact and reliable system. This implies customised modules using commercial standards (CAMAC, NIM) and the development of new standards (VXI).

In the case of the GASP spectrometer, which consists of 160 gamma detectors, the electronics were based on NIM and CAMAC standard with the development of special modules to achieve the best performance in energy resolution for the Ge detectors. The general layout of the electronics for GASP is shown in the figure 3.12.

The signals coming from each detector have been divided into two chains, the fast and slow branches, allowing the application of the fast-slow principle to reduce random coincidences. In the fast chain the signals are amplified and discriminated using a Fast Amplifier plus Constant Fraction Discriminator (FA&CFD), a 4-fold module which contains a Timing Filter Amplifier, the logic to perform the Compton suppression and a Gate and Delay Generator for the output signals. The logic outputs (for each kind of detector) are combined together using both Multiplicity and Pattern units (MU&PU) in order to identify the detectors fired and generate the trigger signal (T1). The fast NIM output from the MU&PU module is also used to open linear gates in the slow amplifiers in the energy branch of just those detectors present in the fast line, thus generating the Energy Sum signal (summed signal for all Ge and for all . In addition, in the case of the Ge detectors, the energy signals are amplified using spectroscopic amplifiers (Mod. Silena 7611) whose unipolar signals are treated in the special Linear Gate and Stretcher modules (LGS), developed by the INFN-PD electronic group, to make the pile-up rejection, to obtain the maximum amplitude of the input signal and give a measure of the peaking time with a resolution better that 50 nsec. The good performance of these LGS modules has resulted in a global energy resolution of 2.3 keV at an energy of 1.3 MeV.

A large part of the electronics is controlled by a computer in order to set the parameters. Multiplexer modules are also used to control the signals without disconnecting the cables from the modules.

The acquisition system [LNL90] is based on the standard FERA read-out (Fast Encoding and Read-out of ADCs), a transputer network (T-net) for event formatting, filtering, sorting and storing, VME ram histogram storage with FDDI (Fibre Distributed Data Interface) readout and graphics workstation for monitoring, control, display and analysis of data. When the external event signal or trigger is detected by the FERA driver module, the digitization phase starts. The linear signals from the germanium detectors are converted through a programmable ADC conversion system based on CAMAC and NIM stardards and developed at INFN-PD in order to give the best performance in terms of stability and differential linearity. The Ge time signals are converted through standard TDC Camac modules. The signals from the BGO and/or other ancillary detectors are also converted using also standard ADC and TDC Camac modules.

A FERA Serialize module receives the external event signal and collects the different signals on the data bus, writing together the data that belong to the same event. The data are sent through an interface module to the transputer network where the event will be formatted with the specifications defined by the user. Afterwards, the event is distributed in parallel to the several channels of the T-network where it is checked for possible format errors, gain shifted and calibrated, filtered and stored in tape media and analysed in different histograms. All these functions are performed via software using a specific multiprocessor- based language that can be modified by the user to meet their experimental requirements. The histogrammed data are sent to a VME histogramming memory via transputer links and a VME card, obtaining in this way an enhancement in the performance. The memory readout is made using a 68030 CPU VME card connected to the workstation via FDDI optical network. The control of the whole system is performed at the graphics workstation using the specific programs developed for it.

The use of a larger number of detectors, as well as the expectation of higher data rates in the EUROBALL project, made necessary the design and implementation of an innovative integrated electronics and data acquisition system. The large number of detectors, 239 Ge plus the BGO anti-Compton shields make it difficult to manage

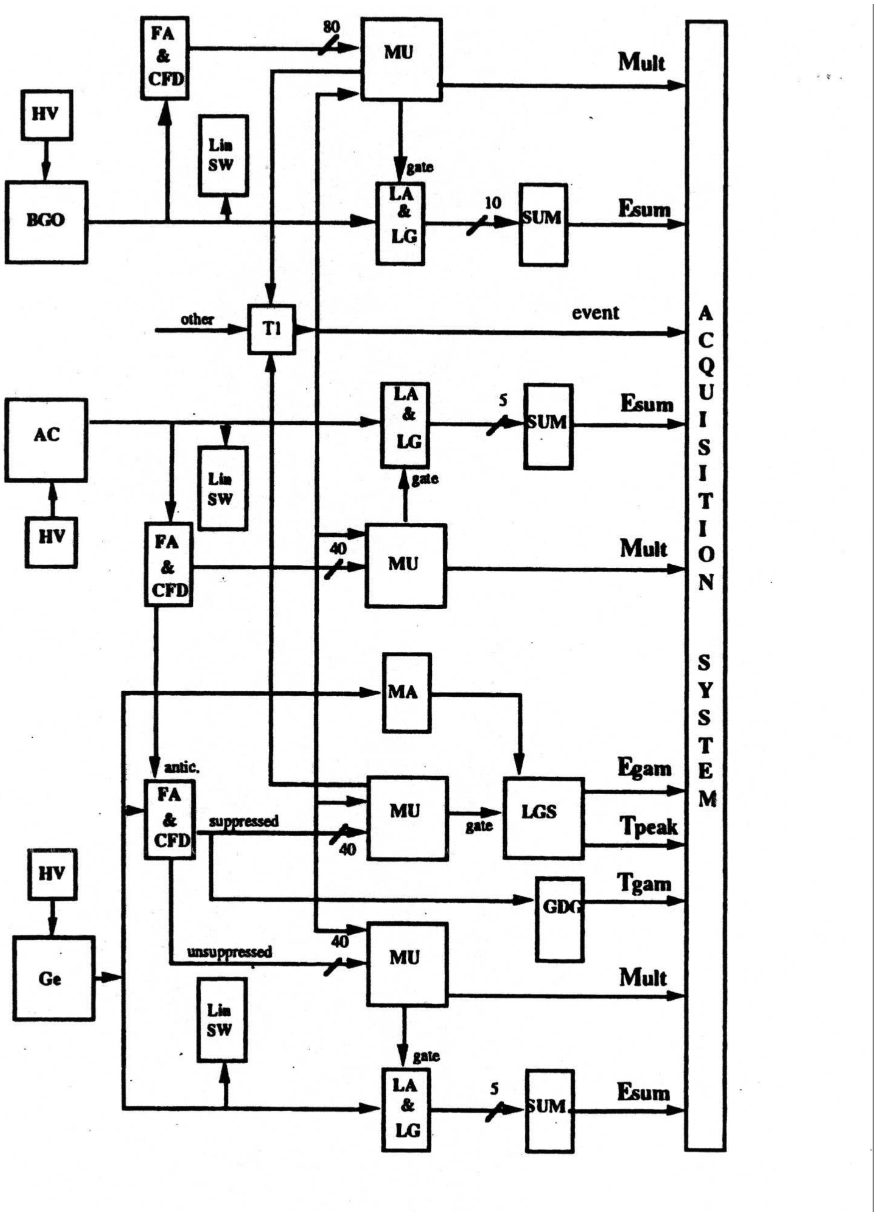

Figure 3.11: *Layout of the GASP electronics.*

a system based on CAMAC and NIM standards due to the high power consumed.

The design of the new system is based on the use of the VXI bus (VME bus eXtension for Instrumentation system) and comprises:

- VXI cards for analog and logic electronics that handle several channels with all the necessary electronic modules integrated. Each electronic channel also includes ADC and TDC converters for digitization of the pulses controlled by a local trigger (LT) section.

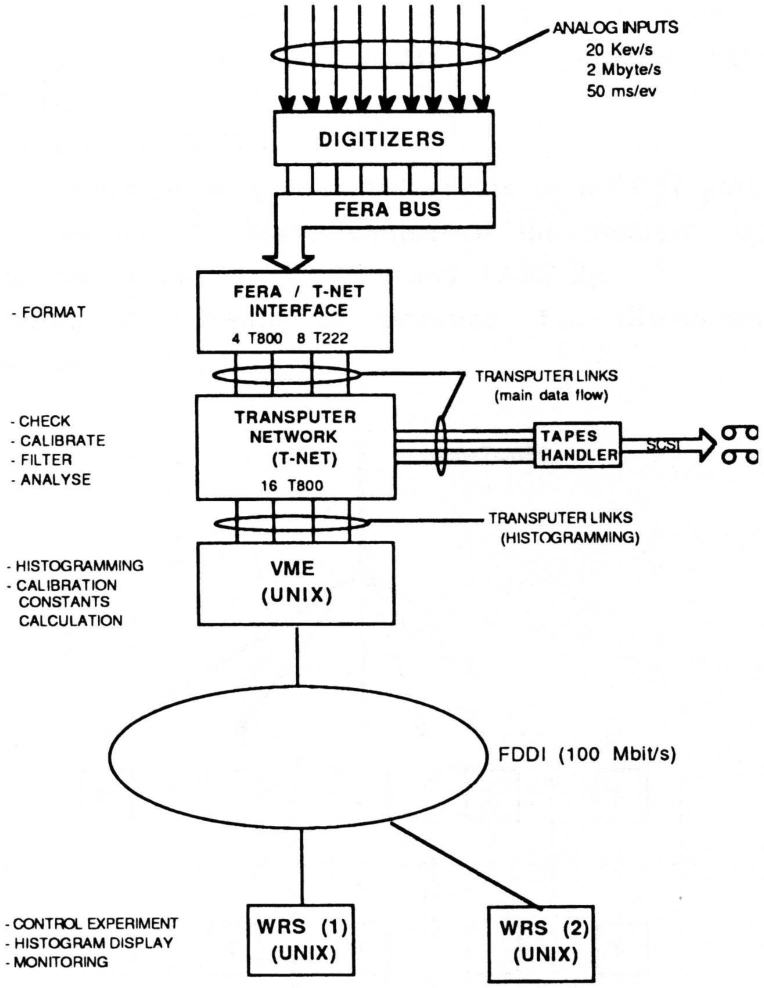

Figure 3.12: *Layout of the GASP acquisition system.*

- A VXI *Master Trigger* card controls the whole system and validates the operation of the different VXI cards. The master trigger for an event is typically correlated with the Ge multiplicity, but it can depend on some other signal and may be validated later by the ancillary detectors, for example.

- The acquisition system works in a common dead-time mode through the Read-Out COntroller cards (ROCO), one for each VXI crate. The readout time is about 1-4μs and the digitized data are stored in buffers.

- Event Collector cards collect the data streams from the different crates to form a common event data block that is forwarded to the Event Processor

Farm where the super-event is built. Each Event Collector has a Hardware Histogramming Unit where pseudo-spectra can be increased.

3.3.2 Detection of light charged particles

As mentioned at the begining of this chapter, in the reactions we are dealing with many interesting reaction channels are populated with small cross sections. Therefore, they are very often hidden by the radiation from the most intense channels. To achieve a good selection of the channel of interest one of the solutions is to detect the γ-rays and the evaporated particles in coincidence. In this sense by requiring the presence in the event of the right evaporated particles we can select the gamma rays from the nucleus of interest.

In the de-excitation of the compound nucleus in the mass A$\sim$70 region there is competition between the evaporation of charged particles (protons and alphas) and neutrons, the former having higher probability. Therefore, an efficient detection system is needed to carry out a good identification of the charged particles emitted.

Because we are dealing with the combination of a gamma array and an array to detect the charged particles, the later should meet certain conditions:

a) Good detection efficiency, which requires geometrical coverage close to 4π and a low energy threshold for particle detection.

b) Good discrimination between different types of particle. In particular protons and alphas must be cleanly separated over the whole energy range of the evaporation spectra.

c) High granularity, in order to minimize the probability of multiple hit events and also limit the counting rate in the individual detectors, particularly in the forward direction.

d) Minimum disruption of the γ-ray array, which means both the use of low mass material to minimize absorption and scattering of γ -rays and a counting rate capability which will not limit the data rate in the γ array.

e) The ability to allow the energy spectroscopy of particles, which means optimum energy resolution and a detector thickness sufficient to stop the particles of interest.

To satisfy these conditions different techniques have been used based on the use of semiconductor or scintillator materials. Then, the array configuration covering the 4π solid angle is the most commonly used structure. In the first case, Si detectors are commonly used, and a good discrimination between protons and α particles is achieved making use of the ΔE-E configuration telescope. In the second technique, CsI(Tl) detectors are used to give a high detection efficiency and good discrimination is achieved by using the pulse shape.

Charged particles interact with matter mainly through the Coulomb interaction with the electrons of the medium. They lose their kinetic energy continuously up to the point where they stop. The energy transferred to electrons can excite and even ionize the atoms of the material thus creating ion pairs. Each ion pair is then made up of a free electron and the corresponding ion.

In the first technique, using the specific energy loss or stopping power for a charged particle in a determined material described by the Bethe formula [Kno89]

$$\frac{dE}{dx} = k_1 \frac{mz^2}{E} ln k_2 \frac{E}{m} \tag{3.16}$$

where m and z are the mass and the atomic number of the particle, E is its energy and k_1 and k_2 are constants that depend on the material, it is easy to deduce that a combined measurement of the differential energy loss, dE/dx, and the residual energy, E, allows the characterization of each kind of charged particle, from the product mz^2. This can be achieved by using a thin detector to measure ΔE followed by a thick detector to measure E. If the coincident signals from both detectors are plotted in a 2-dimensional matrix, ΔE versus E, the signals from each type of particle will be distributed in hyperbolic curves as we can see in fig 3.13 right. The main advantage of using this Si detectors for this purpose is that they can be easily made.

The second technique, based on scintillation detectors, makes use of the differences in the decay component for the different particles detected which allows one to discriminate between them. Thus, in the case of CsI(Tl) detectors, the output pulse is a combination of two components with different decay times: a fast component with a mean decay time τ= 0.4-1.0 μs, the amplitude and fall time of which depends on the particle type detected, and a slow component with a decay time of 7 μs, which is independent of particle type. Using the pulse shape discrimination technique good discrimination between different types of particle is obtained.

Charged particle detector arrays.

In this section I will describe briefly the charged particle detector arrays based on the two techniques described above that have been used in the experiments performed in this work.

The ISIS array fig. 3.13 consists of 40 silicon ΔE-E telescopes which are used to detect light charged particles (protons and alphas) produced in reactions.

The silicon ball uses the same geometry as the 40 Ge detectors of GASP, with the telescopes positioned on a compact (16 cm diameter) sphere. This geometrical configuration has been chosen in order to optimize particle efficiency and minimize scattering which would reduce the detection efficiency.At the same time low Z material and thin detectors are used to minimize gamma-ray absoption and keep the good the peak-to-total ratio of the gamma ray spectra in GASP.

The ΔE and E detectors have thicknesses of 130 μm and 1 mm respectively. The Si-ball covers a solid angle of about 65% of 4π and has a telescope detection

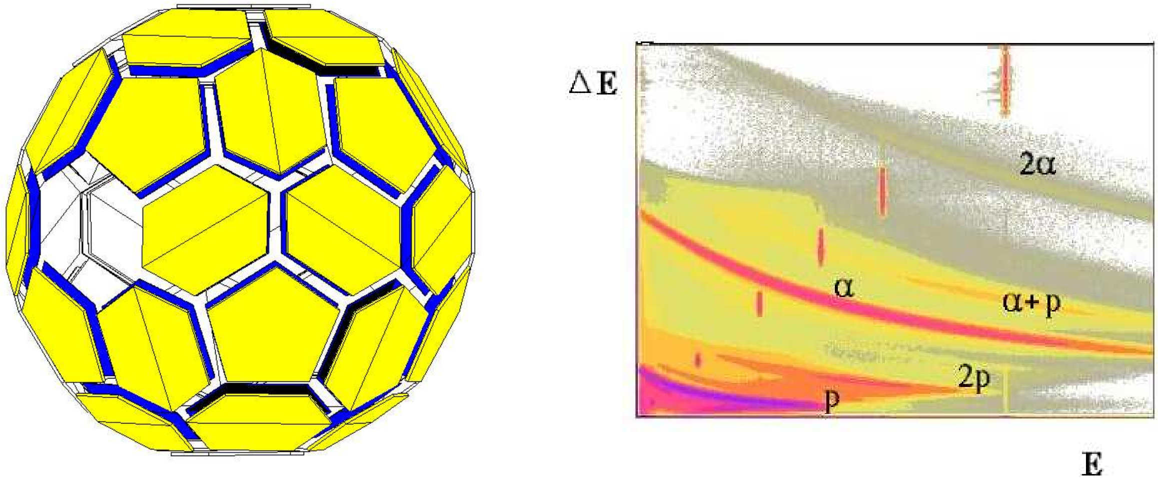

Figure 3.13: *Left: schematic view of ISIS detector array. Right: DE-E plot with the particle identification obtained with the Si-telescopes.*

efficiency of up to 60% and 45% for protons and alphas respectively. Typical values of energy resolution using an ^{241}Am α source are 75 keV for the ΔE and 40 keV for the E detectors.

The efficiency reduction with respect to the geometrical coverage is mainly due to total absorption of the light charged particles in the thin aluminium foils placed in front of the telescopes to prevent radiation damage from elastically scattered heavy beam ions. As expected, the reduction is higher for alpha particles. Clearly the channel selectivity using GASP coupled to ISIS is increased considerably and this is particularly important when studying weak reaction channels.

The EUCLIDES array is the charged particle detector used at EUROBALL. It is a development of the ISIS array, with 40 ΔE-E Si detector telescopes. The main differences with respect to ISIS are the smaller dimensions, due to a smaller space inside the γ-spectrometer. The ΔE and E detectors are put together in the same frame separated by thin Kapton spacers, with the internal faces connected to a common ground and the external faces of both E and ΔE to the bias voltages. The main improvement is the electrical segmentation of the two most forward rings, which means an increase in the efficiency by allowing the handling of higher rates and reducing the probability of multiple hits.

With the ΔE detectors placed in a reversed configuration (the biased face in the direction of the incoming particles) the pulse shape discrimination technique with Si detectors can be used [Pau92]. Detection efficiencies of up to 70% and 55% for protons and alphas respectively have been obtained in good measurement conditions for the EUCLIDES array.

The HYBALL array fig. 3.14 consists of 96 CsI(Tl) scintillators [Gal92, Sar96] with thicknesses varying from 3 mm (at forward angles) to 1.1 mm (at backward angles). These detectors are arranged in 9 concentric rings and coupled to large area photo-diodes. The distance to the target varies from 4.2 cm to 10.7 cm and overall subtends ∼95% of the solid angle. Thus a high granularity and high efficiency is obtained in a compact structure.

Particle identification is achieved by pulse shape discrimination with electronic gates on the output pulses. Thus from each CsI(Tl) element, three signals are acquired: a) the Energy (E) or FAST signal which corresponds to the charge collected in a gate of ∼1.0 μs width, centred on the fast component or peak of the output pulse; b) the Pid or SLOW signal which corresponds to the charge collected in a 10 ns gate that corresponds to the slow component of the output pulse and is shifted respect to the 1μs gate by $\sim$ 9μs in order to optimize the discrimination. c) Time or Zero crossing time (Z/C) signal obtained by taking the preamplified pulse through a bipolar shaping amplifier [Bia89].

Average total detection efficiency values around 80% and 70% for protons and alphas have been obtained with the Hyball array.

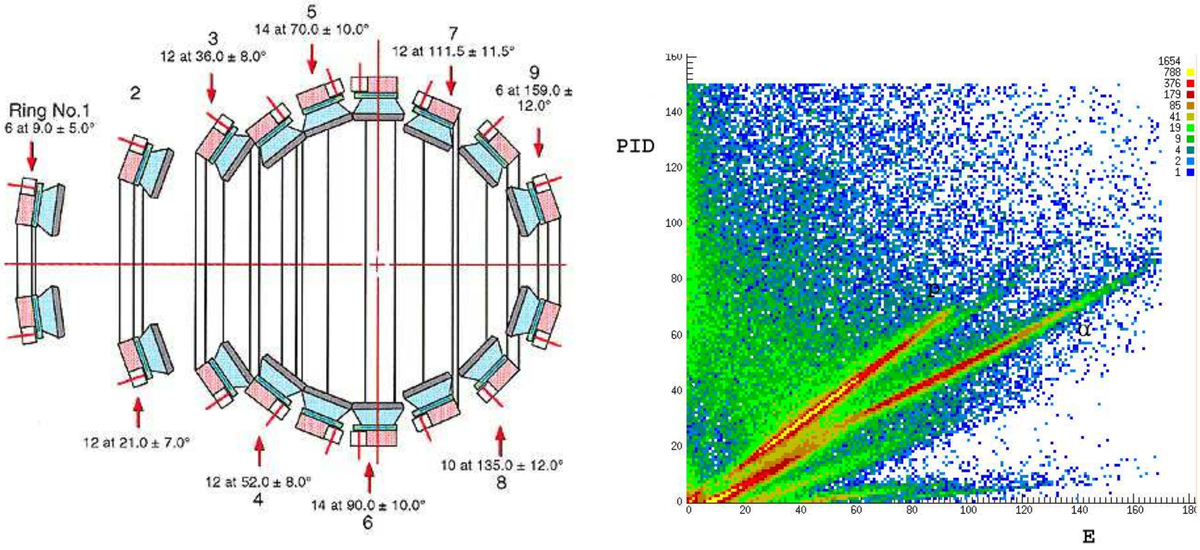

Figure 3.14: *Left.Schematic view of the Hyball detector array angles. Right, particle identification spectra for Hyball obtained by combining PID vs E signals.*

3.3.3 Detection of neutrons

The combination of detectors for neutrons and light charged particles with efficient γ detector arrays has become a powerful and essential tool in the spectroscopy of exotic neutron-deficient nuclei close to $N = Z$ and the proton drip line, populated in reaction channels with extremely low cross section, e.g. in the ^{84}Mo [Mar02] and ^{88}Ru [Mar01] experiments at GASP.

Neutrons emitted in the decay of the compound nucleus can be detected using different methods. The most common technique is based on organic scintillation detectors and the scattering of neutrons by light nuclei [Kno89]. Usually organic liquid scintillators such as NE213 and BC501A which contain a large amount of hydrogen are used. After the scattering of neutrons by the hydrogen nuclei the energy of the recoiling proton, which ranges from zero to the energy of the neutron, is absorbed by the molecules of the scintillation liquid. The decay of the molecular excited states proceeds through the emission of light with two components, a fast component due to fluorescence (with $\tau \sim 1$ns) and a slow component due to delayed fluorescence ($\tau \sim 10^2$ ns). The intensity and shape of the light pulse depends on the type and energy of the ionizing particle providing the possibility to discriminate between them when different radiations interact with the scintillator. For instance, neutrons producing protons and gammas producing electrons in the scintillator can be discriminated. This light output is converted to an electrical signal by coupling an appropriate photo-multiplier tube to the liquid cell.

Good separation of neutrons and γ rays is obtained by use of fast n-γ pulse shape discriminators (PSD) fig. 3.15. This method is based on the difference in intensity of the slow component of the light pulse in the organic scintillator. This intensity is larger for recoiling protons than for gamma-induced electrons. The PSD utilises the zero crossing technique (Z/C) and dc feedback stabilization as described by Bialkowski et al. [Bia89]

The signal from the anode is fed into the n-γ pulse shape discriminator (PSD) and to a constant fraction discriminator (CFD). The CFD produces a time reference signal (t_{ref}) which is obtained from the leading edge of the fast component of the anode signal. The pulse shape discriminator consists basically of an RC filter shaper that converts the input pulse into a bipolar signal, and a Zero discriminator which creates a logic signal when the bipolar pulse crosses the base-line.

A time distribution spectrum is obtained from an external time-to-pulse height converter (TPHC). This spectrum gives the distribution in time between the leading edge of the fast component of the signal (output;t_{ref}) and the Z/C of an integrated and differentiated bipolar version of the same signal (output;n+γ).

The Neutron Wall at EUROBALL

The Neutron Wall array [Ske99] (fig. 3.16) consists of 15 hexaconical detectors and 1 smaller pentagonal detector based on the Cluster geometry of EUROBALL to ensure compatibility with the mechanical design of the γ-spectrometer. Each detector is subdivided into three separate segments for the hexagonal units and 5 for the pentagonal units. This amounts to a granularity of 50 segments at a distance of 510 mm from the focal point. The array replaces the forward shell of γ detectors (tapered detectors) and covers a solid angle of 1π.

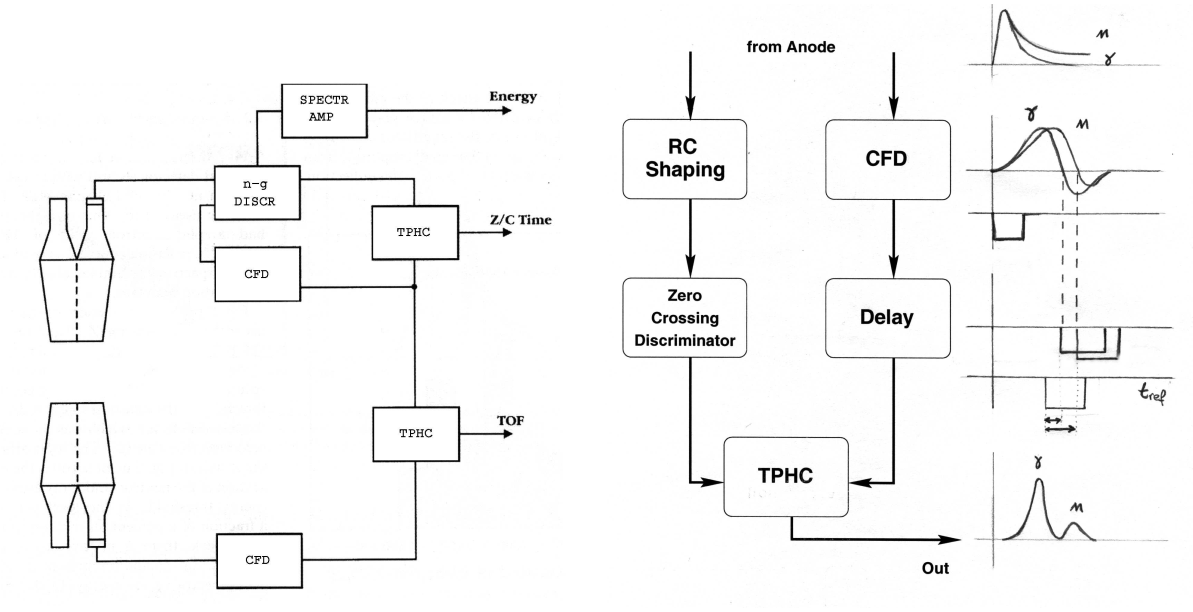

Figure 3.15: *Block diagram of the electronics used to separate neutrons and gammas by means of zero-crossing pulse-shape discrimination and the time of flight method [Ske99].*

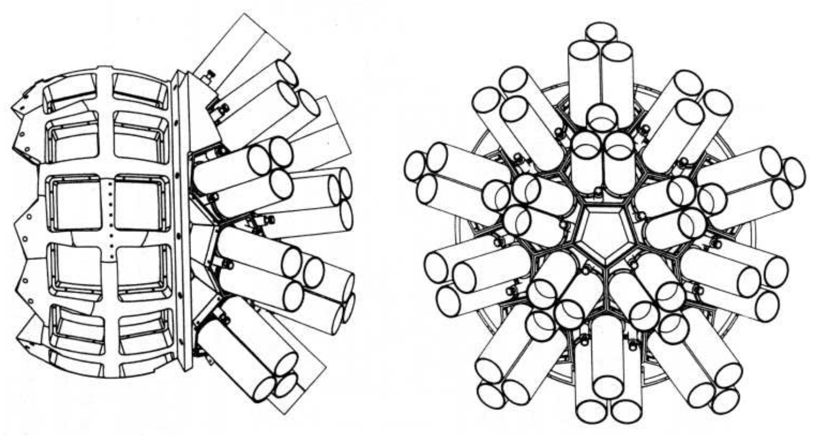

Figure 3.16: *Schematic view of the Neutron Wall detector array [Ske99] at EUROBALL IV.*

Each segment is coupled to a photo-multiplier tube characterized by high quantum efficiency and very good photo-electron efficiency collection.

The detection efficiency depends on the solid angle Ω subtended by the detectors, on the detector thickness, which provide an intrinsic efficiency ε_{int} of 50%, on the losses due to simultaneous n and γ hits in one detector cell, on the cross talk between neibourgh detectors and on the kinematical focusing. With all of these factors, a detection efficiency of about 20% has been achieved for neutrons.

The N-Ring array at GASP

The N-Ring array coupled to the GASP γ-ray array consists of 6 individual detectors. The detectors replace the 6 most forward elements of the BGO inner ball and are placed in a ring at 20^o to the beam axis. The distance from the target to the front face of the neutron detectors is about 30 cm. Each detector is filled with 1 litre of BC501A liquid scintillator. This scintillator is characterized by good timing properties (∼3 ns.). The inner walls of the detectors were painted with reflector paint BC622A to improve the light collection efficiency.

The 10 cm. depth of the detectors yields an intrinsic efficiency for evaporated neutrons of about 25%. Each detector subtends a solid angle of 1%. The resulting total efficiency of the detector system is of the order of *3-5 %* depending on the reaction kinematics.

To reduce the large counting rate produced by the X-rays from the target emitted following the reactions, composite absorbers made of Pb/Cu/Cd were placed in front of each detector. The signals from the PMTs are analyzed by CAMAC modules that produced three output signals: energy, zero crossing (Z/C) and time. The neutron energy accepted by these modules ranges from 200 keV to 10 MeV. The Z/C signal is used to discriminate between neutrons and gammas. The modules allow for the multiplexing of both the analogue and digital signals. The programming and control of the neutron modules has been integrated into the GASP computer control system.

The good suppression of the channels with charged particle evaporation makes such a device a unique filter for the selection of proton-rich nuclei close to the $N = Z$ and the proton drip-lines which are populated with extremely low cross sections. In recent experiments with this detector the observational limit of GASP has been pushed down to 10^{-5} in comparison with observational limit of 10^{-3}-10^{-4} reached previoulsy for neutron evaporating channels, as in the case of the $N = Z$ nucleus ^{88}Ru populated with only $\sim$3 μb cross section.

3.3.4 Detection of recoils

As we have seen above the use of ancillary detectors increases the selectivity of Ge arrays and allows the unambiguous identification of gamma rays belonging to the different final product nuclei.

One of the deficiencies of the use of ancillary detectors to select the products of the reaction is that one is not selecting the residue but inferring it from the particles detected. Even with highly efficient ancillary detectors, errors in identifying the nucleus can happen if there is some contamination from isotopic impurities in the target. Impurities at the level of only one per cent can cause problems with the identification of very weak channels due to the large differences in, for example, the neutron evaporation probability between isotopic compound nuclei differing by only a few neutrons.

A more direct way of identifying gamma transitions for very weak channels such as those leading to nuclei near the $N = Z$ or to the proton drip line, is by detecting the recoiling nucleus itself. To do that a recoil separator is needed in order to collect and separate the recoils from the beam particles and fission products. This can be achieved using electric and magnetic fields which separate the ions as a function of energy and mass-to-charge ratio (A/Q). A good example is the Recoil Mass Separator (RMS) at HRIBF.

The HRIBF Recoil Mass Spectrometer.

The HRIBF RMS [Gro00, Gin99] (fig. 3.17) is a spectrometer which combines a momentum separator (or momentum achromat) with the traditional mass separator to provide enhanced beam suppression with highly efficient transportation and separation of reaction products. The two distinct optical components consist of: two electrostatic dipoles (E1 and E2), three magnetic dipoles (D1-D3) seven magnetic quadrupoles (Q1-Q7) and two magnetic sextupoles(S1 and S2) arranged as shown in fig 3.17 This configuration creates three focal planes: (i) the momentum dispersed focal plane inside quadrupole Q3, (ii) the achromatic focal plane after the momentum separator, and (iii) the A/Q dispersed focal plane at the end of the 25 m flight path.

In the momentum achromat the magnetic dipole D1 creates a focal plane inside the quadrupole magnet Q3 in which particles leaving the target are dispersed by momentum. Here, it is possible to insert up to 7 thin rods (fingers) to intercept the primary beam charge states which remain spatially well-defined (mainly used with strongly inverse kinematic reactions). The second half of the momentum separator recombines the ions and focuses them at the achromatic focus, which can be thought of as a virtual target for the mass separator. Quadrupole Q3 matches the energy dispersion of the two magnetic dipoles (D1 and D2). Sextupoles S1 and S2 are used to correct for higher order aberrations of the image at the focal plane.

The mass separator is a typical, split electric dipole arrangement. With this particular combination the electric dipoles disperse the recoils of a given charge state according to energy and the magnetic dipole disperses the recoils according to momentum. In the experiments reported here, we used the A/Q dispersed focal plane at the end of the spectrometer.

Focal Plane detectors

The A/Q separation and beam suppression capabilities offered by the RMS cannot alone provide the high channel selectivity necessary for studying nuclei very far from stability. This high sensitivity comes from the detector systems used together with this device.

The PSAC (position sensitive avalanche counter) has a 36x10 cm^2 active area and consists of five wire planes which are separated by ∼3 mm. The physical arrangement of the planes with respect to the beam direction is Cathode(1) - X

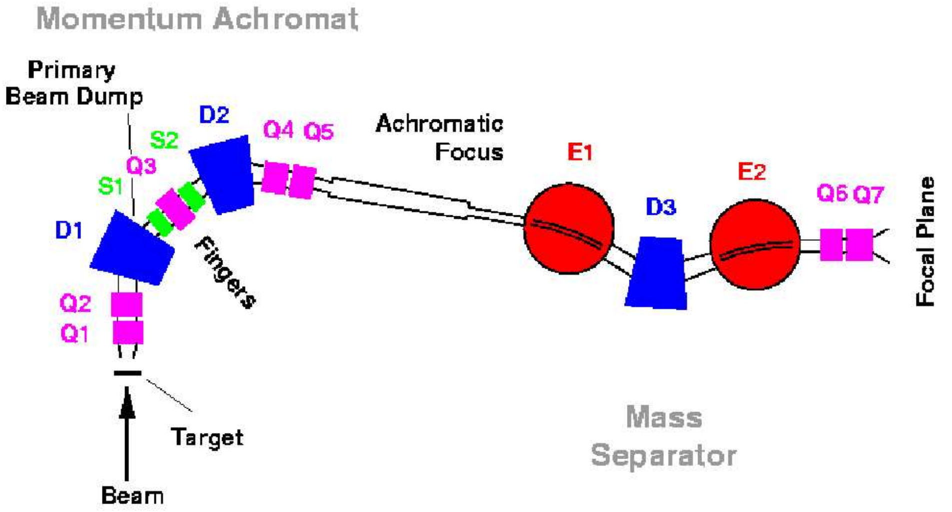

Figure 3.17: *Schematic view of the Recoil Mass Spectrometer at HRIBF.*

position - Anode - Y position - Cathode(2). The 20μm thick, gold-plated tungsten wires are separated from each other by 1 mm, resulting in an overall transmission of approximately 90%. The voltage between the cathode and the anode is around 500 volts and the X-Y position wire planes are operated at ground potential. This arrangement provides a uniform field with the horizontal sensing wire plane (X) between cathode 1 and the anode and the vertical sensing plane (Y) immediately following the anode. In order to reduce the attenuation of the signals in the x-direction the detector is subdivided into two halves with separate read-outs at the four ends.

The position is derived through time delay lines, with adjacent pairs of wires connected to the same pin of a multipin connector that acts as an interface to a second board containing the integrated 20 ns passive delay chips with a delay of 2 ns per pin. The resulting total delay is of 180 ns. Fast timing amplifiers and constant fraction discriminators are used, and ~2 mm position resolution has been measured using an alpha source.

The detector is filled with isobutane gas at a pressure of 3-4 Torr. In addition to the X and Y signals, signals from the anode and cathode are also collected. One of these signals is used to gate any additional detectors firing in coincidence and classify the event as a recoil event. A typical matrix X-Y with the mass distribution is shown on the left side of the figure 3.18.

The IC (ionization chamber) is a multi-segmented device built at Daresbury Laboratory (U.K.). The anode is split into three segments along the beam direction of 58, 50 and 202 mm respectively. The 8mm of the first anode is placed over the re-entrant window and provides a uniform electric field region inside the gas volume. Thus, the ionization for energy loss measurements is collected from two 50 mm anodes which may be added together. The total energy of the ions may be obtained by adding the signals from all three anodes. The anode and cathode planes are constructed of circuit board which allows them to be made cheaply and easily modified. The anode is shielded by a Frisch grid and a position sensitive wire grid. This grid can be used to reject events scattered at large angles in the PSAC or to provide some position information in cases when the PSAC is not present.

The first two segments, which should detect 66% of the recoil's total energy, measure the energy loss crucial to the determination of Z. In addition, the first two segments allow the rejection of bad events caused by Rutherford scattering in the gas. Further segmentation across the focal plane allows the detector to be run at higher overall counting rates. This is because events entering the chamber simultaneously but in different segments will be processed separately and will not be rejected as pile-up. In figure 3.18 (right) we can see a typical plot of ΔE_1 vs E_{tot} with the distribution of recoils.

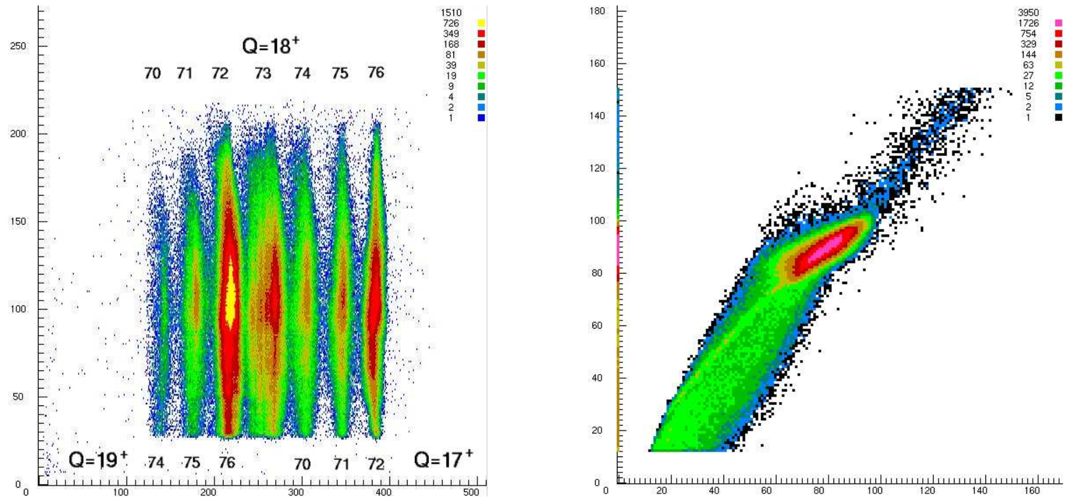

Figure 3.18: *Left) Matrix plot of the A/Q distribution obtained in the PSAC detector. Right)* ΔE*-E plot obtained in the Ion Chamber at the Focal plane of RMS.*

3.4 Experiments: gasp/euroball/ornl

In the work described in this thesis we have performed several experiments at different facilities, using some of the most competitive arrays for gamma detection and highly efficient ancillary detectors. This is important because we are looking at nuclei far from the valley of stability, i.e. produced through exit channels populated with very small cross sections. For this reason one requires the highest possible sensitivity. Basically, two kinds of reaction, ^{40}Ca+^{40}Ca and ^{32}S+^{40}Ca reactions, in five experiments at different energies have been used to populate the nuclei of interest, namely ^{71}Br, ^{71}Kr and ^{70}Br.

Table 3.1: *Summary of the experiments carried out in this work.*

reaction	^{40}Ca(^{40}Ca,2α1p)^{71}Br		
Energy:	160 MeV	180 MeV	156 MeV
I_{beam}:	$\sim$ 5 pnA	$\sim$ 5-10 pnA	$\sim$ 3 pnA
Target:	1mg/cm^2	1mg/cm^2	0.5mg/cm^2
Backing:	12mg/cm^2	16mg/cm^2	-
Set-up	GASP ISIS	EUROBALL ISIS	CLARION HYBALL PSAC+IC
efficiency:	ϵ_γ=0.03 ϵ_p=0.40 ϵ_α=0.20	ϵ_γ=0.09 ϵ_p=0.45 ϵ_α=0.22	ϵ_γ=0.026 ϵ_p=0.68 ϵ_α=0.43
trigger:	$(\gamma)^2_{Ge}$+$(\gamma)_{BGO}$	$(\gamma)^4_{Ge}$-part $(\gamma)^5_{Ge}$	$(\gamma)^2$-part-recoil

reaction	^{40}Ca(^{32}S,2p1n)^{70}Br	
Energy:	95 MeV	95 MeV
I_{beam}:	$\sim$ 8-10 pnA	$\sim$ 8-10 pnA
Target:	1mg/cm^2	1mg/cm^2
Backing:	14mg/cm^2	13mg/cm^2
Set-up	GASP ISIS N-Ring	EUROBALL EUCLIDE N-WALL
efficiency:	ϵ_γ=0.03 ϵ_p=0.53 ϵ_α=0.29 ϵ_n=0.03	ϵ_γ=0.09 ϵ_p=0.60 ϵ_α=0.32 ϵ_n=0.30
trigger:	$(\gamma)^2_{Ge}$+$(\gamma)^2_{BGO}$	$(\gamma)^2$ + NW(n) $(\gamma)^3$ + NW

Table 3.1 summarizes the details of the five experiments carried out. The first experiment was performed with the GASP spectrometer and ISIS because it was the best array available at the time with its 40 HpGe Compton suppressed detectors and an absolute efficiency of $\varepsilon = 0.03$. Among the main advantages of the GASP array we should note its symmetry at different angles which is important in the extraction of angular distributions W(θ), the good timing response with a time resolution of 12 ns that allow us to reduce the random events by selecting narrow

gates on prompt signals, the good energy resolution (2.3 keV at 1.3 MeV) reached with stable standard electronics, etc. The use of the gamma spectrometer coupled to the charged particle detector array, increases the selectivity making possible the selection of specific channels by gating on different combinations of detected particles.

During the course of the analysis of this experiment a more powerful array became available, namely EUROBALL. This array is composed of 239 detectors with a total efficiency $\varepsilon = 0.09$ and a resolving power of $R \sim 9$ wich gives us a sensitivity one order-of-magnitude higher than GASP with an optimum fold value of 4 in comparison with 3 for GASP (fig. 3.8). This higher condition on the fold allows us to increase the statistics by unpacking events with higher multiplicity into lower multiplicity events. One should note that a 4-fold event can be unpacked into four triple-events or into six double events and so on. This was the reason why we performed the same experiment in order to improve the data obtained with GASP.

In these two experiments, the reaction ^{40}Ca+^{40}Ca was used and the ^{40}Ca beam was delivered by the XTU Tandem of the National Laboratories of Legnaro (Italy) at energies of 160 and 180 MeV respectively. The energies were chosen in order to optimize the cross sections accordingly to the calculations. A higher energy for the Euroball experiment was used in order to gain some higher spin taking advantage of the capabilities of the spectrometer. The beam intensity was limited by the counting rates in the forward Si detectors, which was kept below 25 kHz, and the dead time of the acquisition system. Average values around 5 pnA were used in both measurements. One should keep in mind that the beam intensity is not constant during the experiment because of the technical difficulties in the operation of the ion source.

The target consisted of an enriched (99.99%) ^{40}Ca foil of thickness 1 mg/cm^2 with a gold backing of the order of 12 mg/cm^2. The main idea is to have a relatively thin target in order not to loose too much energy of the incoming beam in the target, to stop all the recoils in the backing to keep the gammas in focus of the collimated Ge detectors and to let the beam to go through the backing to control the focusing during the experiment. This kind of calcium target is very delicate because it oxidizes in contact with the atmosphere. Hence, to avoid oxidation, the target is mounted within the reaction chamber in an Ar atmosphere. In spite of all this attention one is not always able to avoid the presence of oxygen and hence, its reaction products.

A careful examination of the projected spectrum of the gamma matrix with a particle condition of 2 alpha and 0 proton and its comparison with other particle conditions (shown in fig 5.3) from the experiment at GASP and EUROBALL allowed us to identify all the lines observed as being from the various reaction channels open at 160 and 180 MeV bombarding energy and to identify the lines belonging to ^{71}Br.

Accordingly, we also studied the ^{40}Ca+^{40}Ca reaction at ORNL using the CLARION array of Compton suppressed Ge detectors in coincidence with the HYBALL array of CsI detectors for charged particle detection and the Recoil Mass Separator

(RMS) to detect the recoiling nuclear residues. In principle the combination of particle selection and the recoil detection identified by A and Z in the RMS focal plane should allow more sensitive channel selection than in the earlier measurements.

In practice it was not possible to separate the residual nuclei by Z in the experiment and this fact limited the sensitivity severely. Possible reasons for this will be discussed in chapter 5. However in this experiment it was possible to identify the γ-rays from ^{71}Br unambiguously using the combination of HyBALL and the RMS. A clean spectrum of γ-rays identified in this way from ^{71}Br is shown in fig 7.2.

At the end of the experiment the gamma-ray spectrum was measured in singles mode to allow a measure of the absolute cross-section for the strong reaction channels (see chapter 5).

In the ORNL experiment the target consisted of a self-supporting 0.5 mg/cm^2 ^{40}Ca target, enriched to 99.95%, chosen to give sufficient counting rate and at the same time to allow the recoils to enter the RMS. The beam energy was chosen to be 156 MeV so that the mean energy in the target was essentially the same as in our first experiment with GASP.

Table 3.2: *Summary of the energies of the beams used on the five experiments at various points relative to the targets.*

	Ion	E_{beam} (MeV) β (%)	E^{m}_{beam} (MeV)	E^{f}_{beam} (MeV) β (%)	E^{back}_{beam} (MeV) β (%)
GASP	^{40}Ca	160	151.5	143	37
		12.6		12.0	6.0
EUROBALL III	^{40}Ca	180	172.0	163	25
		13.4		12.8	5.0
ORNL	^{40}Ca	156	151.8	147	-
		12.5		12.1	-
GASP	^{32}S	95	88.2	81.2	1.5
		10.9		10.1	1.2
EUROBALL IV	^{32}S	95	88.2	81.2	3.7
		10.9		11.1	2.1

In order to study the N=Z odd-odd ^{70}Br we proposed to study the ^{32}S+^{40}Ca reaction at the Vivitron Facility in Strasbourg, the new EUROBALL site, where a very efficient neutron detector, the Neutron Wall, was available. The project was delayed and the same experiment was proposed at the GASP facility in coincidence with the recently available Neutron-Ring detector.

In the GASP experiment we were able to identify for the first time the most intense transitions in ^{70}Br. The ^{32}S beam was delivered by the XTU tandem at 95 MeV bombarding energy. Using a trigger condition of two suppressed Ge detectors and two BGO detectors firing in coincidence and making use of the neutron efficiency of 3% offered by the N-Ring detector. In the EUROBALL IV experiment, due to the higher efficiency of the N-WALL, improved statistics was recorded.

Chapter 4

Data Analysis

In order to construct level schemes for ^{71}Br and ^{70}Br based on measured γ-ray energies, polarisations, DCO ratios, etc., we must perform a quite sophisticated analysis. In the following sections I will describe the different steps that we have to follow for a proper analysis, the programs used to manage the data, etc.

4.1 Sorting of data.

The signals coming from the detectors are converted and collected on tapes only when the trigger condition is satisfied. These data are coded in a specific format defined by the data acquisition system and make up the "event structure". Thus, in each event we have information about which germanium detectors, which particle detectors and other ancillary detectors have fired and which values of the parameters (Energy, Time, etc) have been registered. The data (or events) are then written in a sequential mode, event-by-event, and arranged in files, called runs, for easy handling in the off-line analysis (a loogbok is used to record the specific incidents of each run as the time length, current intensity, etc.).

In order to extract useful information from these data, we have to prepare and rearrange the raw data in histograms following a procedure that is called the sorting of data. The sorting program consists of subroutines that decodify the event structure, search for bad events (for instance an event with an energy signal in one detector and not the corresponding time signal), reject them, and treat the good ones for various corrections. Thus, in the first step, we extract the projections of each parameter from each detector (for particles and for gammas) and for all the runs. We also construct the appropriate matrices with the parameters from the ancillary detectors, in principle without energy correction. Secondly, from the projections of the γ detectors we extract the coefficients for gain shift correction of the energies and for the energy calibration. We also create a file with the coefficients for the time alignment of these detectors. Afterwards, with the particle matrices we can set banana gates for each kind of particle, light charged particles, neutrons and/or recoils. Finally, in a further step we create the 2-dimensional and 3-dimensional histograms with the corrected data for gain shift, add-back, Doppler shift, etc. and with various conditions on other parameters.

The sorting of data obtained in the experiments that constitute this thesis work was carried out mainly using the program *GSORT*, developed at Pd-INFN. The *SCANOR* program developed at Oak Ridge National Laboratory, was also used for the analysis of the experiment carried out there.

4.1.1 Gain Matching and calibration

The signals coming from the different Ge detectors are usually amplified from a few mV to several volts to match the ADC characteristics. The gain of the linear amplifiers can undergo changes during an experiment due to variations in temperature and counting rates. Thus, a correction for these possible drifts is required in order to maintain good resolution when adding all the statistics. This process is known as gain matching. Moreover, when a multidetector system, such as a γ -array, is used the gain matching has to be done even between the different detectors because it is important to sum the signals from all of the detectors.

Once the drifts corrections are done, an energy calibration allows one to extract precise values for γ -ray energies or to determine the energies of the particles. This calibration can be done using standard sources or by using beams of given energies of protons, alpha, etc. for the particle detectors. In our case, an energy calibration for gamma energies alone was carried out at the end of each experiment and the alignment of the detectors was done using as a reference the projections from the last run.

In the case of the ancillary detectors used for identification of particles, the energy calibration is not usually needed. The gain matching can be done for easy setting of the gates to select the appropriate particles.

4.1.2 Doppler correction

If thin targets are used in the experiments, the different residues formed in the particle evaporation of the compound nucleus can recoil out the target with a velocity v of the order of the velocity of the compound nucleus (3-5 % c). The gamma transitions emitted during de-excitation will be affected by the Doppler effect, as we have seen in the previous chapter. In particular the energy of the transition will be shifted, when measured with a detector at an angle θ to the recoil direction, by

$$E_s \simeq E_\gamma(1 + \frac{v}{c} cos\theta) \tag{4.1}$$

(in this cases transitions from states with a certain half life will go out of focus)

Thus, when using a multidetector array, the energy of the same gamma transitions will be shifted accordingly to the angle of the detectors. In order to perform a good energy analysis, we need to correct these values using the angle of each

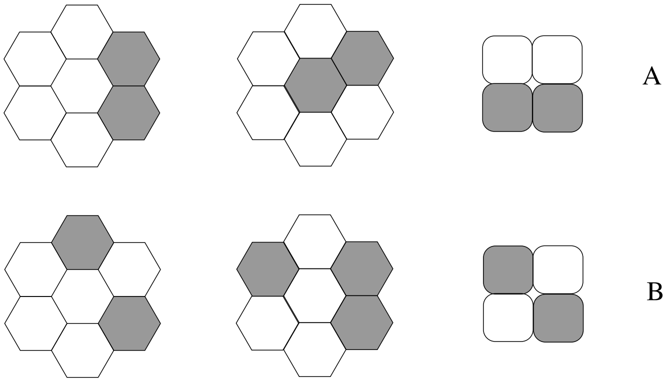

Figure 4.1: *Some examples of events accepted for addback process (A) and events to be rejected (B) for composite detectors.*

detector fired and an estimation of the recoil velocity. This procedure is carried out automatically event-by-event with the off-line analysis programmes.

In the case of the composite detectors, in which several capsules can be hit by the same gamma transition, using the Add-back procedure (see below) we can determine precisely the capsule that was hit first, and use its position or angle to determine the direction of emission of the gamma ray and hence get a better correction for the Doppler effect.

4.1.3 Add-back process

As mentioned earlier the use of composite detectors allows one to measure the full energy of a gamma ray even when it scatters from one capsule to another. The energy of the incident γ ray can be recovered by summing the energy deposited in the neighbouring detectors leading to an increase in the photopeak efficiency. This procedure is called "Add-back". Special care must be put in this process since the two capsules of the composite detector can also be hit by two different γ rays in a single event.

In the analysis, each event is first checked for the number of capsules belonging to the same composite detector which have fired. Then, if more than one capsule has a signal, they are summed or not according to a criterion based on the relative positions of the capsules. In essence the criterion is that if the signals are in adjacent capsules then this is assumed to be the result of the scattering of the same gamma and they are summed. If the capsules which have fired are not all adjacent or are placed diagonally then it is assumed they correspond to the interaction of two different gammas or to some other induced effect. In brief, for signals in adjacent capsules the energies are summed and the total energy is assigned to the capsule which registered the larger part of the energy for further corrections, such as the Doppler shift, if needed.

In the case of Clover detectors (four capsules) this means that addback occurs only when two adjacent capsules are hit. In the case of Cluster detectors (seven capsules) up to three adjacent capsules were analysed initially as belonging to the interaction of the same γ ray. After the analysis of the different spectra produced as a function of the number of capsules hit, it was decided to again accept cases where only two adjacent capsules were hit. In other words, the number of good events in which a gamma deposits its full energy in three capsules is very low, see figure 4.1.

4.2 Matrices and Cubes

In the sorting procedure the corrected and calibrated data are re-arranged in two-dimensional and three-dimensional histograms i.e. matrices and cubes respectively. In gamma-ray spectroscopy, especially in high-spin studies, the correlation of the several parameters that characterize the gamma ray deexcitation has been revealed as a powerful tool to extract information on nuclear structure. Thus, nuclei populated at high excitation energy and high angular momentum decay through many cascades of high gamma multiplicity. Using at least two detectors we can, in principle, correlate the ordering of these gamma transitions. When using correlations the total efficiency is reduced and to compensate for this effect, arrays of many detectors are used.

Different types of matrix are used to extract information, plotting on each axis the parameters of interest. Thus for level scheme determinations we use matrices and cubes where E_γ is plotted on each axis.

For identification and discrimination of the particles evaporated we can also construct matrices with the parameters from the particle detectors. Thus, plotting E_{total} vs ΔE in the charged particle telescope detectors it is possible to discriminate between protons and alpha particles. In the case of the neutron detectors good discrimination and separation of neutrons from gamma events is obtained by plotting the Zero Crossing Time vs time of flight or even Z/C discrimination vs energy signal, see figure 4.2.

These matrices are essential to set the necessary conditions, such as the so-called banana gates, to select weak reaction channels.

4.2.1 Time dependent energy gates

When using multidetector arrays in close configuration or highly integrated electronics that includes several components (preamp, cfd, etc) in the same card, undesirable effects such as scattering between detectors, cross talk, etc. could affect the proper signals. In addition, the coincidence operation mode also involves random coincidence events. These effects are particularly disturbing in Germanium detectors and particle detectors, when a good channel selection is needed to distinguish between poorly populated residual channels.

A common way to reduce random coincidences is to correlate the different parameters of each detector, time and energy. This allows us to set gates on the proper

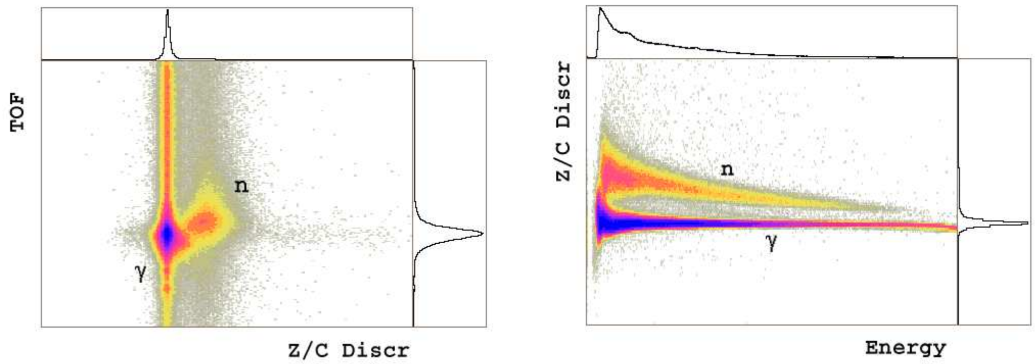

Figure 4.2: *Two dimensional matrices used to select neutron events: left) Tof vs Z/C discrimination and right) Z/C disc vs neutron energy. These matrices correspond to the Neutron detectors coupled with GASP.*

range of values that correspond to good events and restrict the sorting of data to those conditions.

Thus, the Ge time signals show a distribution as a function of the energy of the radiation. This effect is mainly due to the fact that for low energy signals the charge collection time is usually longer. If an isomer is present in the excited nuclei it appear as a delayed component in the time peak or as a line in a T versus E plot (fig 4.3). Random coincidences appear as vertical lines in the mentioned figure. In particular gold lines originated from the backing contribute to the random events only because the states populated in the backing are Coulomb excited, consequently they have low multiplicity and they do not contribute to the trigger.

In the case of particle detectors similar effects can be observed and then by setting gates on the prompt events we can reduce these uncorrelated contaminations.

4.3 Level Scheme and Intensities

In order to determine the level scheme several gates are set and analysed in the search for correlations between different γ transitions. Using known transitions and setting gates on them it is possible to determine the transitions that are in coincidence. Analysing gates in 3-d histograms (cubes) is also a helpful method to reduce uncorrelated gamma events that "contaminate" the 2-d histograms. Hence, the use of cubes allows us to select the gamma transitions belonging to the nucleus of interest. We should however mention here that an event recorded in a 2-dim matrix must have at least multiplicity two (two gammas in coincidence), an event recorded in a cube must have at least multiplicity three. Consequently, analysing these events we are introducing a bias in the kind of events selected.

The level schemes for ^{70}Br and ^{71}Br, the two nuclei studied in the present work, were constructed largely on the basis of the $\gamma - \gamma$ coincidences taking into account

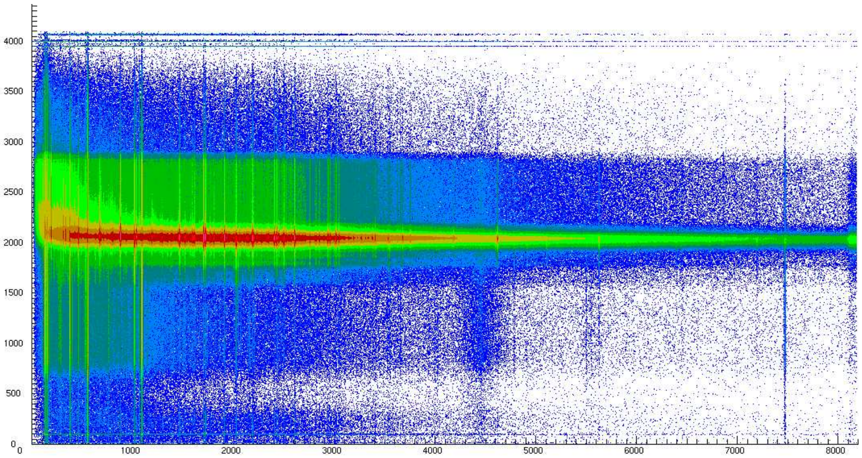

Figure 4.3: *Time versus energy distribution for Germanium detectors.Time is in arbitrary units and Energy expressed in keV.*

the assignment of γ-rays to other nuclei produced in the reactions studied and imposing conditions on the evaporated particles.

The level scheme itself is constructed first on the basis of the observed γ-rays. Ambiguities in the ordering of the levels are resolved, in general, using the relative intensities of the transitions and the observation of the parallel γ-ray cascades between levels. Triple coincidences aid this process further:putting a condition in two gammas belonging to the nucleus of interest, the presence of contaminats is strongly reduced.

After the construction of the level scheme J^{π} values are assigned on the basis of the observed lifetimes, multipolarities and branching ratios of the transitions. Examples of the coincidence spectra and the process of building the level scheme are given in chapter 5.

4.4 Angular Distributions from oriented states

In fusion-evaporation reactions induced by heavy ions (as in other nuclear reactions) the total angular momentum of the system is oriented[1]in the plane perpendicular to the beam direction (quantization axis). In principle, this means that only substates of m=0 are populated. In practice, we approximate the population of m-substates P(m) as a Gaussian distribution centred on m=0 with a width σ. The subsequent evaporation of particles and statistical gammas leading to the residual nucleus does not disturb the alignment very much and we say that the residual nucleus is populated in an oriented state.

---

[1] A nuclear state is said to be "oriented" if the relative populations P(m) of the angular momentum substates are unequal; that is, P(m)$\neq$P(m'). If P(m)=P(-m), the state is "aligned"; otherwise, it is "polarized".

The angular distribution (or anisotropy) of the radiation in any direction interms of θ, the angle between the direction of the emission and the beam direction, can be expressed as:

$$W(\theta) = \sum_{k} A_k P_k(cos\theta) \tag{4.2}$$

where k=2l, and l is the multipolarity of the transition. A_k is the angular distribution coefficient which depends on the initial and final spins, the angular momentum taken away by the γ-ray, the attenuation due to spin de-alignment (or P(m) distribution) and the mixing ratio if the transition is of mixed multipolarity. $P_k(\cos\theta)$ are the Legendre polynomials.

By measuring the distribution in intensity of the γ-ray as a function of emission angle, we can extract the values of the coefficients A_k by fitting this intensity with the function of equation 4.2. The experimental A_k values can be used to distinguish between different multipolarities:

- For a pure dipole (ΔI=1) transition only the A_2 term contributes and it will have a negative value.
- For a quadrupole (ΔI=2) transition the terms up to A_4 are needed and the A_2 will be positive and the A_4 very small, and
- For a mixed transition A_k will depend on the mixing ratio (δ).

In order to extract information on the angular distributions of the γ -rays in an experiment based on an array of Ge detectors, we normally construct a matrix for each angle. In these matrices we will have the gammas emitted at a given angle on one axis versus the coincident gammas in any detector on the other axis. Gating on a fixed transition in the axis with any detector and looking at the gamma ray intensity at the different angles, one can obtain an angular distribution of this γ-ray independently of the gated transition.

The advantages of this method are that we can obtain the angular distribution of a γ -ray without the need to know the multipolarity of the gating transition. We can add several gates together in order to improve the statistics. In general this method is only useful for strongly populated reaction channels or for strong transitions.

4.5 Directional correlations from oriented states (DCO)

An alternative method to obtain information about the spins and parities, I^{π}, of the levels is through the angular correlations of γ transitions de-exciting the levels in a band.

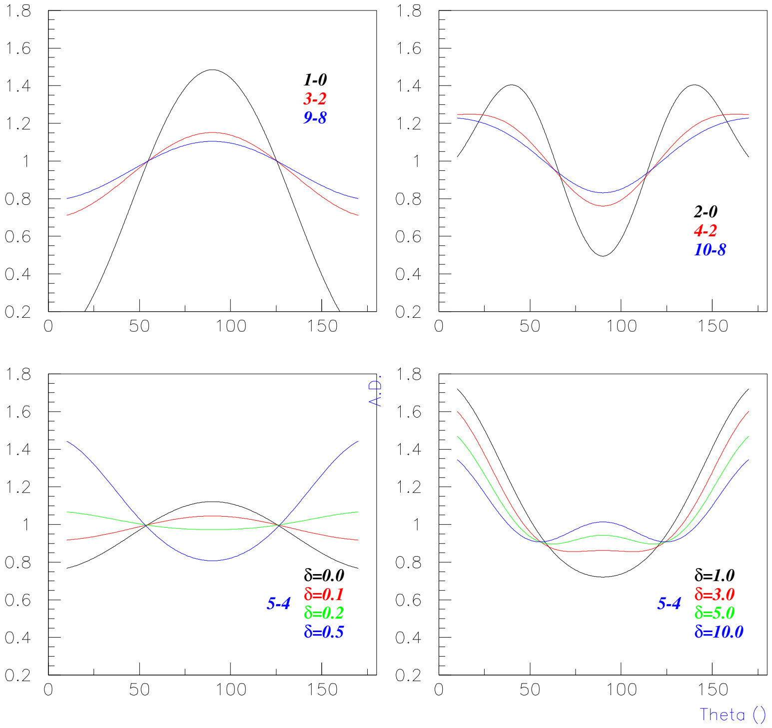

Figure 4.4: *Some examples of angular distributions for dipoles, quadrupoles and not stretched dipoles transitions.*

The angular correlation of two γ rays emitted in cascade has been discussed in the literature[Ste75, Kra73]. Here, I will follow the formalism for directional correlations given by K.S. Krane et al.[Kra73].

Let us consider a cascade of two γ rays depopulating an oriented state. The γ rays X_1 and X_2 are observed at angles θ_1 and θ_2 with respect to the beam axis and with the angle $\phi = \phi_1 - \phi_2$ between the planes defined by the z-axis (beam axis) and the outgoing γ rays. The intensity or *correlation function* (DCO) in these directions is given by:

$$W(\theta_1, \theta_2, \phi) = N \sum_{\lambda\lambda_1\lambda_2} B_{\lambda_1}(I_1) A_{\lambda}^{\lambda_2\lambda_1}(\gamma_1) A_{\lambda_2}(\gamma_2) H_{\lambda_1\lambda\lambda_2}(\theta_1, \theta_2, \phi) \qquad (4.3)$$

where N is a normalization factor, B_{λ_1} are the orientation parameters that describe the alignment and are obtained from the relative populations of the magnetic substates with respect to the beam axis. The physical parameters, namely the spins of the states involved and the multipolarities and mixing ratios of the transitions, are contained in the A coefficients. These coefficients are given in terms of $3j$ and $9j$ symbols and the mixing ratios. Finally, the function $H_{\lambda_1\lambda\lambda_2}$ describes the angular dependence. The indices λ_1[2]and λ_2 are the tensor ranks of the statistical tensor that describe the orientation of the nuclear states I_1 and I_2 respectively. The index λ refers to the tensor rank of the radiation field and its observation; for example, λ=0 correspond to a non observation of the radiation field in a particular direction. For directional correlations of aligned states all λs are even and the angular function can be simplified to some Clebsch-Gordan coefficients and associated Legendre functions.

From the experimental point of view, we can obtain the correlation function, W$(\theta_1, \theta_2, \phi)$ as the intensity of the transition γ_2, determined from a spectrum in a detector at angle θ_2 gated on the transition γ_1 in the detector placed at angle θ_1. By changing the angle at which the transitions are observed we obtain the reversed correlation function W$(\theta_2, \theta_1, \phi)$. Thus, the DCO ratio is given by:

$$R_{DCO} = \frac{W(\theta_2, \theta_1, \phi)}{W(\theta_1, \theta_2, \phi)} \tag{4.4}$$

or translated to experimentally measured quantities by:

$$R_{DCO} = \frac{I^{\gamma_2}_{\theta_1}(gate^{\gamma_1}_{\theta_2})}{I^{\gamma_2}_{\theta_2}(gate^{\gamma_1}_{\theta_1})} \tag{4.5}$$

When using a multidetector array many combinations of angles are available and hence many correlation functions can be analysed but with the limiting factor of statistics. Examining the symmetries of the array, we can increase the statistics by summing detectors positioned at similar angles. Then, to obtain the largest difference in the DCO ratio of both coincident transitions the detectors have to be placed at angles near 90^o and near 0^o to the beam axis.

In the case of the GASP array we have used the eight detectors placed at 90^o and the twelve detectors positioned at 35^o (or equivalently $145^o = \pi - 35^o$) which produced 6 different combinations of $(\theta_1, \theta_2, \phi)$ when integrated over ϕ.

In the case of EUROBALL, we have used the two rings of Clover detectors positioned at 90^o against one of the Cluster rings, placed at 156^o and consisting of 5 Clusters detectors. We have not used detectors at forward angles because of the different sizes of Clusters and Tapered detectors.

4.6 Linear Polarization.

As mentioned earlier, the high spin states of the product nuclei populated after fusion-evaporation reaction are oriented and hence the γ-rays de-exciting these states are emitted anisotropically and are also linearly polarized. A measure of the linear polarization, which expresses the direction of the electric field $(\vec{E})$ of the radiation, can be obtained by measuring the polarization angular distribution from oriented states.

---

[2] For example, λ_1=0 correspond to random orientation

The linear polarization angular distribution of a γ ray transition deexciting an axially symmetric state is given by [Ste75]:

$$W(\theta,\Psi) = \frac{d\Omega}{8\pi}\sum_{\lambda=even} B_\lambda(I)\Big[A_\lambda P_\lambda(cos\theta) + 2A_{\lambda 2}\left(\frac{(\lambda-2)!}{(\lambda+2)!}\right)^{1/2} P_\lambda^{(2)}(cos\theta)cos(2\Psi)\Big] \tag{4.6}$$

where θ is the angle between the beam axis and the direction of the radiation, Ψ is the angle between the reaction plane and the polarization axis of the detector (axis of maximum response to linear polarization), $P_\lambda^{(2)}$ are the general Legendre polynomials and λ is the order of the polynomials. The linear polarization distribution depends on the parity of the electromagnetic radiation, E or M, and hence is useful for the determination of the relative parities of the nuclear states involved in the transition.

When using multidetector arrays in which some of them are segmented and therefore sensitive to polarization [Gar97], measurements of correlations between the γ rays registered in polarimeters and in the remaining standard detectors become a useful tool to measure the polarization of gamma transitions belonging to weak channels populated in the reaction. Such correlations in which the polarization (1) of the first gamma is measured and only the direction (0) of the second is determined can be expressed by the formula [Dro96]:

$$\begin{aligned} W_{10}(\theta_1,\theta_2,\phi,\Psi_1) = N\sum_{\lambda\lambda_0\lambda_1} B_{\lambda_0}(I_0)\big\{& A_{\lambda 0}^{\lambda_1\lambda_0}(\gamma_1)A_{\lambda_1 0}^{0\lambda_1}(\gamma_2)d_{\mu 0}^{\lambda}(\theta_1)d_{\mu 0}^{\lambda_1}(\theta_2)cos\mu\phi \\ &- \frac{1}{2}A_{\lambda 2}^{\lambda_1\lambda_0}(\gamma_1)A_{\lambda_1 0}^{0\lambda_1}(\gamma_2)\big[d_{\mu 2}^{\lambda}(\theta_1)cos(\mu\phi+2\Psi_1) \\ &+ (-1)^\lambda d_{\mu-2}^{\lambda}(\theta_1)cos(\mu\phi-2\Psi_1)\big]d_{\mu 0}^{\lambda}(\theta_2)\big\} \end{aligned} \tag{4.7}$$

where θ_i is the angle defined by the direction of the radiation, ϕ is the angle between the two planes defined by the radiations, Ψ is the angle between the scattering plane and the polarization plane as mentioned above.

Following the formula for Compton scattering given by Klein-Nishina for linearly polarized radiation,

$$\frac{d\sigma}{d\Omega} = \frac{r_0^2}{2}\left(\frac{E}{E_0}\right)^2\left[\frac{E}{E_0} + \frac{E_0}{E} - 2sin^2\theta cos^2\Psi\right] \tag{4.8}$$

where Ψ is the angle between the scattering plane and the polarization plane, the scattering occurs preferentially in a plane perpendicular to the polarization plane ($\Psi = 90^o$). In measurements of linear polarizaton with polarimeters one usually measures the intensity at two values of the angle Ψ (0 and 90 degrees) for an angle $\theta = 90^o$ for which the effect of polarization is a maximum.

Thus, it is convenient to define the degree of linear polarization as [Twi75]:

$$P(\theta) = \frac{W(\theta,0^o) - W(\theta,90^o)}{W(\theta,0^o) + W(\theta,90^o)} \tag{4.9}$$

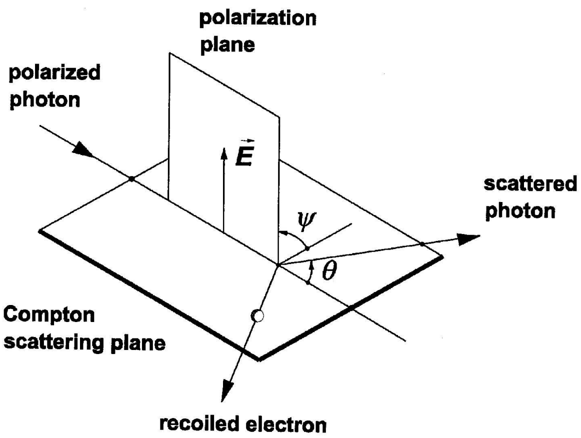

Figure 4.5: *Compton scattering of the polarized γ-ray. The electric vector, $\vec{E}$ determines the polarization plane; θ the angle between the incident and the scattered photon; Ψ the angle between the scattering plane and the polarization plane. Taken from [Dro99]*

where $W(\theta, 0^o)$ and $W(\theta, 90^o)$ describe the probabilities that the emitted γ-ray is polarized in the plane parallel and perpendicular to the emission plane respectively.

Experimentally, one measures the counting rate of photons scattered in directions parallel ($N_{||}$) and perpendicular ($N_{\perp}$) to the emission plane. Defining the experimental asymmetry (A) as:

$$A = \frac{N_{\perp} - N_{||}}{N_{\perp} + N_{||}} \tag{4.10}$$

we can relate the asymmetry to the polarization through the polarization sensitivity of the polarimeter (Q) as:

$$A = Q \cdot P \tag{4.11}$$

The value of Q can be easily calculated for a point-like polarimeter using the formulae:

$$\begin{aligned} N_{||} &= \sigma_{||} W_{||} + \sigma_{\perp} W_{\perp}, \\ N_{\perp} &= \sigma_{\perp} W_{||} + \sigma_{||} W_{\perp} \end{aligned} \tag{4.12}$$

where $\sigma_{||} \propto \frac{d\sigma}{d\Omega}(\Psi = 0^o)$ and $\sigma_{\perp} \propto \frac{d\sigma}{d\Omega}(\Psi = 90^o)$ give the probability that the photon hitting the polarimeter will be scattered in the plane parallel or perpendicular to the polarization plane respectively. It follows then that the sensitivity of the polarimeter is given by:

$$Q = \frac{\sigma_{\perp} - \sigma_{||}}{\sigma_{\perp} + \sigma_{||}} \tag{4.13}$$

For the actual polarimeter, the Clover detectors, the value of Q can be calculated using Monte Carlo codes [Gar97] obtaining a theoretical curve. In practice, the sensitivity is calculated by measuring the response of the polarimeter to radiation with known polarization. In the fig 4.6 it is shown the results of a Monte Carlo calculation of the Clover polarimeter sensitivity and some experimental points.

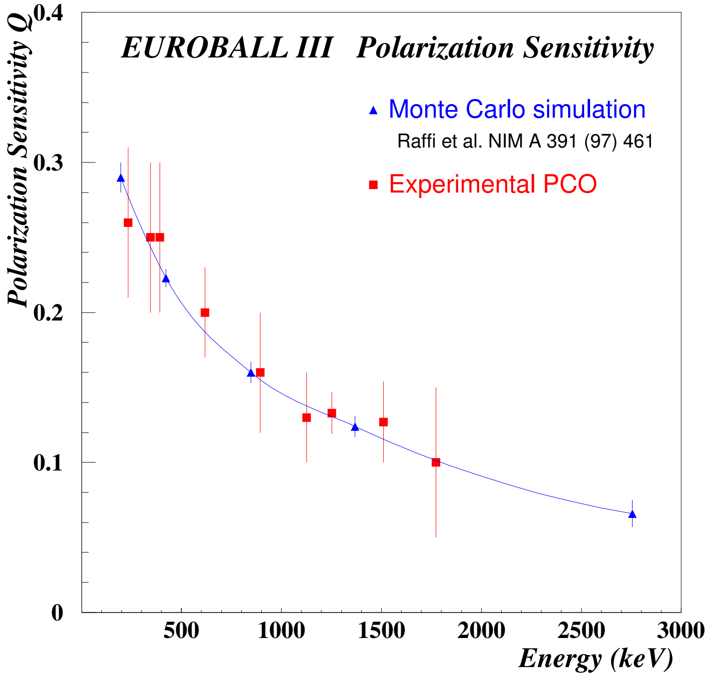

Figure 4.6: *MonteCarlo determination of the sensitivity of the Clover Polarimeter. Experimental points have been measured to confirm the calculations [Gad99]*

Table 4.1: *Tipical values and signs for angular distribution coefficients, DCO ratio values and asymmetry or polarization for the tansitions with given multipolarity. In the case of mixed multipolarity, the sign and values depend on the δ value.*

MULTIPOLARITY	A_2	A_4	$R_{DCO}(gateQ)$	$R_{DCO}(gateD)$	Asym (P)
E1 ($\Delta J = 1$)	< 0	$= 0$	0.5	1.0	> 0
M1 ($\Delta J = 1$)	< 0	$= 0$	0.5	1.0	< 0
E1 ($\Delta J = 0$)	> 0	$= 0$	1.0	2.0	< 0
M1 ($\Delta J = 0$)	> 0	$= 0$	1.0	2.0	> 0
M1/E2 (δ)	f(δ)	f(δ)	f(δ)	f(δ)	f(δ)
E2 ($\Delta J = 2$)	> 0	< 0	1.0	2.0	> 0
M2 ($\Delta J = 2$)	> 0	< 0	1.0	2.0	< 0
M2/E3 (δ)	f(δ)	f(δ)	f(δ)	f(δ)	f(δ)

Chapter 5

Results for ^{71}Br

As we described in a previous chapter, high spin states in ^{71}Br have been populated through the reaction $^{40}Ca(^{40}Ca, 2\alpha 1p)$ at different beam energies, 160 and 180 MeV, using two similar setups involving gamma-ray spectrometers and light charged particle detectors. In both cases a thick backing was used to stop the recoiling nuclei. Hence, Doppler correction was not applied in these two cases (see table 3.1). The level scheme has been built from the analysis of the $\gamma - \gamma$ coincidences based on few known transitions from the literature. This was necessary in order to identified the nucleus, however the order of the transitions and consequently of the levels comes from our own data. They confirm previous in-beam data [Arr90]. We have proceed similarly with the I^{π} assignments, they are based exclusively on the assumption of the $9/2^{+}$ assignment to the isomeric level. This assumption is in agreement with the systematics of the $9/2^{+}$ isomers in the region [Gri88]. The same assumption was made by Arrison *et al.* in their article. The rest of the I^{π} assignments are based on angular distributions, DCO ratios, polarization data and intensity balance of highly converted transitions from our experimental results. The final result is summarized in the level scheme shown in figures 5.1 and 5.2 which we will explain in detail in the following sections.

5.1 Building level scheme

In order to build the level scheme, E_{γ}-E_{γ}-particle matrices and E_{γ}-E_{γ}-E_{γ} cubes have been created. Since the efficiency of the light particle detectors is intrinsically lower than 100%, the statistics for each channel is distributed between different particle gates. Thus, using matrices with different particle conditions and comparing them, it should be possible to identify transitions that belong to a particular nucleus. In order to avoid mistakes with contaminants we have to choose the most favourable conditions that produce the cleanest matrices. In other words we need good quality in the channel selection.

In this spirit, we have evaluated the particle detection efficiency for different

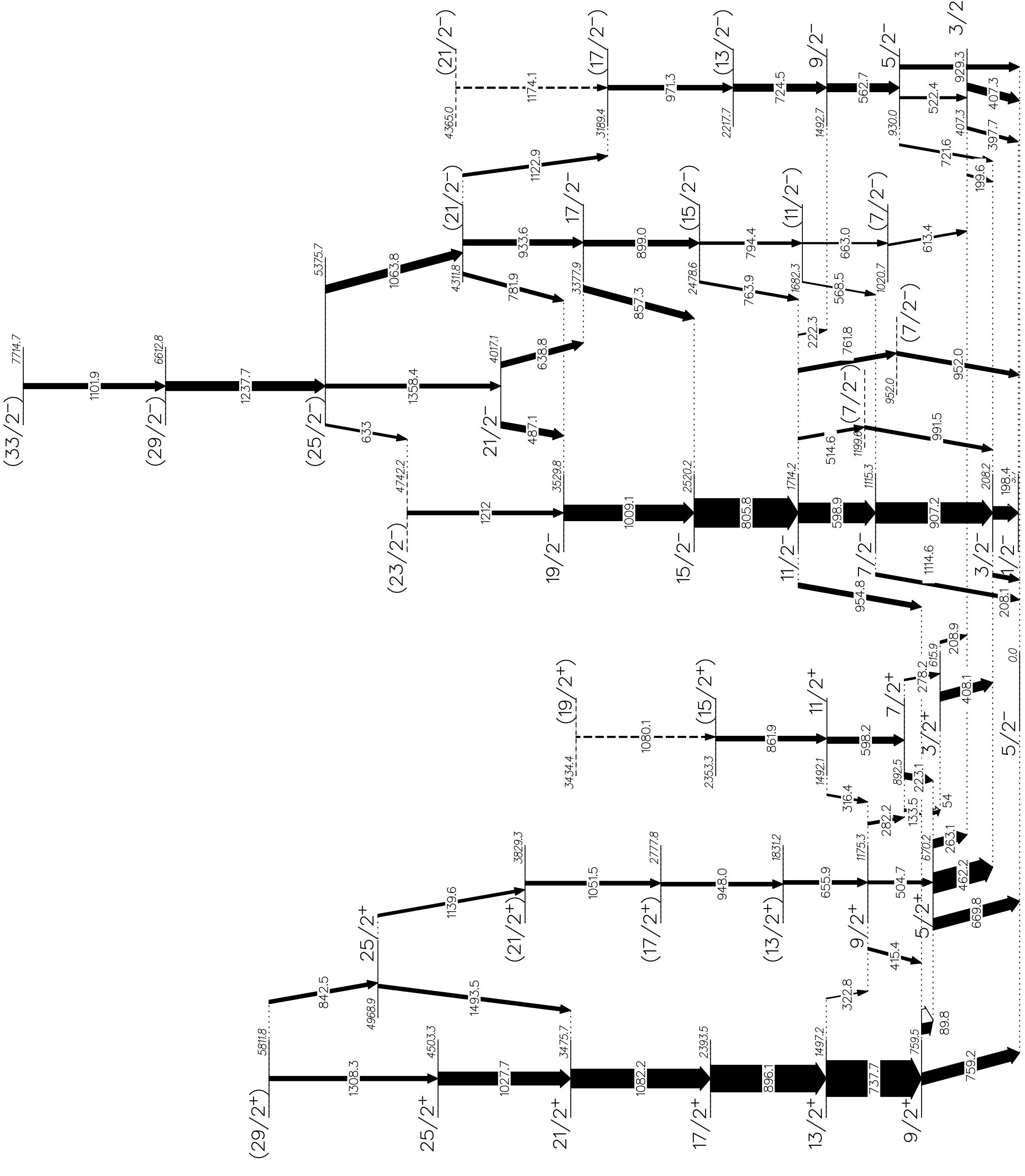

Figure 5.1: *Level scheme of* ^{71}*Br the width of the transitions are proportional to the intensities.*

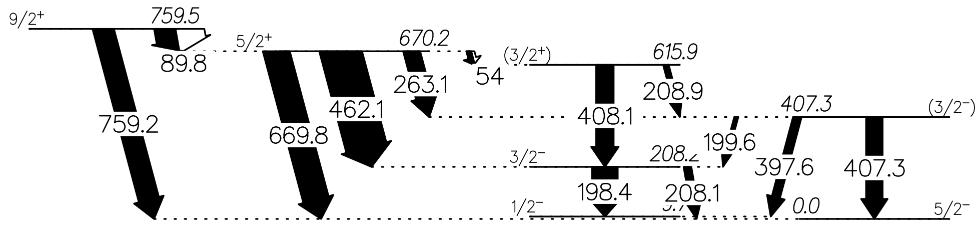

Figure 5.2: *Partial level scheme of ^{71}Br showing the delayed transitions.*

channels in both experiments carried out with the ISIS particle detector array. To achieve that, several gamma spectra gatted with different particle condition have been examined and the ratio of intensity of the γ-rays is related to the particle detection efficiency by the expression:

$$\frac{I_\gamma(m,N)}{I_\gamma(m-1,N)} = \frac{N-m+1}{m} \cdot \frac{\varepsilon}{(1-\varepsilon)} \tag{5.1}$$

where N is the number of evaporated particles and m is the number of detected particles.

The results for the particular case of the evaporated charged particles are shown in table 5.1. It is interesting to note the drop in efficiency depending on the number of evaporated particles. This must be related to the energy distribution of the evaporated particle which can be affected by the kynematics of the process. For instance, when more particles are evaporated their energies will be affected in a higher degree. If the distribution of the energy changes, then the effect of the absorbers and the CFD settings will modify the particle detection according to it.

From these results, we find $\varepsilon_{p,\alpha} < 50\%$, which means that we will have more statistics when we do not detect one of the particles. Thus, for the ^{71}Br we will have more statistics in the matrix with condition 1α 1p than in the matrix with 2α 1p and in the 2α 0p than in the 2α 1p.

This applies not only to the nucleus we are interested in, but also to the contaminants, so we have to analyse the ratios of the signals of interest to those of possible contaminants in order to choose the best matrices for the analysis. Thus following this logic, in the 1α1p we will have more events for ^{71}Br than in the 2α1p but we will have also more counts from ^{70}Se and ^{73}Br. Hence, we have calculated the probability for each channel for different particle conditions and from these values (shown in table 5.2) and from the projections of the matrices E$_\gamma$-E$_\gamma$ in coincidence with different particle conditions (fig 5.3) we can see that in the 2α0p we have a

Table 5.1: *Particle detection efficiency for ISIS detector array from the GASP and EUROBALL III experiments.*

Nucleus	channel	GASP Exp.		EUROBALL Exp.	
		$\varepsilon_p(\%)$	$\varepsilon_\alpha(\%)$	$\varepsilon_p(\%)$	$\varepsilon_\alpha(\%)$
^{77}Rb	3p	46.3 (14)	-	-	-
^{76}Kr	4p	41.7 (3)	-	48.8 (8)	-
^{74}Kr	1α2p	38.6 (4)	22.0 (6)	46.1 (9)	22.7 (6)
^{73}Br	1α3p	33.1 (6)	15.2 (7)	47.2 (12)	21.2 (8)
^{71}Br	2α1p	31.3 (19)	20.2 (12)	45.5 (12)	28.1 (7)
^{70}Se	2α2p	26.0 (17)	17.0 (13)	43.2 (13)	23.4 (9)

cleaner matrix than if we were using the particle condition 1α0p where the contamination from ^{73}Br and ^{74}Kr is higher. This is the main reason why we prefer to use the matrix gated by 2α0p to carry out the final analysis.

Table 5.2: *Channel probability for different particle conditions for some of the residual nucleus produced in the reaction.*

	Nucleus	Yield (mb)	Channel Probability					
		(hivap)	$2\alpha 0p$	$2\alpha 1p$	$1\alpha 0p$	$1\alpha 1p$	$0\alpha 0p$	$0\alpha 1p$
GASP 160 MeV	^{71}Br	0.82	0.028	0.013	0.221	0.101	0.437	0.199
	^{70}Se	22.2	0.016	0.011	0.155	0.109	0.377	0.265
	^{73}Br	66.0	-	-	0.046	0.068	0.254	0.377
	^{74}Kr	50.8	-	-	0.083	0.104	0.294	0.370
EBIII 180 MeV	^{71}Br	0.51	0.043	0.036	0.220	0.184	0.282	0.235
	^{70}Se	97.7	0.018	0.027	0.115	0.176	0.189	0.288
	^{73}Br	88.2	-	-	0.031	0.084	0.116	0.311
	^{74}Kr	33.3	-	-	0.066	0.113	0.225	0.384

Again the products of the reaction of the beam with oxygen following the oxidation of the target are also a major possible source of contaminants. Isotopes of ^{48}Cr, ^{47}V and ^{46}Ti are produced by the evaporation of 2α0p, 2α1p and 2α2p particles respectively in these reactions. These contaminants could be taken into account because the gammas belonging to these nuclei are well known.

Once we have chosen the cleanest conditions, we used the fact that some transitions were already known to put gates on them and extend the level scheme. Thus, using the $\gamma-\gamma$ matrix in coincidence with 2α0p particles and gating on known transitions such as 737, 896, 598, 907 and 806 we have established new candidates to extend the level scheme. These candidates have been then confirmed by observing their presence when the same gates were put on the $\gamma-\gamma$ matrix with the 2α1p particle condition and their absence when the same gates were put on the matrix

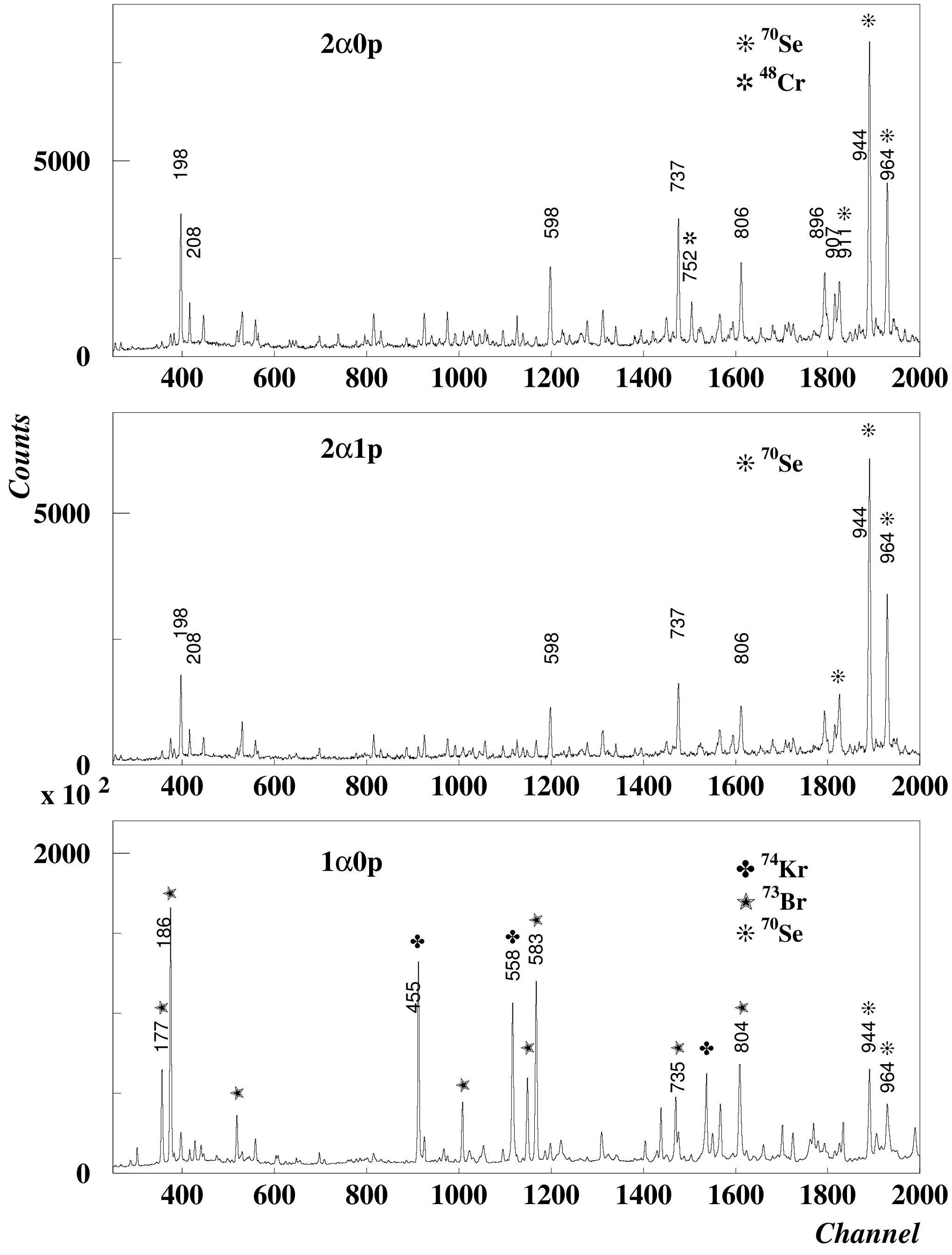

Figure 5.3: *Projections of the $\gamma-\gamma$ matrices in coincidence with different particle conditions in the GASP experiment. The most intense lines belonging to the ^{71}Br have been marked with the energies.*

requiring the coincidence with 2α2p. A further confirmation of candidate transitions was made by setting double gates in the γ-γ-γ cube. Up to six bands have been observed in the analysis of the data from the two experiments with GASP and EUROBALL (see figures 5.4 and 5.5).

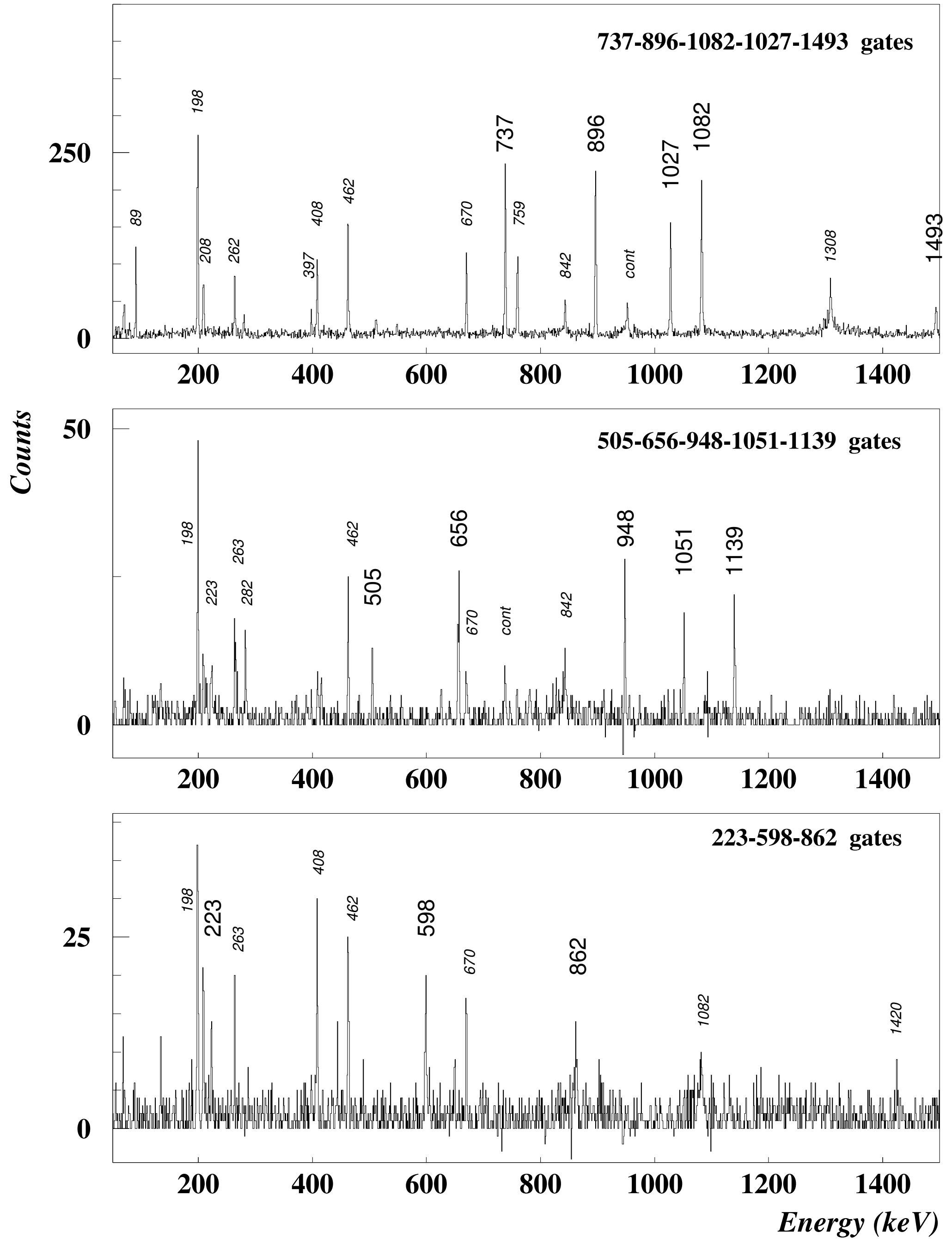

Figure 5.4: *Spectra corresponding to the positive parity bands in* ^{71}Br *obtained by adding doubled gated spectra from the EUROBALL experiment. Big numbers correspond to the gatting transitions; small numbers are other gammas in coincidence with them.*

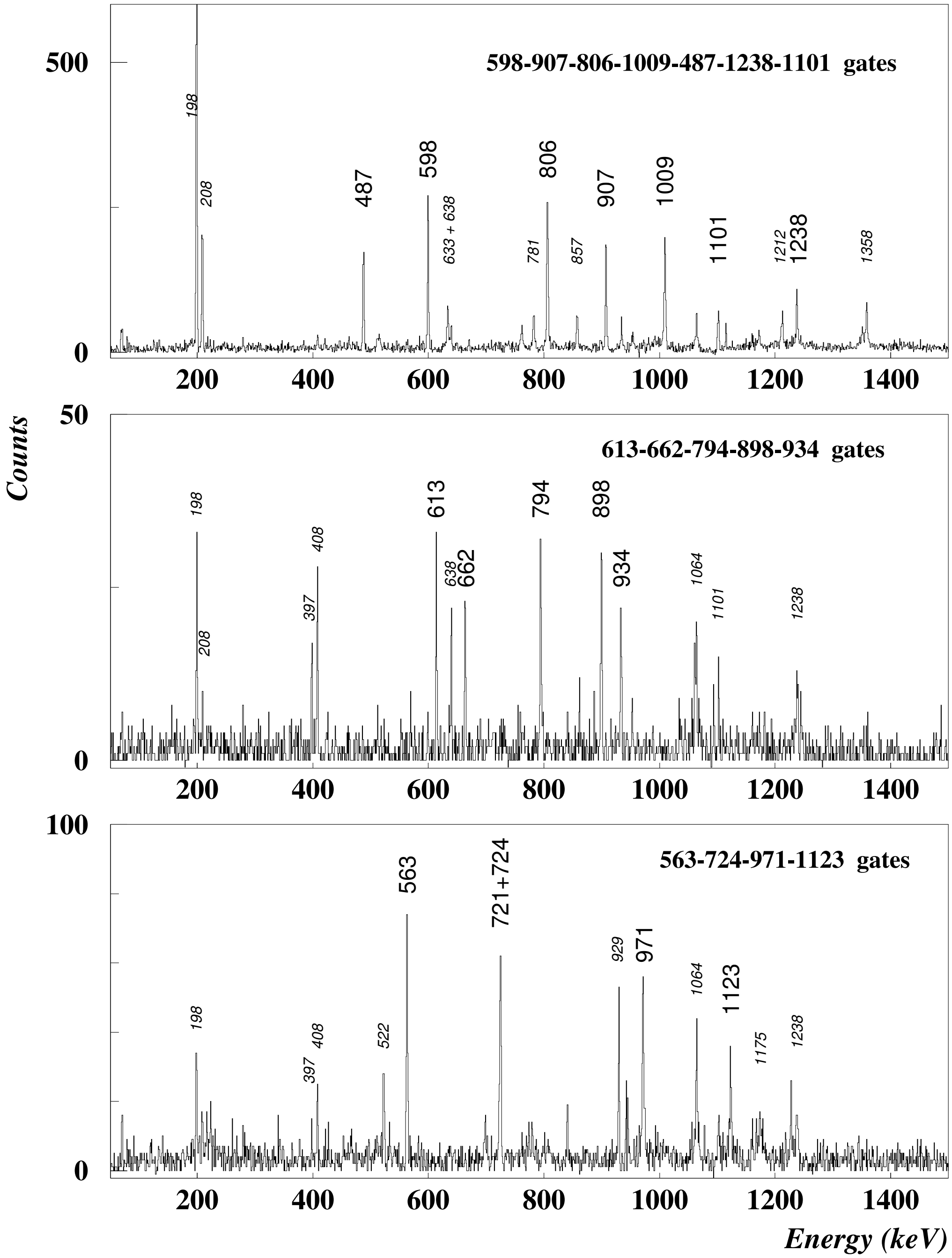

Figure 5.5: *Spectra corresponding to the negative parity bands in* ^{71}Br *obtained by adding doubled gated spectra from the EUROBALL experiment. Big numbers correspond to the gatting transitions; small numbers are other gammas in coincidence with them.*

5.2 Energy and intensity data

The energy calibration in the GASP and EUROBALL III experiments was done following the procedure explained in section 4.1.1. The calibration sources used in the GASP experiment were ^{56}Co and ^{152}Eu. They cover a range of energy from 30 keV up to 3 MeV. The calibration measurement was done at the end of the run and the energy shift were done to match this last run. For the EUROBALL experiment only ^{152}Eu was used covering an energy range of 30 keV up to 1.4 MeV.

The response function of HP Germanium detectors to the gamma radiation is not constant with energy. This means that the photopeak efficiency of the detector will vary with energy. In order to determine the intensities of the transitions emitted from a nucleus we have to measure the photopeak efficiency of the detector as a function of the gamma-ray energy. This efficiency calibration was carried out using standard sources with gamma rays covering the energy range of interest to allow the construction of an empirical efficiency curve.

When working with γ-detector arrays, the global efficiency is obtained by adding the spectra from the source from all of the detectors. If different detectors are used including composite detectors, special care has to be taken in order to calculate the efficiency when the "add-back" mode is used. Other problems that can appear in evaluating the efficiency in this high multiplicity set-up is that the different trigger conditions during the acquisition of the source data and the reaction data. A further modification to the efficiency curve has been introduced using internal data.

In our case, the efficiency curve for the different arrays has been calculated using standard sources available, namely ^{152}Eu, ^{56}Co and ^{133}Ba, where the relative gamma intensities are well known. The behaviour of the efficiency as a function of the energy was studied for typical Ge detectors by Jäckel et al. [Jac87], obtaining a semiempirical function:

$$\begin{aligned} &ln\varepsilon + 25 = 2/\pi \cdot (a_1 + a_2x + a_3x^2) \cdot atan(exp(a_4 + a_5x + a_6x^2)) \\ &where\ x = ln(E/E_0)\ and\ E_0 = 1keV \end{aligned} \tag{5.2}$$

where a_1,...a_6 are the fitting parameters.

Then, using this expression, we have fitted the efficiency data as a function of the energy using the Minuit libraries from CERN packages. The results for each gamma array are shown in fig. 5.6 and 5.6.

In these figures a correction has been introduced. Every time a trigger signal is accepted, a time gate is opened in the TDC for 200 ns, and the time signal of any Ge detector fired during this interval is recorded. This parameter give us the difference between the trigger signal and the Ge signal. In creating the matrices a time difference smaller than 200 ns is imposed (in our case ∼30 ns). This "prompt" time condition is imposed to the reaction data but not to the measured source since there the trigger condition is reduced to one (consequently any time condition will be accepted).

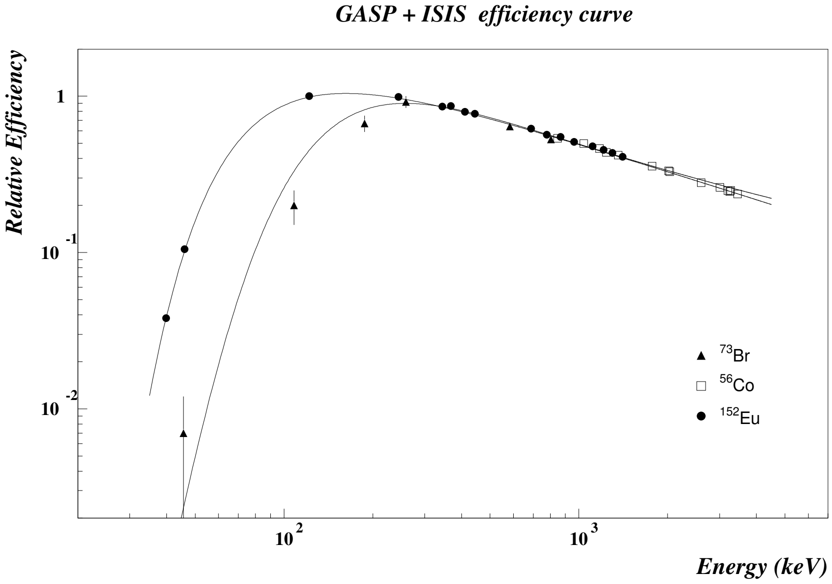

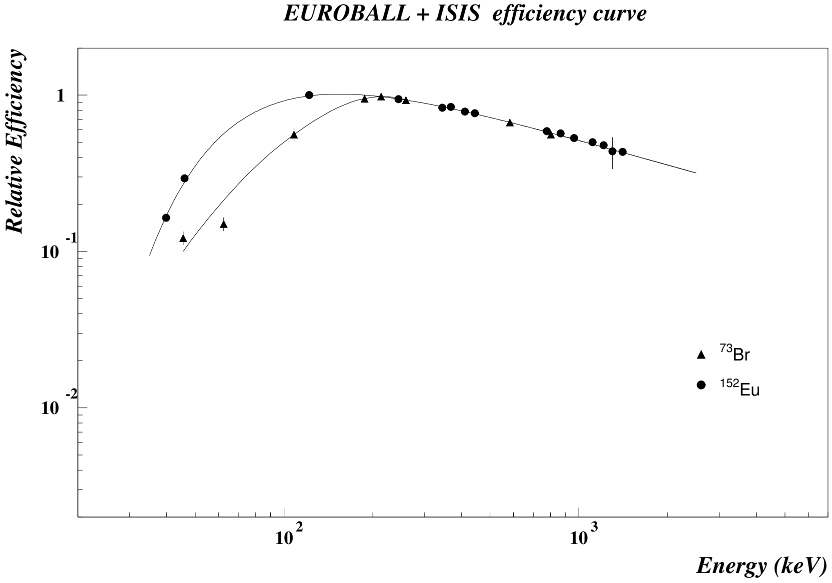

Figure 5.6: *Efficiency curve for the GASP array and the EUROBALL array coupled to the ISIS particle detector. Calculated with the* ^{152}*Eu and* ^{56}*Co sources and correcting the low energy part with known lines in* ^{73}*Br; see text.*

The response of a Ge detector to gamma rays of low energy is slower to the response to gamma rays of high energies. In other words, in the real data a drop in the efficiency will take place at lower energies in comparison to the efficiency obtained from the calibrating sources. Thus, in order to take into account this difference, we have used well known transitions in a nucleus present in our reaction to make a correction in the efficiency. In our case, ^{73}Br has been used; this nucleus

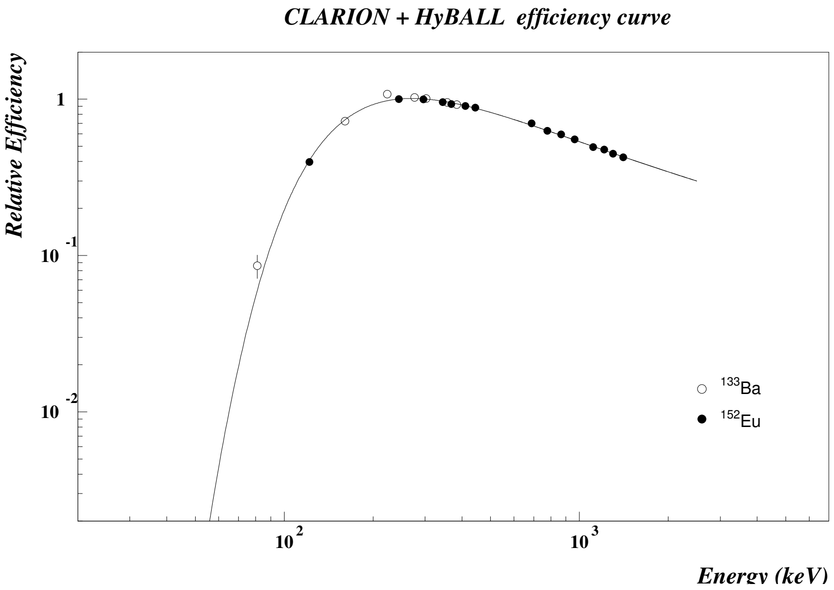

Figure 5.7: *Efficiency curve for the CLARION array coupled to the HYBALL particle detector, using the* ^{133}*Ba and* ^{152}*Eu sources.*

present several advantages: i) It is well produced in the reaction. ii)It has a cascade of high multiplicity (and hopefully not strongly affected by the trigger condition). iii) It includes low energy transitions, where the timing conditions are stronger. This effect can be clearly appreciated in fig. 5.6

Once the efficiency curve has been determined, the areas of the peaks will be corrected by the appropriate value of the efficiency to deduce the intensity. In principle, the best way to deduce the intensities of the gamma transitions would be to extract the areas from the single spectra. These spectra were not measured in our case. Consequently, the intensities were extracted from the projection of the $\gamma-\gamma$ matrices, which were further cleaned by requiring conditions on the particles. Actually the condition on particles 2α0p have been the most commonly used. But even in this case not all of the transitions could be identified in the projected spectra (either because the gamma peak was too close to other transition of similar energy or because the transition was too weak) and we have calculated their intensities by setting gates on coincident transitions and calculating the branching ratio when the gate was set from above or calculating the ratio to another known transition situated above when gated from below.

We have analysed data from three experiments and the measured values of the intensities of the gamma transitions are shown in table 5.3. It is clear that the intensity of the post-isomeric transition is cut by the condition on the prompt. In the data from the experiment with EUROBALL, the matrices were sorted with wide gates set on the time spectra of the detectors, because the two trigger conditions created a double peak time of coincidences, with a loss of time resolution. This effect was observed in the offline analysis and was probably due to some problem in the electronic settings during the experiment. For that reason it was impossible to clearly distinguish between the prompt and the post isomeric transitions.

Unlike the previous experiment, in the data from the experiment with the GASP spectrometer, the good timing conditions of the apparatus allow us to sort two kind of matrices one with a gate on the prompt part of the time spectrum and the other with the gate on the delayed part. This delayed matrix has allowed us to separate the contribution of the decay of the isomer to the population of the low-lying levels from the contribution of the prompt decay through the non-yrast bands.

In the third experiment performed with the CLARION gamma array coupled to the RMS spectrometer, the thin target without backing allowed the ^{71}Br nuclei to flight away of the focal plane with the result that no delayed transitions were detected at the target position. Thus, only the prompt contribution to the intensity have been measured. To calculate the intensities, we have used not only the $2\alpha0$p data but its sum with the $2\alpha1$p data in order to have more statistics. Despite this the poor energy resolution did not allow us to obtain good accuracy for the intensity values. The reason of the worse resolution in this case is the Doppler effect on the emitted gamma energies. This effect was corrected using one value for the $\beta = \frac{v}{c}$, but the kinematic correction produced by the evaporation of the alphas could not be included.

Table 5.3: Energy and intensity for the transitions of the ^{71}Br nucleus observed in the different experiments.

E_γ (keV)	I_γ(EB) Time open	E_γ (keV)	I_γ(Gasp) Time prompt	I_γ(Gasp) Time delayed	E_γ (keV)	I_γ(Clarion) Time prompt
54.3 (2)	107 (32)^{e,1}	53.9 (2)	-	5852 (2888)^{c,1}		
89.7 (1)	456 (91)^{a,2}	89.4 (2)	<204 (38)^{b,2}	4831 (1444)^{c,2}		
133.6 (1)	89 (4)^{a,3}	133.5 (2)	74 (23)^{e,3}		133.5 (2)	56 (9)^{d,3}
198.3 (1)	854 (30)^{e}	198.2 (1)	547 (35)^{e}	1512 (195)^{e}	198.1 (2)	449 (40)^{d,r}
199.5	42 (30)^{f}	199.5	12 (7)^{e}	67 (209)^{f}		
208.0 (1)	239 (15)^{f}	208.0 (1)	151 (10)^{f}	403 (52) ^{f}	207.8 (2)	188 (23)^{d,r}
208.6 (2)	30 (10)^{e}	208.4 (2)	31 (8)^{e}	122 (33)^{g}		
222.1 (1)	12 (5)^{o}	222.2 (2)	21 (9)^{o}			
223.0 (1)	135 (12)^{e}	222.9 (2)	131 (9)^{b}		222.7 (2)	160 (24)^{d}
263.0 (1)	122 (24)^{e}	263.0 (2)	73 (5)^{b}	351 (20)^{c}	263.1 (5)	47 (9)^{d}
276.7	17 (10)^{e}	276.7 (2)	30 (9)^{e}			
282.0 (2)	45 (12)^{a,e}	282.4 (2)	61 (5)^{b}		282.3 (5)	53 (12)^{d}
316.5 (2)	38 (3)^{a}	316.6 (2)	34 (3)^{b}			
397.4 (1)	103 (20)^{e}	397.7 (1)	74 (5)^{b}	144 (20)^{c}	398.1 (5)	46 (9)^{d}
407.1 (2)	203 (20)^{e}	407.8 (2)	146 (21)^{e}	248 (22)^{e,f}	407.0 (2)	174 (22)^{d,r}
408.0 (1)	145 (20)^{h}	408.1 (1)	53 (21)^{e}	382 (44)^{h}		
415.4 (1)	83 (3)^{a,e}	415.6 (2)	80 (15)^{e}		415.6 (5)	53 (11)^{d}
462.1 (1)	359 (24)^{e}	462.3 (2)	195 (9)^{b}	1000 (51)^{c}	462.4 (5)	144 (20)^{d}
487.0 (1)	114 (7)^{i}	487.4 (1)	171 (16)^{i}		487.4 (2)	167 (42)^{i}

Table 5.3: (continued)

E_γ (keV)	I_γ(EB) Time open	E_γ (keV)	I_γ(Gasp) Time prompt	I_γ(Gasp) Time delayed	E_γ (keV)	I_γ(Clarion) Time prompt
504.7 (1)	69 (12)^{e}	505.4 (1)	81 (10)^{b,e}		506.7 (5)	119 (20)^{d}
514.6 (1)	105 (9)^{e}	514.9 (2)	103 (22)^{b,e}		514.4 (5)	163 (30)^{e}
522.3 (1)	47 (10)^{e}	522.7 (1)	60 (10)^{e}		522.9 (5)	165 (24)^{d}
562.5 (1)	169 (4)^{a}	562.9 (2)	196 (17)^{b}		563.5 (2)	374 (43)^{d}
568.8 (2)	29 (10)^{e}	569.0 (2)	10 (4)^{k}			
598.3 (1)	168 (25)^{e}	598.7 (1)	193 (24)^{q}		599.3 (5)	98 (28)^{q}
598.9 (1)	389 (33)^{f}	599.2 (2)	421 (42)^{f}		599.7 (1)	534 (70)^{f}
613.3 (2)	24 (4)^{j}	613.9 (2)	27 (10)^{j}			
633.3 (2)	43 (4)^{i}	633.5 (2)	37 (15)^{i}			
639.0 (2)	96 (15)^{e}	639.1 (2)	147 (34)^{e}			
656.1 (2)	61 (6)^{l}	656.1 (2)	45 (6)^{l}			
663.0 (2)	21 (4)^{j}	663.1 (2)	17 (4)^{j}			
669.7 (1)	261 (7)^{a}	670.0 (2)	163 (13)^{b}	430 (48)^{c}	670.0 (2)	112 (17)^{d}
721.3 (2)	40 (10)^{e}	721.5 (1)	52 (10)^{e}		723.3 (5)	340 (40)^{o,r}
724.4 (2)	146 (14)^{m}	724.2 (2)	166 (25)^{m}			
737.7 (1)	1000 (47)^{a}	738.0 (1)	1000 (54)^{b}		738.0 (2)	1000 (46)^{d}
759.1 (1)	279 (3)^{a}	759.4 (2)	$<$118 (9)^{b}	401 (39)^{c}		
762.0 (2)	113 (8)^{a}	762.2 (2)	128 (10)^{b}		761.9 (5)	179 (31)^{d,r}
764.2 (3)	52 (8)^{k}	764.2 (3)	63 (21)^{b,k}			
781.7 (2)	81 (8)^{i}	782.1 (2)	106 (34)^{i}		783.1 (5)	167 (42)^{i}
793.9 (2)	18 (3)^{j}	793.9 (2)	15 (4)^{j}			
805.8 (1)	598 (46)^{k}	805.8 (1)	660 (85)^{k}		806.1 (2)	793 (79)^{d}
842.7 (3)	46 (10)^{n}	843.1 (3)	52 (16)^{n}			
857.1 (2)	134 (20)^{i}	857.5 (1)	168 (27)^{i}		858.3 (5)	126 (42)^{i}
862.2 (2)	98 (11)^{q}	862.7 (5)	88 (17)^{q}			
896.1 (1)	680 (30)^{a,i}	896.4 (1)	652 (43)^{b}		896.3 (5)	970 (100)^{d,r}
899.3 (2)	140 (30)^{e}	899.3 (2)	95 (30)^{e}			
907.2 (1)	407 (30)^{a}	907.4 (1)	452 (33)^{b}		906.3 (5)	495 (60)^{d}
929.2 (1)	103 (10)^{e}	929.5 (3)	147 (20)^{b,e}			
933.7 (1)	81 (11)^{e}	934.2 (2)	116 (22)^{e}			
947.6 (2)	94 (20)^{l}	947.9 (3)	110 (20)^{l}			
952.2 (2)	127 (16)^{e}	952.4 (2)	147 (22)^{e}		952.4 (2)	465 (158)^{e,r}
954.5 (2)	113 (16)^{e}	955.1 (2)	127 (20)^{e}			
971.2 (1)	81 (9)^{o}	971.2 (1)	152 (24)^{o}		971.7 (5)	263 (40)^{d}
991.7 (1)	126 (18)^{h}	991.8 (2)	140 (25)^{h}		993.0 (10)	57 (18)^{h}
1009.1 (1)	323 (30)^{a}	1009.5 (1)	402 (31)^{b}		1010.2 (5)	691 (85)^{d}
1027.8 (1)	304 (22)^{n}	1028.0 (1)	297 (27)^{n}		1028.2 (5)	440 (58)^{n}
1051.8 (2)	56 (18)^{l}	1051.5 (5)	51 (13)^{l}			
1064.0 (1)	111 (10)^{e}	1063.5 (2)	140 (38)^{e}			
1082.2 (1)	470 (32)^{n}	1082.4 (1)	442 (42)^{n}		1082.8 (5)	849 (100)^{d}
1101.9 (1)	114 (15)^{p}	1101.9 (1)	198 (20)^{b}			
1114.7 (2)	66 (10)^{e}	1115.5 (2)	61 (24)^{e}			
1123.1 (2)	59 (6)^{o}	1123.7 (2)	61 (24)^{o}		1123.5 (5)	133 (30)^{d}
1139.2 (2)	48 (10)^{l}	1139.6 (5)	30 (12)^{l}			
1212.3 (2)	75 (10)^{i}	1212.5 (2)	81 (30)^{i}			
1237.8 (2)	152 (15)^{a}	1238.0 (2)	259 (23)^{b}			

Table 5.3: (continued)

E_γ (keV)	I_γ(EB) Time open	E_γ (keV)	I_γ(Gasp) Time prompt	I_γ(Gasp) Time delayed	E_γ (keV)	I_γ(Clarion) Time prompt
1308.2 (2)	97 (8)[n]	1309.3 (3)	74 (20)[n]		1310.2 (5)	321 (58)[n]
1358.4 (2)	67 (10)[e]	1359.0 (2)	63 (18)[e]			
1493.7 (2)	102 (24)[n]	1494.6 (3)	84 (20)[n]		1496.9 (5)	191 (72)[n]

[1] $I_{tot}=I_\gamma(1+\alpha_t)= 1.65\cdot I_\gamma$ (M1 is assumed)
[2] $I_{tot}=I_\gamma(1+\alpha_t)= 2.34\cdot I_\gamma$ (E2 is assumed)
[3] $I_{tot}=I_\gamma(1+\alpha_t)= 1.054\cdot I_\gamma$ (M1 is assumed)
[a] From projection of matrix 2a0p from EB exp.
[b] From projection of prompt matrix 2a0p from GASP exp.
[c] From projection of delayed matrix 2a0p from GASP exp.
[d] From projection of prompt matrix 2a0p+2a1p from OR exp.
[e] From branching ratios gatting above.
[f] From projection by subtracting other contribution.
[g] From gate on E_γ=397.7 keV
[h] From gate on E_γ=198.4 keV
[i] From gate on E_γ=805.8 keV
[j] From gate on E_γ=407.3 keV
[k] From gate on E_γ=907.2 keV
[l] From sum of gates 415.3, 282.2 and 504.7 keV
[m] From gate on E_γ=929.3 keV
[n] From gate on E_γ=737.7 keV
[o] From gate on E_γ=562.7 keV
[p] From gate on E_γ=1123.1 keV
[q] From gate on E_γ=223.0 keV
[r] Doublet.

5.3 Spin-parity assignments.

In order to assign the spins and parities to the levels established in the previous section, a knowledge of the character and the multipolarity of the transitions de-exciting the levels is needed. Several methods were used to access this information: angular distribution, directional correlations, polarization correlations, etc. in gamma spectroscopy with detector arrays as described earlier.

5.3.1 Angular Distribution data.

In order to determine the spins of the levels decaying by the most intense transitions, we can use the intensity of the γ transitions plotted accordingly to the different polar angles subtended by the detectors relative to the beam axis. Fitting the distribution of these intensities to the expression given in the previous chapter:

$$W(\theta) = 1 + A_2P_2(cos\theta) + A_4P_4(cos\theta) \tag{5.3}$$

we can deduce A_2 and A_4 which are characteristics of a given multipolarity and spin difference.

In the case of the GASP experiment, in which the detectors can be sorted in seven rings with the same polar angle, the statistics were too low to afford a good analysis of angular distributions. We only obtained good results for the known intense E2 transitions. In the EUROBALL experiment the statistics available were better and we grouped the Tapered, Clovers and Clusters detectors into 13 ring sets according to their polar angle θ:

Table 5.4: Polar angle for the different types of detector in the EUROBALL array.

Ring N^o	θ	N^o det.	Type	Ring N^o	θ	N^o det.	Type
1	15	5	Tapered	8	122	10	Cluster
2	35	10	Tapered	9	130	30	Cluster
3	52	15	Tapered	10	139	25	Cluster
4	72	26	Clover	11	148	15	Cluster
5	81	26	Clover	12	155	15	Cluster
6	99	26	Clover	13	163	10	Cluster
7	107	26	Clover				

We have sorted a group of thirteen matrices corresponding to the thirteen angles with the following content: n^o of coincidences between a certain γ-ray at an angle θ_i (i=1,...,13) with other γ-rays at any angle. These matrices contain a condition on the particles in order to avoid contamination from other channels. Then, by selecting a gate in the E_{all}-axis we obtain the spectra at each angle. Each spectrum has to be corrected for the respective efficiency curve in order to get the intensities of the transitions. In addition, a geometrical factor has to be included in order to compare the different detector angle coverage. As we know, the Euroball detectors are positioned at different distance from the target position and therefore the efficiencies are different. These geometrical factors can be estimated by using known transitions with known angular distributions. In our case we have deduced a mean value for each geometrical factor using transitions in ^{68}As.

By using these factors, we have obtained the intensities at each angle and then, using the MINUIT package from the CERN libraries software [CERN81], we have fitted the angular distribution function and have deduced the best values for the A_2 and A_4 coefficients for the main transitions. The results are summarized in table 5.9. In figure 5.8 we have shown the fit to the angular distribution of some of the most intense transitions.

5.3.2 Directional correlation data.

In the analysis of the directional correlations from oriented states (DCO) the data have been sorted in matrices $\gamma(\theta_1) - \gamma(\theta_2)$ corresponding to coincidences of gamma transitions emitted in the directions θ_1 and θ_2. Using the fact that the correlation

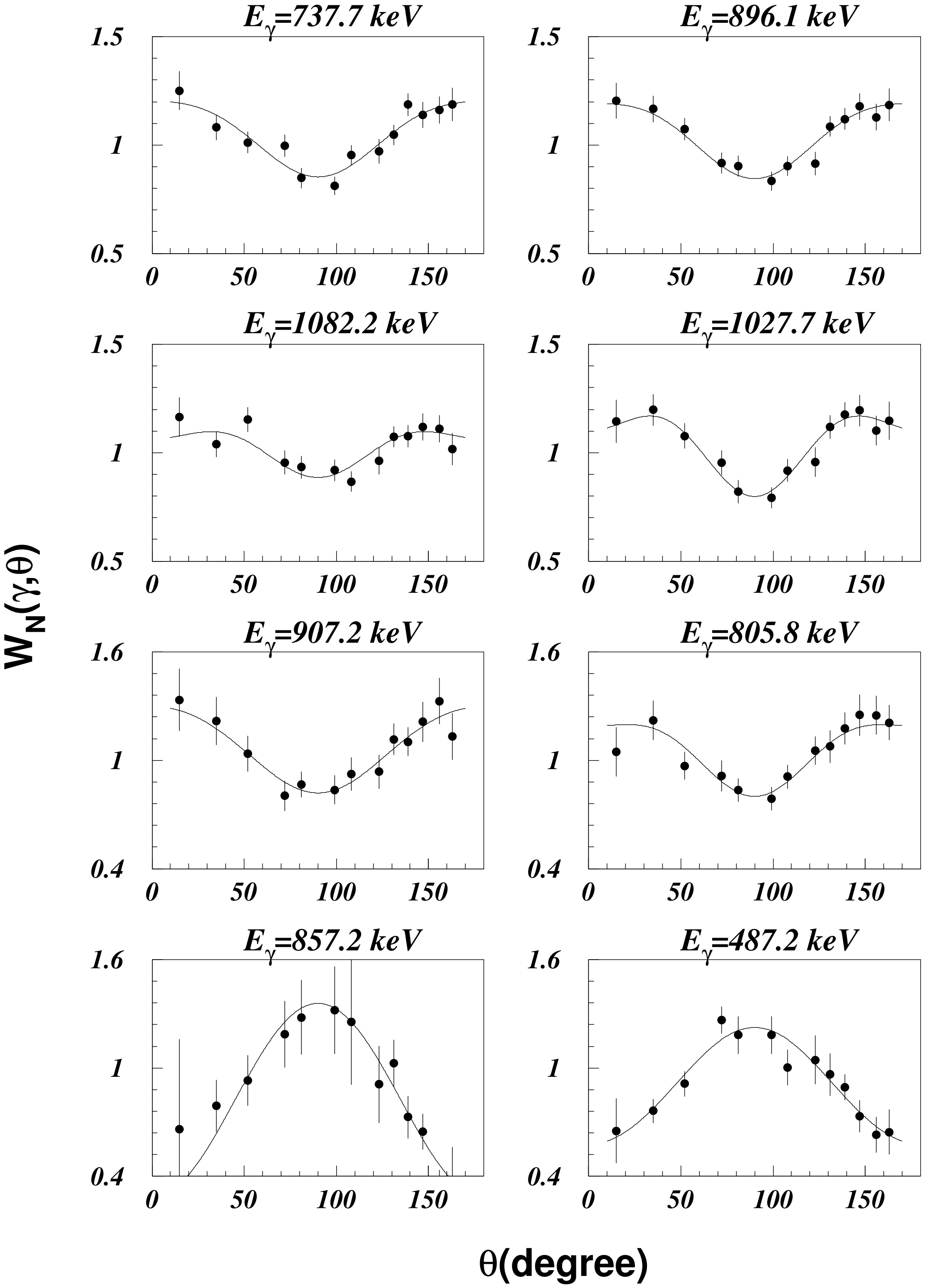

Figure 5.8: *Angular distribution for some of the main γ-ray transitions in ^{71}Br.*

function does not depend strongly on the $\Delta\phi$ angle between detectors, all possible combinations of detectors have been included in the matrices to increase the statistics.

In the GASP experiment it was not possible to take advantage of the high degree of symmetry of the spectrometer because of the poor statistics, even summing the statistics from both rings at 36 and 150 degrees against the ring at 90 degree, and it was only possible to calculate the DCO ratio for the known transitions. In the experiment with EUROBALL, the detectors placed in rings were sorted with the following distribution: 26 Clover detector at 90 degree and 5 Cluster at 153 degree. To calculate the DCO ratio we used the formula deduced in the previous chapter,

$$R_{DCO} = \frac{I^{\gamma_2}_{\theta_1}(gate^{\gamma_1}_{\theta_2})}{I^{\gamma_2}_{\theta_2}(gate^{\gamma_1}_{\theta_1})} \tag{5.4}$$

where $\theta_1 = 153^o$ and $\theta_2 = 90^o$.

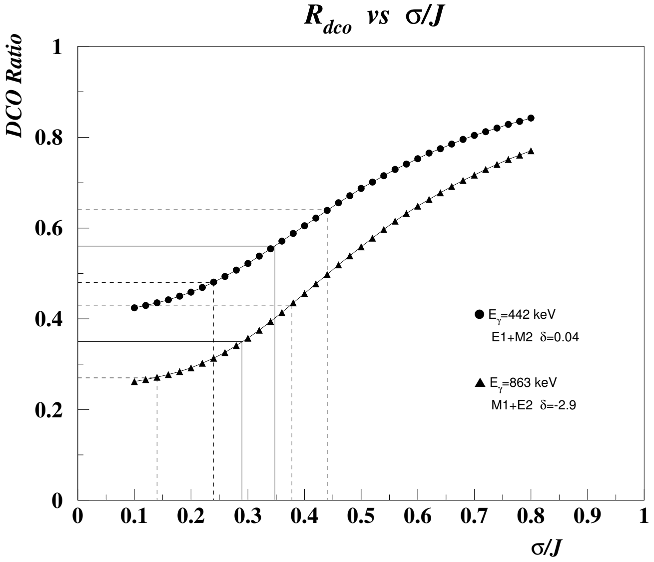

Figure 5.9: *Experimental σ/J determination from measuring the DCO ratio of known dipole transition in ^{69}As 442.9 keV ($9/2^+$-$7/2^-$) and 863.0 keV ($7/2^-$-$5/2^-$) when gatting on the 854.1 keV quadrupole transition.*

The DCO ratio, for a quadrupole-dipole cascade, is a function of both (σ/J) and δ. The first step in the DCO analysis is therefore to estimate the de-alignment parameter (σ/J) using known transitions. Finding dipole transitions in the literature with δ values measured with accuracy is really difficult in this region of nuclei. Thus, we have only found two good candidates, the 442.9 keV and the 863.0 keV transitions in ^{69}As. We have obtained the experimental DCO ratio for these transitions and comparing with theoretical DCO estimate for these δ values as a function of the de-alignment parameter (σ/J) has allowed us to determine the best range for the σ/J parameter. Thus, from the experimental values $0.29\ ^{+0.09}_{-0.15}$ and $0.35\ ^{+0.09}_{-0.11}$ we have obtained an averaged value of $\sigma/J = 0.33 \pm 0.08$

Table 5.5: Experimental DCO Ratio results for the main transitions in ^{71}Br.

E_γ	E_{gate}	XL_{gate}	R_{dco}(exp)	XL_γ
198[a]	599[a]	Q	0.30 (2)	D+Q
	907	Q	0.35 (3)	
	806	Q	0.31 (3)	
	737	Q	0.36 (4)	
	896	Q	0.32 (5)	
208	599	Q	0.62 (7)	D+Q
	907	Q	0.70 (10)	
	806	Q	0.47 (14)	
	737	Q	0.55 (8)	
	896	Q	0.57 (14)	
	463	D	0.97 (11)	
	408	D	1.1 (2)	
223	198	D	1.1 (2)	D+Q
	463	D	0.84 (15)	
	408	D	0.93 (13)	
	599	Q	0.87 (9)	
	670	D	0.7 (5)	
263	737	Q	0.31 (11)	D+Q
397	263	D+Q	1.5 (2)	D+Q
407	263	D+Q	1.1 (2)	D+Q
408	737	Q	0.40 (5)	D
	198	D+Q	1.4 (1)	
	208	D+Q	0.9 (1)	
462	737	Q	0.65 (6)	D
	198	D+Q	1.7 (1)	
	208	D+Q	0.86 (8)	
487	1009	Q	0.45 (5)	D+Q
	599	Q	0.37 (10)[a]	
	806	Q	0.38 (12)[a]	
	907	Q	0.52 (15)[a]	
514	806	Q	0.6 (3)	Q
522	563	Q	1.0 (7)	D or Q
563	724	Q	1.0 (2)	Q
	929	Q	1.0 (6)	
599	198	D+Q	3.2 (2)	Q
	208	D+Q	1.6 (2)	
	463	D	2.1 (5)	
	907	Q	1.16 (7)	
	806	Q	0.94 (8)	
639	806	Q	0.5 (4)	D
670	737	Q	0.98 (11)	Q
	89	Q	1.7 (2)	
722	563	Q	0.8 (3)	Q (D)
724	563	Q	1.3 (3)	Q
	929	Q	0.7 (3)	
759	737	Q	0.85 (8)	Q
	896	Q	1.4 (2)	
	1082	Q	1.4 (2)	
762	806	Q	0.89 (20)	Q

[a] Doublet, see level scheme.

Once we have established the average σ/J value, it is possible to make assump-

Table 5.6: DCO data (continued)

E_γ	E_{gate}	XL_{gate}	R_{dco}(exp)	XL_γ	E_γ	E_{gate}	XL_{gate}	R_{dco}(exp)	XL_γ
737	198	D+Q	3.3 (3)	Q	955	806	Q	0.4 (3)	D
	896	Q	1.19 (5)						
	1082	Q	0.82 (5)		971	563	Q	0.9 (3)	Q
781	806	Q	0.7 (3)	D+Q	991	806	Q	0.8 (3)	Q
806	198	D+Q	3.1 (2)	Q	1009	599	Q	0.95 (9)	Q
	208	D+Q	2.2 (2)			806	Q	0.68 (15)	
	487	D+Q	3.8 (4)			487	D+Q	4.3 (6)	
	599	Q	1.23 (7)						
	907	Q	0.95 (6)		1027	737	Q	1.01 (10)	Q
						896	Q	1.27 (8)	
857	599	Q	0.63 (12)	D+Q		1082	Q	1.21 (8)	
	806	Q	0.35 (14)						
					1082	737	Q	0.95 (6)	Q
862	223	D	1.6 (14)	Q		896	Q	1.19 (7)	
						1027	Q	1.16 (8)	
896	737	Q	1.15 (5)	Q					
	1082	Q	1.01 (6)		1101	806	Q	1.1 (3)	Q
	1027	Q	0.88 (6)			1238	Q	0.9 (3)	
907	198	D+Q	3.1 (3)	Q	1238	806	Q	0.9 (3)	Q
	208	D+Q	2.7 (3)						
	599	Q	1.09 (7)		1308	737	Q	0.6 (5)	Q
	806	Q	1.09 (10)			1082	Q	0.5 (4)	
929	563	Q	1.2 (4)	Q	1493	737	Q	0.9 (3)	Q
						896	Q	0.9 (3)	
934	806	Q	0.6 (5)	D+Q					
952	806	Q	0.6 (2)	D+Q					

tions about the multipolarities of dipole transitions when the gate is set on E2 transitions. The quadrupole "stretched" transitions always have a DCO ratio equal to unity when gatting on E2 transitions. In tables 5.5 and 5.6 we present the results of the DCO analysis of the transitions belonging to the ^{71}Br. Different gates have been set for each transition when possible, in order to compare and better estimate the multipolarities of the transitions.

In figure 5.10 we show an example of the spectra obtained following this method.

Comparing the gamma spectrum from the Clover detectors at 90^o with the spectrum from the Cluster detectors of the ring at 155^o, both corrected for efficiency and gated on the same transition, we can deduce the value of the DCO ratio of the transitions by evaluating the areas of the peaks observed in coincidence.

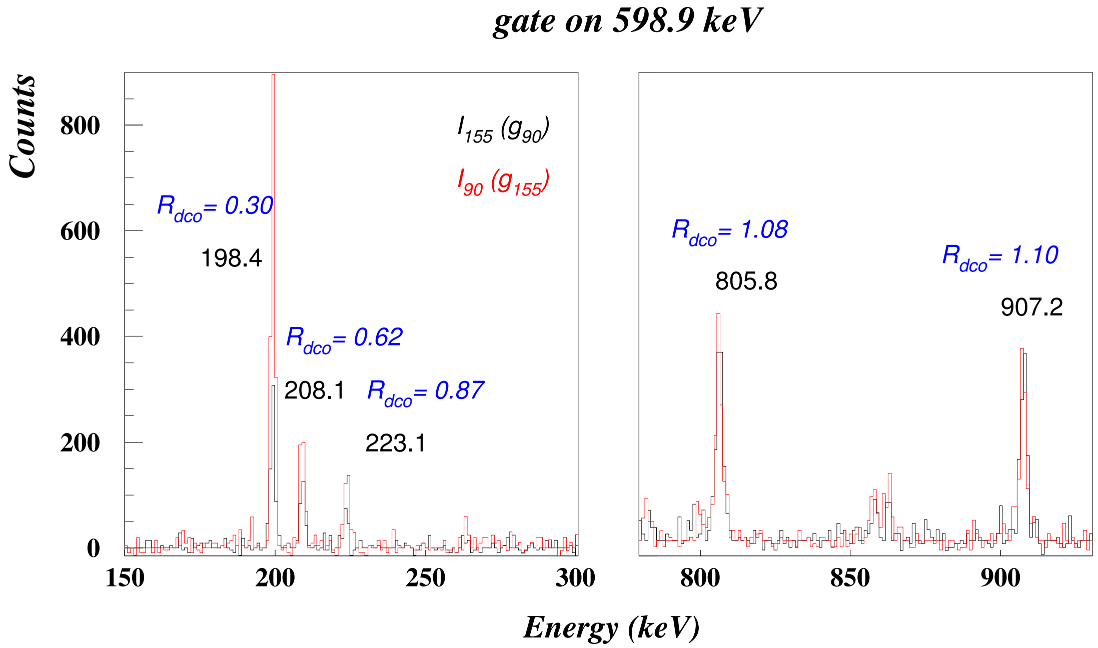

Figure 5.10: *Plot with the DCO gated spectra, the Clover at 90º spectrum in red and the Cluster at 155º in black. The gate is set on the 598.9 keV γ-ray transition in the Cluster and Clover ring respectively.*

5.3.3 Polarization-Directional correlation data.

More information on the spin-parities of the levels connected by the gamma transitions can be determined from the measurement of the "Asymmetry" presented by the transitions. The electric field orientation with respect to the scattering plane when observed at $\theta = 90^o$ serves as a measure of the linear polarization of the transitions that depend on the character and multipolarity and mixing ratio, δ. The asymmetry can then be calculated using the correlation between two coincident gammas following the expression:

$$A = \frac{N_{\perp} - N_{\|}}{N_{\perp} + N_{\|}} \tag{5.5}$$

In order to calculate the asymmetry of the transitions, we have sorted the data into two matrices where on one axis is represented the gamma detected in any detector and on the other axis is represented the coincident gamma detected in two Clover capsules added with perpendicular or parallel orientation relative to the beam axis: E_{ALL}-$E_Q^{\perp}$ and E_{ALL}-$E_Q^{\parallel}$ matrices. Setting gates on the axis corresponding to all detectors, and comparing the results on the Clover axis for the parallel and perpendicular conditions we have obtained the Asymmetry values for the main transitions. These values are given in table 5.7.

Table 5.7: Polarization data

E_γ	E_{gate}	$N_\perp$	$N_\parallel$	Asym	Pol
198	907	272 (18)	380 (21)	-0.17 (4)	-0.59 (14)
	462	530 (26)	620 (27)	-0.08 (3)	-0.28 (10)
	407	190 (18)	171 (9)	0.05 (6)	0.17 (21)
	599	479 (23)	514 (25)	-0.04 (3)	-0.14 (10)
	737	450 (24)	420 (24)	0.03 (4)	0.10 (14)
208	907	109 (13)	118 (13)	-0.04 (8)	-0.14 (29)
	462	176 (17)	209 (16)	-0.09 (6)	-0.32 (21)
	407	132 (17)	120 (14)	0.05 (9)	0.18 (32)
	599	161 (14)	206 (15)	-0.12 (6)	-0.43 (21)
	737	180 (19)	246 (20)	-0.15 (7)	-0.54 (25)
223	599	112 (10)	132 (27)	-0.08 (12)	-0.3 (4)
263	737	395 (28)	325 (26)	0.10 (5)	0.37 (18)
397	263	39 (7)	58 (19)	-0.2 (2)	-0.9 (9)
407	263	468 (27)	474 (25)	-0.006 (40)	-0.03 (17)
408	198	608 (21)	624 (38)	-0.01 (4)	-0.04 (17)
	737	445 (27)	463 (28)	-0.02 (4)	-0.09 (17)
462	198	1720 (45)	1597 (44)	0.04 (2)	0.19 (10)
	208	461 (25)	543 (26)	-0.08 (4)	-0.38 (19)
	737	115 (9)	91 (10)	0.12 (7)	0.57 (33)[a]
487	907	210 (16)	178 (16)	0.08 (6)	0.38 (29)
	806	299 (20)	327 (27)	-0.04 (5)	-0.19 (24)
	1009	383 (20)	373 (20)	0.01 (4)	0.05 (19)
598	223	269 (33)	236 (31)	0.07 (9)	0.37 (47)
599	198	1444 (43)	1088 (39)	0.14 (2)	0.74 (11)
	208	351 (22)	311 (21)	0.06 (5)	0.32 (26)

Table 5.7: Polarization data (continued)

E_γ	E_{gate}	$N_\perp$	$N_\parallel$	Asym	Pol
	907	783 (30)	668 (28)	0.08 (3)	0.42 (16)
	806	984 (40)	720 (36)	0.15 (3)	0.79 (16)
	1009	340 (19)	305 (17)	0.05 (4)	0.26 (21)
670	737	432 (28)	543 (30)	-0.11 (4)	-0.6 (2)
737	198	1295 (42)	999 (39)	0.13 (3)	0.76 (18)
	263	395 (28)	325 (26)	0.10 (5)	0.59 (29)
	407	556 (28)	395 (22)	0.17 (4)	1.00 (24)
	462	781 (32)	693 (30)	0.06 (3)	0.35 (18)
	896	1338 (38)	1214 (35)	0.05 (2)	0.29 (12)
	1082	771 (29)	690 (26)	0.06 (3)	0.35 (18)
759	737	581 (32)	580 (31)	0.00 (4)	0.0 (2)
	896	267 (24)	339 (22)	-0.12 (5)	-0.71 (29)
	1082	154 (13)	176 (13)	-0.07 (6)	-0.41 (35)
806	198	1251 (41)	1025 (37)	0.10 (2)	0.63 (12)
	208	396 (24)	330 (21)	0.09 (4)	0.56 (25)
	599	886 (34)	680 (31)	0.13 (3)	0.81 (19)
	907	615 (28)	564 (25)	0.04 (3)	0.25 (19)
	1009	391 (19)	356 (19)	0.05 (4)	0.31 (25)
	487	402 (22)	310 (20)	0.13 (4)	0.81 (25)
857	599	328 (46)	313 (28)	0.02 (8)	0.1 (5)
	806	507 (54)	496 (55)	0.01 (8)	0.1 (5)
862	598	488 (68)	344 (44)	0.17 (10)	1.1 (6)
896	407	368 (23)	296 (22)	0.11 (5)	0.69 (31)
	737	1702 (48)	1501 (46)	0.06 (2)	0.38 (13)
	1082	649 (26)	514 (23)	0.12 (3)	0.75 (19)
907	198	1034 (37)	876 (34)	0.08 (3)	0.50 (19)
	208	270 (21)	225 (19)	0.09 (6)	0.56 (37)
	599	960 (67)	847 (46)	0.06 (4)	0.37 (25)
	806	678 (39)	485 (38)	0.17 (5)	1.06 (31)
	1009	271 (17)	239 (16)	0.06 (5)	0.37 (31)
1009	599	542 (29)	396 (27)	0.16 (4)	1.14 (29)
	806	571 (30)	520 (30)	0.05 (4)	0.36 (29)

Table 5.7: Polarization data (continued)

E_γ	E_{gate}	$N_\perp$	$N_\parallel$	Asym	Pol
	487	368 (20)	389 (20)	-0.03 (4)	-0.21 (29)
1027	896	599 (27)	534 (25)	0.06 (3)	0.43 (21)
	1082	476 (22)	440 (22)	0.04 (3)	0.29 (21)
1082	737	1214 (44)	948 (40)	0.12 (3)	0.86 (21)
	896	880 (34)	765 (31)	0.07 (3)	0.50 (21)
1308	737+1082	397 (52)	373 (56)	0.03 (10)	0.2 (8)
1493	737+1082	286 (41)	243 (85)	0.08 (18)	0.7 (15)

[a] Clean matrices used (2a+2a1p)

The linear polarization is then related to the asymmetry through the sensitivity of the polarimeter Q, which for the Clover detectors placed at 90 degree on the EUROBALL spectrometer has been determined from the asymmetry of known transitions and compared with a calculation with the Monte Carlo method as mentioned in the previous chapter (4.6).

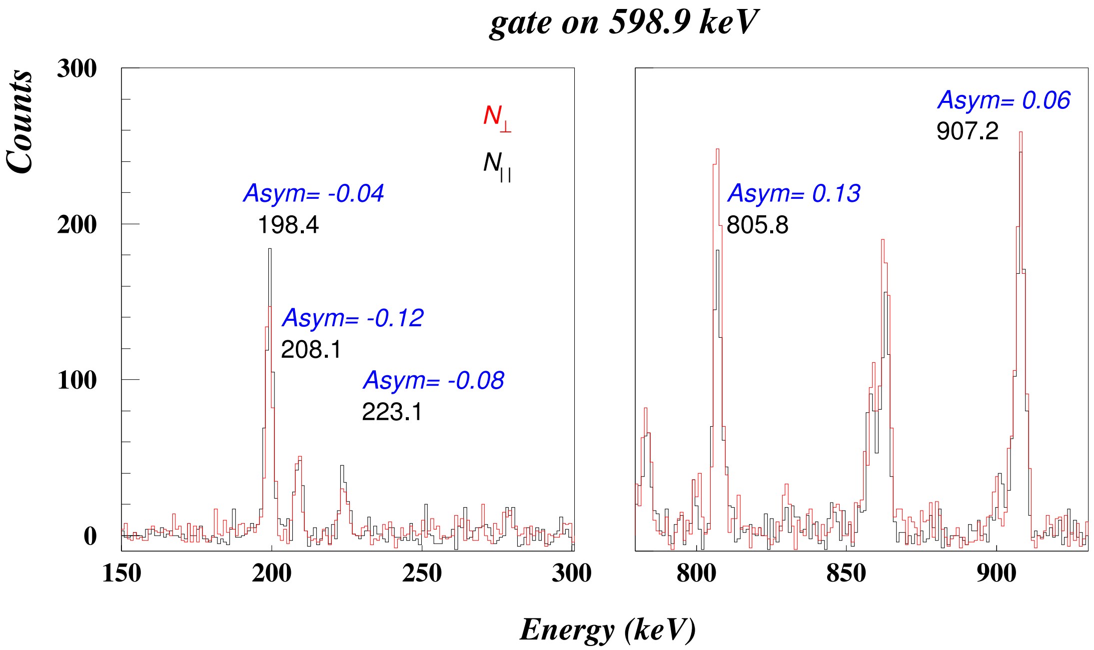

Figure 5.11: *Plot with the Clover gated spectra, parallel polarization (black) and perpendicular polarization (red). The gate is set on the 598.9 keV transition in the sum of all detectors.*

In figure 5.11 we show an example of the spectra obtained using this technique. From the comparison of the two spectra, corresponding to the scattering in capsules with perpendicular orientation relative to the beam direction and in parallel orientation, we can deduce the value of the asymmetry of the transitions by evaluating the areas of the peaks.

Then, by combining both analyses, DCO ratios and Polarization values of the γ-ray transitions, it is possible to solve some ambiguities in the assignment of spin-parity I^{π} to the states. Thus, for example, in the case of the 198.4 and 208.1 keV transitions, we have obtained the following values:

Table 5.8: Combined analysis of the DCO ratios and asymmetries for the 198.4 and 208.1 keV transitions.

I_i - I_f	E(keV)	R_{dco}	δ	Asym	Pol	δ
3/2 - 1/2	198.4	0.35 (3)	-0.19 (8)	-0.12 (5)	$-0.41\ (17)^m$	$-1.2\ (^{+3}_{-5})$
3/2 - 1/2			-1.1 (2)			-0.17 (15)
3/2 - 1/2						1.3 (2)
3/2 - 1/2						$2.3\ (^{+6}_{-2})$
5/2 - 3/2	198.4	0.35 (3)	-0.18 (6)	-0.12 (5)	$-0.41\ (17)^m$	$-1.7\ (^{+8}_{-20})$
5/2 - 3/2			-1.8 (2)			-0.03 (15)
5/2 - 3/2						1.3 (3)
5/2 - 3/2						$10\ (^{+20}_{-7})$
3/2 - 5/2	208.1	0.70 (10)	-0.3 (3)	-0.06 (10)	$-0.21\ (35)^m$	$-0.1\ (^{+5}_{-4})$
3/2 - 5/2			-2.0 (10)			$2.6\ (^{+180}_{-19})$
5/2 - 5/2	208.1	0.70 (10)	$-0.32\ (^{+14}_{-20})$	-0.06 (10)	$-0.21\ (35)^m$	$-4.0\ (^{+26}_{-500})$
5/2 - 5/2			$4.0\ (^{+10}_{-15})$			$-1.4\ (^{+9}_{-15})$
5/2 - 5/2						0.6 (3)
5/2 - 5/2						$1.0\ (^{+12}_{-4})$

^{m} Average value.

In the case of the 198.4 keV transition the possible delta values obtained from the DCO ratio that overlap with the delta values obtained from the linear polarization measurement agree with a 3/2→1/2 transition and with a 5/2→3/2. In the case of the 208.1 keV transition de-exciting the same level, only the 3/2→5/2 transition is compatible with DCO and polarization data (see figure 5.12), leading to the following spin assignments: g.s. 5/2, 9 keV 1/2 and 208 keV 3/2 spins with no change of parity among them. A final discussion on I^{π} assignments is given at the end of this chapter.

In the following table we have summarized all the results for the transitions observed in the ^{71}Br nucleus. The intensity correspond to the Euroball experiment where most of the intensity is collected, even below of the isomer. The A_2 A_4 coefficients of the angular distributions fitted where obtained for the transitions

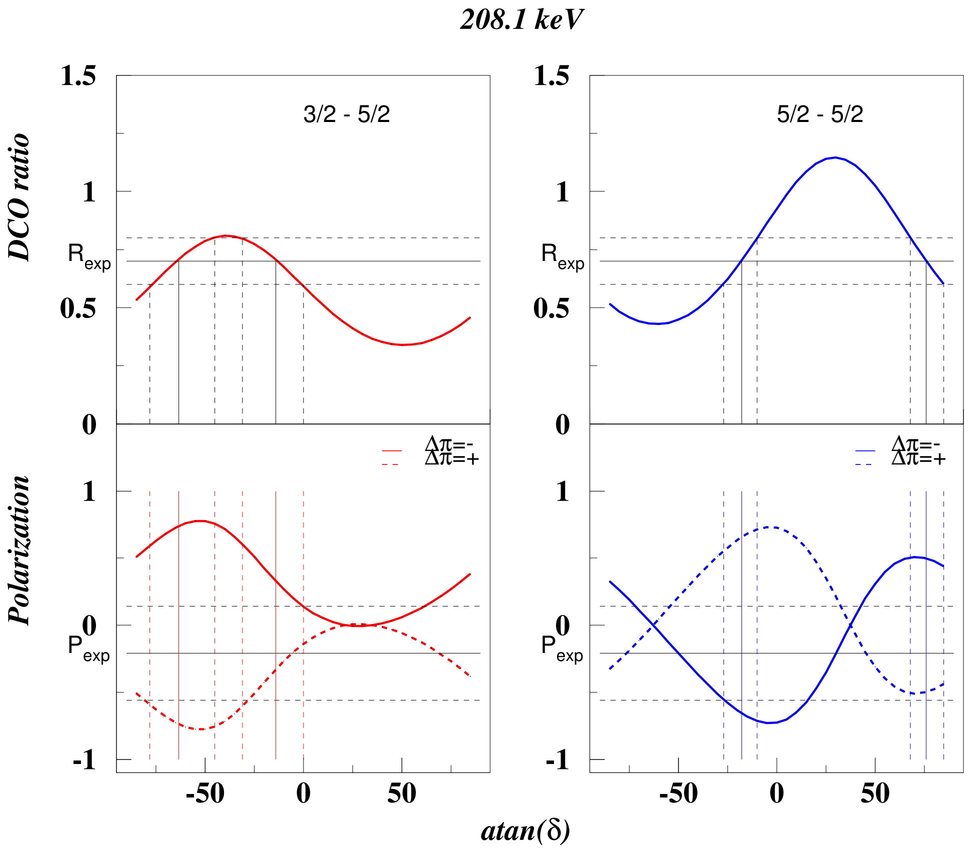

Figure 5.12: *Analysis of the DCO ratio and polarization values. The common δ values obtained for both data allow us to fix the amount of E2 in the mixed dipole 208 keV transition. Therefore a better assignment of I^π to the states.*

whenever was possible. The R_{dco} ratio and asymmetry value for the main transitions.

Table 5.9: Summary of the main results for the γ-ray transitions belonging to the ^{71}Br. Energies, intensities, DCO ratios, Angular ditributions and asymmetries from the EB experiment.

E_x (keV)	E_γ	I_γ	R_{DCO}	A_2	A_4	Asymm.	$I_i^\pi \rightarrow I_f^\pi$
9.7 (2)	not obs.						$1/2^- \rightarrow 5/2^-$
208.2 (2)	198.4	854 (30)	0.35 (3)			-0.17 (4)	$3/2^- \rightarrow 1/2^-$
	208.1	239 (15)	0.70 (10)			-0.04 (8)	$3/2^- \rightarrow 5/2^-$
407.3 (2)	199.5	42 (30)					$3/2^- \rightarrow 3/2^-$
	397.7	103 (20)	1.5 (2)[d]			<0	$3/2^- \rightarrow 1/2^-$
	407.3	203 (20)	1.1 (2)[d]			<0	$3/2^- \rightarrow 5/2^-$
615.9 (3)	208.9	30 (10)					$3/2^+ \rightarrow 3/2^-$
	408.1	145 (20)	1.4 (1)[d]			0.01 (4)	$3/2^+ \rightarrow 3/2^-$
670.2 (2)	54.3	107 (32)[a]					$5/2^+ \rightarrow 3/2^+$

Table 5.9: (continued)

E_x (keV)	E_γ	I_γ	R_{DCO}	A_2	A_4	Asymm.	$I_i^\pi \rightarrow I_f^\pi$
	263.1	122 (24)	0.31 (11)			0.10 (5)	$5/2^+ \rightarrow 3/2^-$
	462.2	359 (24)	0.65 (6)			0.002 (30)	$5/2^+ \rightarrow 3/2^-$
	669.8	261 (7)	0.98 (11)			-0.11 (4)	$5/2^+ \rightarrow 5/2^-$
759.6 (2)	89.8	456 (91)[b]					$9/2^+ \rightarrow 5/2^+$
	759.2	279 (3)	0.85 (8)			-0.12 (5)	$9/2^+ \rightarrow 5/2^-$
892.5 (2)	133.6	89 (4)[c]					$7/2^+ \rightarrow 9/2^+$
	223.1	135 (12)	0.87 (9)			-0.08 (12)	$7/2^+ \rightarrow 5/2^+$
	276.7	17 (10)					$7/2^+ \rightarrow 3/2^+$
929.4 (3)	522.4	47 (10)	1.0 (7)			>0	$5/2^- \rightarrow 3/2^-$
	721.5	40 (10)	0.8 (3)				$5/2^- \rightarrow 3/2^-$
	929.3	103 (10)	1.2 (4)			<0	$5/2^- \rightarrow 5/2^-$
952.0 (3)	952.2	127 (16)	0.6 (2)				$(7/2^-) \rightarrow 5/2^-$
1020.7 (5)	613.3	24 (4)					$(7/2^-) \rightarrow 3/2^-$
1115.3 (3)	907.2	407 (30)	1.09 (7)	0.334 (61)	-0.036 (82)	0.06 (4)	$7/2^- \rightarrow 3/2^-$
	1114.7	66 (10)					$7/2^- \rightarrow 5/2^-$
1175.3 (3)	282.1	45 (12)	0.6 (3)[d]				$9/2^+ \rightarrow 7/2^+$
	415.3	83 (3)					$9/2^+ \rightarrow 9/2^+$
	504.7	69 (12)					$9/2^+ \rightarrow 5/2^+$
1199.3 (7)	991.7	126 (18)	0.8 (3)				$(7/2^-) \rightarrow 3/2^-$
1492.1 (3)	316.4	38 (3)					$11/2^+ \rightarrow 9/2^+$
	598.3	168 (25)	2.5 (9)[d]				$11/2^+ \rightarrow 7/2^+$
1492.7 (4)	562.7	169 (4)	1.0 (6)			>0	$9/2^- \rightarrow 5/2^-$
1497.3 (3)	737.7	1000 (47)	1.19 (5)	0.255 (35)	-0.052 (46)	0.05 (2)	$13/2^+ \rightarrow 9/2^+$
1682.3 (6)	662.8	21 (4)					$(11/2^-) \rightarrow (7/2^-)$
1714.2 (3)	222.1	12 (5)					$11/2^- \rightarrow 9/2^-$
	514.5	105 (9)	0.6 (3)				$11/2^- \rightarrow (7/2^-)$
	598.9	389 (33)	1.16 (7)	0.402 (47)	-0.019 (64)	0.08 (3)	$11/2^- \rightarrow 7/2^-$
	762.0	113 (8)	0.89 (20)				$11/2^- \rightarrow (7/2^-)$
	955.0	113 (16)	0.4 (3)				$11/2^- \rightarrow 9/2^+$
1831.1 (5)	655.9	61 (6)					$(13/2^+) \rightarrow 9/2^+$
2217.7 (5)	724.5	146 (14)	1.3 (3)				$(13/2^-) \rightarrow 9/2^-$
2353.3 (6)	862.0	98 (11)	1.6 (14)[d]				$(15/2^+) \rightarrow 11/2^+$
2393.4 (4)	896.1	680 (30)	1.15 (5)	0.260 (34)	-0.067 (46)	0.06 (2)	$17/2^+ \rightarrow 13/2^+$
2478.6 (6)	764.2	52 (8)					$(15/2^-) \rightarrow 11/2^-$
	794.5	18 (3)					$(15/2^-) \rightarrow (11/2^-)$
2520.2 (3)	805.8	598 (46)	0.95 (6)	0.309 (52)	-0.120 (70)	0.04 (3)	$15/2^- \rightarrow 11/2^-$
2777.8 (7)	947.6	94 (20)					$(17/2^+) \rightarrow (13/2^+)$
3189.4 (5)	971.4	81 (9)	0.9 (3)				$(17/2^-) \rightarrow (13/2^-)$
3377.9 (4)	857.1	134 (20)	0.35 (14)	-0.716 (91)	<<0	0.01 (8)	$17/2^- \rightarrow 15/2^-$
	899.3	140 (30)					$17/2^- \rightarrow (15/2^-)$
3475.7 (5)	1082.2	470 (32)	0.95 (6)	0.158 (35)	-0.094 (49)	0.12 (3)	$21/2^+ \rightarrow 17/2^+$
3529.8 (4)	1009.0	323 (30)	0.68 (15)	0.142 (56)	-0.167 (76)	0.05 (4)	$19/2^- \rightarrow 17/2^-$
3829.3 (5)	1051.5	56 (18)					$(21/2^+) \rightarrow (17/2^+)$
4017.1 (4)	487.2	114 (7)	0.38 (12)	-0.437 (56)	0.005 (84)	-0.04 (5)	$21/2^- \rightarrow 19/2^-$
	638.8	96 (15)	0.5 (4)				$21/2^- \rightarrow 17/2^-$
4311.8 (4)	781.9	81 (8)	0.7 (3)				$(21/2^-) \rightarrow 19/2^-$
	933.7	81 (11)					$(21/2^-) \rightarrow 17/2^-$

Table 5.9: (continued)

E_x (keV)	E_γ	I_γ	R_{DCO}	A_2	A_4	Asymm.	$I_i^\pi \rightarrow I_f^\pi$
	1123.1	59 (6)					$(21/2^-)\rightarrow(17/2^-)$
4503.4 (5)	1027.7	304 (22)	1.01 (10)	0.274 (39)	-0.173 (53)	0.06 (3)	$25/2^+\rightarrow21/2^+$
4742.1 (6)	1212.5	75 (10)					$(23/2^-)\rightarrow19/2^-$
4968.9 (7)	1493.5	102 (24)	0.9 (3)			0.08 (18)	$25/2^+\rightarrow21/2^+$
5375.7 (5)	633	43 (4)					$(25/2^-)\rightarrow(23/2^-)$
	1063.8	111 (10)					$(25/2^-)\rightarrow(21/2^-)$
	1358.4	67 (10)					$(25/2^-)\rightarrow21/2^-$
5811.6 (7)	842.6	46 (10)					$(29/2^+)\rightarrow25/2^+$
	1308.2	97 (8)	0.6 (5)			0.03 (10)	$(29/2^+)\rightarrow25/2^+$
6612.8 (6)	1237.7	152 (15)					$(29/2^-)\rightarrow(25/2^-)$
7714.9 (7)	1101.9	114 (15)		0.35 (5)	-0.10 (8)		$(33/2^-)\rightarrow(29/2^-)$

[a] $I_{tot}=I_\gamma(1+\alpha_t)=177$ (26) (M1 is assumed)
[b] $I_{tot}=$ 1067 (212) (E2 is assumed)
[c] $I_{tot}=$ 94 (5) (M1 is assumed)
[d] R_{DCO} value with gate on dipole transition.

5.4 Lifetime measurement: The isomeric $g_{9/2}$ state

The lowest single-particle orbitals in this mass region are the closely spaced $p_{1/2}$, $p_{3/2}$ and $f_{5/2}$ and the somewhat higher $g_{9/2}$ states. The proximity of the $g_{9/2}$ to the low-lying negative parity orbitals of the fp shell induce a change in the structure of the nucleus due to the different features of both kind of orbitals positive parity and high-j against negative parity and low-j. This produces an isomeric $9/2^+$ state in many of the odd-A nuclei in this mass region since the most favourable decay is a relative low-energy M2 transition (or an E2).

In the previous study on high spin states of ^{71}Br, the isomer state was deduced at an excitation energy of 759.8 keV and the lifetime value was deduced based on the coincidences. In their article, Arrison *et al.* report a value of $T_{1/2}$=32.5±2.5 ns for the isomeric state. In our study, using the data obtained with the GASP γ-spectrometer we have created a cube with E_γ-E_γ-ΔT, where ΔT means the time differences between the γ transitions in coincidence. Then, selecting a gate with the prompt yrast transitions (737.7, 896.1 and 1082.2 keV) we have extracted a matrix E_γ-ΔT. Then by gating on the transitions below the isomer we get a time spectrum with the lifetime of the level. Thus, puting a gate on 759 keV transition we have obtain this kind of time spectrum, and fitting an exponential curve we have obtain a half life value for the $9/2^+$, see figure 5.13. Then, puting a gate on the transition de-exciting the 670 keV state we obtained a new time spectrum which in principle is composed by the lifetimes of the 759 and the 670 keV states. Here, fitting a more complex exponential function given by the Bateman equations

$$N(t) = N_0 \frac{\lambda_1}{\lambda_2 - \lambda_1} \cdot (e^{-\lambda_1 t} - e^{-\lambda_2 t}) \tag{5.6}$$

where λ_1 is the decay probability of the first isomeric state and λ_2 is the decay probability of the second isomeric state.

From the fits we have obtained the following values for the half life of the states:

E_x(keV)	$T_{1/2}$ (ns)
759	32 (10)
670	2 (2)

which agree with the previuosly obtained by Arrison et al. These fits have been shown in the following figure.

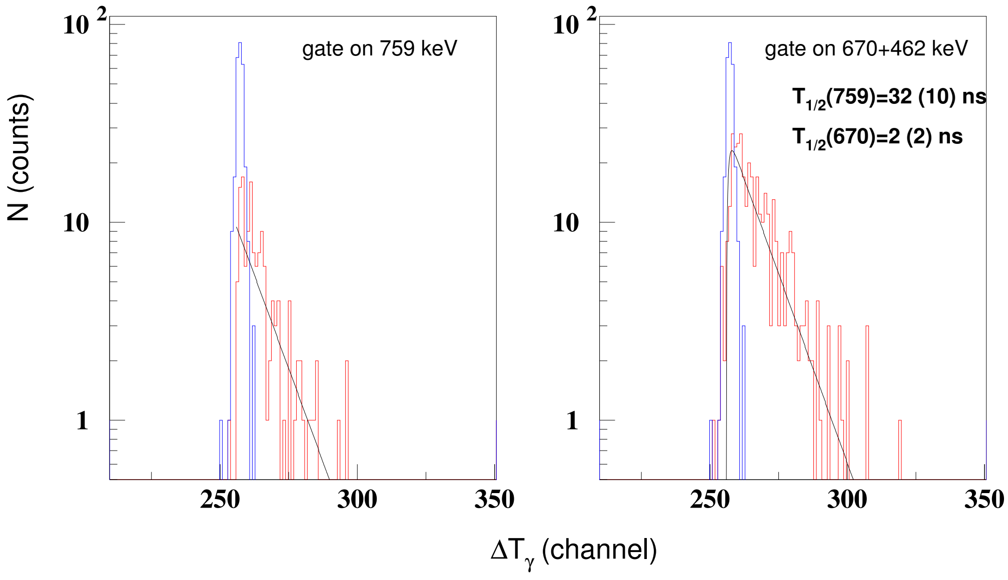

Figure 5.13: *Plots with the fit to the time spectra (red) obtained by gating on 759 kev transition (right panel) and gating on 670 and 462 keV transition de-exciting the 670 keV state. The prompt time spectrum is also shown (blue) for reference. The time calibration was 0.25 ns/chan.*

5.5 The I^π level assignments.

One difficulty we have encountered here is to evaluate the deviation of the DCO values from the expected theoretical value due to the de-alignment produced by the 32 ns isomer. In order to take into account this problem we have systematically compared the values obtained in ^{71}Br with the very similar ^{73}Br case ($T_{1/2}$=1.1 ns for the $9/2^+$ state at 473.6 keV and $T_{1/2}$=35.0 ns for the $(3/2,5/2)^-$ state at 240.5 keV) where one has internal conversion data [Hee90], except for the 759 keV M2 transition which has no equivalent in ^{73}Br.

The 759.6 keV state.
As mentioned at the beginning of this chapter, in the following we will assume that the $9/2^+$ assignment to the 759 keV level is correct.

The ground state.
The ground state spin parity of the ^{71}Br was known to be $(3/2,5/2,7/2)^-$ from the β-decay work to the daughter nucleus ^{71}Se [Hag82], which ground state was known to be a $5/2^-$ from an experiment on $n\gamma\gamma$-coincidences. In the work of Arrison *et al.* [Arr90], they assign an I^π value of $5/2^-$ consistent with the M2 character of the 759.2 keV deduced from angular correlations.

In our work, we have obtained a DCO ratio value of $R_{dco}(737,759) = 0.85(8)$ compatible with a pure quadrupole nature as well as a mixed dipole-quadrupole nature for the 759.9 keV transition. But from the negative value obtained for the polarization value, it is clear that the transitions should be either an M2 or M1/E2. Since the parity of the ground state has been fixed to have negative parity we conclude that the ground state of ^{71}Br is a $5/2^-$, in accord with the previous $I\pi$ assignment [Arr90] based on less conclusive data (no polarization).

I_i - I_f	E(keV)	R_{dco}	δ	Asym	Pol	δ
9/2 - 7/2	759.2	0.85 (8)	0.32 $(^{+4}_{-9})$	-0.12 (5)	-0.71 (29)	0.46 $(^{+30}_{-40})$
9/2 - 7/2			$\sim$ 10	-0.07(6)	-0.41(35)	0.08 $(^{+38}_{-20})$
9/2 - 7/2		1.4 (2)	1.2 $(^{+9}_{-6})$			1.7 $(^{+11}_{-7})$
9/2 - 5/2	759.2	0.85 (8)	-0.18 (9)	-0.12 (5)	-0.71 (29)	0.09 $(^{+27}_{-8})$
9/2 - 5/2			-6 $(^{+2}_{-5})$			0.7 $(^{+5}_{-3})$
9/2 - 5/2		1.4 (2)	0.46 $(^{+50}_{-20})$	-0.07(6)	-0.41(35)	-0.17 $(^{+26}_{-30})$
9/2 - 5/2			1.9 $(^{+18}_{-9})$			1.2 $(^{+5}_{-5})$
9/2 - 5/2						-1.3 $(^{+6}_{-99})$

The 670.1 keV level.
This level is fed by the 89.7 keV transition from the 760 keV $9/2^+$ level. Since in this case we have no information from DCO or polarization we will try to estimate the nature of this transition from intensity balance arguments.

- Assuming 89.7 keV transition is an E1 the conversion coefficient would be $\alpha_t = 0.118$ and therefore $I_{tot} = 510(101)$
- For an M1 the conversion coefficient would be $\alpha_t = 0.156$ and therefore $I_{tot} = 527(105)$

- For an E2 the conversion coefficient would be $\alpha_t = 1.34$ and therefore $I_{tot} = 1067(213)$

Table 5.10: Transition probabilities in W.u. for transitions de-exciting the $9/2^+$ isomer state in the A∼70 mass region. The data are taken from the ENSDF web site ($http://www.nndc.bnl.gov/ENSDF$) and from the present work.

Z	A	$E_{9/2^+}$(keV)	$T_{1/2}$ (ns)	E_γ(keV)	I_f^π	B(XL) (W.u.)
37	75	610			$(5/2)^+$	
37	77	331.7	0.687 (25)		$5/2^+$	B(E2)∼ 60
37	79	96.7	18 (4)		$5/2^+$	B(E2)=84 (19)
36	75	377.8	13.9 ps	377.8	$5/2^+$	B(E2)=77 (8)
36	77	279.0	133 (7) ps	279.0	$5/2^+$	B(E2)=15 (2)
35	71	759.6	32.5 (25)	89.7	$5/2^+$	B(E2)=57 (15)
				759.1	$5/2^-$	B(M2)=0.055 (10)
35	73	473.3	1.1 (2)	187.5	$5/2^+$	B(E2)=115 (21)
35	75	220.8	31.7(3)	88.3	$5/2^+$	B(E2)=75.6 (7)
35	77	106	4.28min	105.8	$3/2^-$	B(E3)=0.122(5)
34	69	573.9	960 (23)	534.5	$5/2^-$	B(M2)=0.044(1)
34	71	260.5	19 μs	260.5	$5/2^-$	B(M2)=0.079 (13)
33	67	1422.4	12 (2)	319	$7/2^-$	B(E1)= 3.1 (5) x 10^{-7}
				725	$7/2^-$	B(E1)= 0.5 (1) x 10^{-7}
				1422	$5/2^-$	B(M2)= 2.9 (6) x 10^{-3}
33	69	1306.8	1.35 (4)	442.9	$7/2^-$	B(E1)=1.58 10^{-6} B(M2)=0.06
				1306.7	$5/2^-$	B(M2)=0.177 (6) B(E3)=0.6(5)
33	71	1000.2	19.8 (3)	1000.2	$5/2^-$	B(M2)=0.091(1)
32	65	1216	7 (1)	325.8	$7/2^-$	B(E1)=5.8 (8) x 10^{-7}
				1104.8	$5/2^-$	B(M2)=0.111 B(E3)=0.091
32	67	751.7	110.9 (14)	733.5	$5/2^-$	B(M2)=0.079 (1)
32	69	397.9	2.81μs	397.9	$5/2^-$	B(M2)=0.0657 (12)

Requiring that the intensity feeding the $9/2^+$ state, I(737+133+415)=1177 (48), should be less or equal to the total intensity de-exciting the state, allow us to rule out the E1 or M1 possibilities. In conclusion the 89.7 keV transition is an E2 (an M2 is ruled out by half life arguments). This fix the I^π of the 670 keV level as $5/2^+$

Another argument supporting the I^π assignments of the ground state, the 670 and the 760 keV levels is the partial half life and the corresponding reduced transition probabilities:

$$\begin{aligned} P_\gamma(E2, 89.7) &= \frac{ln2}{32.5\times10^{-9}}\,\frac{456}{1417} \approx 6.9\times10^6 \\ P_\gamma(M2, 759.1) &= \frac{ln2}{32.5\times10^{-9}}\,\frac{350}{1417} \approx 5.3\times10^6 \end{aligned} \tag{5.7}$$

$$B(XL) = \frac{L[(2L+1)!!]^2\hbar}{8\pi(L+1)}\left(\frac{\hbar c}{E_\gamma}\right)^{2L+1} P_\gamma(XL) \tag{5.8}$$

Using eq. (5.8) and the Weisskopf estimate we can deduce for both transitions:

$$\begin{aligned} B(E2, 89.7) &= 57(15)\ W.u. \\ B(M2, 759.1) &= 0.055(10)\ W.u. \end{aligned} \tag{5.9}$$

that agree with the values found in the literature for the similar transitions in the nuclei of the mass region $A \sim 70$ as we can see in the table 5.5.

The 9.7, 208.2 and 407.3 keV level states.

The level at 670.1 keV decays by three transitions: 669.8, 462.1 and 263.1 keV which agree with E1 not-stretched for the first one and E1 stretched nature for the other two transitions. Very similar transitions are observed in ^{73}Br, there they de-excite the level at 286.1 keV through the transitions 259.2, 108.0 and 45.6 keV. Based on the remarkable similarity between these two cases (see table 5.5 and the agreement with our DCOs and polarization values, we assign $3/2^-$ to both levels at 208 and 407 keV. The DCO and polarization of the 669.8 keV also corroborates the $5/2^+ \rightarrow 5/2^-$ transition.

The 9.7 keV level was not fixed in the previous work of Arrison and could be placed at 10 or 198 keV. Here, using the 397.7 and 407.4 keV transitions we fixed the excitation energy at 9.7 keV. The two dipoles de-exciting the 208.2 and 407.3 keV levels agree with the $3/2^-$ assignment and at the same time fix the 9.8 keV level as $1/2^-$.

Table 5.11: Comparison between ^{73}Br and ^{71}Br low-lying states

	^{73}Br				^{71}Br			
Gate	I_i	I_f	E_γ	R_{DCO}	I_i	I_f	E_γ	R_{DCO}
Q	$5/2^+$	$5/2^-$	259.2	0.70 (10)	$5/2^+$	$5/2^-$	669.8	0.98 (11)
prompt-delayed		$3/2^-$	108.0	0.33 (5)		$3/2^-$	462.1	0.65 (6)
		$3/2^-$	45.6	0.57 (10)		$3/2^-$	263.1	0.31 (11)
Q	$3/2^-$	$5/2^-$	151.2	0.50 (3)	$3/2^-$	$5/2^-$	208.0	0.70 (10)
prompt-prompt		$1/2^-$	177.9	0.35 (5)		$1/2^-$	198.3	0.35 (3)
D	$3/2^-$	$5/2^-$	151.2	1.60 (20)	$3/2^-$	$5/2^-$	407.1	1.1 (2)
delayed-delayed		$1/2^-$	177.9	1.26 (12)		$1/2^-$	397.4	1.5 (2)

Then, the level at 208 keV is fed by a sequence of quadrupole transitions 907 and 598 keV transitions. Parallel to this two transition de-exciting the 1714.2 level there is a sequence of transitions that combines the 761.7 keV quadrupole and the 952.0 keV dipole transitions, deduced from the DCOs of $R_{dco}(761, 806) = 0.89(20)$ and $R_{dco}(952, 806) = 0.6(2)$. The best way to combine this two sequences, assuming the $I^\pi = 5/2^-$ of the ground state is to assign $I^\pi = 3/2^-$ to the 208.2 keV level and then $I^\pi = 1/2^-$ to the 9.7 keV level.

The 407.3 keV level was not observed in the previous work [Arr90] and here, it appears clearly in the delayed coincidences by observing the transitions 397.7 and 407.4 keV when gating on 89.8 or 263.2 keV transitions and not when gating on 198 keV transitions.

The 615.8 keV state.
This level is deduced from our data by observing the 278.2 keV γ-ray transition as a link to the 893.2 state and then confirmed from the triple-γ coincidence data by observing the 278.2 keV transition together with 223.1 and the 54 keV transitions in the double gated spectrum of 598.3 and 408.1 keV transitions. The 278.2 keV gamma peak disappear in the double gated spectrum of 54 and 408.1 keV transitions.

The key transition to define the I^π of this level is the 54 keV feeding transition and the question is if it has M1 or E1 character. From the point of view of the intensity balance and considering that $\alpha_T(54, M1) = 0.65$ and $\alpha_T(54, E1) = 0.52$, both solutions are possible (and no other, for instance an E2 is impossible). However, if 54 keV transition were an E1 it would have 300 times more Weisskopf units that the other three E1 transition de-exciting the same level. We therefore prefer an M1 assignment to this transition which suggest the I^π of the 615.8 keV level to be $(3/2, 5/2, 7/2)^+$.

The only information we have from the transitions de-exciting this level is the DCO of the 408 keV transition, $R_{dco}(408, 198) = 1.4(1)$. This would agree with $3/2^+$ or $5/2^+$, we exclude the M2 character for the 408 and therefore rule out the $7/2^+$ possibility.

The DCO ratio of the 408.1 transition obtained $R_{dco}(408, 198) = 1.4(1)$ is consistent with a dipole or mixed D+Q transition and therefore, I^π of the state can take values of 3/2 or 5/2. The result from the experimental asymmetry A=-0.05 (19), is consistent with a transition between 3/2-3/2 states and $\delta = -0.14(4)$ but also between a 5/2-3/2 states with $\delta = 8(1)$. However, the latter case means almost quadrupole transition. So, an dipole transition with $\Delta I = 0$ is the best suggestion which provide an spin assignment of $3/2^{(+)}$. The positive parity is not clear due to the large error, so an M1 character is not ruled out.

The 893.2 keV state
The level placed at 893 keV excitation energy is supported by the coincidence observed between the 223.1 and the 669.8, 462.2 and 263.2 keV gamma-ray transitions de-exciting the $5/2^+$ state. From the DCO ratio observed for the 223 keV transition $R_{dco}(223, 598) = 0.87(9)$ a mixed M1/E2 is deduced which is compatible with other R_{dco} values (see table 5.5). Thus the suggested spin assignment from these data is a $7/2^+$.

The 1497.3, 2393.4, 3475.7, 4503.4, 4969.1 and 5811.6 keV states of the yrast band.
These states have been associated to the $\pi g_{9/2}$ rotational band. They are connected

through a sequence of E2 transitions except in the case of the 842 for which the low statistics do not allow evaluate properly its DCO ratio to confirm its multipolarity. The quadrupole nature of these transitions have been deduced from the DCO ratios, which values are close to 1, and from the angular distribution coefficient A_2 and A_4 of the most intense transitions in the band. The positive values obtained from the experimental asymmetry allow us to fix the electrical character of the transitions, that follows a similar trend as in other light bromine isotopes.

The 1175.3, 1831.2, 2777.8 and 3829.3 keV states.
These states have been associated as members of a new band following the observation of the 655.9, 947.0, 1051.5 and 1139.6 keV transitions on the single gate spectra when gating on 223.1 and 282.1 keV transitions. Then by using the triple coincidence data the sequence has been confirmed even though the reduced statistics. Unfortunately only the DCO values for the 223 and 282 keV transitions were possible to obtain, they suggest $9/2^{+}$ assignment to the 1175 keV state. The parity of the band is assumed based on the fact that no communication with the negative bands have been observed, as in the other light bromine isotopes.

The 1492.1, 2353.3 and 3434.4 keV keV states.
Analogously, the presence of the 598.3, 861.9 and the 1081.1 keV transitions in the single gated spectrum of the 223.1 γ-ray and in the double gated spectra on the 223 and 598 keV transitions have allowed us to extend the other band to these states. The DCO ratio value of the 223.1 keV transition and the regular increasing in energy suggest a ΔI=2 rotational band. No extra information about the multipolarity of the upper transitions have been obtained from the DCO matrices due to the low statistics.

The 1115.3, 1714.2, 2520.2 and 3529 keV states.
In the previous work of Arrison *et al.* three states were deduced at 806, 1611 and 2518 keV excitation energy and tentatively assigned as the $7/2^{-}$, $11/2^{-}$ and $15/2^{-}$ members of the rotational band with $K = 3/2^{-}$. From our data and based on the γ-γ and γ-γ-γ particle gated coincidences we have modified the energy of these states and the relative ordering of the de-exciting transitions, in addition we have extended the band. Thus, we can either locate the 598 keV transition or the 907 keV transition feeding the yrast $3/2^{-}$ level; we prefer the later after the observation of the 1115.3 keV transition in coincidence with the 598.9 and 805.8 keV transitions and not with the 907.2 keV transition, see figure 5.14. We assign $I^{\pi}=7/2^{-}$ to this level based on the DCO, angular distribution coefficients and polarization data.

The following state is inferred at 1714.2 keV by the presence of several transitions (515, 598, 762 and 954 keV) de-exciting the level and observed in coincidence with the 805.8 keV transition feeding this state. The absence of these transitions in the γ gated spectra on 907.2 keV confirm our assumptions. The spin suggested for this level is $11/2^{-}$ based on the E2 character of the 598 keV transition supported by the

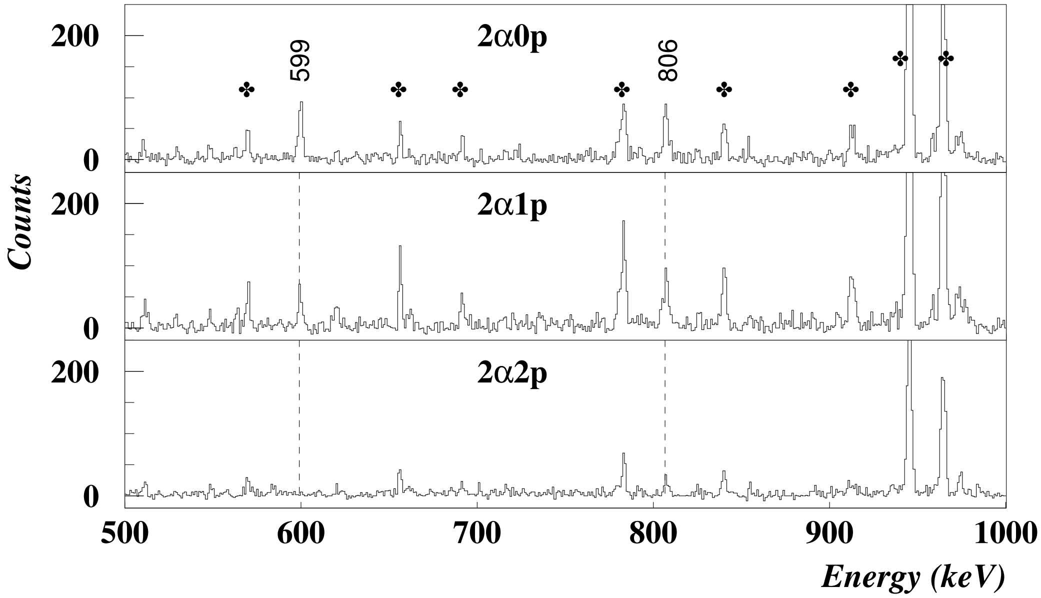

Figure 5.14: *Gamma spectra gated on the 1115 keV transition for different charged particle condition. Transition belonging to the* ^{70}*Se are labeled with the symbol. The coincidence with the 598.9 and 806.7 keV transitions support his presence in the* ^{71}*Br.*

DCO, polarization and angular distribution data.

The state at 2520 keV excitation energy is de-excited through the 806 keV transition which E2 character is deduced from the correlation data and suggests an I$^\pi$=15/2$^-$ for the level. Finally, the state at 3529 keV is de-excited through the 1009.0 keV γ-ray transition and has been assigned as I$^\pi$=19/2$^-$ from the DCO ratios and the $A_{2,4}$ angular distribution coefficient values of the 1009 keV transition. The negative parity assignment is also supported by the experimental asymmetry values obtained from the clover data, see table 5.7.

The 4017, 4311, 4742 and 5375 keV states

From the triple coincidence data and following the observation of three parallel sequences of gamma transitions 487.2 - 1358.3, 781.9 - 1063.8 and 1212.5 - 633.1 keV in coincidence with the 1009 and 806 kev transitions, it has been possible to extend the negative parity sequence of levels above the 3529 keV state. Thus, these three sequences allow to fix the state at 5375 keV excitation energy. The intermediate state at 4017 keV energy is corroborated by the presence of the 638 keV linking transition. Similarly the state at 4311 keV is fixed by the 933 and 1122 keV transitions connecting other states. The placement of the state at 4742 keV has been inferred from the intensity of the transitions of the corresponding sequence (see level scheme fig 5.1).

The DCO ratio $R_{dco}(487, 806) = 0.38(12)$ and the angular distribution coefficients $A_2 = -0.437(56)$ of the 487 keV transition, see fig 5.8, support the mixed M1/E2 character and allow to assign a $21/2^-$ spin value to the 4017 keV state. The 4311 keV state is also tentatively assigned as a $21/2^-$ from the DCO ratio of the 781 keV transition. Unfortunately the data do not provide any information on the I^π of the 5375 keV level, from there we omit I^π assignment

The 6613 and 7714 keV states

These levels placed above the precedent states are de-excited by the 1237 and 1101 keV gamma rays which DCO values suggest a sequence of E2 transitions.

The 1020, 1682, 2478 and 3378 keV states

These states are connected by a sequence of transitions 662, 793 and 899 keV. The poor statistics do not allow to deduce DCO ratio for these transitions and thus to establish the spin of the states. The spin of the 3378 state is suggested as $17/2^-$ based on the mixed dipole character of the 857 keV transition. The I^π written in the level scheme are based on energy assignments.

The 930.0, 1492.7, 2217.7, 3189.4 and 4365.0 keV states.

The 930 keV state has been stablished by the de-excitation through three pathways, the coincidence of the 522.4 with the 407.4, 397.7 and 199.6 keV transitions, the coincidence of the 721.5 with the 198.4 and 208.1 keV transitions and the direct 929.3 keV cross-over transition. The DCO value $R_{dco}(929, 563) = 1.2(4)$, fixes the 929 keV transition as a quadrupole or a non-stretched dipole. Considering the other two branches of the level and the fact that J=1/2 is unprobable (too much above the yrast) we assign 5/2 to this level.

From the coincidences with the previously mentioned transitions a new band has been built by observing the sequence of 563, 724, 971 and 1174 keV γ-ray transitions in the triple coincidences. The DCO ratios of them support the ΔI=2 character of the band, making possible an spin assignment of 9/2, 13/2 and 17/2 spin values. The parity of the band is suggested to be negative by comparison with similar bands observed in other odd-A bromine isotopes. The band seems to continue up to 21/2 spin and is connected through the 1123 keV transition to the previously discussed band.

Chapter 6

Interpretation of the Level Scheme of ^{71}Br. Conclusions.

In this chapter, we will try to summarise the main results obtained from the various experiments performed and show how these results can allow us to establish the features and structure of the nucleus considered. The analysis of this structure, through comparison with similar nuclei and within the context of theoretical models, allows us to describe the physics behind the gamma spectroscopy phenomena observed in the ^{71}Br nucleus.

6.1 Introduction

The properties of the ground states of the nuclei in this mass region are characterised by rapid changes with the number of nucleons, mainly due to the low density of levels in the Nilsson diagram. Another interesting aspect is the variety of ground state shapes that appear in a relatively small part of the Segrè chart: spherical, prolate and oblate. Several calculations have shown that for nuclei with neutron or proton number equal to 38-40 the prolate deformation dominates; these particle numbers correspond to gaps in the single-particle energy spectrum. Thus neutron-deficient isotopes of Rb, Sr, Y and Zr show typical examples of good prolate rotors. For N,Z=34,36 oblate deformation has been predicted in the same calculations, related to the gaps for these particle numbers. As a consequence of this variety of nuclear shapes in neighbouring nuclei it may also happen that in the same nucleus different shapes co-exist. This is both very interesting and a challenge because one needs a great variety of experimental information to disentangle the problem.

In order to get a good description of the changes in ground state deformation as a function of nucleon number and to provide precise limits for the different regions of deformation, quadrupole measurements provide the most direct information. A good example is the quadrupole moment determination of the Kr isotopes obtained by Keim *et al.* [Kei95] using the technique of collinear fast-beam laser spectroscopy at the ISOLDE facility of CERN. The quadrupole measurement together with spins and radii offer a wide perspective of the changes in structure with the number of neutrons. This kind of measurement is not always possible, particularly when the isotopes cannot be produced in a clean way (without isobaric contaminants). In these cases other kinds of technique providing information on other observables should be employed to get information about the shapes. For instance, nuclear magnetic dipole moment measurements provide information mainly about the configuration of the ground state, and looking at the Nilsson diagram one can draw conclusions about the deformation.

Another alternative method recently used is based on β-decay studies. As has been shown by Hamamoto *et al.* [Ham95] and later by Sarriguren *et al.* [Sar98], the distribution of the strength observed in the β-decay as a function of the energy depends on the deformation of the parent nucleus.

In the next section, we will show the information presently available about deformation in the Br nuclei and how our data can help to understand it better and to make a comparison with the calculations available.

6.2 The low-lying states.

In the present work we have considerably increased our knowledge of the low-lying intrinsic states in ^{71}Br. In the previous spectroscopic experiment [Arr90] only the low-lying excited states with 9, 208, 263, 670 keV and 759 keV excitation energy were identified. From our results we have observed the states at 9, 208, 670 and 759 keV but not the 263 keV state. In addition, we have identified two other excited states at 407 and 615 keV excitation energy, see figure 5.2. Therefore we have modified considerably the low-lying spectrum.

The intrinsic states of the odd-A nuclei in the deformed regions are mainly determined by the Nilsson orbits ($\pm\Omega$) occupied by the odd nucleon [Rin80]. Thus, in this mass region they originate from the occupation of the following single particle orbits: $p_{3/2}$, $f_{5/2}$, $p_{1/2}$ and $g_{9/2}$. Then, because of the negative parity character of the $pf_{5/2}$ orbits and their proximity in energy, we can expect that the wave functions of the observed states consist of mixed configurations of these occupied orbits.

From a first inspection of the Nilsson diagram (see fig 1.1) it seems really difficult to combine the available Nilsson orbits for 35 protons with the ordering observed in our level scheme considering only one kind of deformation. In fact, from calculations and experimental data in nuclei of this region, shape coexistence has been proposed (observed) in order to explain the behaviour at low spin of some observed rotational structures, mainly in even-even nuclei but also in odd-A nuclei. We will try to combine information from the nuclear magnetic dipole moments, beta decay and from our own data in order to draw a picture of the possible configurations involved in the low-lying states.

6.2.1 Magnetic moments and shape coexistence.

In a previous work on nuclear magnetic dipole moments, the question of the spin of the ground state for the odd-A Br isotopes was addressed. The ground state spins for the odd-A $^{75-87}$Br isotopes are all $I^{\pi}=3/2^{-}$. This is interpreted as the last proton occupying the Nilsson orbital [301]3/2 for deformations $\varepsilon < 0.22$ and [312]3/2 for larger prolate deformations. Using the fact that the magnetic dipole moments of these two configurations differ by a factor of 3 one can deduce information about the single-particle configuration ([301] or [312]) and hence the approximate deformation of the ground state.

In the particular case of the ^{73}Br isotope the lack of anisotropy in the measurements of the magnetic dipole moments allowed the assignment of $I^{\pi}=1/2^{-}$ to the ground state. This different assignment with respect to the heavier odd-A isotopes was also supported by comparison with the low-lying states of ^{71}Br provided by the work of Arrison *et al.* The position and I^{π} of these states in ^{71}Br have also been confirmed in our work.

In order to understand the differences in the ground state and the lowest-lying levels of ^{71,73}Br nuclei relative to heavier odd-A bromine isotopes, the authors of [Gri92] then studied the experimental data available with the help of the Lund Particle Triaxial Rotor model. The calculations were performed with two kinds of single-particle potential: the modified oscillator (MO) with two set of parameters and the Woods-Saxon potential (WS). The results were very satisfactory because they agreed with the experimental values of magnetic and quadrupole moments available for the odd-A bromine isotopes and with the prolate configuration [301]3/2 or [312]3/2 for the ground state of $^{75-81}$Br depending on the deformation. Then, they used the same model to reproduce the lowest levels in the lightest odd-A isotopes. Thus, in both nuclei, the first three states are $1/2^{-}$, $5/2^{-}$ and $3/2^{-}$ with a very small energy difference between the first two states. By requiring in the calculations with the modified oscillator (PTR-MO), first a sequence of levels of $1/2^{-}$, $5/2^{-}$ and $3/2^{-}$ in ^{73}Br and $5/2^{-}$, $1/2^{-}$ and $3/2^{-}$ in ^{71}Br, and secondly the fact that the first excited state is very low in energy, the model gave as the best solution a low value for the ε_2 deformation parameter and $\gamma=60^{o}$. In other words, these states can be interpreted only in terms of oblate deformation. See fig. 6.1.

Hence, as a result of the calculation they suggest the following description for the low-energy levels in $^{71-81}$Br isotopes. Going from ^{81}Br to ^{75}Br there is a smooth change in prolate ground state structure from [301]3/2 to almost pure [312]3/2 configuration with the deformation increasing at the same time. In contrast, the structure of ^{73}Br can be understood in terms of shape co-existence between a less deformed oblate ground state and first excited state, and a more deformed prolate $3/2^{-}$ yrast band. The oblate $5/2^{-}$ and $1/2^{-}$ states agree well with the calculations for the Se isotopes (oblate), and the prolate $3/2^{-}$ agrees well with the corresponding Kr core (prolate). A second 3/2 state is observed in ^{73}Br at 241 keV excitation energy which is not discussed in Griffiths *et al.*'s paper. But since their calculations predict an oblate $3/2^{-}$ level we interpret the second 3/2 in ^{73}Br as this oblate state.

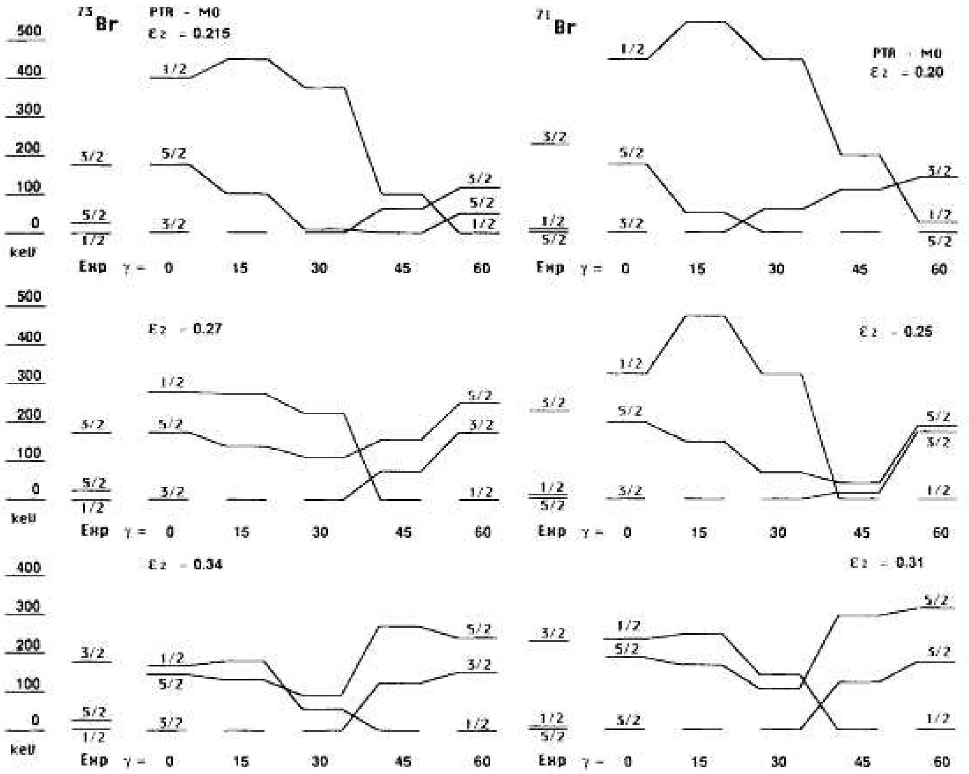

Figure 6.1: *Position of the* $\frac{1}{2}^-$, $\frac{3}{2}^-$ *and* $\frac{5}{2}^-$ *intrinsic states in* ^{71,73}*Br calculated with the PTR-MO model. Figure taken from [Gri92].*

The nucleus ^{71}Br is slightly different. In this case the 5/2, 1/2 and 3/2 order can be explained as a result of the calculations of Griffiths *et al.* for oblate states. We think the first $3/2^-$ level at 208 keV excitation energy is in this case the oblate $3/2^-$ because the observed prolate band built on the $3/2^-$ bandhead in ^{73}Br-^{77}Br isotopes is not observed in this case. We observed a second $3/2^-$ level in ^{71}Br which could have similar structure to the prolate level in the other cases. There are two energy sequences built on this second state in our case and except for the 3/2 to 5/2 level spacing which increases systematically from ^{75}Br to ^{71}Br (120 keV, 303keV and 522 keV respectively) the other members of both signature partners ($\alpha = \pm 1/2$) look very similar to the prolate band observed in the heavier odd-A Br isotopes This fact corroborates the possible interpretation of the second 3/2 level in ^{71}Br as the prolate deformed state which was the g.s. in the ^{77,75}Br nuclei and the first excited 3/2 state in ^{73}Br.

In general terms we can see that the oblate states are lower in energy in ^{71}Br with respect to ^{73}Br. This is also in agreement with the fact that in this case, not only has the ^{70}Se core an oblate component in the ground state structure but also the possible ^{72}Kr core ground state is oblate. In this case two 0^+ states have been observed experimentally with the excited 0^+ prolate state lying at 671 keV energy [Dea97, Kor01].

6.2.2 The β-decay question.

The following discussion is based on two articles. The experimental work on the decay of ^{71}Kr by Oinonen et al. [Oin97] and the theoretical interpretation of these observations by Urkedal and Hamamoto [Urk98].

The experimental study of ^{71}Kr

The nucleus was produced through a spallation reaction at the CERN PS booster using 1 GeV protons and a Nb target. The resulting nuclei were separated at the ISOLDE on-line mass separator and the typical activity reaching the measuring station was 1 atom/s of ^{71}Kr. There they installed a proton detector for β-delayed proton decay based on a gas-Si detector, a 70% HpGe detector, a 20 mm thick Ge detector to detect the gammas and a β plastic scintillator detector.

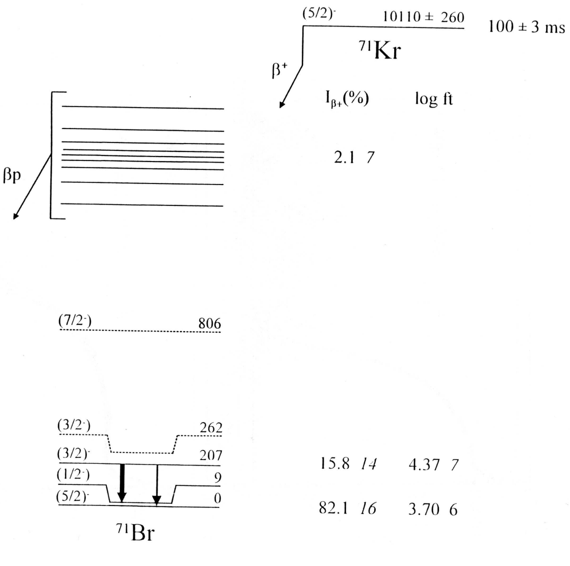

Figure 6.2: *Level scheme of* ^{71}*Br deduced from the* β*-decay experiment.*

The resulting level scheme is shown in fig 6.2. As can be seen two states in ^{71}Br are strongly populated in the decay of ^{71}Kr. One is the excited state at 208 keV excitation energy, the other is unclear. It could be the $5/2^-$ ground state or the $1/2^-$ state at only 9 keV excitation energy since the set-up was not optimized to measure this low energy transition either as a gamma or as a conversion electron (it could also be both). From this work Oinonen *et al.* assign the g.s. of ^{71}Kr as a $5/2^-$ state, a conclusion that we question in the present work and that was also questioned by the authors of [Urk98].

As discussed previously, in order to interpret the experimental data, we have to assume that the first three states in ^{71}Br are all oblate. If we assume that one of the lowest states in ^{71}Br becomes the g.s. in ^{71}Kr, we should investigate the spherical components of the possible parent g.s. and of the possible levels populated in the decay and thus see if there is enough overlap between the wave function of the parent state after applying the σ and $\sigma\tau$ operators and the wave function of the levels populated in the daughter nucleus ^{71}Br. In table 6.1 we have used an estimate of these components assuming the wave functions given by Griffiths *et al.* in their paper and assuming $[301]3/2^-$ to be the main component to the $3/2^-$ excited state at 208 keV energy. As we see, there is a large enough overlap of the several $p_{1/2}$, $p_{3/2}$, $f_{5/2}$ components contributing to these states to make the decay to these levels an allowed decay. But the fact that the spin-parity of the ^{71}Kr g.s. is probably either $1/2^-$ or $5/2^-$ makes a clear difference.

Table 6.1: Wave function components for the lowest states in ^{71}Br nucleus expressed in the Nilsson deformed basis and the spherical basis

Iπ (experiment)	%	Nilsson basis (Griffiths et al.)	Spherical basis (approximate content)
$1/2^-$	75%	$[310]1/2^-$	$p_{3/2}$ $f_{5/2}$ $p_{1/2}$
	23%	$[321]1/2^-$	mainly $p_{3/2}$
$5/2^-$	43%	$[303]5/2^-$	mainly $f_{5/2}$
	26%	$[321]3/2^-$	$p_{3/2}$
	18%	$[321]1/2^-$	$p_{3/2}$
	10%	$[310]1/2^-$	$p_{3/2}$ $f_{5/2}$ $p_{1/2}$
$3/2^-$		$[301]3/2^-$	mainly $f_{5/2}$

If experimentally we could see that the levels populated in the decay are $1/2^-$ and $3/2^-$ the ground state of ^{71}Kr will be $1/2^-$ and if the states populated were the $5/2^-$ and $3/2^-$ the g.s. will be $5/2^-$. From the fact that the $7/2^-$ state is not observed in the decay we clearly prefer the idea that in ^{71}Kr the $1/2^-$ has become the g.s. This is not surprising since even in mirror nuclei, the difference in the Coulomb energy can account for small shifts in excitation energy of the order of 10 keV, enough to invert the $5/2^-$, $1/2^-$ sequence known in ^{71}Br to the possible $1/2^-$, $5/2^-$ sequence in ^{71}Kr. One thing is very clear in the β-decay: only one out of the two $3/2^-$ levels in ^{71}Kr discussed earlier is populated in the decay. This strongly suggest that they are different in structure and that the $3/2^-$ states in

^{71}Br, interpreted so far as oblate and prolate, are not mixed.

We have not considered here the fact that the oblate $3/2^-$ state could become the g.s. in ^{71}Kr. We think that the 208 keV excitation energy in ^{71}Br makes this possibility very unlikely, but if eventually the β-decay experiment would clarify which states are populated in the daughter nucleus and the three states discussed were populated this will immediately fix the g.s. of ^{71}Kr as $3/2^-$ and the two mirror nuclei ^{71}Br and ^{71}Kr will differ rather more than other mirror pairs studied before.

This is not, however, the only possible explanation for this observation in the β-decay. Urkedal and Hamamoto [Urk98] have discussed the one particle orbitals in both mirror nuclei. The main assumption here is that in the β-decay of deformed nuclei one has the following selection rules:

$$\Delta N = 0 \; ; \; \Delta n_z = 0 \; ; \; \Delta\Lambda = 0 \; ; \; \Delta\Omega = 0, \pm 1 \qquad (6.1)$$

Since two orbitals are populated in the β-decay of ^{71}Kr, they tried first to find two single particle orbitals with identical N, n_z and Λ in the Nilsson diagram for 35 particles. Looking at figure 6.3 we find only the [301]1/2 and [301]3/2 orbitals which fulfill these conditions and they are too far apart in energy either at the oblate or the prolate side to be the two states observed in the experiment. The authors of the [Urk98] article propose another possible explanation based on the idea that the two states are the band-head and the first rotational member of the same intrinsic state.

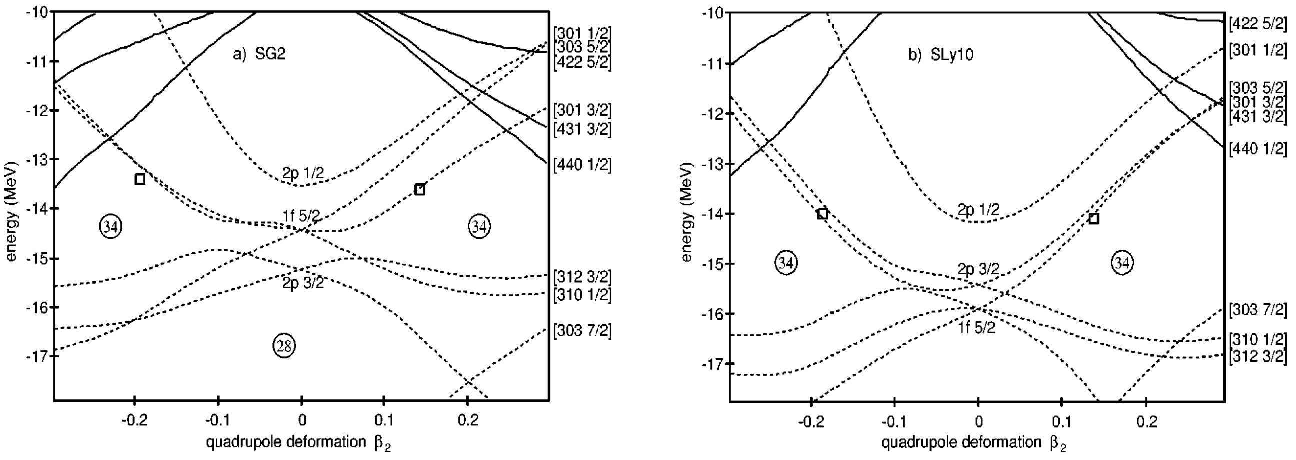

Figure 6.3: *Nilsson diagram from the work of Urkedal and Hamamoto.*

At the time that article was written it was thought that the spin of the 9 keV state was $1/2^-$ or $3/2^-$ and the excited 208 keV state was $3/2^-$ or $5/2^-$. Somehow arbitrarily they chose the second possibility and thus they assign the 9 keV state as the bandhead with $K^\pi = 3/2^-$ based on the [301 3/2] Nilsson orbit (see left part of fig 6.4) and the 208 keV state as the $5/2^-$ rotational member.

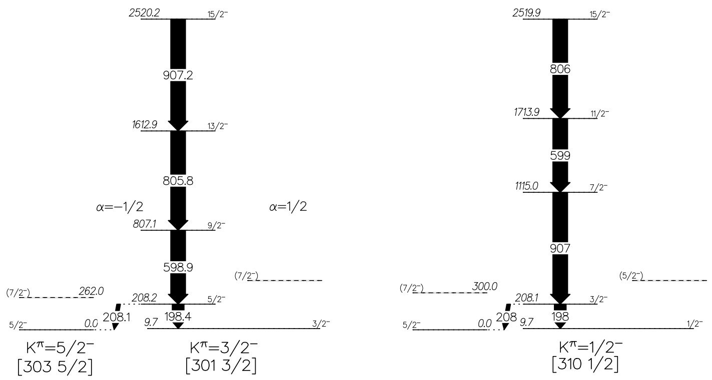

Figure 6.4: *Intrinsic states associated with the low-lying levels. Left: previous knowledge of* ^{71}*Br level scheme, used in reference [Urk98] to draw their conclusions. Right: the results of the present work.*

Z								
36	^{70}Kr	^{71}Kr ?	^{72}Kr oblate Korten	^{73}Kr prolate Kelsall	^{74}Kr mixed Korten	^{75}Kr prolate Skoda	^{76}Kr prolate	
35		^{70}Br ?	^{71}Br oblate Griffiths	^{72}Br prolate G. Bermudez	^{73}Br oblate Griffiths	^{74}Br prolate G. Bermudez	^{75}Br prolate Luhmann	
34	^{68}Se oblate Fischer	^{69}Se oblate Wiosna	^{70}Se obl-prol Hamilton	^{71}Se oblate Zhao	^{72}Se obl-prol Mylaeus	^{73}Se oblate Heiguchi	^{74}Se oblate Hamilton	
	34	35	36	37	38	39	40	N

From our data we know now that the state at 9 keV is I$^{\pi}$=1/2^{-} and the 207 keV has I$^{\pi}$=3/2^{-}. This, however, does not change the basic argument of the theoretical paper but simply the intrinsic state the band is built on (see right part of the figure 6.4). The other change with regard to their interpretation is that if the argument of Urkedal and Hamamoto is valid, then the g.s. of ^{71}Kr is oblate in shape.

This possible interpretation would give a different explanation for the first 3/2^{-} level from that based on the Griffiths *et al.* calculations.

6.3 Interpretation of the Rotational bands.

Once the spin-parities of the lowest states have been established, the rest of the states deduced in this work have been placed in bands according to sequences of transitions that reflect, to some extent, the same structures observed in the other light odd-A bromine isotopes and other odd-A neighbouring nuclei in this mass region. Following the criteria of intensity, and the spin-parity assignments obtained from the analysis of DCO and polarization data, several positive parity bands and the already mentioned negative parity bands have been identified. In the following, we will try to study the features of these bands by means of different models in order to draw some conclusions about the nature of these rotational structures.

6.3.1 Positive parity bands.

As in other odd-A nuclei in the region around $A \simeq 70$ the most striking structure is a rotational band built on the $\pi g_{9/2}$ or $\nu g_{9/2}$ single-particle orbit. This band constitutes the yrast band. Thus, it is observed in in-beam studies in terms of a series of relatively low energy E2 transitions connecting states in the decoupled $\mathrm{g}_{9/2}$ band (see rotational alignment limit in section 1.2.2.) Such a band is based on the low-Ω $\mathrm{g}_{9/2}$ unique parity orbital that lies near the Fermi level for deformed prolate shapes and is therefore of easy access for the unpaired proton, producing a strongly deformed intrinsic state and consequently a rotational band built on it.

Let us recall here the nature of this band structure. In a particle-core description the members of the band correspond to the coupling of the motion of the odd-nucleon to the rotational structure of the deformed core. For oblate deformation and the valence particle in a high-j orbital the strong coupling is realized. In this case the lowest level in the Nilsson diagram is the largest Ω value ($\Omega = j$). Its Coriolis matrix element is very small and a strongly coupled band with $\Delta I = 1$ is observed. For moderate prolate deformations, the low-Ω values are the lowest in energy and the Coriolis effect tends to align the total spin with the rotational motion generating a decoupled band with energy levels given by the expression:

$$E_{rot}(I) = E_0 + \frac{1}{2\Im}(I - J_x)(I - J_x + 1) \tag{6.2}$$

where $I - J_x$ takes values 0, 2, 4,... because of the symmetry condition. The lowest lying states are those which are maximally aligned, ($J_x = j$, favoured states). This corresponds to the picture of a valence particle whose spin is oriented perpendicular to the symmetry axis while the core is completely decoupled and rotates with $R = I - J_x$, giving rise to a band sequence with $\Delta I = 2$, which is otherwise equivalent to that of the neighbouring even nucleus.

Both kinds of band have been predicted in the light odd-A bromine isotopes as a consequence of a possible shape coexistence, already present in the neighbouring even nuclei, however, only the prolate, rotational, decoupled band based on the $g_{9/2}$ orbit is observed. As we show in fig. 6.5 the rotational decoupled band is compared to the ground state band in the even neighbouring nuclei. As we can see in the figure the energy separation between levels is almost equivalent to the separation in the even cores as expected for this kind of rotational aligned band.

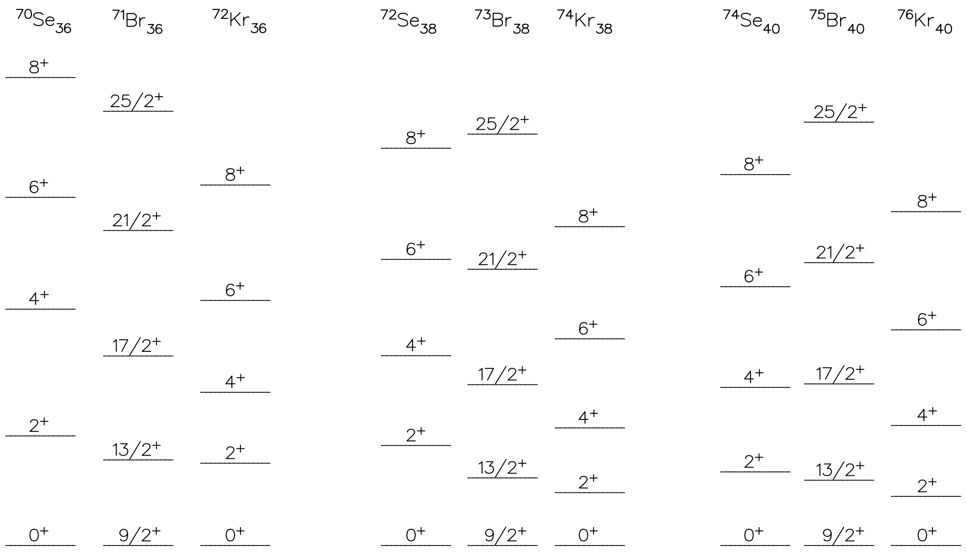

Figure 6.5: *Comparison of the* $\pi g_{9/2^+}$ *decoupled band with the ground state band in the core nuclei for the light odd-A bromine isotopes.*

Studying the level ordering and spacings within the $g_{9/2}$ rotational band and comparing them with the same structure in the odd-A ^{73,75}Br isotopes, we can suggest a value for the deformation parameter. Thus, the presence of the $5/2^+$ state below the $9/2^+$ state would give a qualitative idea of the deformation as Kreiner *et al.* have shown for ^{75}Br [Kre81]. The $5/2^+$ state originates from the coupling of the $j = 9/2^+$ with the 2^+ state of the core $(9/2^+ \otimes 2^+)$ and the resulting energy goes below the $9/2^+$ state for values of large deformation [Ste75a].

Kreiner *et al.* have calculated the excitation energy of the favoured states relative to the $9/2^+$ state as a function of the deformation parameter β, see fig 6.6, obtaining a good agreement with the trend of the energy separation between levels in ^{75}Br. The eigenfunction obtained allowed them to estimate the quadrupole deformation from the measured half-life of the $I = 9/2^+$ isomeric state. Following their calculation and making use of the $B(E2; \frac{9}{2}^+ \rightarrow \frac{5}{2}^+)$ deduced for the 89.9 keV transition we have inferred, as a simple exercise, a deformation value of $\beta = 0.37$ for ^{71}Br, which is in accord with the other two light bromine isotopes, see table 6.3.1.

Hence, a large deformation, comparable with that of the heavier odd-A bromine isotopes is suggested. On the other hand, the energy spacing between the $13/2^+$ and $9/2^+$ states should also reflect the deformation just as the spacing 2^+ to 0^+

Table 6.2: Deformation parameter β estimated from the B(E2) value of the $9/2^+ \rightarrow 5/2^+$ transition in the light odd-A bromine isotopes.

A	$E_{9/2^+}$(keV)	$T_{1/2}$ (ns)	E_γ(keV)	B(E2) (e^2fm^4)	β
71	759.8	32.5 (5)	89.9	900 (57)	0.35
73	473.3	1.1 (2)	187.5	2081 (378)	0.40
75	220.8	31.7 (3)	88.3	1420 (13)	0.37

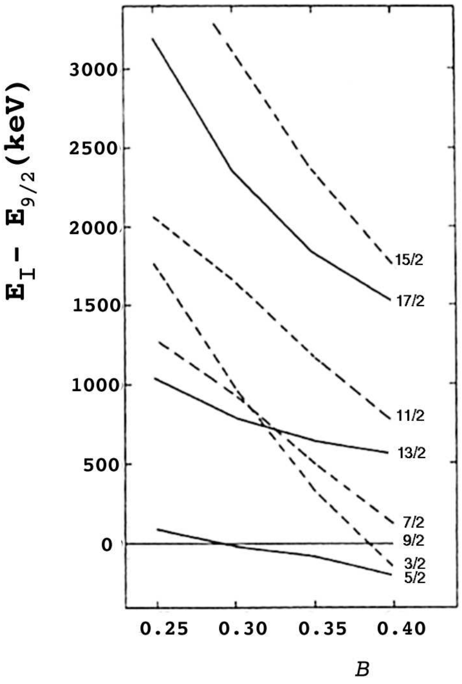

Figure 6.6: *Relative position of the levels of the* $\pi g_{9/2^+}$ *decoupled band as a function of deformation parameter* β*. From [Kre81]*

does in the even-even core. From the value of this γ-ray transition a slightly lower deformation value of $\beta \sim 0.3$ is obtained.

With these conditions we can study the behaviour of the rotational motion by studying the different collective variables within the framework of the cranked shell model (CSM). Thus by studying the kinematic and dynamic moment-of-inertia as a function of the frequency (the latter is a variable that depends only on the collective properties of the motion) and the variation of the aligned angular momentum we can make suggestions on how the collective rotation takes place in the nucleus. The expression that relates the moments-of-inertia and the aligned angular momentum with the frequency are given in the intrinsic reference frame. Thus we need to transform the experimental data which are referred to the laboratory reference system by using the formulae:

$$\frac{\Im^{(1)}}{\hbar^2} = \frac{I_x}{\hbar\omega} = \frac{\sqrt{I(I+1)-K^2}}{E_\gamma/2}, \tag{6.3}$$

and

$$\frac{\Im^{(2)}}{\hbar^2} = \frac{dI_x}{\hbar d\omega} \approx \frac{4}{\Delta E_\gamma/2}, \tag{6.4}$$

where $\hbar\omega \approx \frac{E_\gamma}{2}$ for high-spin values (I≫K).

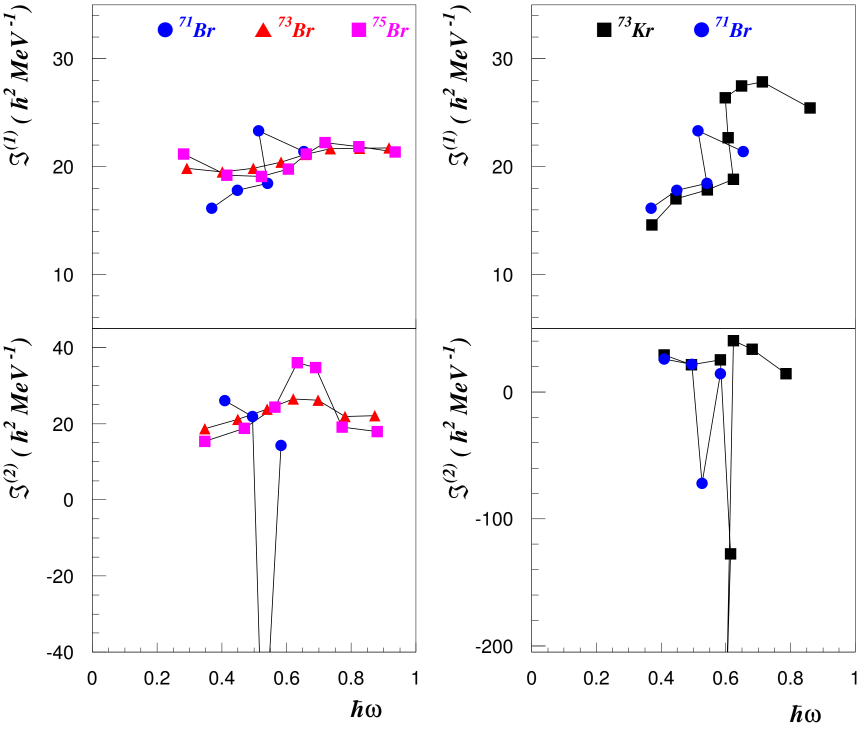

Figure 6.7: *Kinematical and dynamical moment-of-inertia of the decoupled band.*

In fig 6.7 the kinematical and dynamical moments-of-inertia of the $g_{9/2}$ decoupled band have been plotted as a function of the frequency for ^{71}Br. Similar plots for ^{73,75}Br and ^{73}Kr are included for comparison. In the calculations a value of K=1/2 has been adopted for ^{71}Br based on the [440]1/2 orbital following the same deformation criteria as in ^{75}Br. A value of K=3/2 has been adopted for ^{73}Br ([431]3/2 orbit) following the deformation criteria and K=5/2 for ^{73}Kr [Kel02] based on the [422]5/2 orbit. The almost constant behaviour of the $\Im^{(1)}$ moment-of-inertia in the A=73,75 bromine isotopes show the stable prolate deformation along the yrast band. The broad peaks observed at $\hbar\omega \sim$ 0.6-0.7 MeV in the $\Im^{(2)}$ moments have been interpreted by the authors in terms of neutron alignment due to Pauli blocking by the odd $g_{9/2}$ proton. In contrast, the moments-of-inertia observed in ^{71}Br would show a behaviour (backbend?) more like that observed in ^{73}Kr but at $\hbar\omega \sim 0.5$ MeV in our case. In the ^{73}Kr isotope the proton alignment observed occurs at $\hbar\omega \sim$ 0.62 MeV. The causes of this behaviour are not understood as yet.

Other variables we can check are the angular momentum alignment and the Routhians. In order to calculate these variables we need to extract the Harris parameters for the reference rotor which are not so trivial in the cases where shape-coexistence is present in the core, as happens in these nuclei. This can produce some discrepancies between interpretations, as for example in ^{75}Br, where several authors have proposed different values. In order to compare data we have used the following parameters:

Table 6.3: Harris parameters for the rotor reference.

	$\Im_0^{(1)}$ $(\hbar^2 MeV^{-1})$	$\Im_2^{(1)}$ $(\hbar^4 MeV^{-3})$	Ref.
^{75}Br	15	3	Solomon et al.
^{73}Br	10	15	Hesse et al.
^{73}Kr	18	0	Kelsall et al.
^{71}Br	12.5	1.5	this work

With these values, we can calculate the quasi-particle, aligned spin and experimental Routhians using the following expressions:

$$e(\omega) = E_x^\omega[I(\omega)] - E_{ref}^\omega[I(\omega)], \tag{6.5}$$

where $E_x^\omega[I(\omega)]$ is the excitation energy in the intrinsic (rotating) frame and $E_{ref}^\omega[I(\omega)]$ is the reference rotor whose values are given in terms of the Harris parameters by:

$$E_{ref}^\omega[I(\omega)] = -1/2 \cdot \Im_0^{(1)}\omega^2 - 1/4\Im_2^{(1)}\omega^4 + \hbar^2/(8\Im_0^{(1)}). \tag{6.6}$$

The contribution of the quasi-particles to the total angular momentum I(ω) is given by:

$$i_x(\omega) = I_x(\omega) - I_{ref}(\omega), \tag{6.7}$$

where $I_{ref}(\omega)$ can be computed using the formula:

$$I_{ref}(\omega) = \hbar^{-1}(\Im_0^{(1)} + \Im_2^{(1)}\omega^2)\omega. \tag{6.8}$$

From fig 6.8 we can observe a large increase in the aligned angular momentum $i_x(\omega)$ in ^{73}Kr that can be attributed to the nearly complete alignment of the odd

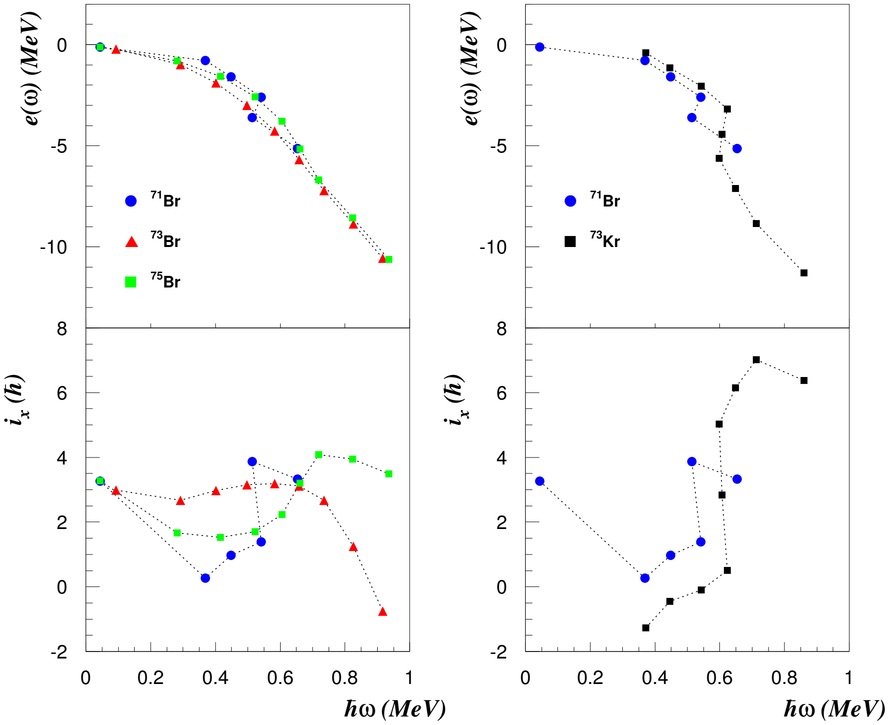

Figure 6.8: *Experimental quasi-particle Routhians and alignment for the different nuclei discussed in the text.*

neutron in the $g_{9/2}$ orbital with the axis of rotation. The increase observed in ^{73,75}Br is not so clear. Thus it is very hard to extract any conclusion about the case of the ^{71}Br nucleus.

The unfavoured bands.

Evidence of two extra, positive parity bands has been observed in ^{71}Br. They have analogies in the isotope ^{75}Br where two similar positive parity bands have been observed [Luh85, Mar89, Sol99]. The experimental information is too poor to allow a conclusive interpretation, so here we only make a simple comparison of the weakly observed bands with the bands discussed in the above cited references.

The first (lower excitation energy) unfavoured band is built on the "band-head" state with $I^{\pi}=7/2^{+}$ at 893 keV. From the energy spacings between the levels we can observe a similar behaviour to that of the excited band at 374 keV in ^{75}Br. From the [Sol99] work it is suggested that this band corresponds to the unfavoured $g_{9/2}$ decoupled band with $I = j_x - 1, j_x + 1, j_x + 3, \ldots$ with $j_x = 9/2$. The band seems to extend to spin $(19/2^{+})$ but the last few transitions are difficult to observe in double coincidences. Another interpretation suggested by [Luh85, Mar89] is that the energy splitting is so large that the unfavoured decoupled band is so high in energy that it is not observed. Thus, this $I^{\pi}=7/2^{+}$ state could correspond to an excited 3qp band. A similar band is also present in ^{73}Kr and reported in [Kel02], but no theoretical interpretation was given.

The other weakly populated band has been associated with the 1175 keV state whose spin-parity has been suggested to be $9/2^{+}$ and extends to spin $I=(29/2^{+})$. The similar band observed in ^{75}Br has been associated with an oblate excited configuration [Sol99]. This interpretation could make some sense because in the core nuclei ^{72,76}Kr, the observation of the coexistence of the 0^{+} prolate ground state with a 0^{+}_{2} oblate excited state has been reported. Unfortunately the available experimental information is insufficient to test this hypothesis.

6.3.2 Negative parity bands.

In the neighbouring ^{73,75}Br nuclei, two main bands with negative parity have been observed in several experiments ([Hee90, Luh85, Sol99]). These bands have been interpreted in the case of ^{75}Br as bands built on the odd proton, strongly coupled to the deformed core and based on the prolate $[312]3/2^{-}$ configuration of the g.s. (as in the case of ^{77}Br) [Gri92] and they correspond to both signature partners $\alpha = \pm 1/2$.

In the case of ^{73}Br, one of the two negative parity bands observed would correspond to the $\alpha = -1/2$ signature of the prolate [312]3/2 1qp configuration, as for its counterpart in ^{75}Br. The other band would be built on the $I^{\pi}=5/2^{-}$ state and corresponds to the signature $\alpha = +1/2$ component of the band. The configuration of the bandhead state would be more complicated but Griffiths *et al.* suggested in their calculations the following 1 qp oblate configuration ([312]5/2, [321]3/2, [321]1/2, [310]1/2) for this band [Gri92].

In the case of ^{71}Br we have reported up to three negative parity bands. The most intensely populated negative parity band was already observed in the first spectroscopic experiment done by Arrison *et al.*, following the sequence of 598, 806 and 907 keV transitions. In our experiments we have observed other cross-linking transitions that allow us to modify the order of those transitions. Hence, the level sequence consists of states at 208, 1115, 1714, 2520, 3530 and 4742 keV excitation energy with spin values of I=3/2, 7/2, 11/2, 15/2, 19/2 and (23/2) as we can see from figure 5.1. In principle, from intensity arguments, we could suggest that the band is based on the $3/2^{-}$ state (or even on the $1/2^{-}$ state) but from the energy spacings the $7/2^{-}$ state fits best as the bandhead. Another possibility could be that the band is the result of the mixing of an oblate structure at low spin with a prolate structure as the spin increases. This hypothesis could explain the fact that the band is built on states that are expected to be oblate and the high spin states show the typical spacings of a prolate band, as in the ^{73,75}Br nuclei.

To find the best possible explanation, theoretical calculations may be helpful. In this sense, we have calculated the moments-of-inertia for the band within the

Cranked Shell Model. Thus, assuming the value of K=3/2$^-$ for the Nilsson single-particle orbit and using the Harris parameters given above we have calculated the kinematical $\Im^{(1)}$ and dynamical $\Im^{(2)}$ moment-of-inertia and compared them with the moments-of-inertia obtained for the main negative parity bands in the ^{73,75}Br nuclei and ^{73}Kr nuclei (see figure 6.9).

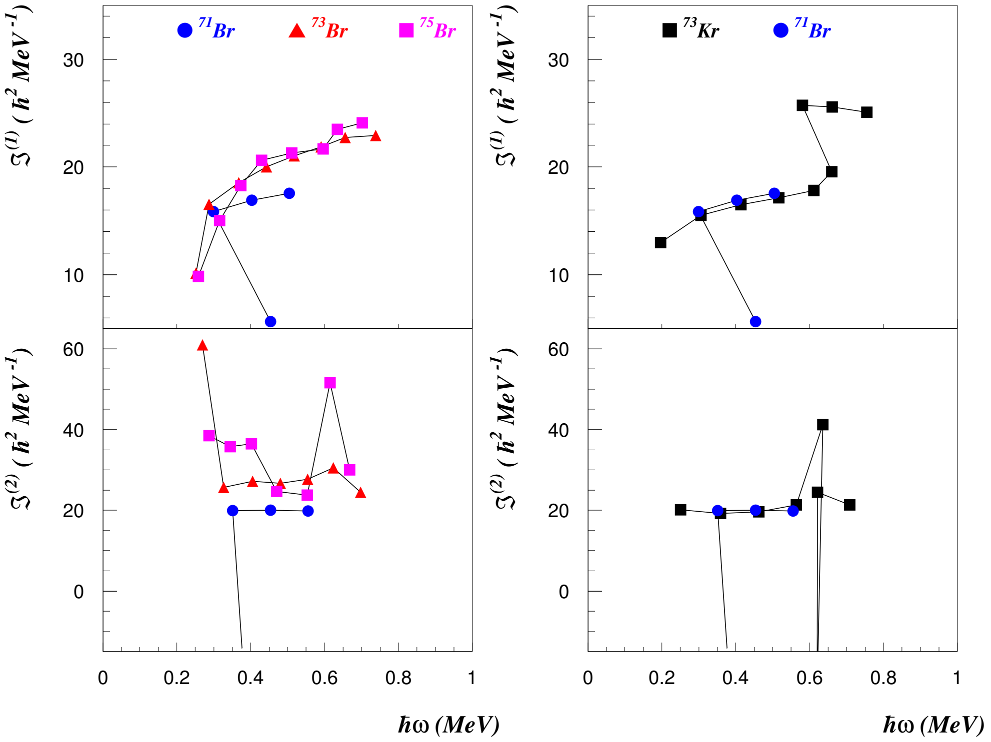

Figure 6.9: *Kinematical and dynamical moments-of-inertia of the negative parity band with signature α=-1/2*

From the figure we can observe nearly constant moments-of-inertia, except for the first transition. This would mean a stable prolate deformation, as we can deduce from the moment-of-inertia of a prolate rigid rotor. Again the behaviour of the band seems to be closer to that of the band in the odd-A ^{73}Kr nucleus than to those in the heavier odd-A Br isotopes. The fact that ^{71}Br seems to be closer to ^{73}Kr than to ^{73}Br, could be understand in terms of the fact that they share the same ^{72}Kr core.

The unfavoured bands.

Two more bands with negative parity have been observed for the first time in this work. The band character of those sequences of states is supported to some extent by the presence of $\Delta I = 2$ transitions connecting the states and deduced from the

DCO ratios in the case of some intense transitions and by the regularly increasing spacings between levels. The weak population of these bands makes it difficult to deduce the main characteristics of the levels.

The band with level sequence $I^{\pi}= 5/2^{-}$, $9/2^{-}$, $(13/2^{-})$, $(17/2^{-})$ and $(21/2^{-})$ at excitation energies of 930, 1493, 2218, 3189 and 4365 keV (see figure 5.1) is suggested as the α=+1/2 signature partner of a band built on the $3/2^{-}$ state, based on the similarities with the neighbouring odd-A Br isotopes. This band is considered to be a prolate band in the heavier isotopes. We have also calculated the $\Im^{(1,2)}$ moments-of-inertia for this band and compared them with those of the same structures in neighbouring nuclei. The plot is shown in figure 6.10.

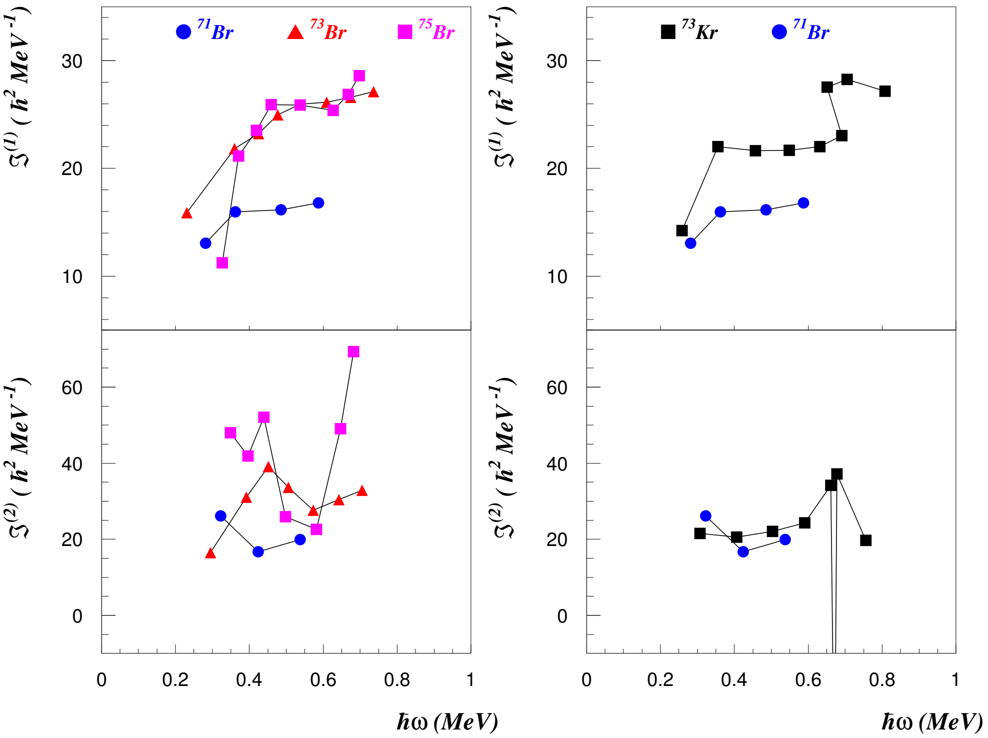

Figure 6.10: *Kinematical and dynamical moments-of-inertia of the negative parity band with signature α=+1/2*

The second unfavoured "structure" is even more difficult to associate with a band. We have suggested the spins for the sequence of states based on the increasing energies of the transitions connecting the levels. The low intensity makes it almost impossible to extract any information from the correlation data.

6.4 Conclusions on ^{71}Br.

The light bromine isotope ^{71}Br has been studied with different experimental set-ups in order to shed light on the question whether shape co-existence or polarization towards prolate shapes dominates the nuclear structure of the low spin states of the neutron deficient, odd-A bromine isotopes. In principle, from the high spin studies or in-beam experiments carried out on these nuclei, a main prolate deformed shape was suggested based on the rotational bands observed in those nuclei, similar to the medium heavy odd-A Bromine nuclei.

Magnetic dipole moment measurements have supported in some cases, the ^{75,77}Br nuclei, the prolate shape, but in other cases, as in the case of ^{73}Br, the magnetic moment suggests, together with particle-rotor calculations, the presence of oblate shapes for the low spin states. This calculation would suggest a similar situation in the case of the ^{71}Br nucleus. This result would be in accord with previous calculations which suggested a prolate-oblate transition in the bromine nuclides [Mol81, Ben84, Naz85] although it was expected to occur at higher masses, between ^{78,79}Br [Mol81]. Beta decay studies have, in principle, not clarified the situation and thus, the experimental results obtained by Oinonen *et al.* [Oin97] and Miehé *et al.* [Mie99] did not determine a clear deformation for the ground states and first excited states in ^{71,73}Br. The theoretical calculation offered by Urkedal *et al.* [Urk98] and Sarriguren *et al.* [Sar01] cannot exclude any of the possibilities.

In this context, our in-beam study has provided a series of results that to some extent can help to give support to the particle-rotor calculation [Gri92] suggesting shape co-existence against the Hartree-Fock calculation [Urk98] that would indicate prolate shape even at low spin. We can summarize the results obtained:

- The ground state and first excited state have been assigned as $5/2^-$ and $1/2^-$ which are difficult to obtain on the prolate side of the Nilsson diagram.

- We have observed two $3/2^-$ states at 208 and 407 keV with bands built on top of them. The band built on the second $3/2^-$ state seems to be similar to the prolate bands that appear in heavier odd-A bromine isotopes and hence it would give support to the interpretation of the second $3/2^-$ state as the prolate state with configuration $[312]3/2^-$.

- The band built on top of the first $3/2^-$ state has a behaviour that is hard to interpret. Further calculations would be interesting in order to deduce the nature of this structure.

The results obtained greatly extend the level scheme presented by Arrison *et al.* The new level scheme is characterized by the presence of several rotational bands, with both kinds of parity. The positive parity bands originate from the presence of the unique parity single-particle orbit $g_{9/2}$ that dominates the structure of the nuclei in the A=70 mass region, showing an yrast positive parity band built on the I$^{\pi}$=9/2^{+} state and driving the nuclei to high deformation. The negative parity bands are based in the $p_{3/2}$, $f_{5/2}$ and $p_{1/2}$ orbits.

- The yrast band in ^{71}Br is suggested as a decoupled prolate band within the particle-rotor framework. The bandhead state with I$^{\pi}$=9/2^{+}, is an isomer whose half life has been deduced as T$_{1/2}$=32 (10) ns. A deformation parameter of β=0.35 has been deduced based on the relative positions of the low spin members of the band.

- A second positive parity band with spin sequence I$^{\pi}$=7/2^{+},11/2^{+},15/2^{+} has been suggested as the unfavoured decoupled partner of the yrast band.

- The sequence of E2 transitions (598,806,907 keV) reported in the work of Arrison *et al.*, have been modified in our study and the result shows a band with an irregular energy spacing at low energy which may be due to the shape mixing phenomenon. At medium spin values the band seems to behave as a prolate band.

- A second negative parity band built on an I$^{\pi}$=3/2^{-} state has been observed and the similarities with a prolate band in ^{73,75}Br nuclei suggest such a structure.

It should be noted that more information about electromagnetic properties would be very useful in order to determine better the deformation of the different structures, in particular at low spin. Moreover, some theoretical calculations would be very helpful in order to draw a complete picture of the structure of ^{71}Br.

Chapter 7

Results for ^{71}Kr

In this chapter we will present the results obtained in the off-line analysis of the data taken in the experiments described earlier. The first part of the chapter is devoted to the results obtained for the ^{71}Br in the three experiments related to the $^{40}Ca +^{40} Ca$ reaction. In the second part, we discuss the results that can be obtained for ^{71}Kr in the experiment performed with recoil mass selection at Oak Ridge laboratory.

Unlike its partner mirror nucleus, the ^{71}Kr nucleus has not been identified in any high spin measurement so far. The main reason is the very low cross section in fusion-evaporation reactions, $\sigma \sim 1\mu b$ from statistical codes, and the performance of the γ-arrays available so far. In the experiments performed for this thesis a big effort has been put into identifying it. In this section we will describe the procedure followed to try to identify the transitions from excited states and a measurement of its production cross-section. Since we have not succeeded in identifying ^{71}Kr, we will try to explain at the end some of the possible reasons why it was so difficult.

7.1 Identification.

In a first trial, we have analyzed the data obtained in the reaction ^{40}Ca on ^{40}Ca at 160 and 180 MeV beam energy. The ^{71}Kr is produced in the reactions via the evaporation of 2α0p1n, which means that we should observe the de-excitation γ-rays of the ^{71}Kr nucleus in the 2α0p and not in the 2α1p matrix. In principle, we could observe the trasitions in the 1α0p $\gamma\gamma$ matrix but as mentioned in a previous section the cleanest matrix is the 2α0p.

Comparing both matrices we can determine the possible candidate transitions. A careful inspection of both projection spectra, see fig. 7.1, indicates no clear evidence for any transition belonging to ^{71}Kr. The marked transitions shown in the figure belong to other nuclei, as the analysis of the coincidences has demonstrated. Thus, the transitions at 146, 401, 478 and 879 keV belong to ^{47}V, the 319 and 774 keV to ^{67}As, the 369 and 469 keV to ^{44}Ti, the 531 and 752 keV to ^{48}Cr and the 612, 710 and 793 keV belong to ^{72}Kr.

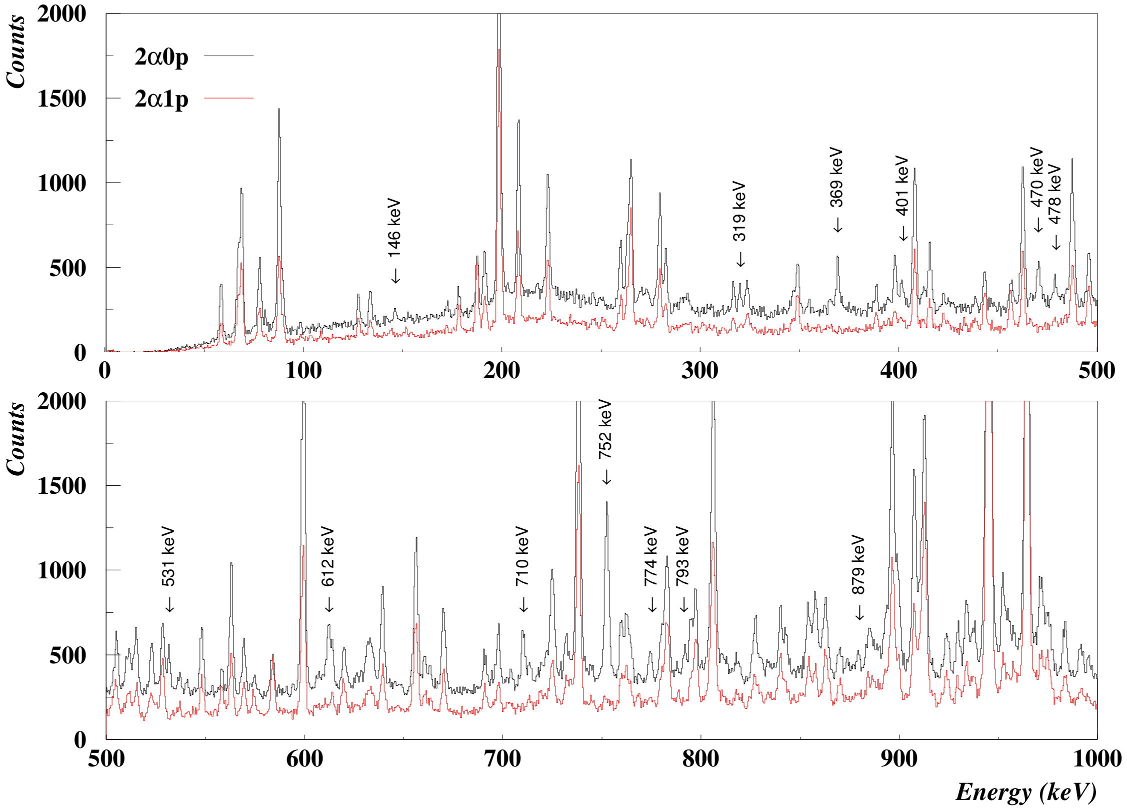

Figure 7.1: *Comparison between particle gated γ-matrix projections obtained in the GASP experiment. Candidate transitions for ^{71}Kr should appear in 2α0p but not in 2α1p. The marked transitions correspond to known contaminants or known nuclei. See the text.*

In a dedicated measurement we have run the reaction ^{40}Ca on ^{40}Ca at 156 MeV using a very complete experimental set-up: Clarion γ -array spectrometer, the Hyball particle detector, the RMS recoil mass separator, the PSAC recoil detector and the Ion Chamber detector. The trigger condition for good events was two Compton-suppressed germanium detectors, one CsI(Tl) particle detector and the PSAC focal plane detector. This is a very restricted condition, resulting in a large reduction in the counting rate, however it was decided to do so in order to minimise the deadtime. We ran the experiment for two weeks of beam time.

The events obtained in this way were sorted in different histograms with different conditions in order to identify the gamma transitions associated with each recoil. The idea was to tag the events belonging to each recoil nucleus. To achieve that we made use of the fact that the recoils are separated by their A/Q ratio in the Recoil Mass Spectrometer and are detected at the PSAC focal plane detector distributed according to this ratio. Afterwards, they lose their kinetic energy in the Ion chamber according to their Z value if the recoil velocity is high enough. For a specific mass value we expect that the higher Z isobar will undergo a higher loss of energy in the Ion chamber. The Z resolution achieved will depend on the FWHM of the ΔE signal. Thus, by plotting in a matrix the energy loss against γ-ray energy, a series of γ-ray spectra can be produced corresponding to increasing energy loss. If we compare the intensities of the γ-ray peaks and make the corresponding substractions it is possible to separate the various Z-elements.

In our case, we did not get full Z separation in the IC: the recoil velocity was at the limit of the values required (usually values $v > 4.6\%$ of c are required). We decided to use the condition on particle detected in the HYBALL detector to select the reaction channel and the mass selection in the PSAC detector. Thus, we have produced a gamma spectrum with the following conditions:

- gate on mass A=71 in the PSAC detector, and
- particle condition of $2\alpha0$proton.

In this spectrum, the contribution from ^{71}Br is present and we have subtracted this part using a clean spectrum produced with the appropiate conditions: A=71 and $2\alpha1$p. The subtracted spectrum is shown in fig. 7.2 and no evident candidate transitions have been obtained. The candidate transitions marked on this figure were checked in the coincidence γ-γ matrix with no further results.

7.2 Cross section limit.

After the failure to observe any candidate transitions in the nucleus ^{71}Kr, we have estimated a limit on the production cross-section for this nucleus. This also allows us to establish the sensitivity of our system. For that, we have made use of a cross-section measurement performed during the Oak Ridge experiment, as well as the data obtained in the previous experiments at GASP and EUROBALL.

The probability of a nuclear process to occur is often expressed in terms of the cross section, σ, which has the dimensions of an area. Thus, in the fusion-evaporation reactions, the production cross-section of each open channel is a measure of the probability of evaporation of the right number of particles for each reaction channel. From the basics of nuclear reactions it follows that the production cross-section depends on the reaction properties according to:

$$\sigma = \frac{N_{cr}}{I \cdot N} \tag{7.1}$$

where N_{cr} is the counting rate in the outgoing channel, I is the particle flux or the number of beam particles per unit time and N is the number of target nuclei per unit area. The counting rate N_{cr} of a product nucleus can be determined by measuring the total intensity of the gamma transitions that go to the ground state

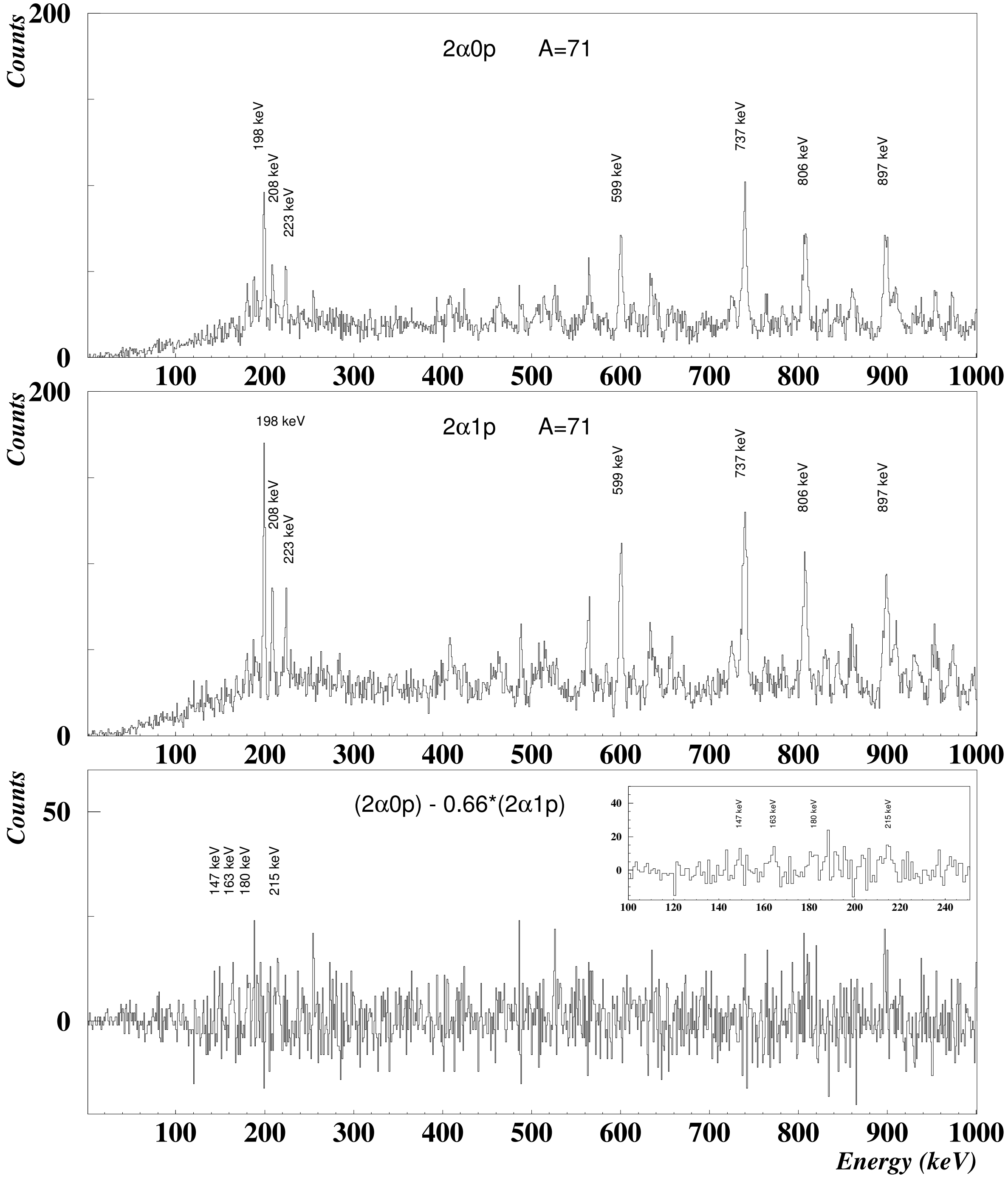

Figure 7.2: *Spectra obtained by requiring the appropriate conditions for mass 71 on the evaporated particles (upper and middle). In the lower panel the spectrum produced by subtracting the above spectra shows some "peak-like" structures at low energy.*

directly if we assume that the entire flux passes through them. Thus, it can be expressed as:

$$N_{cr} = \frac{1}{\Delta t(1-\tau_d)} \cdot \sum_i \frac{N_\gamma(i)}{\varepsilon_\gamma(i)} \tag{7.2}$$

where Δt is the measurement time, τ_d is a global dead time for the DAQ system, N_γ(i) is the number of counts of the i-th gamma transition to the g.s. and $\varepsilon_\gamma(i)$ is its absolute efficiency in a measurement of γ-singles.

The particle flux of the beam can be calculated as $I = i/Q$, where i is the beam current in electrical nano-Amperes and Q is the charge state of the beam particles. The number of target nuclei is obtained from $N = (N_{Av} \cdot t)/A$ where N_{Av} is Avogadro's number, t is the thickness in $mg \cdot cm^{-2}$ and A is the atomic mass number in a.m.u.

Thus, a cross section measurement has been performed during the experiment, under the following conditions:

1. trigger condition of 1 Ge detector fired (singles),
2. defined charge state of $Q=8^+$,
3. average current intensity i=0.88 nA,
4. measurement time of Δt_m=11 min, and
5. global dead time of τ_d=35 (5)%.

The data obtained were sorted in 1-dim. gamma spectra with and without conditions on the other detector parameters. From the direct γ-spectrum, with no additional condition, we have obtained an estimate of the cross section for the ^{76,74}Kr nuclei:

A	Channel	E_γ	σ_{exp} (mb)	σ_{calc} (mb)
^{76}Kr	4p	424.0	223 (40)	280
^{74}Kr	1α2p	455.8	95 (23)	48

Table 7.1: *Cross section values obtained from a gamma-singles spectrum, without any extra condition.*

In this direct γ-spectrum, the other reaction channels are hidden by the high background. In order to estimate their cross-sections, a condition on particle detection is necessary to see their transitions. In this way, we will be able to check the agreement between our estimates and the statistical calculations. Using different particle conditions, we have created a series of particle-gated, gamma spectra.

In a first step, we have calculated the efficiency of particle detection using some transitions in the ^{76,74}Kr nuclei by comparing their intensities with different particle conditions. Thus, we have deduced ϵ_p=74 (3)% for protons and ϵ_α=56 (3)% for alphas.

The cross-sections of ^{72}Se and ^{73}Br have then been extracted from the 1α3p gated spectrum, the cross-section for ^{70}Se and ^{71}Br from the 2α1p gated spectrum and as a check we have calculated the cross section of ^{76}Kr from the 4p-gated spectrum and the ^{74}Kr from the 1α2p-gated spectrum. The values obtained are:

A	Channel	E_γ	σ_{exp} (mb)	σ_{calc} (mb)
^{72}Se	1α4p	862.0	19 (4)	50
^{70}Se	2α2p	944.6	15 (5)	40
^{73}Br	1α3p	$\sum$	62 (9)	75
^{71}Br	2α1p	$\sum$	6.4 (12)	0.8
^{76}Kr	4p	424.0	224 (10)	280
^{74}Kr	1α2p	455.8	89 (10)	48
E_γ= E(198)+E(208)+E(397)+E(408)				

Table 7.2: *Cross section values obtained from particle gated γ spectra.*

In the case of the even-even Se and Kr nuclei we have used the $2^+ \rightarrow 0^+$ transition and in the case of odd-A Br nuclei the sum of all the transitions going to the ground state. The numbers we have obtained are approximate because of the low statistics in the particle gated spectra, which made it difficult to get a good estimate of the cross section. In particular, in the case of the ^{71}Br cross section, not all the transitions going to the ground state could be seen. The σ value is obtained from the sum of I_γ for the 198, 208, 397 and 408 keV transitions. Since it is a thin target experiment the delayed intensity due to the $g_{9/2}$ isomer is not taken into account in these transitions. So, we need to estimate what fraction of the total intensity we have evaluated.

Thus, from the γ-γ data in this experiment, taken with the main trigger condition (2 Ge + 1 CsI + Psac) we had established the relative intensities for the prompt transitions in ^{71}Br, see table 5.3. Assuming that no delayed decay from the isomer is observed in the gamma array and there is no direct feeding to the isomeric state, we can assume that the missing delayed intensity can be taken into account with the intensity that feeds the isomer:

$$\begin{aligned} I_{delayed} &= I_\gamma(737) + I_\gamma(415) + I_\gamma(955), \\ &= 1000(46) + 53(11) + 17(17) = 1070(50) \end{aligned}$$

Then, the total prompt intensity of the transitions going to the ground state can be evaluated as follows:

E_γ	I_γ	E_γ	I_γ
198.4	431 (40)	669.8	112 (17)
208.1	170 (23)	761.7	179 (31)
397.7	46 (9)	929.3	103 (10)
407.4	82 (22)		
$\sum I_{eval}$= 729 (52)			
I_{prompt}=$\sum I_\gamma$= 1123 (64)			

Table 7.3: *Total prompt intensity going to the ground state.*

Therefore, the fraction of the intensity which we have evaluated is:

$$f = \frac{I_{evaluated}}{I_{delayed} + I_{prompt}} = \frac{729}{2193} = 0.33$$

Correcting the estimated cross-section by this number we obtain as a more realistic cross section for ^{71}Br:

$$\sigma(^{71}Br) = \frac{6.4}{f} = 19\ mb$$

This value can also be confirmed from the GASP data if we assume the cross section values of ^{74,76}Kr ($\sigma_{^{74}Kr} = 95mb$, $\sigma_{^{76}Kr} = 223mb$) are a good estimate. Thus, calculating the ratio between cross sections by means of the intensities of the transitions to the g.s. observed in particle gated spectra and the corresponding particle efficiency given in table 5.1., we can obtain:

$$\frac{\sigma(^{71}Br)}{\sigma(^{74}Kr)} = 0.21, \qquad \sigma(^{71}Br) \approx 20mb$$
$$\frac{\sigma(^{71}Br)}{\sigma(^{76}Kr)} = 0.10, \qquad \sigma(^{71}Br) \approx 22mb$$

In order to determine a limit for the ^{71}Kr cross section, we should compare possible lines in ^{71}Kr with the ^{71}Br weakest line that we can identify, assuming that we expect the same pattern of feeding of the g.s. in the two nuclei. Thus, in the γ-spectrum gated by 2α particles obtained during the trigger condition of singles, it is difficult to see any line from ^{71}Br, and hence we need to go to other spectra. In the 2α gated γ-spectrum lines, with the trigger condition 2Ge+1CsI+PSAC, the weakest transition observed is 397 keV, with an intensity around $I_\gamma(397) \sim 0.02 I_{g.s.}$, then

$$\sigma(^{71}Kr) < \frac{I_\gamma}{I_{gs}}(1 - \varepsilon_p) \cdot \sigma(^{71}Br) \tag{7.5}$$

and by inserting the right number, $\varepsilon_p = 0.68$, in the above expression we obtain as a limit:

$$\sigma(^{71}Kr) < 128\mu b$$

We can use the data obtained in the GASP experiment and try to obtain a lower limit. For that, the weakest transition in ^{71}Br that we have identified in the data is the 316 keV line. This line has I_γ=3.6% of $I_\gamma(737)$ (see table 5.1.), this means I_γ=1.66% of $I_\gamma(g.s.)$ then, the cross section of ^{71}Kr has to be less than this intensity, and inserting the particle detection efficiency, $\varepsilon_p = 0.31$ in the previous expression, eqn 7.5, we obtain:

$$\sigma(^{71}Kr) < 218\mu b$$

Looking carefully at the projection, in principle we should be able to see a peak with a third of the statistics of the 316 keV transition, so we estimate that the cross section should be $\sigma(^{71}Kr) < 73\mu b$ at this bombarding energy of 156 MeV.

7.3 Why are the cross-section limits so poor?

In principle from the numbers obtained and considering that the expectation values for the cross section of the 2αn channel in the $^{40}Ca +^{40} Ca$ reaction are of the order of 1μb one could consider that the technique is not suitable for making this kind of measurement, in particular because with other techniques such as neutron detector combined with charged particle detectors one has been able to identify nuclei produced with cross-sections of the order of $\sim$10μb.

This RMS+IC technique was used very succesfully in the Daresbury laboratory and allowed the identification of nuclei produced with very low cross-sections [Lis87, Gel91]. A recent experiment [Pau98] performed at the Holifield Radioactive Ion Beam Facility (HRIBF) of the Oak Ridge National Laboratory, using the RMS separator showed the capabilities of the technique allowing the identification of the nucleus ^{79}Y For reasons that we are not able to understand the expected Z resolution and therefore the low cross-section was not reached with the set-up used in our experiment at the HRIBF facility. All the reaction parameters and detector settings were calculated in order to optimize the production and detection of ^{71}Kr ions at the focal plane detectors.

In principle the Z resolution in the IC at the focal plane depends on the velocity of the residue, and we will have an adequate Z separation for velocities $v >$ 4.6% of c [Jam91]. In fact, in the article of Lister *et al.* [Lis90] they claimed the poor Z separation obtained for the ^{76}Sr nucleus was due to the low velocity (v=5.4% of c) of the residue, but in any case it was enough to observe the nucleus of interest. In our case a velocity of v=4.2% was determined for 71 mass Br recoils. In figure 7.3 we show the Z separation obtained for A=75 mass nuclei (Br and Kr) which have a similar A/Q ratio to the A=71 mass nuclei of interest.

Therefore, we think that this lack of Z separation is the most important factor that has reduced drastically the sensitivity of the technique.

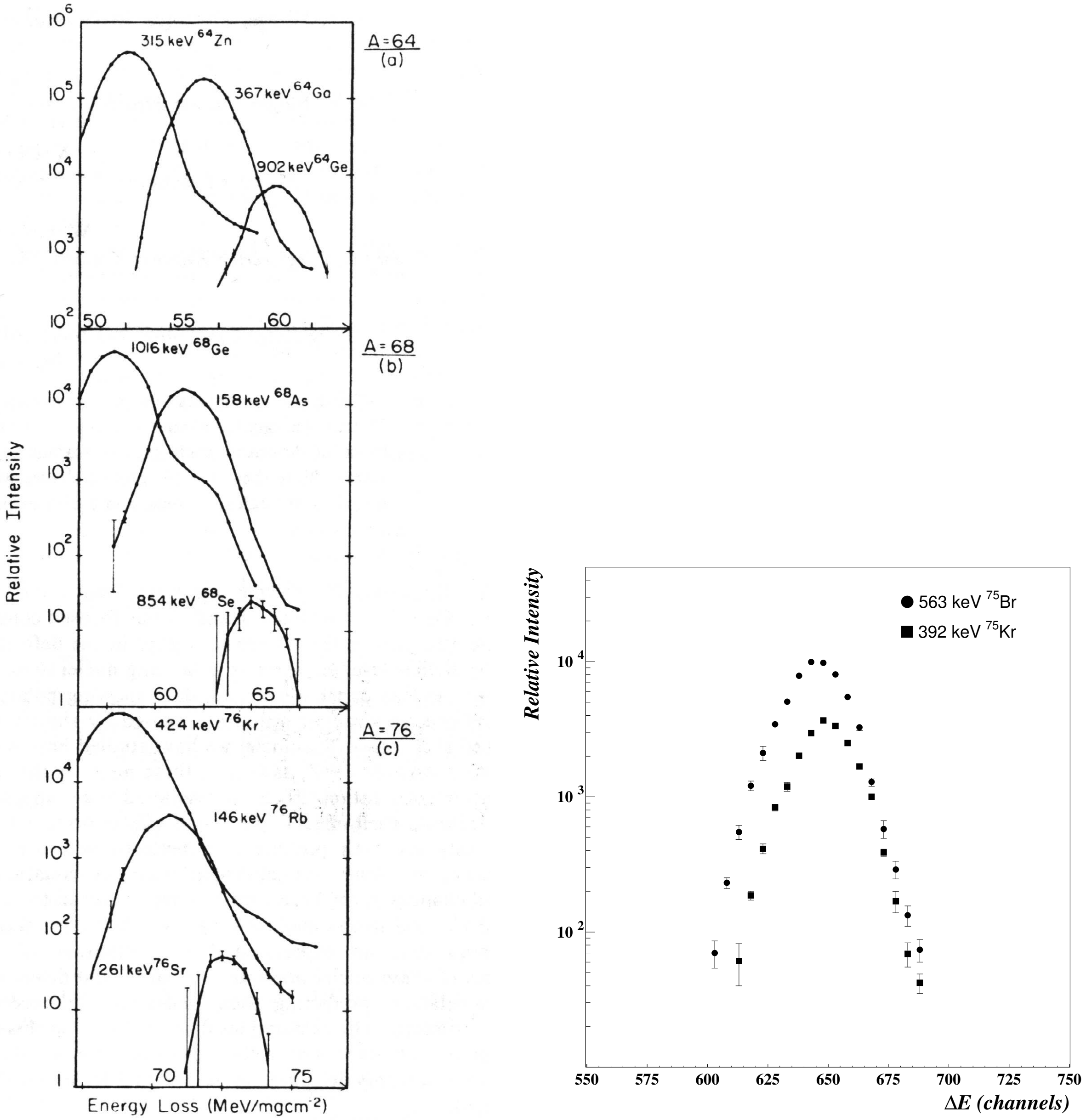

Figure 7.3: *Z separation observed in the Daresbury Ion Chamber (left) in three experiments* $^{12}C(^{54}Fe, 2n)^{64}Ge$, $^{12}C(^{58}Ni, 2n)^{68}Se$ *and* $^{24}Mg(^{54}Fe, 2n)^{76}Sr$ *where the recoil velocity was 6.3, 6.5 and 5.4 % of c respectively [Lis90]. On the right side we show the Z separation observed in the Oak Ridge Ion Chamber for* ^{75}Br *and* ^{75}Kr *nuclei produced in the reaction* $^{40}Ca +^{40} Ca$.

Chapter 8

Results for ^{70}Br

In this chapter we will present the results that have led to the first identification and to the spin assignments for the excited states of the N=Z, odd-odd ^{70}Br nucleus. The excited states of ^{70}Br have been studied in two experiments through the reaction $^{40}Ca(^{32}S, 1p1n)$ at a beam energy of 95 MeV. In the next sections we will describe the procedure followed to identify the gammas belonging to this odd-odd nucleus, the construction of the level scheme and the spin-parity assignments to the states based on the angular correlation data. Based on intensity and decay criteria, and also comparisons with similar odd-odd systems, we have assigned the isospin to the different states. Finally, we will try to present some ideas to interpret the features found in this nucleus and we will compare our results to the results obtained by other authors in the article [Jen02]

8.1 Identification and construction of the level scheme.

In the first experiment performed with the GASP spectrometer a few gammas were identified as belonging to ^{70}Br by requiring the coincidence with 1 proton detected in the ISIS Si telescopes and 1 neutron in the Neutron Ring detectors. In the second experiment with the EUROBALL spectrometer coupled to the EUCLIDES Si detector and to the Neutron WALL, higher statistics were collected confirming our identification and allowing the construction of a more precise level scheme.

In order to be sure of a correct identification of the γ transitions, various different E_γ-E_γ matrix projections corresponding to different particle conditions were compared. Thus, as a first step we have compared the projection spectra corresponding to events in which the gamma-rays are in coincidence with 1p1n and with 2p1n. Possible candidate transitions should be present in the first particle condition spectrum but not in the second. Amongst the possible candidate transitions most of them have been seen to proceed from the reaction of the beam with oxygen,

$^{32}S +^{16}O$; contamination due to oxidation of the target. Thus, lines that belong to ^{46}V (1p1n channel), ^{42}Sc (1α1p1n channel), etc., appear in the spectra as shown in fig 8.1.

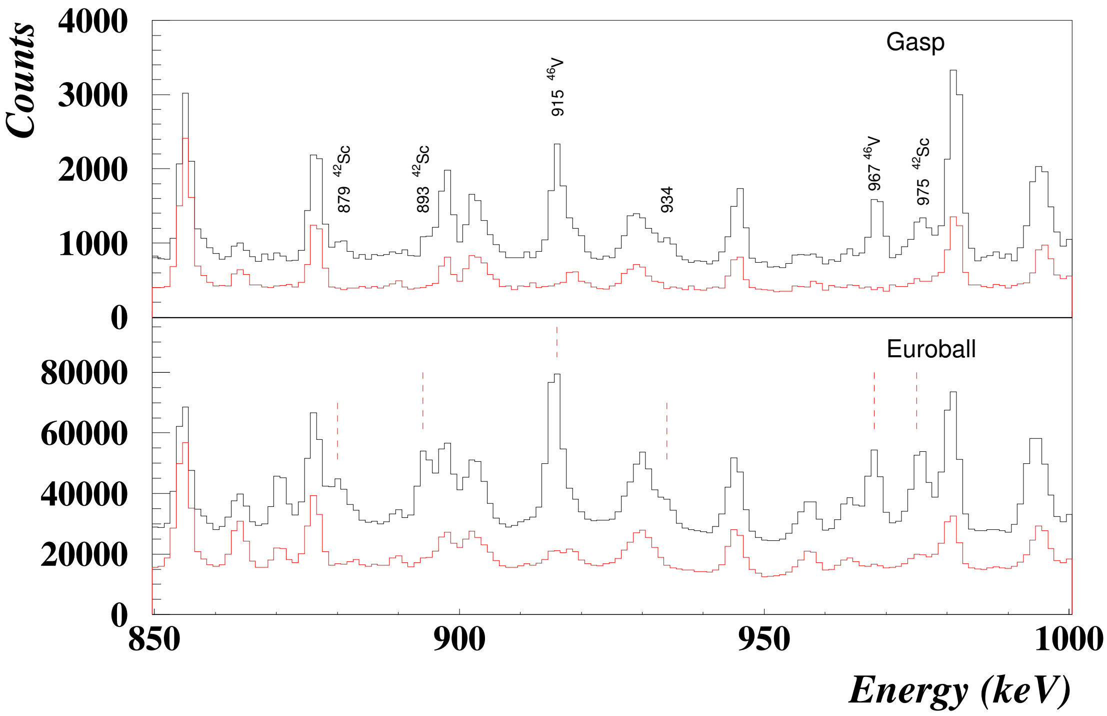

Figure 8.1: *A portion of the particle-gated γ projection spectra from the GASP and EUROBALL experiments. Possible γ-ray candidates are the transitions that appear in the 1p1n particle gated spectra (black) and not in the 2p1n spectra (red).*

In a second step we have put some gates on the proposed candidate transitions in order to see new coincident transitions. These gates allow us to confirm the candidate transitions and/or to check the presence of possible contaminants in the gates. In the figure 8.2 are shown different spectra in coincidence with some candidate transitions and different particle conditions. We can see how the transitions in coincidence with 0p1n and 1p1n disappear when we ask for two protons or one α in the event.

A further control has been made in order to validate the identifications. Thus, we have plotted the ratios of the γ intensities for transitions observed in coincidence with one proton in the EUCLIDES array to those without a proton in EUCLIDES, see figure 8.3 upper part. Transitions corresponding to the evaporation channel 1p and 2p are clearly separated and we can distinguish the candidate transitions of ^{70}Br from the transitions of ^{70}Se (2p exit channel). In addition, we have plotted similar ratios of the γ intensities for transitions in coincidence with one neutron

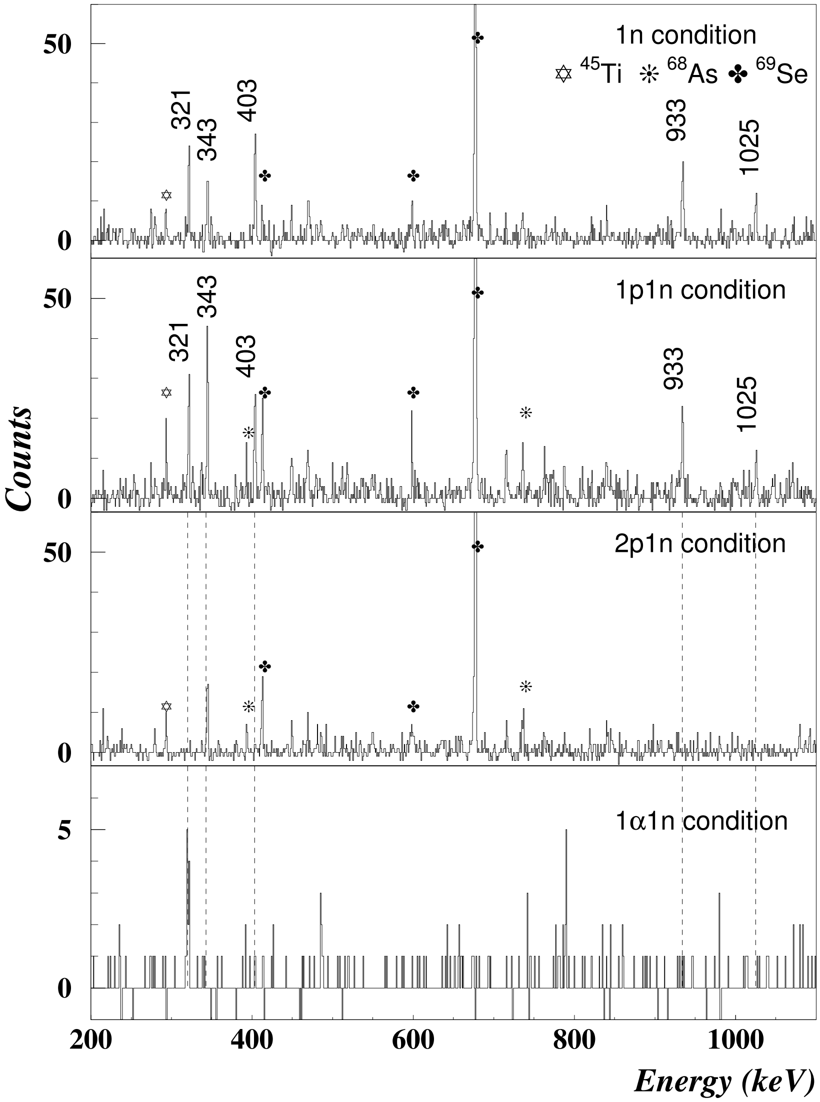

Figure 8.2: *Spectra of γ transitions gated on the 933, 321 and 1025 keV lines and in coincidence with different particle conditions in the GASP experiment (lower statistics).*

detected in the N-WALL and one proton detected in EUCLIDES to those with no neutron detected in the N-WALL and one proton in EUCLIDES (bottom part of the same figure). Transitions corresponding to ^{70}Br and ^{69}Se (2pn channel) are compared. The solid lines in the figure are the intensity ratios deduced from the detection probability, which is calculated according to the expression:

$$P(f, m) = \binom{m}{f} \varepsilon^f (1 - \varepsilon)^{(m-f)}, \tag{8.1}$$

where $P(f, m)$ is the probability to detect f identical particles out of m emitted, and ε is the particle detection efficiency. Thus, for the 1p and 2p exit channels the intensity ratios are:

$$R_{m=1} = \frac{I_\gamma(1p1n)}{I_\gamma(0p1n)} = \frac{\varepsilon_p}{1-\varepsilon_p} \qquad and R_{m=2} = 2\frac{\varepsilon_p}{1-\varepsilon_p}. \tag{8.2}$$

Inserting the particle detection efficiency obtained from the Euroball experiment, $\varepsilon_p \sim$ 58-60%, we obtain values of R_{1p}=1.4 and R_{2p}=2.8. For neutron evaporation channels we can follow the same exercise and we obtain a value of R_{1n}=0.4 for a detection efficiency of $\varepsilon_n \sim$ 28%.

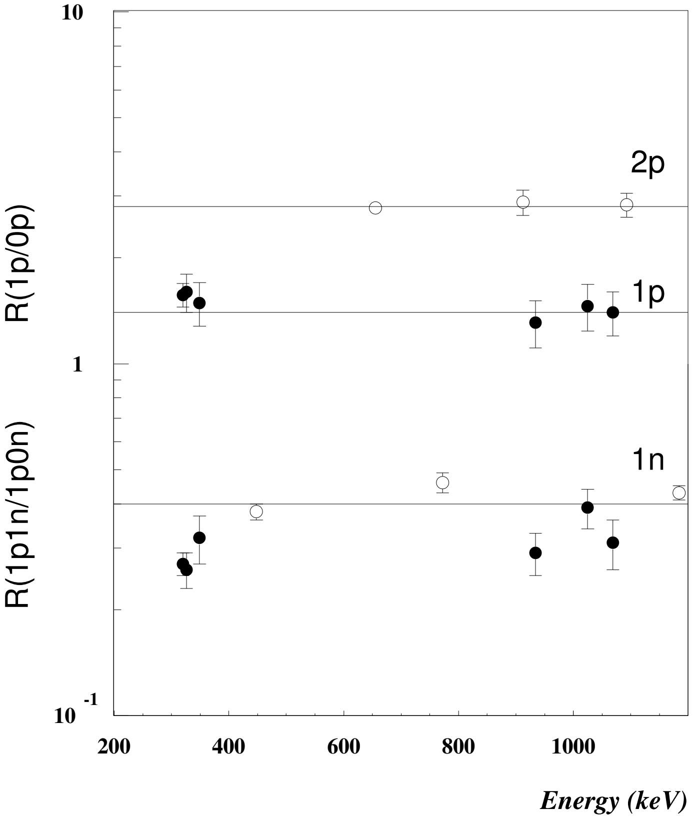

Figure 8.3: *Intensity ratios for selected γ -rays (321, 326, 350, 933, 1025 and 1069 keV) from the ^{70}Br pn reaction channel (filled symbols) and from the ^{69,70}Se 2pn and 2p reaction channels respectively (empty symbols) with and without proton detection (upper part). Comparison of the same transitions in ^{70}Br with transitions in ^{69}Se with and without neutron detection (lower part). The three solid lines show the calculated ratio values for the 1p, 2p and 1n reaction channels, see the text.*

8.2 Energy and intensity data

Once the identification was clear, the level scheme has been built based on the γ-γ and γ-γ-γ coincidences and on the relative intensities of the transitions. The level scheme is shown in fig. 8.4. The usual calibrations of energy and efficiency have been carried out making use of the standard sources ^{152}Eu and ^{56}Co. The intensities of the transitions were deduced from the gated spectra due to the difficulty of obtaining clear values from the projection. A value of 100 for the intensity of the 933 keV transition has been assumed. The values for the energies and intensities have been summarized in table 8.1

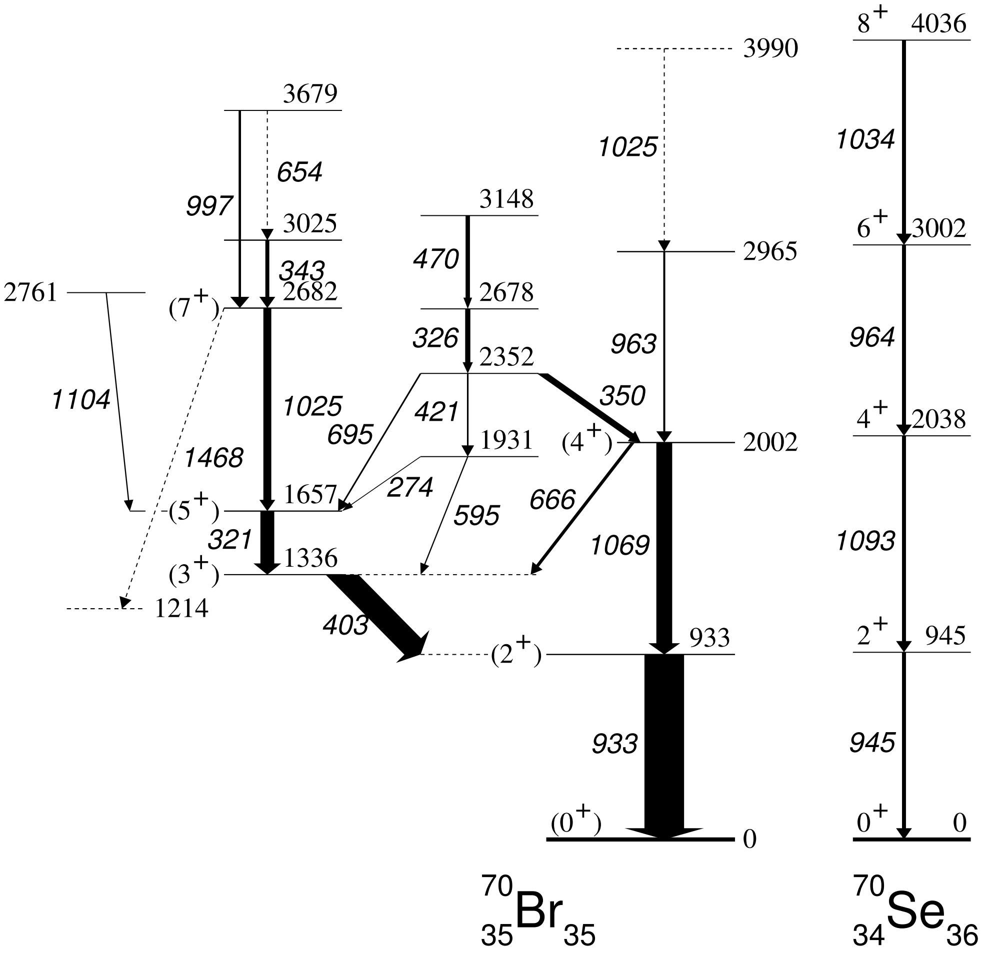

Figure 8.4: *Level scheme of T_z=0 ^{70}Br deduced from this work. The widths of the transitions are proportional to the intensities. For the lowest state I^π=0^+ T=1 is assumed; as a consequence all spin assignment are left in brackets. The T=1 states are compared with analogous states in ^{70}Se.*

8.3 Angular correlation data.

In order to extract information about the spin-parities of the levels we have created and analysed matrices corresponding to angular correlations between detectors placed at different angles as explained in chapter 4. For statistical reasons, we have used again the data from the Euroball experiment. Thus, we have determined the DCO ratios and the asymmetry of the main transitions in ^{70}Br.

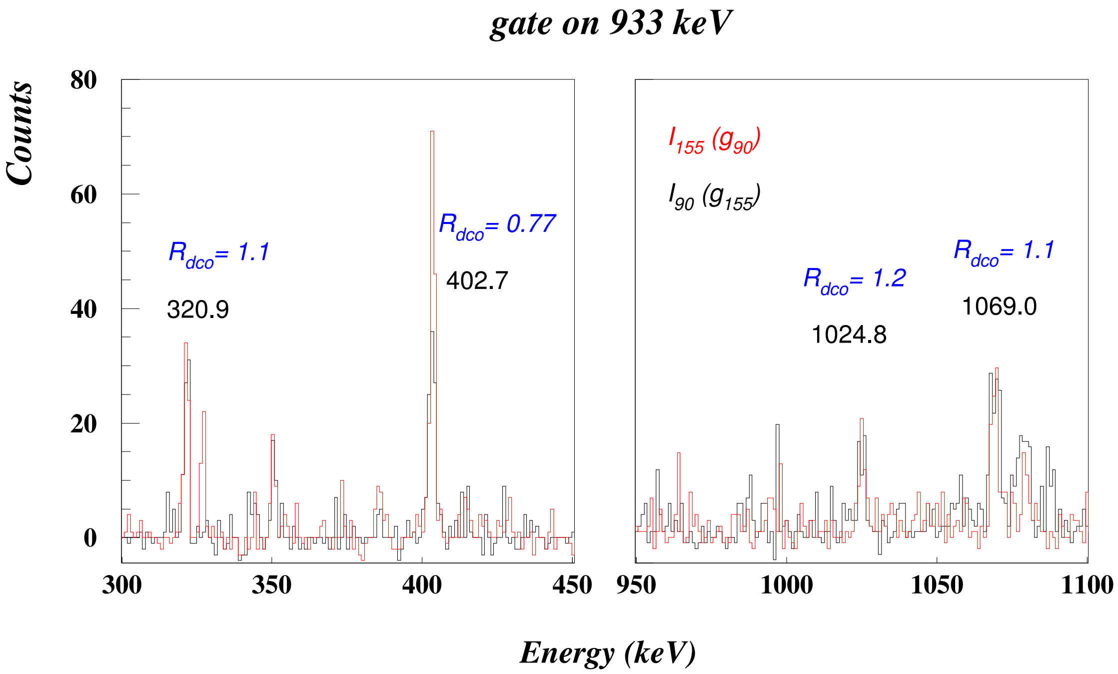

Figure 8.5: *Plot with the DCO gated spectra, Clover (red) and Cluster (black). The gate is set on the 933 keV transition in the cluster and clover rings respectively.*

In the case of the DCO ratios, a particle gated γ-γ matrix has been built with $E_{Clover}(90^o)$ versus $E_{Cluster}(155^o)$. In this way, asking for the events in coincidence with 1p1n we have reduced the contaminants as much as possible, even if it results in a reduction in statistics.

For the determination of the asymmetry, we have used the sensitivity of the Clover detector to the polarization and we have constructed two matrices: E_{all} vs $E_Q^{\perp}$ and E_{all} vs $E_Q^{||}$. The results of the analysis of these correlation matrices are summarized in table 8.1. A tentative assignment of spin-parity (I^{π}) has been tried for the excited states, based on the results from the angular correlation analysis and systematics.

E_{γ} (keV)	Intensity	DCO	Asymmetry	E_x (keV)	$I^i \rightarrow I^f$
274 (1)	2 (1)			1931	$\rightarrow(5^+)$
320.9 (4)	35 (4)	1.1 (3)	0.27 (17)	1657	$(5^+) \rightarrow (3^+)$
326.2 (5)	13 (2)	0.31 (14)	0.29 (17)	2678	
343.1 (5)	9 (2)	0.9 (2)	-0.09 (8)	3025	$\rightarrow(7^+)$
349.6 (5)	16 (2)	0.83 (15)	0.3 (4)	2352	$(5^+) \rightarrow (4^+)$
402.7 (4)	59 (6)	0.77 (11)	-0.06 (8)	1336	$(3^+) \rightarrow (2^+)$
421.0 (6)	4 (2)			2352	
470.4 (6)	11 (2)			3148	
595 (1)	3 (1)			1931	$\rightarrow(3^+)$
654 (1)	2 (1)			3679	
665.6 (6)	8 (2)			2002	$(4^+)\rightarrow(3^+)$
694.7 (5)	4 (1)			2352	$\rightarrow(5^+)$
933.4 (4)	100 (8)	1.1 (3)[a]	0.11 (10)	933	$(2^+)\rightarrow(0^+)$
963.4 (6)	5 (2)			2965	
997.0 (5)	6 (2)			3679	$\rightarrow(7^+)$
1024.8 (5)	20 (2)	1.2 (3)	0.05 (27)	2682	$(7^+) \rightarrow (5^+)$
1025 (1)	3 (2)			3990	
1069.0 (5)	41 (5)	1.1 (3)	0.04 (8)	2002	$(4^+)\rightarrow(2^+)$
1104 (1)	3 (1)			2761	$\rightarrow(5^+)$
1468 (1)	3 (1)			2682	

[a] Value obtained from the angular distribution ratio instead of from DCO

Table 8.1: Energies, relative intensities and angular correlations (DCO) or distribution ratios and asymmetries of γ-ray transitions assigned to ^{70}Br from the reactions used in the present experiments. The intensities are normalized to the 933 keV transition (assumed to be 100). The DCO ratios were obtained by gating on the stretched ΔI=2, 933 keV transition. Only for the 933 keV transition the angular distribution ratio was obtained from the singles spectra. In all cases particle gates were used.

8.4 The I^{π} assignments

In this section we summarise the results obtained from the two experiments carried out on the ^{40}Ca(^{32}S,pn)^{70}Br reaction and give an interpretation for the different states deduced. The I^{π} assignments are based on the angular correlation data (DCO and polarization) whenever possible. However, the statistics was so limited that one solution was preferred but never firm (all the I^{π} are written in brackets)

The 933 keV state

This state is de-excited via the 933 keV transition, the probable quadrupole nature of which has been deduced from the angular distribution ratio. The positive polar-

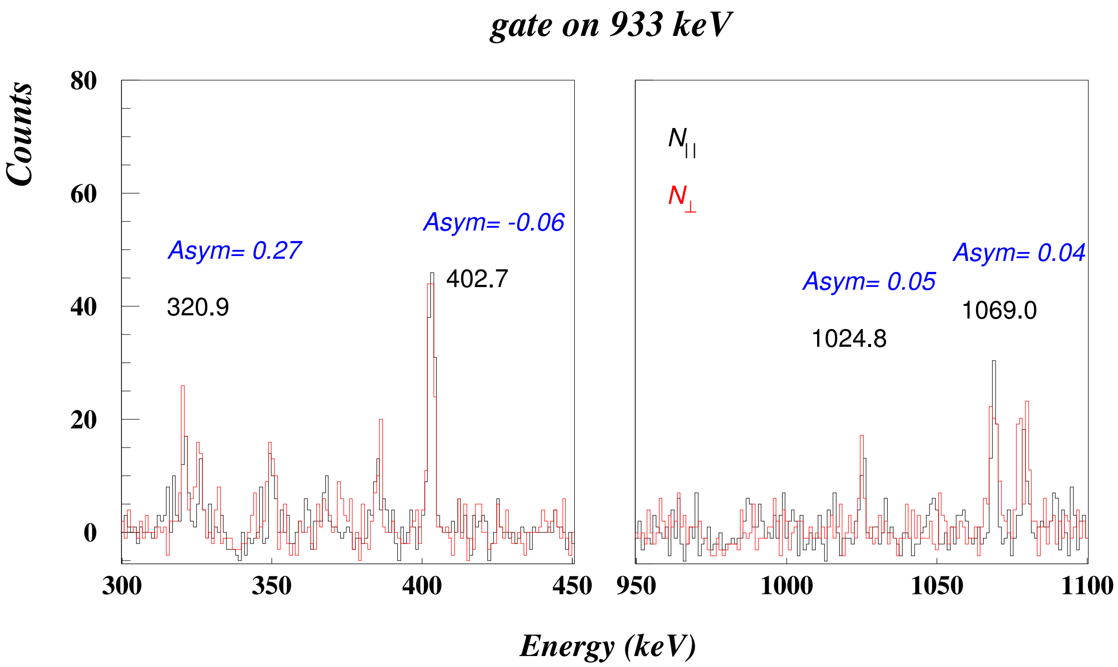

Figure 8.6: *Plot with the Clover gated spectra, parallel polarization (black) and perpendicular polarization (red). The gate is set on the 933 keV transition in the sum of all detectors.*

ization value indicates its electrical character. The I^π assignment of 2^+ has been preferred (with respect to a possible 11^+ built above the 9^+ isomer, described in chapter 2.3 page 27) due to the fact that we are dealing here with a reaction bringing low angular momentum to the compound nucleus. Therefore the strong population of an 11^+ state would be unlikely here. A level of similar energy is observed in ^{70}Se. The two 2^+ states are the isobaric analogue states.

The 2002 keV state

This state de-excites to the 933 keV state through the 1069 keV transition. The results from the DCO ratio and polarization measurements are consistent with E2 character, allowing us to suggest an I^π=4^+ assignment. From similarities with the 1093 keV transition in the ^{70}Se nucleus this state is suggested to be the isobaric analogue of the 2038 keV state in the bromine isotope.

The 2965 keV state

This state is deduced from the coincidence data and from comparison with the isobaric analogue state in ^{70}Se at an excitation energy of 3002 keV. The 963 keV transition is observed in the spectra gated by the 933 and 1069 keV gamma rays and in the double gated spectrum from the triple coincidences (see fig. 8.7). The last condition reduces drastically the possibility of it belonging to another nucleus. In fact, the intensity ratio of the 963 keV gamma ray between the $1p1n$ and the $0p1n$ gated γ-spectrum has a value of R=1.2 (8) which is consistent with the values expected for the *pn* channel (see figure 8.3).

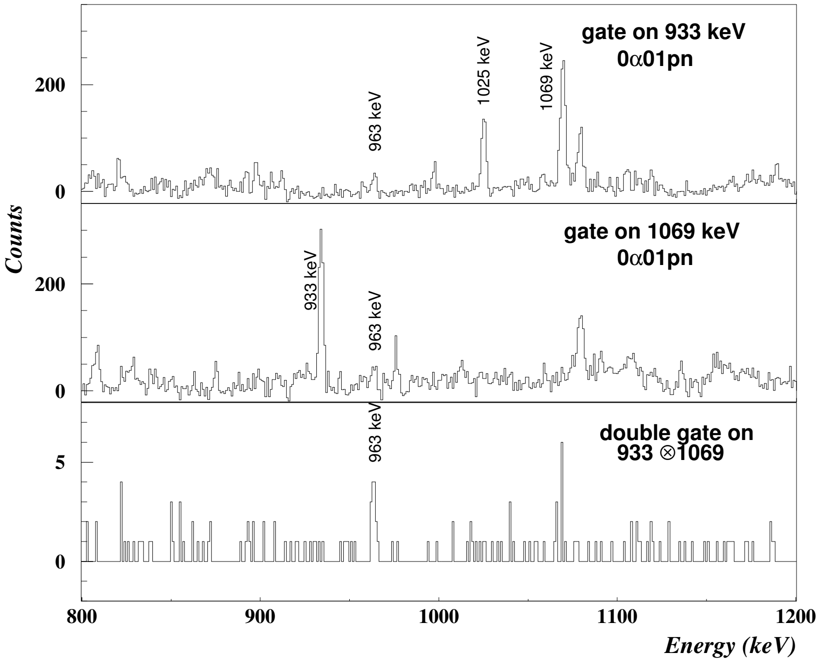

Figure 8.7: *Gamma gated spectra on the 933 and 1069 keV transitions and the double gated spectrum on both transitions showing the presence of the 963 keV gamma-ray transition de-exciting the 2965 keV state.*

The 3990 keV state

The 1025 keV transition de-exciting this state is observed in double gated spectra in coincidence with the other three members of the cascade of 933, 1068 and 963 keV γ-rays. The weak population of the state prevents a definitive assignment.

The 1336 keV state

This state is suggested to be $I^\pi=3^+$ based on the results of the DCO and polarization data for the 403 transition: $R_{dco}(403, 933) = 0.77(11)$ and Asym=-0.06 (8) or P=-0.26 (35) which are consistent with an M1 (+ E2, $\delta \sim 0.30$).

The 1657 keV state

This state de-excites via the 321 keV transition to the previous state. The DCO ratio and the asymmetry values are consistent with an E2 character. The spin-parity suggested for the state is therefore $I^\pi=5^+$.

The 2682 keV state

This state de-excites by the 1025 keV transition. The DCO ratio and the polarization values of $R_{dco}(1025.933) = 1.2(3)$ and Asym=0.05 (27) are consistent with E2 character for the transition, and would suggest that the state has $I^\pi=7^+$.

The 3025 keV state
This state de-excites via the 343 keV transition. The DCO ratio would suggest E2 character for the transition and therefore I$^\pi$=9$^+$. However the negative value of the asymmetry would rule out this option. A better suggestion would be a mixed transition and an I$^\pi$=8$^+$ assignment.

The 3679 keV state
The 997 keV transition that de-excites this state is observed in coincidence with the 1025 keV transition but with a very low intensity.

The 1931 keV state
This state has been established by observing the coincidence of the weak transitions that de-excite the state to the 1657 and 1336 keV levels. No additional information on correlations is available.

The 2352 keV state
This state is de-excited through three transitions: the 350, 421 and 695 keV γ-rays. The DCO ratio of the first transition $R_{dco}(350, 933) = 0.83(15)$ does not allow us to assign unambiguously the spin-parity of the state. In principle it is consistent with a mixed dipole-quadrupole transition but a pure quadrupole transition is not ruled out. Thus our suggestion would be I$^\pi$=(5,6$^+$).

The 2678 keV state
This level de-excites via the 326 keV transition. The DCO ratio $R_{dco}(326, 933) = 0.31(14)$ suggests a mixed multipolarity. The possible spin values could be I=5,6 or 7.

The 3148 keV state
This state de-excites via the 470 keV transition to the 2678 keV state. The low intensity of the transition does not allow us to make any spin-parity assignment.

The 2761 keV state
This state is suggested from the coincidence data where we can observe the presence of the 1104 keV transition in the spectra gated with 321, 402 and 933 keV transitions and not in the gate of the 1025 keV. There is no additional data from the angular correlations which allows us to suggest any value for the possible spin.

8.5 Interpretation of the ^{70}Br level scheme.

In the following section, we will analyse the main results obtained from the experiments performed in order to establish the features and structures of the self-conjugate ^{70}Br nucleus. The analysis of these structures through comparison with other known N=Z nuclei and within the actual background of theoretical models allows us to suggest some ideas behind the phenomena observed.

8.5.1 T=0 versus T=1 states.

The self-conjugate N=Z nuclei are special systems where the study of the symmetries between protons and neutrons in terms of proton-neutron correlations allows us to test recent developments in theoretical models. If we assume that the nuclear interaction is charge independent, that is, the proton-proton interaction has the same strength as the neutron-neutron interaction ($V_{pp} = V_{nn}$), it means that the nuclear interaction commutes with the operators of the total isospin:

$$T = t_1 + t_2 \tag{8.3}$$

Thus, the Pauli principle allows two nucleons to occupy the same state if not all quantum numbers are equal, and hence the states of two nucleons can be constructed as combinations of eigenstates of T^2 and T_3 with values T=0, T_3=0 and T=1, T_3=-1, 0, +1. These pairs of nucleons are called Cooper pairs and the eigenstates are interpreted as "superconducting" nuclear states within the BCS framework.

The charge invariance of the nuclear forces also means that the interactions in T=1 states have to be the same (*pp*, *nn* or symmetric *pn* states). However, they may be different in the T=0 states (antisymmetric *pn* states). Studying these states may allow us to look deeply into this issue.

In the N=Z nuclei bellow ^{100}Sn, both kinds of state that consist of *pn* pairs coupled to spin J=0,2,4,..., S=1 and isospin T=1 and pairs coupled to spin J=1,...,J=J_{max}, S=0 and isospin T=0 are available, due to the fact that protons and neutrons occupy the same orbitals and therefore the Fermi levels are nearly degenerate. The question of the importance of the contribution of both types of *pn* pair is still open. In this sense the structure of medium mass, odd-odd N=Z nuclei, in which the lowest T=0 and T=1 states are almost degenerate, is of particular interest.

In these unique cases one can study the interplay of T=0 and T=1 structures by means of the spectroscopy of bound states. As we mentioned in chapters 1 and 2 the odd-odd, N=Z systems are interesting from the point of view of the competition between T=0 and T=1 states. These states should be almost degenerate in the odd-odd systems while in the even-even systems the I^π=0^+, T=0 ground state is separated from the excited T=1 states by a large energy gap. Recently, some results on excited states in medium mass odd-odd N=Z nuclei in the A=60-80 region ^{58}Cu [Rud98], ^{62}Ga [Vin98], ^{66}As [Grz98], ^{74}Rb [Rud96] have been published. Our results on ^{70}Br can be added to the systematics in order to increase our knowledge of the low spin structure of the odd-odd N=Z systems.

As mentioned before, the analysis of the coincidences and intensities of the transitions has lead to the level scheme shown in fig. 8.4. From the analysis of the angular correlation and the polarization data we have suggested a tentative assignment of spins and parities to the main levels as we have explained in detail in the previous section. Here we will discuss the possible configurations of the excited states on the basis of the single-particle orbits involved that in our case correspond to the $p_{3/2}$, $f_{5/2}$, $p_{1/2}$ and the $g_{9/2}$ orbits as observed in neighbouring odd-A nuclei. Similarly to the rest of odd-odd N=Z nuclei we expect that the ground state of ^{70}Br will involve a *pn* configuration with a mixture of the subshells mentioned above. This admixture is responsible for the energy lowering of the T=1, I^π=0^+ ground state configuration below a T=0 configuration typical of odd-odd N=Z nuclei in the region A<40.

From the comparison with the isobaric analogue states in ^{70}Se, the states observed at 0, 933, 2002, 2965 and 3990 keV have been associated with T=1 states, with $I^{\pi}=0^+,2^+,4^+,6^+$ and 8^+. We should mention here that the last two states are too weakly populated to draw clear conclusions on the assignment. The rest of the states have been associated with the T=0 coupling type from comparison with the odd-odd, N=Z systematics and thus, we have a 3^+ state at 1336 keV and a 5^+ state at 1657 keV. The configurations of these states should involve mainly $\pi p_{3/2}\nu p_{3/2}$ and the $\pi f_{5/2}\nu f_{5/2}$ with some small admixtures from the other shells if the deformation is low. In the case of large deformation a configuration based on $\pi g_{9/2}\nu g_{9/2}$ should be considered.

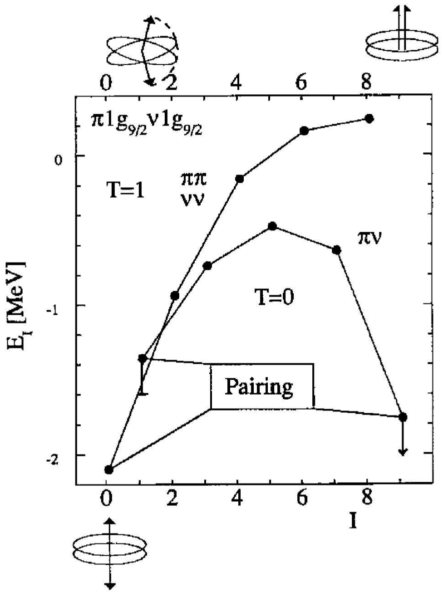

Figure 8.8: *Two-body nuclear residual interaction (NRI) for the different states built on the* $g_{9/2}$ *s-p orbit for configurations based on* $\pi\nu$ *and* $\pi\pi$ *or* $\nu\nu$*. Figure taken from [Gra97].*

The 7^+ assignment based on the DCO ratio and experimental polarization for the level at excitation energy of 2682 keV agrees with the systematics. This I^{π} can be obtained with a configuration based on $\pi\nu p_{3/2}f_{5/2}$ and also $\pi g_{9/2}\nu g_{9/2}$. Following the calculation of the $\pi\nu g^2_{9/2}$ two-body matrix element (TBME) [Gra97] we expect the 9^+ state lower in excitation energy than the 7^+ component of the multiplet. In fact from this calculation it turns out that the T=0, 1^+ and 9^+ are the most bound components of the multiplet (see figure 8.8). Thus, tentatively we have proposed the 1214 keV level, connected to the 2682 keV state by the weak 1468 keV transition as the 9^+ partner of the $\pi\nu g^2_{9/2}$ configuration.

In the figure 8.9 a comparison of the experimental levels obtained in this work with the states obtained with the interacting boson model has been presented.

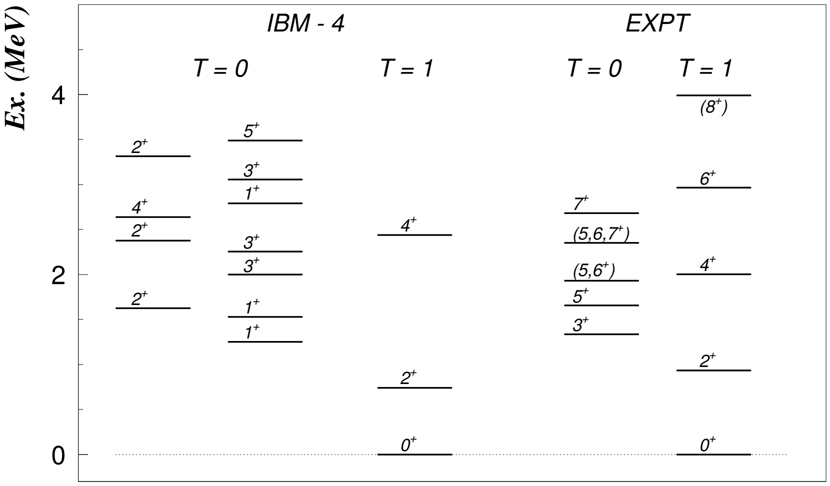

Figure 8.9: *Comparison of the experimental levels deduced in this work with the states obtained by Juillet et al. with the isospin invariant interacting boson model (IBM-4) [Jui01].*

A comparison of the excitation energy of the above mentioned T=0 states relative to the 0^+ state and the evolution with mass number A is shown in fig. 8.10. Different features can then be observed, such as the lowering of the 9^+ state, that can be associated with the $\pi\nu$ nuclear residual interaction when the orbit $g_{9/2}$ is occupied. We should mention here that such a 9^+ state does not appear in the calculation of reference [Jui01] although the $g_{9/2}$ orbital has been included.

Two aspects that have not been addressed by this experimental work tell us about the difficulty of dealing with these exotic nuclei. Firstly, from the experimental data no evidence of a low-lying state with $I^\pi=1^+$ has been observed as we expected from the systematics for the lowest T=0 states. Secondly, the lack of an estimate of the reduced transition probability $B(M1,3^+ \rightarrow 2^+)$ that in this kind of self-conjugate system should give information about the *pn*-quasideuteron coupling [Bre02]. New experiments to answer these questions would be useful.

8.5.2 Isobaric analogue states in ^{70}Br and ^{70}Se.

In principle, charge independence ($V_{pp} = V_{nn}$) together with the isospin symmetry ($V_{pp} = V_{pn}$) of the strong nuclear interaction would suggest the same binding energy for equal numbers of nucleons (taking into account the correction for proton-neutron mass difference) and would show nearly identical spectra in mirror nuclei. The

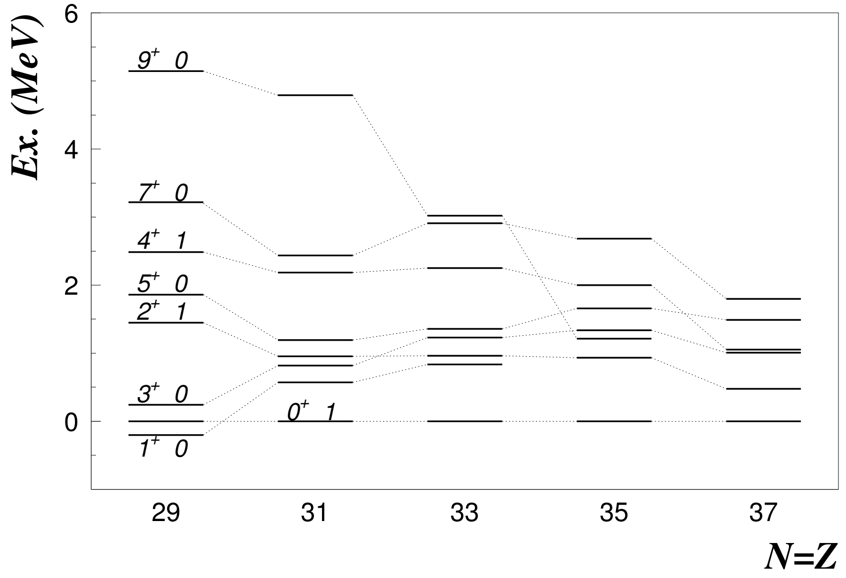

Figure 8.10: *Level systematics for odd-odd N=Z nuclei. The states are classified by (I^π, T) values. The excitation energies are normalized to the 0^+ states. Unidentified states were taken from isobaric analogue states as in the case of* ^{62}*Ga.*

Coulomb interaction is mainly responsible for that not occurring, but other effects have to be taken into account. In fact, Nolen and Schiffer found a deviation of $\sim$ 7% between calculated[1]values and experimental values of the difference between the binding energies of the ground states,

$$\Delta E_C = B(N+1, Z) - B(N, Z+1), \tag{8.4}$$

in mirror nuclei. This is the so-called Nolen-Schiffer anomaly (NSA) [NS69]. Several effects have been suggested (other than the neutron-proton mass difference) to explain this anomaly, among them there are: -core polarization, -electromagnetic contribution of the spin-orbit term, -finite proton size, -wavefunction Coulomb perturbation, -Coulomb distortion of the wavefunction of the level occupied by the valence proton (Thomas-Ehrman shift). Estimates of the sizes of these effects have been made [Aue83] but the size of the discrepancy has not yet been explained.

A related question is the Coulomb Energy Difference (CED) between isobaric analogue states (states of the same total isospin). In principle the difference in energy of the excited states relative to the ground state for the partners of a isospin multiplet could be interpreted as due to the Coulomb interaction and its influence on the wave function of the orbitals involved in the configuration of the excited states.

$$CED(I^\pi) = E_x(Z_>) - E_x(Z_<), \tag{8.5}$$

---

[1] Nolen and Schiffer have used a meanfield potential type for their calculations, reproducing well the π distribution radius but overstimating the ν distribution radius.

Recently, the CED has been studied in a series of experiments on nuclei of the $f_{7/2}$ shell. The behaviour of the CED has been studied in mirror nuclei A=47,49 (isobaric multiplets $T_z=\pm1/2$) up to high spins and it has been shown [Ole97, Ben98] to be sensitive to structural effects such as particle alignment, deformation changes and to the mechanisms by which the nucleus generates angular momentum. These effects give rise to changes in the spatial distributions and spatial correlations between valence nucleons and therefore to changes in the Coulomb energy with the spin.

Higher mirror isospin multiplets with T=1 have also been studied in this f-shell region, in particular isobaric analogue states with T=1 configuration have been studied in A=46,50 mass nuclei [Gar01, Len01]. The study of the CED between mirrors of these isobaric systems showed the influence of other "one-body" effects in the behaviour of the Coulomb energy differences along the yrast line. In particular, in the A=50 partners the Coulomb energy associated with levels where the valence nucleons occupy orbitals with different radii ($f_{7/2}$ and $p_{3/2}$), will change depending on the relative occupation of such orbitals and this occupation might change with excitation energy and spin. These differences contribute to the CED and were taken into account in the calculation.

These results have been reached with the aid of new developments in the theoretical models based on the fact that for the pf-shell nuclei there is a particularly large amount of experimental data. Higher mass regions, represent a challenge for this kind of models where more experimental data are welcome, especially now that some limitations in populating these proton rich nuclei are being overcome. In any case, studies of this type are difficult because not all the members of the multiplets are available due to the lack of statistics as a result of the proximity of the proton-drip line. A very interesting question should be how would the CED behave in these loosely proton bound or almost unbound systems.

In higher masses it is difficult to compare mirror nuclei because the most exotic one is normally not known experimentally. We will compare odd-odd N=Z systems with its $T_z=1$ partner. In these N=Z systems, under the assumption of the charge independence of the nuclear force, the states associated with the T=1 structure should have energies similar to those in the isospin multiplet partners (Z±1,N∓1). The slight differences are expected to be due to the Coulomb effects originating from the different numbers of protons within the multiplet members. The systematics of the CED between the isobaric analogue states in the N=Z nuclei and their respective $T_z=+1$ partners in the A=50-74 mass region is found to be positive and increasing with the spin (see figure 8.11).

From the data of this work, we have observed an anomalous behaviour of the excitation energies of the T=1 states in ^{70}Br, normalized to the ground state, compared to the energies of the isobaric analogue states in ^{70}Se [Myl89]. The CEDs between both partners ($T_z=0$,$T_z=1$) have negative values.

We have proposed a qualitative interpretation of the behaviour of the CED in terms of the Thomas-Ehrman Shift and residual interaction [Dea01]. When we compare the $T_z=0$ and the $T_z=1$ nuclei in mass A=70 we have to consider the fact

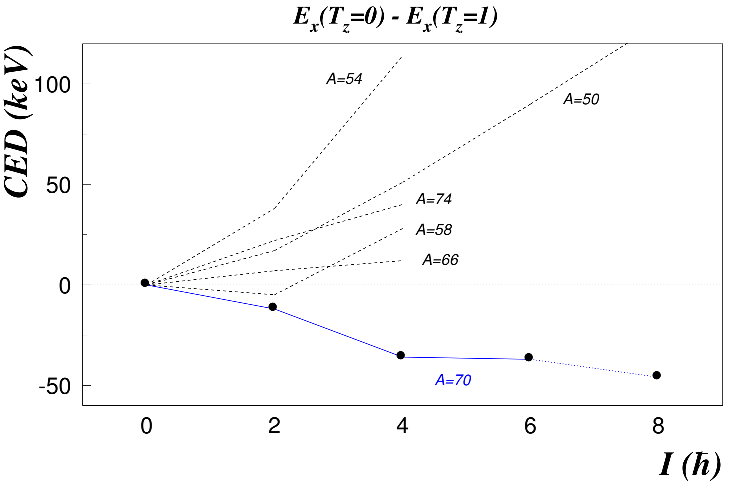

Figure 8.11: *Coulomb energy differences between isobaric analogue states in ^{70}Br (T_z=0) and ^{70}Se (T_z=1) nuclei as a function of the angular momentum. CED for other odd-odd system is also shown for comparison.*

that the last proton is only very weakly bound in the T_z=0 nucleus (S_p = 2600±400 keV). As a consequence the spatial wave function of this proton is more extended and the overlap with the wave function of the valence neutron and the rest of the nucleons in the nucleus decreases. This would have two different effects, one is the reduction in the Coulomb repulsion, which decreases the total mass for the state. This is the Thomas-Ehrman effect. In our case, the contribution to the ground state has low L number and therefore the effect is more pronounced for the 0^+. The result is an expansion of the spectrum. The other effect is a reduction in the atractive π-ν residual interaction, bigger in the 0^+ state because of the overlapping of the π and ν wave functions. The consequence of this is a compression of the spectrum. Since in our case we observe a compression in the spectrum, we conclude that the second effect dominates over the first.

Let us remember that the Thomas-Ehrman Shift generally occurs in the A∼16 region where the $1s_{1/2}$ proton is unbound or loosely bound (the 1S, L=0, wave function is not affected by the centrifugal barrier) and therefore it has a broad radial distribution. Here, the orbits involved have L≠0 but are still low enough to have some noticeable effect. Some authors, Ogawa *et al.* **??** include the effect of the nuclear residual interaction of this weakly bound proton with the neutron as a contribution to the energy shift, calling the total shift the Thomas-Ehrman Shift (TES).

We have calculated the $\pi\nu$ two-body matrix elements (TMBE) for a delta interaction using the Woods-Saxon single particle wave functions in the $pf_{5/2}g_{9/2}$ model space. When the proton separation energy is close to zero, the calculations show a

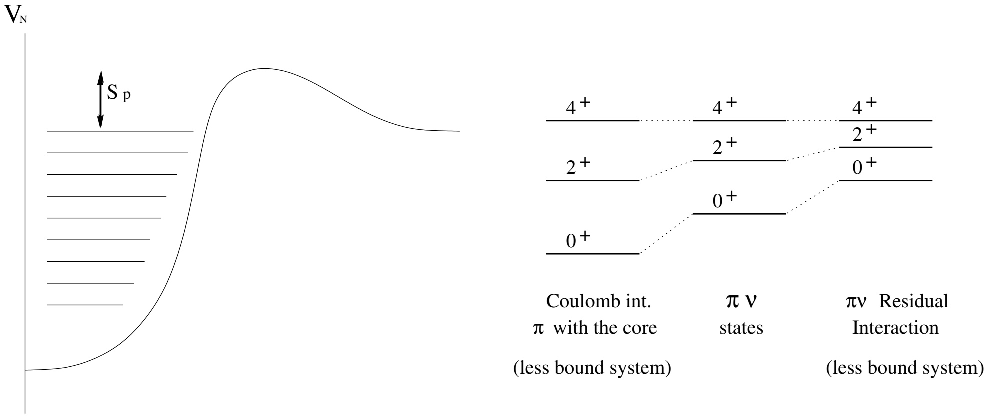

Figure 8.12: *Due to small proton separation energy, S(p), two effects take place in the nucleus energy spectrum: a decrease of Coulomb repulsion with a shift down of the states and a reduction of the residual pn interaction with a shift up of the states (schematic plot).*

reduction of the values of the TMBEs with respect to the $\nu\nu$ ones, of the order of 2-10 %. The effect depends on the single particle orbit involved, being larger for low-l values. This results in an increase of the excitation energy spectrum. A larger effect, of the order of 10-20 %, is calculated for the $\pi\pi$ matrix elements [Dea02].

8.6 Comparison with Jenkins *et al.*

The published work of Jenkins *et al.* seems to be more complete than our work due to the different kind of reaction used to investigate the structure of the ^{70}Br nucleus. In their study they populate the low spin states through the same reaction as us, the ^{32}S+^{40}Ca reaction, at 85 MeV. Then, using the ^{36}Ar+^{40}Ca reaction at 145 MeV they populate the ^{70}Br nucleus at higher angular momentum and hence this allows them to observe a rotational band built on the 9^+ isomeric state that goes up to spin I=(29^+).

As a result of their analysis of both data sets they have identified the gamma-ray transitions belonging to ^{70}Br. Using double and triple coincidences they have placed the candidate transitions in a level scheme. The low-spin part is basically similar to our level scheme, except for some weak transitions that we can see due to the higher statistics in our EUROBALL experiment.

In the article [Jen02] they disagree in some aspects with our work published in [Dea01]. Here, in this section, we will try to resolve the misunderstandings that we think have confused Jenkins et al. Thus, the first disagreement they mention are the intensities of some transitions reported in our level scheme and the spectra we showed in our article. In the paper we showed the GASP spectra, with lower statistics compared to the EUROBALL spectra because of the cleaner conditions of the GASP experiment. Indeed, in the EUROBALL experiment we have a factor of

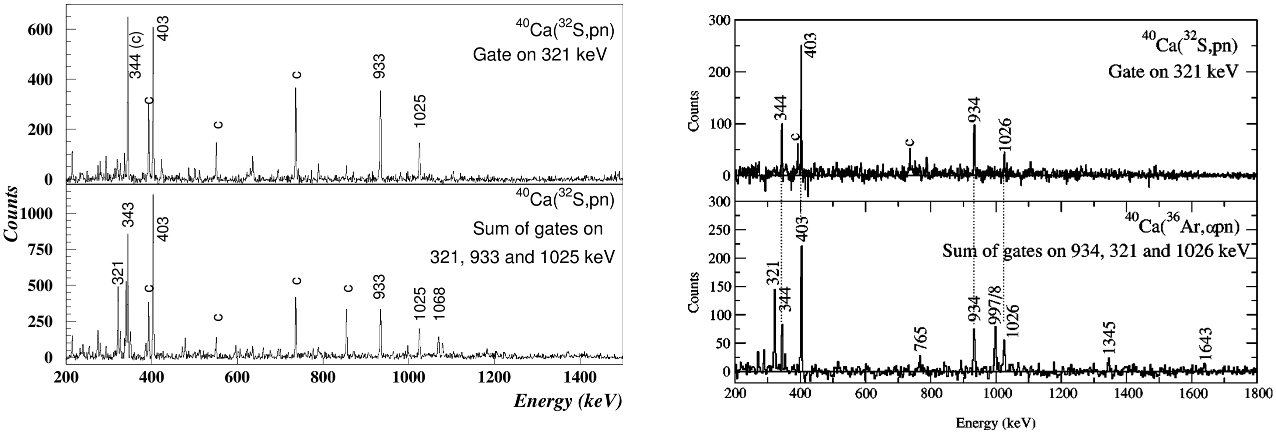

Figure 8.13: *Comparison of gamma gated spectra obtained from the experiment performed with EUROBALL, left, and with GAMMASPHERE, right. The right part of the figure is taken from [Jen02].*

10 more statistics than in the GASP experiment as we can see by comparing figure 8.2 to the figure 8.13. Then, from this last figure we can observe that we have a factor of 2 more statistics than in the experiment performed at gammasphere.

The second point, actually related to the statistics, is the presence of the 963 keV transition that we see from our data in coincidence with the 933 and 1069 keV transitions extending the T=1 band. Thus, in the figure 8.14 we show the gamma double gated spectra on the 933 and 1069 keV transitions obtained in our data (left panel) and the same spectrum as it appears in the article of Jenkins *et al.* (right panel). Therefore, the analysis of the triple coincidences in our higher statistics data set have allowed us to identify the 963 keV transition as belonging to the ^{70}Br nucleus.

Of course, in our EUROBALL experiment we have also more contamination from products of the reaction of the beam with oxygen and other target contaminants, as we can see in our spectra in the figure 8.13. But we have been able to reduce this contamination by doing a careful analysis of the particle gated gamma-gamma matrices. As a result Jenkins *et al.* have also deduced mainly the same candidate transitions in their low spin experiment.

8.7 Conclusions on ^{70}Br.

One of the aims of this thesis work has been the study of the proton rich N=Z ^{70}Br nucleus. Following the reaction $^{40}Ca(^{32}S, 1p1n)$ at 95 MeV beam energy, we have identified for the first time the low-lying excited states in this nucleus. The high sensitivity achieved by the combination of the two gamma spectrometers in

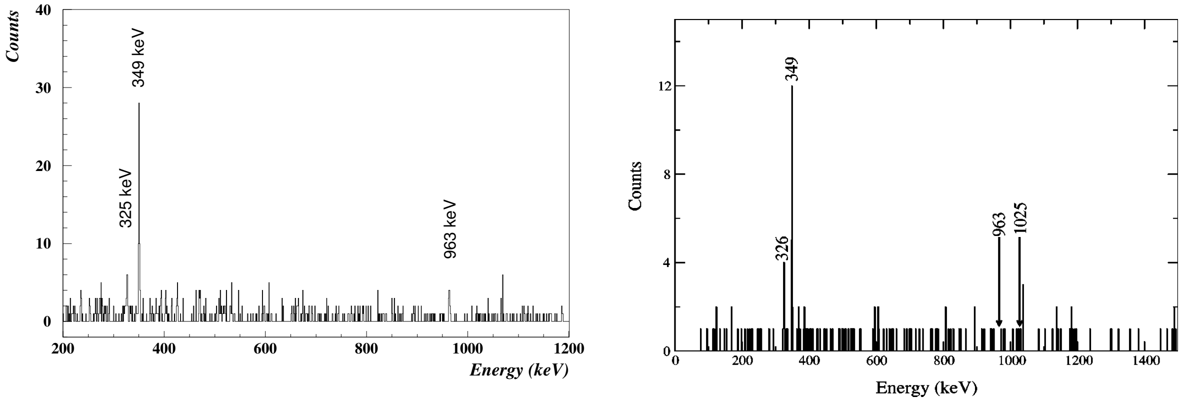

Figure 8.14: *Gamma spectrum double gated on the 933 and 1069 keV transitions. On the right panel of the figure we show the spectrum obtained by Jenkins et al.[Jen02]. On the left panel we show the spectrum obtained in our* $^{40}Ca(^{32}S,pn)$ *experiment with EUROBALL IV* γ*-spectrometer.*

combination with the charged particle and neutron detector systems have made possible this success.

From the correlation data (DCO and Polarization) of the most intense γ-ray transitions we have assigned spins and parities to most of the observed states. In principle, two main structures have been observed and assigned to states in which: *a*) the *pn* pair that defines the main features is coupled to isospin T=1 giving the ground state band with even spins and positive parity states, and *b*) a second structure, that crosses the previous one at spin $I^{\pi} \approx 4$ and therefore becomes yrast, corresponding to the *pn* pair coupled to isospin T=0.

An anomalous behaviour has been observed related to the even-spin states with T=1, the CED value obtained showed a negative trend as a function of the spin, while in other odd-odd self-conjugate systems the positive behaviour has been observed. A qualitative explanation in terms of the Thomas-Ehrman Shift and a reduction of the two body interaction due to the extended wavefunction originated from the almost unbound nature of the valence proton close to the drip-line.

Regarding the interpretation of the particular behaviour of the CED, one could raise some questions. The proton separation energy in the case of ^{66}As and ^{74}Rb are $S_p = 2700 \pm 220$ and $S_p = 2130 \pm 730$ keV very close to the $S_p = 2600$ keV for the ^{70}Br case. Thus we would expect the same behaviour. Why, if we are as close to the drip line in our case as for the ^{66}As and ^{74}Rb we have not observed positive values for the CED here? One reason is that we are dealing with very small differences, of the order of a few keV, and, as mentioned before, other effects have to be taken into account. The other reason, at least for the difference with the ^{74}Rb case, is that here the $g_{9/2}$ orbital (with higher L) might contribute more strongly to the configurations of the low lying states.

Bibliography

[Abe90] S. Aberg, H. Flocard and W. Nazarewicz, Ann. Rev. Nucl. Part. Sci. 40 (1990) 439.

[Arr90] J.W. Arrison, T. Chapuran, U.J. Hüttmeier and D.P. Balamuth, Phys. Lett. B 248 (1990) 39.

[Aud97] G. Audi, O. Bersillon, J. Blachot and A.H. Wapstra, Nucl. Phys. A 624 (1997) 1

[Aue83] N. Auerbach, Phys. Rep. 98 (1983) 273.

[Baz92] D. Bazzacco. Proc. Workshop on Large γ-ray Detector Arrays (Chalk River, Canada 1992) AECL-10613 p.376

[Bea92] C.W. Beausang et al., Nucl. Instrum. Methods A 313 (1992) 37.

[Bec92] F.A. Beck et al., Prog. Part. Nucl. Phys. 28 (1992) 443.

[Ben84] R. Bengtsson et al., Phys. Scr. 29 (1984) 402.

[Ben98] M.A. Bentley et al., Phys. Lett. B 437 (1998) 243.

[Bia89] J. Bialkowski et al., Nucl. Instrum. Methods Phys. Res. A 275 (1989) 322.

[Boh98] A. Bohr and B.R. Mottelson, *Nuclear Structure* I (1998) 411

[Bor99] C. Borcan et al., Eur.Phys. J. A 5 (1999) 243.

[Bor99a] C. Borcan et al., Eur.Phys. J. A 6 (1999) 481.

[Bre02] P. von Brentano et al., Nucl. Phys. A 704 (2002) 115c.

[Buc97] D. Bucurescu et al., Phys. Rev. C 56 (1997) 2497.

[Bur88] R.H. Burch et al., Phys. Rev. C 38 (1988) 1365.

[Cas90] R.F. Casten, *Nuclear structure from a simple perspective* (1990) Chap. 7.

[CERN81] F. James and M. Roos. MINUIT-Users Guide, Program Library D506. CERN. 1981.

[Coh74] S. Cohen et al., Ann. Phys. 82 (1974) 557.

[Dea97] G. de Angelis et al., Phys. Lett. 415B (1997) 217.

[Dea01] G. de Angelis et al., Eur. J. Phys. A 12 (2001) 51.

[Dea02] G. de Angelis, Private communication.

[Dia80] R.M. Diamond and F.S. Stephens, Ann. Rev. Nucl. Part. Sci. 30 (1980) 85.

[Dro96] Ch. Droste et al., Nucl. Inst. Meth. Phys. Res. A 378 (1996) 518.

[Dro99] Ch. Droste et al., Nucl. Inst. Meth. Phys. Res. A 430 (1999) 260.

[Duc99] G. Duchêne et al., Nucl. Inst. Meth. Phys. Res. A 432 (1999) 90.

[Ebe96] J. Eberth et al., Nucl. Inst. Meth. Phys. Res. A 369 (1996) 135.

[Eji89] H. Ejiri and M.J.A. de Voigt, *Gamma-ray and electron spectroscopy in nuclear physics* (1989) Chap.4,6.

[Fan47] U. Fano, Phys. Rev. 72 (1947) 26.

[Gad99] A. Gadea et al., “Experimental Nuclear Physics in Europe” (ENPE 99). Editors B. Rubio, M. Lozano and W. Gelletly, AIP Conference Proceedings 495 (1999) 195.

[Gal92] A. Galindo-Uribarri et al., Prog. Part. Nucl. Phys. 28 (1992) 463.

[Gar97] L.M. Garcia-Raffi et al., Nucl. Instr. and Meth. A 391 (1997) 461.

[Gar01] P.E. Garrett et al., Phys. Rev. Lett. 87 (2001) 132502.

[Gav80] A. Gavron, Phys. Rev. C 21 (1980) 230.

[Gel91] W. Gelletly et al., Phys. Lett. 253 B, 287 (1991).

[Ger92] J. Gerl and R.M. Lieder, EUROBALL III project (1992).

[Ger01] J. Gerl and W. Korten, AGATA project (2001).

[Gin99] T.N. Ginter, Ph.D. Thesis, Vanderbilt University (1999).

[Gra97] H. Grawe et al., Z. Phys. A 358, (1997) 185.

[Gri88] A.G. griffiths et al. Proc. Intern. Workshop Nucl. Struct. of the Zirconium Region, Bad Honnef, Germany, (1988) p.326

[Gri92] A.G. Griffiths et al., Phys. Rev. C 46, (1992) 2228.

[Gro00] C.J. Gross et al, Nucl. Inst. Meth. Phys. Res. A450 (2000) 12.

[Grz98] R. Grzywacz et al., Phys. Lett. B 429, (1998) 247. R. Grzywacz et al., Nucl. Phys. A 682, 41c (2001).

[Hag82] E. Hagberg et al., Nucl. Phys. A 383 (1982) 109.

[Ham74] J.H. Hamilton et al., Phys. Rev. Lett. 32 (1974) 239.

[Ham95] I. Hamamoto and X.Z. Zhang, Z. Phys. A 353 (1995) 145.

[Hee90] J. Heese et al., Phys. Rev. C 41 (1990) 1553; ibid 36 (1987) 2409.

[Her85] B. Herskind et al., Proc. Int. Conf. on Nucleon-Nucleon Collisions. Visby, Sweden, 1985.

[Ing54] D.R. Inglis. Phys. Rev 96 (1954) 1059.

[Jaa83] M. Jääskeläinen et al., Nucl. Instrum. Methods 204 (1983) 385.

[Jac87] B. Jäckel et al., Nucl. Inst. Meth. Phys. Res. A 261 (1987) 543.

[Jam91] A.N. James et al., Nucl. Inst. Meth. Phys. Res. B 53 (1991) 349.

[Jen02] D.G. Jenkins et al., Phys.Rev. C 65 (2002) 064307.

[Jui01] O. Juillet et al., Phys.Rev. C 63 (2001) 054312.

[Kei95] M. Keim et al., Nucl. Phys. A 586 (1995) 219.

[Kel02] N.S. Kelsall et al., Phys.Rev. C65 (2002) 044331.

[Klu92] E. Kluger et al., Nucl. Inst. Meth. Phys. Res. B 70 (1992) 41.

[Kno89] G.F. Knoll, *Radiation Detection and Measurements*, (Wiley, New York, 1979).

[Kor01] W. Korten, Acta Phys. Pol. B32 (2001) 729.

[Kra73] K.S. Krane et al., Nucl. Data Tables, 11 (1973) 351.

[Kre81] A.J. Kreiner et al., Phys. Rev. C 24, (1981) 148.

[Lee90] I.Y. Lee, Nucl. Phys. A 520 (1990) 641c.

[Len01] S.M. Lenzi et al., Phys. Rev. Lett. 87 (2001) 122501.

[Lis87] C.J. Lister et al., Phys. Rev. Lett. 59 (1987) 1270.

[Lis90] C.J. Lister et al., Phys. Rev. C 42 (1990) R1191.

[LNL90] GASP status project, 1990 LNL Annual Report (1991).

[Lob75] K.E.G. Löbner, in *The electromagnetic interaction in nuclear spectroscopy*, edited by W.D. Hamilton (North-Holland, Amsterdam, 1975) Chap. 5.

[Luh85] L. Lühmann et al., Phys. Rev. C 31 (1985) 828.

[Mar01] N. Mărginean et al., Phys. Rev. C 63 (2001) 031303(R).

[Mar02] N. Mărginean et al., Phys. Rev. C 65 (2002) 051303(R).

[Mar89] N. Martin et al., J. Phys. G. 15 (1989) L123.

[Mie99] Ch. Miehé et al., Eur. Phys. J. A 5 (1999) 143.

[Mol81] P. Möller and J.R.Nix, Atomic Data and Nuclear Data Tables 26 (1981) 165. P. Möller et al., Atomic Data and Nuclear Data Tables 59 (1995) 185.

[Myl89] T. Mylaeus et al., J. Phys. G. 15 (1989) L135.

[Naz85] W. Nazarewicz et al., Nucl. Phys. A 435 (1985) 397.

[Nil55] S.G. Nilsson, Mat. Fys. Medd. Dan. Vid. Selsk. 29-16 (1955)

[Nol85] P.J. Nolan et al., Nucl. Instrum. Methods A 236 (1985) 95.

[Nol94] P.J. Nolan et al., Ann. Rev. Nucl. Part. Sci. 45 (1994) 561.

[NS69] J.A. Nolen and J.P. Schiffer, Ann. Rev. Nucl. Sci. 19 (1969) 471.

[Oga99] K. Ogawa et al., Phys. Lett. B 464 (1999) 157.

[Oin97] M. Oinonen et al., Phys. Rev. C 56 (1997) 745.

[Ole97] C.D. O'Leary et al., Phys. Rev. Lett. 79 (1997) 4349.

[Ole99] C.D. O'Leary et al., Phys. Lett. B 459 (1999) 73.

[Pau92] G. Pausc et al., Nucl. Instrum. Methods Phys. Res. A 322 (1992) 43.

[Pau98] S.D. Paul et al., Phys. Rev. C 58 (1998) R3037.

[Pie00] A. Piechaczek et al., Phys. Rev. C 62 (2000) 054317.

[Pra88] C.R. Praharaj, J. Phys. G 14 (1988) 843.

[Puh77] F. Pühlhofer, Nucl. Phys. A 280 (1977) 267.

[Rei81] W. Reisdorf, Zeitschrift für Physik A 300 (1981) 227.

[Ril98] M.A. Riley (editor) GAMMASPHERE: The beginning...1993-1997. Lawrence Berkeley Laboratory, Berkeley, 1998.

[Rin80] P. Ring and P. Schuck, *The nuclear many-body problem* Springer-Verlag, (1980).

[Rip68] G. Ripka, *Advances in Nuclear Physics* Vol. 1 Ed. M. Baranger and E. Vogt. New York, Plenum 1968.

[Rud96] D. Rudolph et al., Phys. Rev. Lett. 76, 376 (1996).

[Rud98] D. Rudolph et al., Phys. Rev. Lett. 80, 3018 (1998) Nucl. Phys. A694, 132 (2001) and Phys. Rev. C 63, 021301 (2001)

[Sah89] R. Sahu et al., Pramana J. Phys. 32 (1989) 367.

[Sar96] D.G. Sarantites et al., Nucl. Instr. and Meth. A 381 (1996) 418.

[Sar98] P. Sarriguren et al., Nucl. Phys. A 635 (1998) 55.

[Sar01] P. Sarriguren et al., Phys. Rev. C 64 (2001) 064306.

[Sch98] H. Schatz et al., Phys. Rep. 294 (1998) 167.

[Sim80] R.S. Simon. J. Physique 41 (1980) C10.

[Ske99] Ö. Skeppstedt et al., Nucl. Instrum. Methods Phys. Res. A 421 (1999) 531.

[Sol99] G.Z. Solomon et al., Phys. Rev. C 59 (1999) 1339.

[Ste75] R.M. Steffen and K. Alder, “The electromagnetic interaction in nuclear spectroscopy”. Ed. W.D. Hamilton. North-Holland, Amsterdam (1975)

[Ste75a] F.S. Stephens, Rev. Mod. Phys. 47 (1975) 43.

[Str67] V.M. Strutinsky. Nucl. Phys. A 95 (1967) 420.

[Str68] V.M. Strutinsky. Nucl. Phys. A 122 (1968) 1.

[Twi75] P.J. Twin, “The electromagnetic interaction in nuclear spectroscopy”. Ed. W.D. Hamilton. North-Holland, Amsterdam (1975).

[Twi86] P.J. Twin et al., Phys. Rev. Lett. 57 (1986) 811.

[Urk98] P. Urkedal and I. Hamamoto, Phys. Rev. C 58 (1998) R1889.

[Vin98] S.M. Vincent et al., Phys. Lett. B 437, 264 (1998).

[Voi83] M.J.A. de Voigt, J. Dudek, Z. Szymański, Rev. Mod. Phys. 55 (1983) 949.

[Vos81] B. Vosicki et al., Nucl. Inst. Meth. 186 (1981) 307.

[Wie98] M. Wiescher et al., Phil. Tran. Roy. Soc. Lond. A 356 (1998) 2105.

[Wio88] M. Wiosna et al., Phys. Lett. B 200 (1988) 255.

[Wil73] J. Wilczyński, Nucl. Phys. A 216 (1973) 386.

[Wil82] J. Wilczyński et al., Nucl. Phys. A 373 (1982) 109.

[Wys99] R. Wyss, Private communication.

[Zga99] E.F. Zganjar et al., Perspectives in Nuclear Physics, World Scientific, Singapore, 1999, p. 187.